UTILIZATION OF PVDF SENSORS TO DETERMINE IMPACT DAMAGE IN GRAPHITE/EPOXY PLATES BY ACOUSTO-ULTRASONIC TECHNIQUE

I. Christine Smith

A Thesis
in
the Department
of
Mechanical Engineering

Presented in Partial Fulfillment of the Requirements
for the Degree of Master of Engineering at

Concordia University

Montreal, Quebec, Canada

August 1992

ISBN 0-315-81002-5

ABSTRACT

Utilization of PVDF Sensors to Determine Impact Damage in Graphite/Epoxy Plates by Acousto-Ultrasonic Technique

I. Christine Smith

The purpose of this study into the use of metallized polyvinylidene fluoride (PVDF) foil sensors in the detection of impact damage of graphite/epoxy plates is two-fold. First, to establish that low energy, low velocity impact damage of graphite/epoxy plates, undetectable through visual examination and ultrasonic C-scan can be detected through the acousto-ultrasonic (AU) technique. Secondly, to assess the utility of PVDF sensors in obtaining AU signals.

The AU approach to verification of material integrity is based on the premise that structural flaws will cause a greater attenuation of the ultrasonic pulse when compared to the attenuation of the signal through unflawed material. Through the AU technique, material structural integrity can be determined by comparative means. A comparison between two PVDF sensors of different thickness, a ceramic resonant transducer, and a ceramic wideband transducer was completed using a 6061-T6 aluminum test block. Extraneous noise was reduced from the acoustic signals received by the PVDF senors through common mode rejection circuitry. Graphite/epoxy test plates were ultrasonically C-scanned, the PVDF sensors were adhesively bonded to the test plates and used to evaluate the baseline structural integrity by AU signal gathering prior to impact testing. The plates were then subjected to impact and to AU evaluation with PVDF sensors to determine signal attenuation due to impact damage and subsequently ultrasonically C-scanned. The peak frequency and peak to peak voltage of the signal waveforms and the ultrasonic C-scans obtained before and after impact were compared. Pattern classification was used to correlate number of impacts with acoustic waveform features. Acoustic signal pattern classification was accomplished using ICEPAK™ software. After successive impacts and AU evaluation followed by ultrasonic C-scanning, the impacted and non-impacted areas of the test plates were cut into coupons and tested in compression to determine reduction in modulus due to impact damage.

ACKNOWLEDGEMENT

I am deeply indebted to my advisor, Dr. Suong Hoa for providing an opportunity to study composite materials at Concordia University and promoting a composites industry in Canada.

I am forever grateful to my sister Louise for her unwavering support and confidence in my abilities.

I would also like to express my gratitude to John Nagy for his guidance, and professionalism.

TABLE OF CONTENTS

TABLE OF CONTENTS (continued)

page

TABLE OF CONTENTS (continued)

page

APPENDICES

LIST OF TABLES

LIST OF TABLES (continued)

page

LIST OF FIGURES

LIST OF FIGURES (continued)

page

LIST OF FIGURES (continued)

page

1.0 INTRODUCTION

The aspects common to both ultrasonic and acoustic emission nondestructive evaluation techniques provide the basis for acousto-ultrasonics (AU). [1]* AU differs from acoustic emission and more widely used ultrasonics such as C-scan in that it is not a method for the determination of flaw location, size or type. Through AU, detection of global collections of flaws and material anomalies related to the overall material integrity can be assessed. [2] Each evaluation technique is comprised of three stages; stress wave generation, propagation, and detection. In acoustic emission, the test structure is under dynamic loading and transient elastic waves are generated within the material under stress due to rapid release of strain energy occurring at localized sites within the material. In composite materials, these sources may be voids, matrix cracking, fiber breakage, fiber/matrix disbonding, etc. In ultrasonics such as C-scan, wave generation is accomplished via an electromechanical transducer coupled to the test structure through filtered water. Reception of the ultrasonic signal may be through the transmitting transducer (pulse-echo) or a separate receiving transducer (through transmission). Both pulse-echo and through-transmission can be employed in flaw localization by detecting the changes in reflection (signal energy) of the ultrasonic signals. [3] In AU, both the transmitting and receiving transducers are acoustically coupled directly to the test structure and the material is treated as a vibrating structure. [4,5] Through the source (transmitting) transducer, a mechanical excitation is applied to the surface of the test structure. The resulting vibration characteristics of the test structure have been shown [4,5,6] to be affected by the material integrity. Structural flaws such as discontinuities, intralaminar and interlaminar cracks in composites, voids and stress concentrations due to specimen geometry cause changes in the signal waveform as it propagates through the test material. The changes in the signal waveforms are used to determine overall material integrity. A material of good integrity will demonstrate less scattering of the signal between the transmitting transducer and the receiving transducer than a material of poor integrity. [5,7] Through comparison

[*] Numbers in square brackets refer to references at the end of thesis.

of signal waveforms, changes such as signal attenuation can be used to identify occurrence of impact on the test structure and degree of damage with respect to change in stiffness (modulus).

Graphite/epoxy composites are susceptible to impact damage due to their inherent brittleness. Relatively low energy impacts can cause interlaminar damage while little or no damage is detectable on the surface. Impact by tools dropped during assembly of composite structures can reduce strength and stiffness and create sites of micro cracking undetectable by visual examination and C-scan examination. [8]

1.1 Acoustic Waves & Waveforms

Acoustic waves propagating in a material are comprised of longitudinal waves, shear waves and surface acoustic waves (Rayleigh waves). Coupling of the acoustic waves exists in elastic solids having intersecting surfaces (corners). [9] Acoustic waves propagating in isotropic materials belong to three modal types; one longitudinal and two transverse (shear). Group velocity of the longitudinal waves is in the direction of the acoustic wave propagation vector. The shear wave polarizations (vibrational modes) are transverse to the propagation vector. [10] Surface acoustic waves are generated at the free surface of an elastic solid and on surfaces constrained in both normal and tangential directions. [9] They are comprised of two propagation vectors; one parallel and one normal to the elastic surface. [10] Surface acoustic waves propagating in anisotropic materials such as fiber reinforced composites belong to three distinct modal types; one quasi-longitudinal and two quasi-shear. The phase and group velocities depend on the direction of wave propagation in the material and the group velocity direction does not coincide with the normal to the wave front. [11,12] Wave propagation is a function of frequency, where attenuation of wave motion increases with frequency in anisotropic materials. [9] Fiber reinforced composites exhibit high signal attenuation due to scattering and diffraction of waves through complex (anisotropic) fiber media and absorption of energy by the matrix and it is therefore necessary to examine wide frequency ranges. [9,12] Use of a wideband transmitting and receiving

transducer during AU evaluation allows a greater range of frequencies to be examined and more information may be derived from the signal. [4]

The theoretical waveform generated from a seismic surface pulse due to a point source is given in Fig. 1-1. The longitudinal (P) wave causes oscillation of structural particles parallel to the direction of the wave motion. The shear wave (S) causes particles of the structure to oscillate perpendicular to the wave motion resulting in a slower wave speed and later arrival time. The Rayleigh (R) surface waves are generated by reflection of the P and S waves at the surfaces of the structure. Complex geometries and anisotropic media (fiber reinforced composites) result in more reflection of waves propagating through the structure. [9]

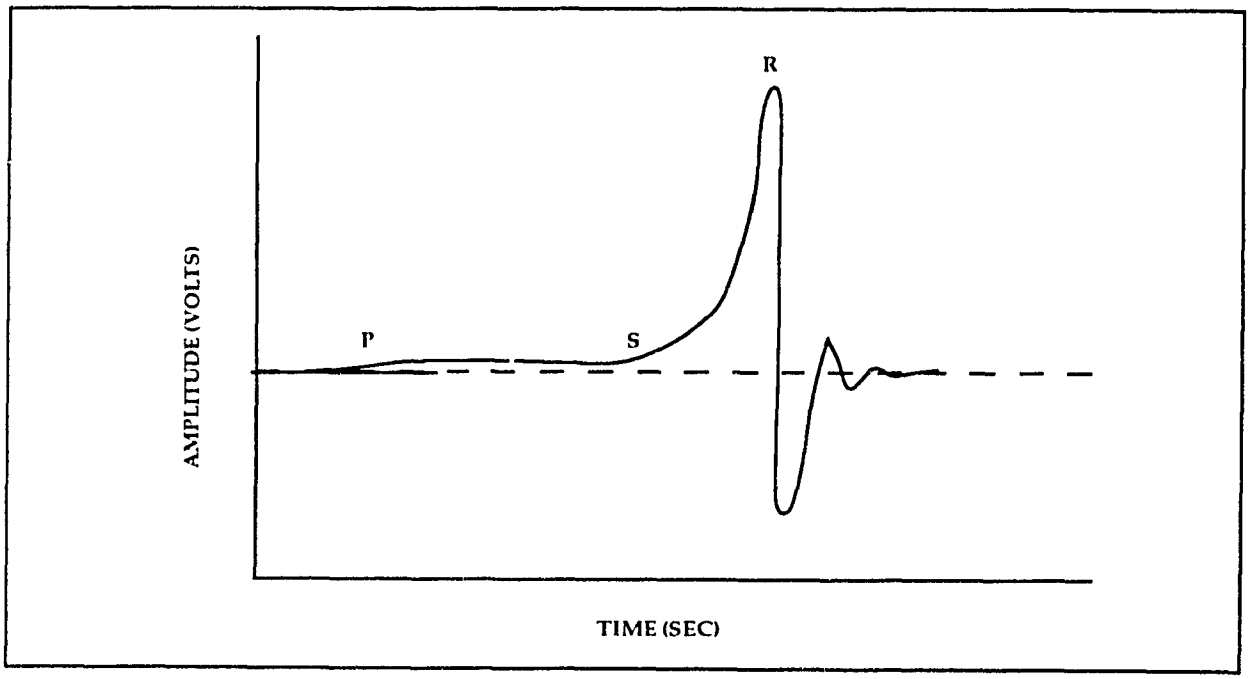

Fig. 1-1: Theoretical Waveform Generated from a Seismic Surface Pulse Due to a Point Source [9]

The acoustic signal waveform is affected by characteristics of the source, the signal path (material properties) from the source to the receiver, the receiver characteristics,

and the measuring system (Table 1-1). Through the use of piezoelectric transducers, a voltage-time signal waveform characterizing the vibrations at the surface of a test material is obtained. The voltage-time signal waveform is identified through cumulative characteristics of the waveform such as; amplitude, signal duration, rise time, decay time, number of counts above a predetermined threshold, etc. (Fig. 1-2). Signal waveform information is extracted and waveforms are compared by statistical means. [1,2] Time-domain (amplitude versus time) data can be transformed into frequency-domain (amplitude versus frequency) data by Fast Fourier Transformation (FFT). The Fourier transformation algorithm splits the time-domain signal into N narrow bands (data points) over a time interval T. The signal amplitude, expressed in decibels (dB), versus frequency, expressed in hertz (Hz), can then be compared. Frequency-domain information is used to measure the signal energy over a range of frequencies. [5,13]

Table 1-1: Test and Material Parameters Affecting AU Signal [14,15,16]

Test Surface	-surface flatness
	-coupling medium (method of adhesion)
	-contact pressure
Signal Transmitter	-transducer type (resonant, wideband)
	-pulse rate
	-pulse energy
	-signal type (pulse, burst)
Signal Receiver	-sensor type (resonant, wideband)
	-gain
	-time interval (window)
	-extraneous noise
	-signal gating
Distance between Transducers	
Method of Support (fixed or free)	
Structure	-method of processing (cure cycle)
	-morphology (degree of isotropy)
	-internal interfaces in structure (adhesive joints)
	-defects (voids, discontinuities, fiber breakage)
Geometry	-area
	-thickness
	-edge conditions (corners)
Material Properties	-elasticity
	-density

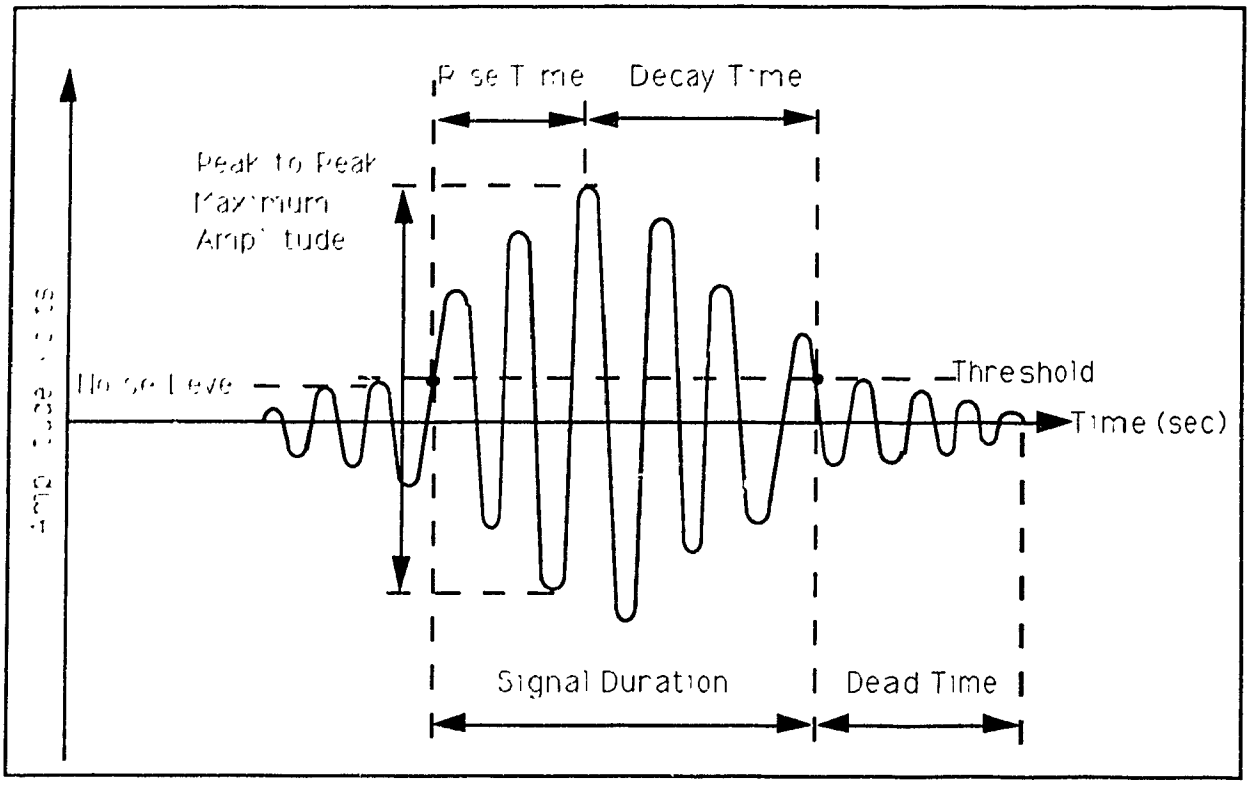

Fig. 1-2: Acoustic Signal Waveform Characteristics [9]

1.2 Piezoelectric Transducers

The stress waves which travel through a structure cause vibrational modes which can be detected by piezoelectric transducers. A piezoelectric transducer transforms the particle motion caused by bulk and surface waves on the surface of the structure into a voltage-time signal. The electrical signal is strongly influenced by the transducer characteristics. Polyvinylidene fluoride (PVDF) is a semicrystalline polymer material which exhibits high electromechanical coupling and piezoelectric properties. Mechanical processing of PVDF which includes unidirectional stretching, thermal treatment to orient the crystallites, and electric poling results in a thin film capable of strong piezoelectric effect. Subsequent metallizing of the film surfaces allows capacitive storage of the energy released by the film vibration. [17,18,19,20] Commercial type resonant and wideband transducers use ceramic piezoelectric elements such as lead zirconate titanate (PZT). Resonant transducers have high sensitivity in a narrow frequency

band. The piezoelectric element oscillates (rings) at or near a natural frequency producing an exponentially decaying sinusoidal voltage and the transducer response is biased by the resonant frequency and the harmonics of the piezoelectric element. [21] Wideband transducers use superposition of multiple resonances to give high sensitivity in narrow bands within a specified bandwidth. The response is independent of frequency since damping prevents oscillation at the natural frequency. [9,21]

The PVDF sensor films and pre-assembled sensors chosen for this study are distributed by Pennwalt Corporation. The sensor films have a film thickness of 52 μm and 28 μm, nickel copper (NiCu) metallized surfaces and are purchased in sheets of 15 cm by 30 cm (6 inch by 12 inch). The pre-assembled sensors have a film thickness of 28 μm and silver (Ag ink) metallized surfaces. The pre-assembled sensors are purchased in a bi-morph arrangement (folded over and inner surfaces bonded together) to produce a configuration as indicated in Figure 1-3, with an active element dimension of 35 mm by 12.7 mm (1.375 inch by 0.500 inch). A shielded plastic base provides a pressure contact to connect the active and ground surfaces to a shielded cable lead. The outer film surface acts as a ground while the laminated inner surfaces provide a voltage output when subjected to any in-plane movement (surface vibration). The pre-assembled sensors have a frequency response range of 40 MHz. [18]

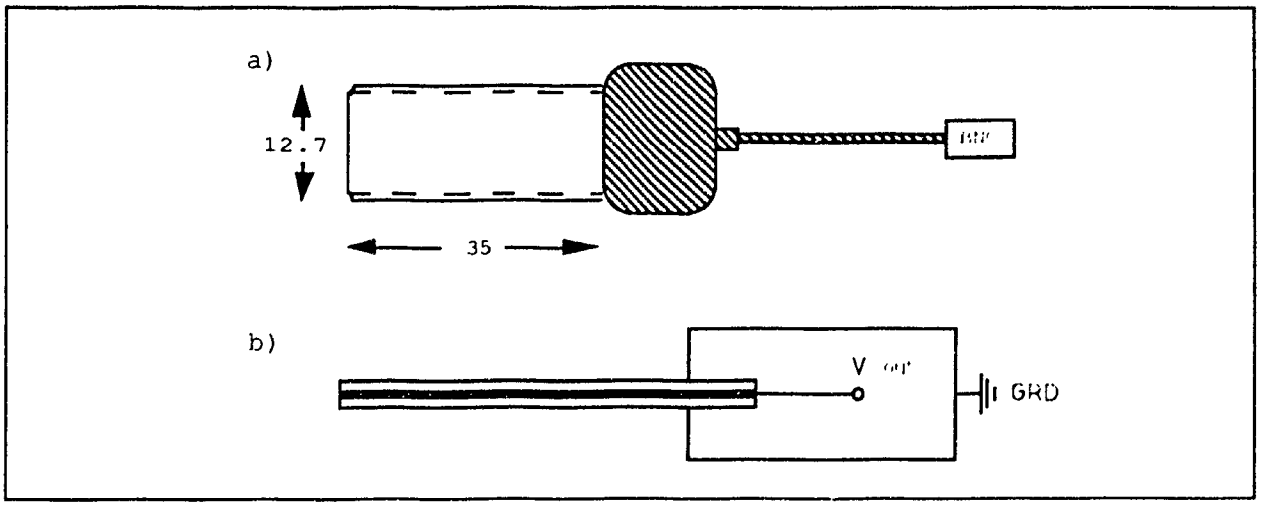

Fig. 1-3: PVDF Sensor; a) Pre-Assembled with Shielded Cable Lead, b) Bi-morph Assembly Configuration [18]

1.3 Theory of Acousto-Ultrasonic Technique

The AU technique is based on the assumption that vibrational waves, artificially introduced on to the surface of a test structure will simulate the spontaneous stress waves that would be generated in the structure during dynamic loading. The response of these benign stress waves to macroscopic and microscopic material defects corresponds to the response of the generated stress waves occurring during dynamic loading. Through AU the interaction of stress waves to material morphology can be used to comparatively determine changes in structural integity. [1,2,5,7,22]

The AU signal gathering technique is illustrated in Figure 1-4. The source transducer (ST) and receiver transducer (RT) are coupled directly to the test piece. Longitudinal (P) waves are introduced into the test piece by oscillation of the source transducer piezoelectric element. The P waves generate shear (S) waves propagating in the direction normal to the material displacement. The resulting surface waves (R) (combination of P and S waves) excite the piezoelectric element in the receiver transducer. In the case of PVDF sensors, the resulting surface waves cause a voltage change due to compression and expansion of the piezoelectric film. [23]

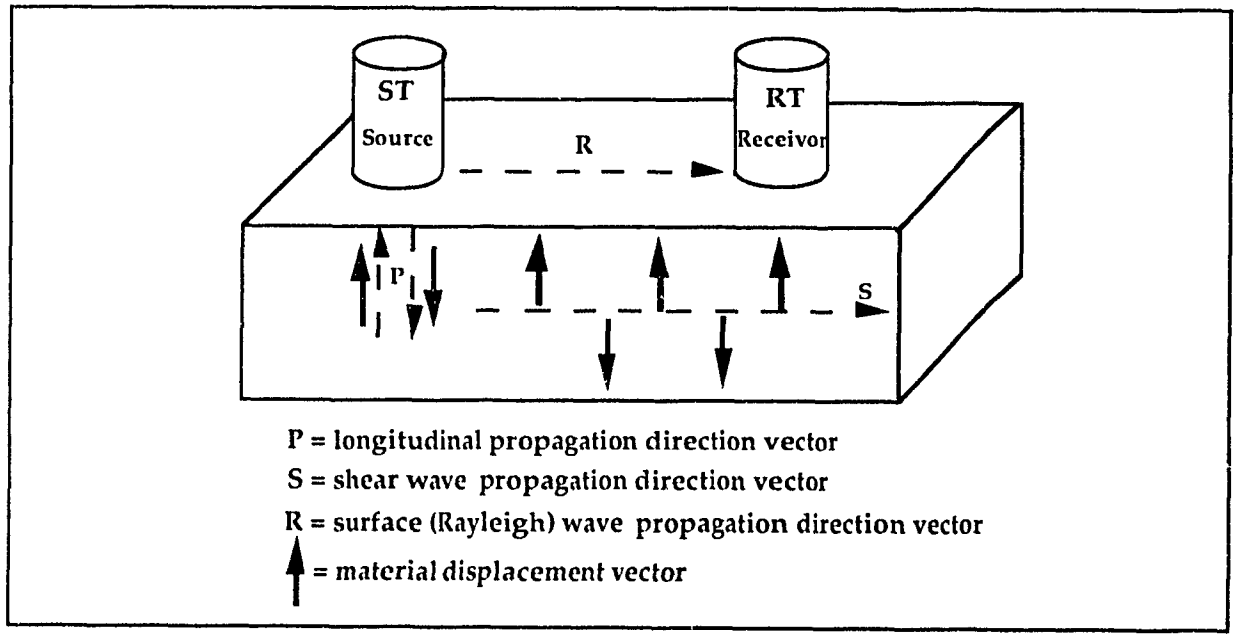

Fig. 1-4: Propagation of Transmitted Signal in Test Material to Receiver [23]

Time-domain information (Fig. 1-2) is obtained by capturing the received signal on a digital oscilloscope. Frequency-domain information is obtained from the time-domain signal by signal processing. In spectral analysis the digitized waveform is transformed into frequency-domain phase and amplitude information by Discrete Fourier Transform (DFT). Fast Fourier Transformation (FFT) approximation algorithms are used to reduce the computation time required for DFT. The frequency components present in the time-domain signal are used to measure the energy in the digitized signal. The frequency power spectrum is used to determine the peak amplitude, calculated in decibels (dB), occurring at peak frequency, calculated in hertz (Hz), within the maximum frequency range. [5,13,24] The maximum frequency range is dictated by the Nyquist frequency limit. The Nyquist limit is equal to the number of data points (N) divided by twice the time interval (T) or one half of the sampling frequency. [25]

The changes in the time-domain information and the changes in the frequency spectrum components are used to evaluate changes in the signal waveform and change in material morphology.

1.4 Ultrasonic C-Scan Damage Detection in Graphite/Epoxy Composites

Conventional ultrasonic evaluation involves C-scan imaging. Under C-scan evaluation, the test piece is placed in an immersion tank filled with filtered water (used as a couplant) (Fig. 1-5). In pulse-echo C-scan an indexing mechanism passes a source/receiver transducer over the test piece in incremental steps. The step size determines the scanning resolution (lines/mm). The source transducer injects sound (rf) waves into the water which propagate to the test piece. A portion of the acoustic waves are reflected back to the transducer due to changes in acoustic impedance of the materials at each interface. [26] The reflected signals (echoes) are used to detect changes in signal amplitude due to delaminations in the fiber reinforced composites. [8,27]

Ultrasonic C-scan images are generated by gating radio frequency (rf) A-scans (Fig. 1-6). Software gates control the amount of signal being received by the signal processor,

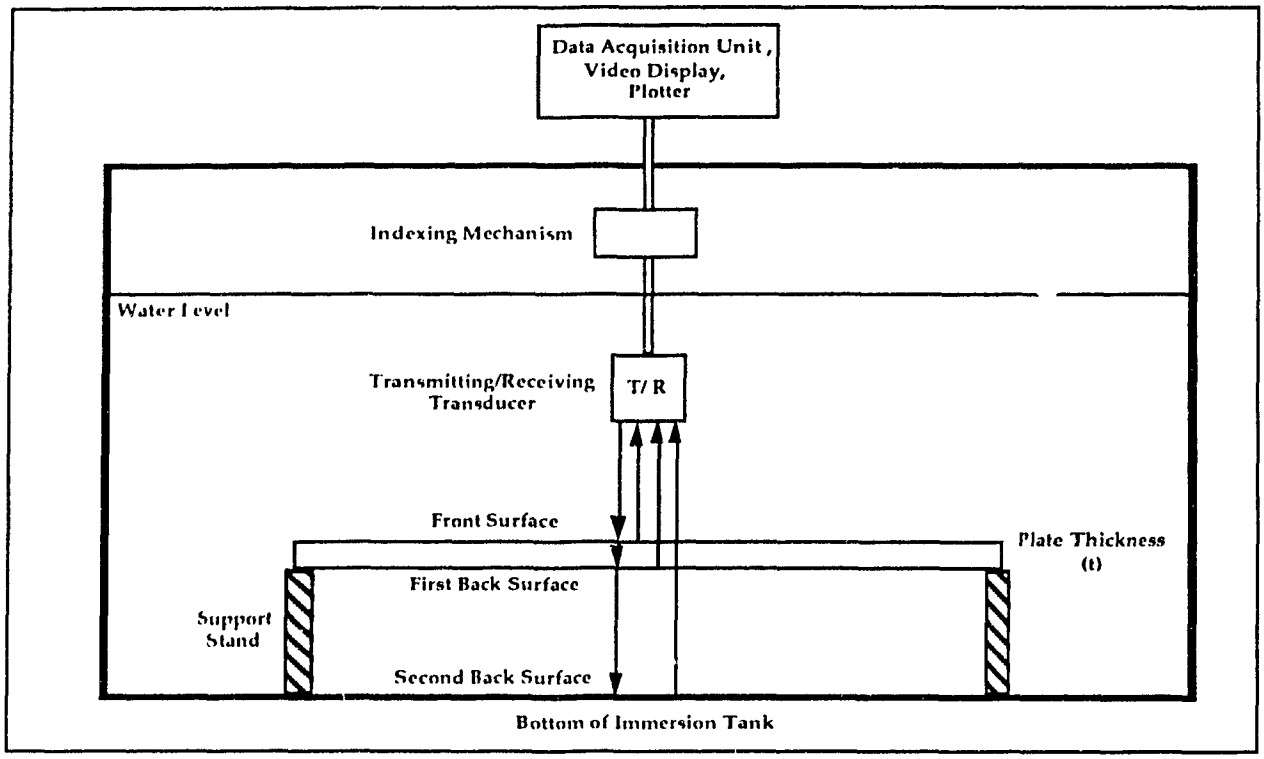

Fig. 1-5: Ultrasonic C-Scan Inspection Set-Up in Immersion Tank

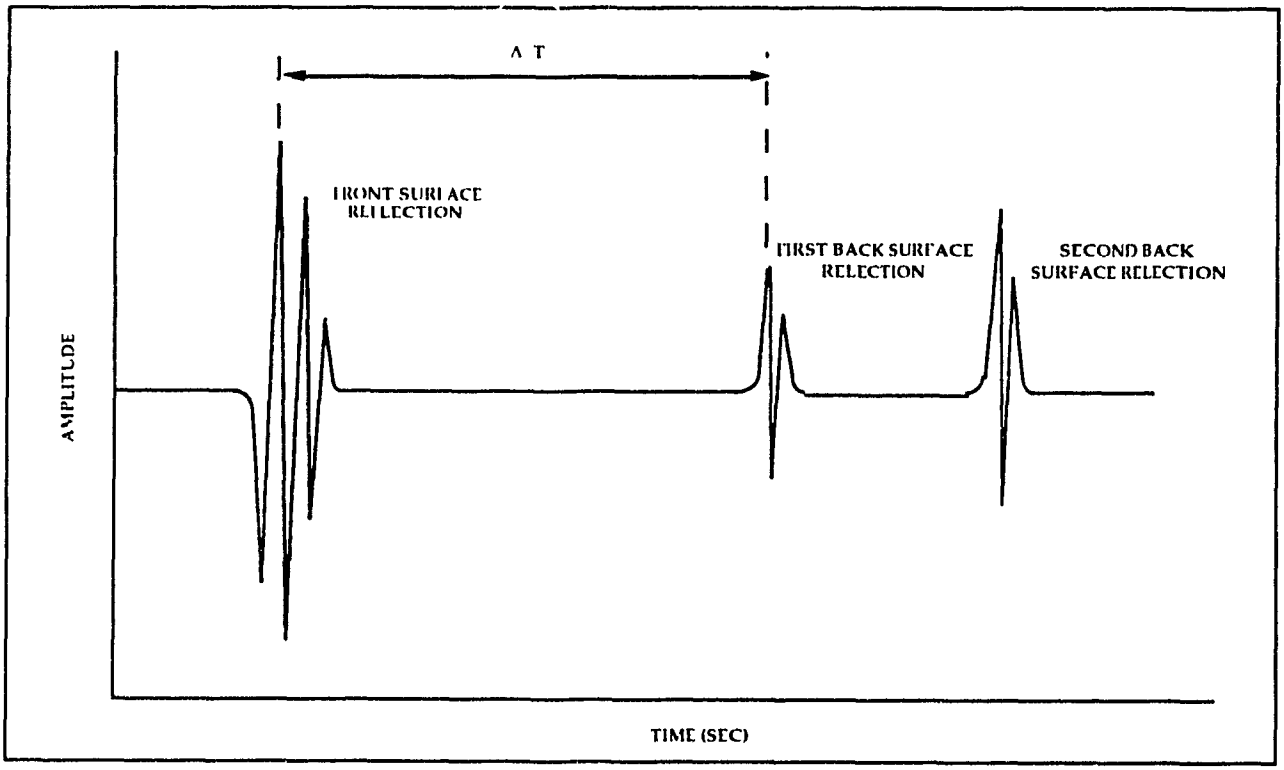

Fig. 1-6: Typical Front Surface and Back Surface Echo Signals in Time-Domain Obtained During Ultrasonic C-Scan Testing

allowing only the signal within a specified time interval to be digitized. Gating generates a single C-scan image which includes damage at all depths in the test piece or at specified depths depending on the position of the gate with respect to the time delay between front surface and back surface echoes. The C-scan image is a map of the amplitude or time-of-flight (velocity) of the received signal versus the position of the scanning transducer relative to the test piece. Through-the-thickness fiber and matrix damage incurred during low energy impact may not be apparent under ultrasonic C-scan due to compaction of the laminate in the planar view. [8] Further information may be derived from A-scans by producing B-prime scans. B-prime scans provide an end-view perspective along a single scanner stroke across the test plate. Damage at the fiber/matrix interface parallel to the fiber direction may not be apparent under B-scanning. [26,27] Damage assessment then requires sectioning of the structure, polishing of specimens and examination with an optical or electron microscope. [8]

The typical signals displayed in time-domain are shown in Figure 1-6. From the time delay (ΔT) between the front surface reflection (first signal) and the first back surface reflection (second signal) the velocity of the wave propagation in the direction normal to the surface of the test plate can be determined from the following equation;

$$v = 2t/\Delta T, \quad \text{where: } t = \text{plate thickness (mm)}$$
$$\Delta T = \text{time delay between reflections}$$

The A-scan display is used for positioning of time gates and adjusting system gain. The time gates will allow only the signal acquired within the specified gate to be mapped. Mapping can be either signal amplitude or time of flight with respect to transducer position. An interply void or delamination causes more signal to be reflected in the area of the void or delamination and the change in signal is represented on the C-scan map as a change in color within a selected signal range. Multiple gates can be used to examine the test piece at various depths within the material. [26]

1.5 Waveform Pattern Classification

Waveform pattern classification is used in this study to compare signal waveforms with receiver sensor type and to correlate signal waveforms with impact damage. The pattern recognition software package used is ICEPAK™ (Intelligent Classification Engineering Package) distributed by Tektrend International Inc. [28]

Pattern recognition by statistical methods provides a means of grouping signal waveforms with related features. Waveform signal features are extracted from digitized acoustic signals and classified by their waveform patterns in time and frequency-domain. A block diagram outlining the signal classification process is given in Figure 1-7. Descriptive features are extracted from the digitized acoustic waveforms to create signal data files and normalized into a bounded value range. The normalized feature files are then split in half to create a training set and a testing set. The development of a classifier able to identify signal features comprises a training stage followed by a testing stage. The training set is used to select descriptive features such as properties and shape factors that identify that group of signal waveforms as belonging to a specific class. During classifier testing, the descriptive features chosen during the training process are used to identify the testing data set. The testing data set, made up of data not used to make the training set, is presented to the classifier and the classifier uses the features to compare the signal waveforms with those used during training. During the testing process a recognition rate in percentage measures the ability of the classifier to correctly identify the test waveforms and any unknown signals with the training waveforms.

ICEPAK™ has a selection of four statistical inference algorithms available for training and testing classifiers; Linear Discriminant (LD), K-Nearest Neighbor (KNN), Empirical Bayesian (EB), and Minimum Distance (MD). The statistical inference algorithms are used to make generalizations based on sample data (signal waveform features). ICEPAK software extracts waveform shape features from 5 domains; time, power, phase, cepstral, and autocorrelation. Frequency spectrum, amplitude and phase are found through Fast Fourier Transformation (FFT) of the time-domain signal and are

used to determine the ratio of energy stored to energy dissipated in the system under test. Through the cepstral function, the number of echoes present, amplitudes, and times of occurrence in the medium of propagation are compared. The autocorrelation function gives the periodicity of the signal by comparing the signal with itself at various positions in the waveform to determine degree of similarity between the waveform segments. [29] A list of the 108 features available to classify a signal using ICE-PAK™ is given in Table 1-2. Refer to references 28, 30 and 31 for detailed analysis of the statistical functions used for pattern classification.

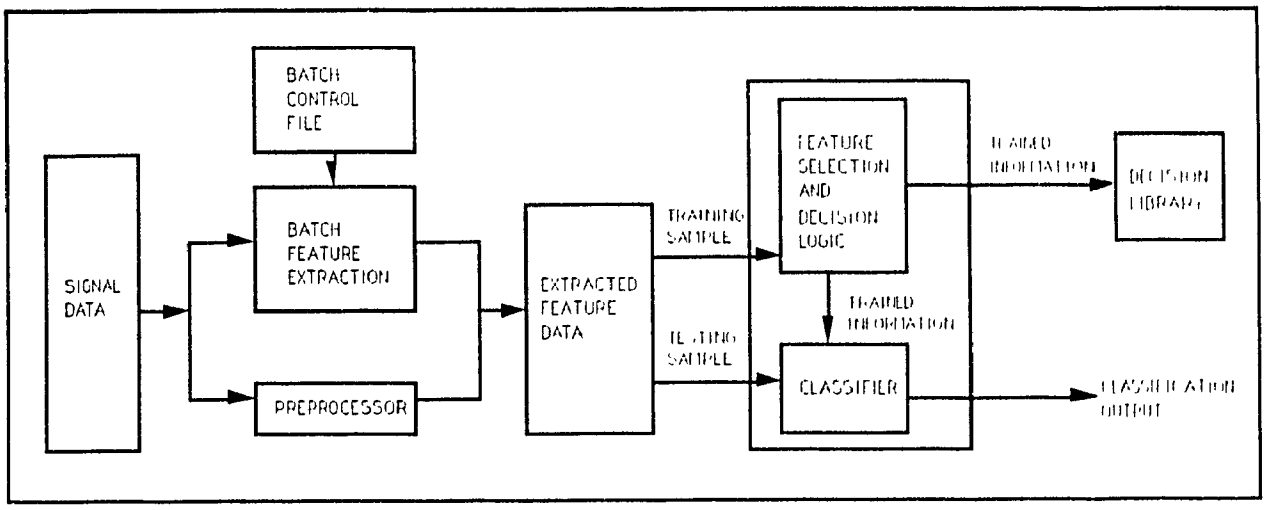

Fig. 1-7: Waveform Pattern Classification Process [28]

Table 1-2: List of 108 Classification Features Available with ICEPAK™ Software [28]

FEATURE DESCRIPTION	TIME DOMAIN	FREQUENCY DOMAIN POWER	FREQUENCY DOMAIN PHASE	CEPSTRAL TRANSFORM	AUTO-CORRELATION
# of peaks above signal threshold	1	37	55	73	91
# of peaks above 10% maximum signal amplitude	2	38	56	74	92
# of peaks above 25% maximum signal amplitude	3	39	57	75	93
greatest peak	4	40	58	76	94
greatest peak amplitude	5	41	59	77	95
2nd greatest peak position	6	42	60	78	96
2nd greatest peak amplitude	7	43	61	79	97
3rd greatest peak position	8				
3rd greatest peak amplitude	9				
Total time under greatest peak	10	44	62	80	98
Total time under 2nd greatest peak	11	45	63	81	99
Total time under 3rd greatest peak	12				
Inter peak distance from 1st to 2nd greatest	13	46	64	82	100
Inter peak distance from 1st to 3rd greatest	14				
Inter peak distance from 2nd to 3rd greatest	15				
greatest peak rise time	16				
greatest peak rise slope	17				
greatest peak fall time	18				
greatest peak fall slope	19				
greatest peak full pulse width	20				
greatest peak half pulse width	21				
greatest peak width	22				
2nd greatest peak rise time	23				
2nd greatest peak rise slope	24				
2nd greatest peak fall time	25				
2nd greatest peak fall slope	26				
2nd greatest peak full pulse width	27				
2nd greatest peak half pulse width	28				
2nd greatest peak width	29				
3rd greatest peak rise time	30				
3rd greatest peak rise slope	31				
3rd greatest peak fall time	32				
3rd greatest peak fall slope	33				
3rd greatest peak full pulse width	34				
3rd greatest peak half pulse width	35				
3rd greatest peak width	36				
% of partial power in 1st Octant		47	65	83	101
% of partial power in 2nd Octant		48	66	84	102
% of partial power in 3rd Octant		49	67	85	103
% of partial power in 4th Octant		50	68	86	104
% of partial power in 5th Octant		51	69	87	105
% of partial power in 6th Octant		52	70	88	106
% of partial power in 7th Octant		53	71	89	107
% of partial power in 8th Octant		54	72	90	108

Note: Octants are frequency bands of 250 kHz

1.6 Determination of Compression Modulus in Graphite/Epoxy Composites

Impact damage in graphite/epoxy composites has been shown to reduce the compression modulus and strength. [8,15] The modes of failure of impacted unidirectional and cross-ply graphite/epoxy composites are not readily identifiable. It is generally accepted that fiber/matrix disbonding precedes local matrix yielding and micro-buckling, followed by buckling of fiber bundles. [32,33,34]

Compression testing of graphite/epoxy composites is problematic due to the occurrence of out of plane bending and brooming of coupons causing failure at values below true compressive strength values. For specimens of less than 5 mm (0.2 in) thickness, hydraulic grips equipped with friction blocks provide a relatively good method of quasi-static compression testing for comparative analysis. [35] The strength values obtained from compression testing of flat coupons are considered to be conservative due to premature failure. Stiffness (modulus) values are taken from the initial part of the load/strain curve and are therefore not affected by out of plane deformation of the specimen or specimen brooming occurring during the latter stages of compression testing. [35,36] Therefore, values of modulus obtained during compression testing may be more respresentative of true modulus values.

1.7 Scope of Current Study

Evaluation of the effect of impact damage on the modulus of graphite/epoxy plates and the effectiveness of using PVDF senso. to detect impact damage in graphite/epoxy plates through AU technique was completed in three stages (Table 1-3).

In the first stage, two types of PVDF sensors of 52 μm and 28 μm film thicknesses were assembled. The best method of assembly was determined by evaluating several published methods. [9,19,37] A common mode rejection (CMR) circuit was built to aid in extraneous noise reduction. [37] The assembled PVDF sensors responses were compared with responses from a ceramic resonant and a ceramic wideband transducer.

The signal waveform curves were classified using ICEPAK™ software to identify the respective receiver sensor type. Based on the difficulty in sensor assembly and the amount of extraneous noise interference, it was decided to purchase pre-assembled sensors for the graphite/epoxy plate tests (second stage).

Table 1-3: Stages in Current Study

Stage	Test Piece	Test Type	Objective
1. -Assembly of PVDF Sensors			-Assembly Technique
-Comparison in Response of PVDF Sensors and Ceramic Transducers	-Al Block 6061-T6	-AU -Pattern Classification	-Sensor Sensitivity -Signal Repeatability & Correlation of Signal with Type of Sensor and /or Transducer
2. -Comparison of Signals Acquired with PVDF Sensors and Number of Impacts	-IM7/977-2 Plates (0° & ±45°)	-AU -C-Scan -Pattern Classification	-Reduction in Peak Freq. & Peak to Peak Voltage with Number of Impacts -Identification of Impact Damage -Correlation of Signal with Number of Impact Hits
3. -Determination of Change in Stiffnes.. (Modulus) Due to Impact Damage	-IM7/977-2 Coupons (0° & ±45°)	-Compression	-Reduction in Compress. Stiffness (Modulus) with Impact Damage

In the second stage, pre-assembled PVDF sensors of 28 μm thickness were purchased. The PVDF sensors (Fig. 1-3) required attachment of a male BNC connector before use. The PVDF sensors were used to determine changes in signal waveforms with impact damage in unidirectional and cross-ply (±45°) IM7/977-2 plates. Acoustic signals were gathered from the plates in the as-received condition, after 3 impacts, and after 9 impacts. Each plate was subjected to ultrasonic C-scan in the as-received condition

and after 9 impacts. Signal attenuation with increase in impact damage was investigated by graphing reduction in signal peak frequency and peak to peak voltage with cumulative number of impact hits. Pattern classification using ICEPAK™ software was used to correlate number of impacts with acoustic signal waveform changes.

In the third stage, the change in compression stiffness (modulus) due to impact damage was determined. Impacted (one hit) and non-impacted areas of the test plates were cut into coupons and tested in quasi-static compression. Strain and load data was acquired during testing. Stiffness (modulus) values were determined from the load strain curves and compared with supplier values.

2.0 ACOUSTIC TRANSDUCERS

The PVDF sensors used in this study were evaluated comparatively with a ceramic resonant and a ceramic wideband transducer. The PVDF sensors used in the aluminum block testing required assembly before use. The PVDF sensors used in the testing of the graphite/epoxy plates were purchased in a pre-assembled format and required attachment of a male BNC connector before use. The ceramic resonant and wideband transducers were used as-received.

2.1 PVDF Sensors

Two thicknesses of metallized PVDF film were used to assemble the PVDF sensors used in the aluminum block testing (refer to section 3.0). One sheet each of film of 52 μm and 28 μm thickness, 15 cm by 30 cm (6 inch by 12 inch), with NiCu metallized surfaces was purchased from Pennwalt Corporation [18]. Ten sensors of each film thickness were assembled. For pattern recognition purposes, sensors made of 52 μm film thickness were designated as class 1 and sensors made of 28 μm film thickness were designated as class 2. All ten sensors in each class were used interchangeably to determine repeatability of the sensor performance and assembly process. The assembled PVDF sensors had an effective sensing area of 300 mm^2 (0.5 in^2). The pre-assembled PVDF sensors (Fig. 1-3) used during testing of the graphite/epoxy plates consisted of 28 μm film metallized with Ag ink. The pre-assembled PVDF transducers have an effective sensing area of 445 mm^2 (0.7 in^2).

2.2 PVDF Film Processing

Polyvinylidene fluoride (PVDF) film is commercially available in pre-processed metal-

lized sheets of thicknesses 9 μm to 800 μm. The film is coated with NiCu or Ag ink by vacuum metallization or silk screening. The conductive metal coatings are symmetric to both sides of the film and provide electrical contacts for wire lead attachment. PVDF is a long chain semicrystalline polymer consisting of repeated units of two fluorine atoms opposite two hydrogen atoms along a carbon backbone. Four crystalline structures of PVDF have been identified through infrared transmission and x-ray scattering techniques; I(β), II(α), IIp(αp), and III(γ). The various crystalline structures are obtained through thermal treatment, uniaxial stretching and electrical poling as outlined in Figure 2-1. [38] The non-polar alpha phase (II) results when the polymer is cooled from its melt. Alpha phase (II) PVDF does not exhibit piezoelectric properties. The polar beta phase (I) structure results after deformation of the alpha crystallites by stretching of extruded PVDF film at temperatures below its melting point, aligning the carbon backbone chains in parallel strips. [17] Mechanical drawing of polar gamma phase polymer will also result in beta phase crystallites. Secondary processing of non-polar form II(α) film (Fig. 2-2) produces the PVDF film which is commercially available, form I(β). The form II(α) film is recrystallized into form I (β) by uniaxial stretching and heating to 65°C. Subsequent annealing to 120°C stabilizes the film. The beta phase film is then metallized to provide conductive surfaces and aid in polarization. [17] Thermal poling of the beta phase crystallites by exposing the beta phase polymer to a high gradient electric field of 800kV/cm at 105°C results in alignment of the molecular dipoles within the polymer and enhancement of the material's piezoelectric properties. [37,38] The resulting PVDF film Form I (β) exhibits high sensitivity to in-plane displacements. [9]

2.3 PVDF Film Properties

The measured piezoelectric and pyroelectric constants of PVDF are strongly dependent on the crystal form (crystallinity), draw (stretch) ratio, and poling conditions. Studies have shown [17,19,20] that maximum in-plane sensitivity is observed in the stretched direction. A mechanical force applied to PVDF film results in a compressive or tensile strain due to contraction or elongation of the film. The change in

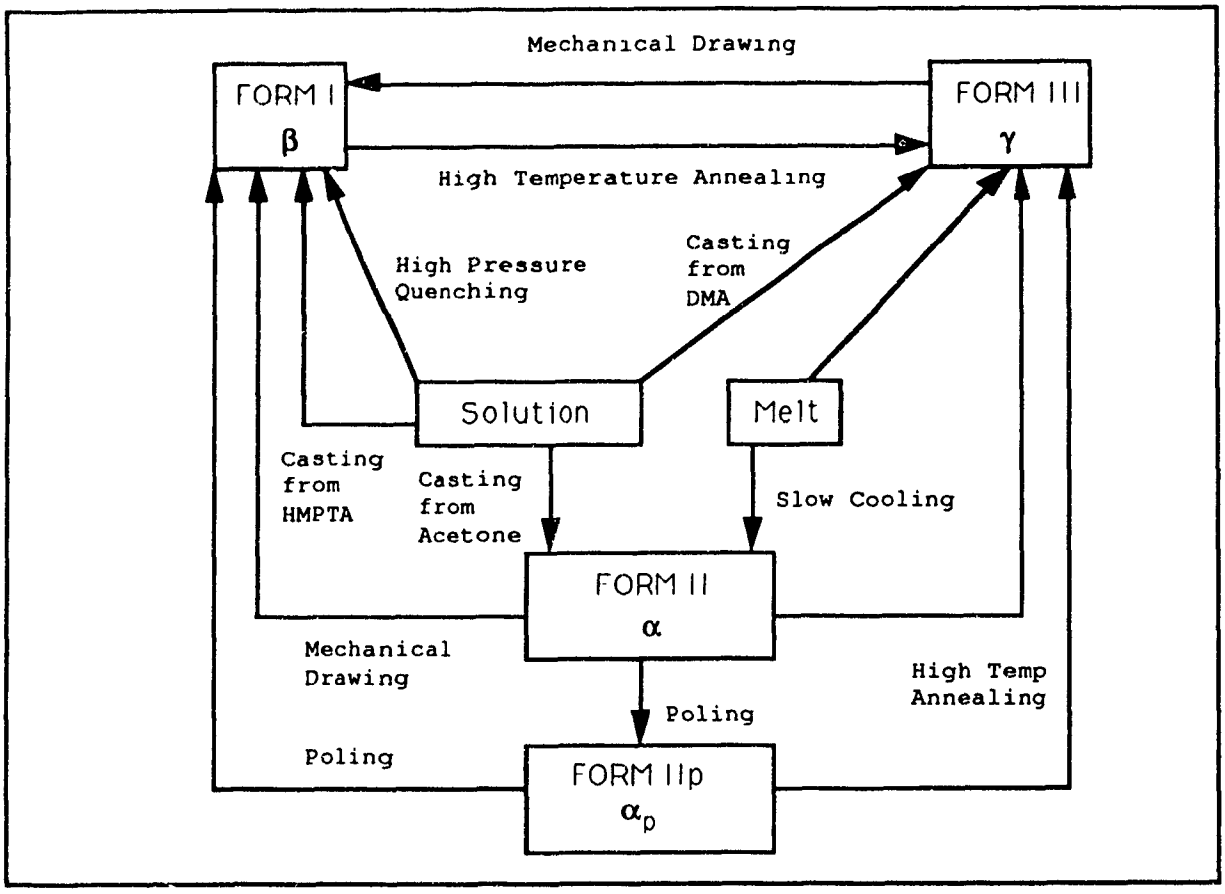

2-1: Processing Steps to Produce Crystalline Forms of PVDF [38]

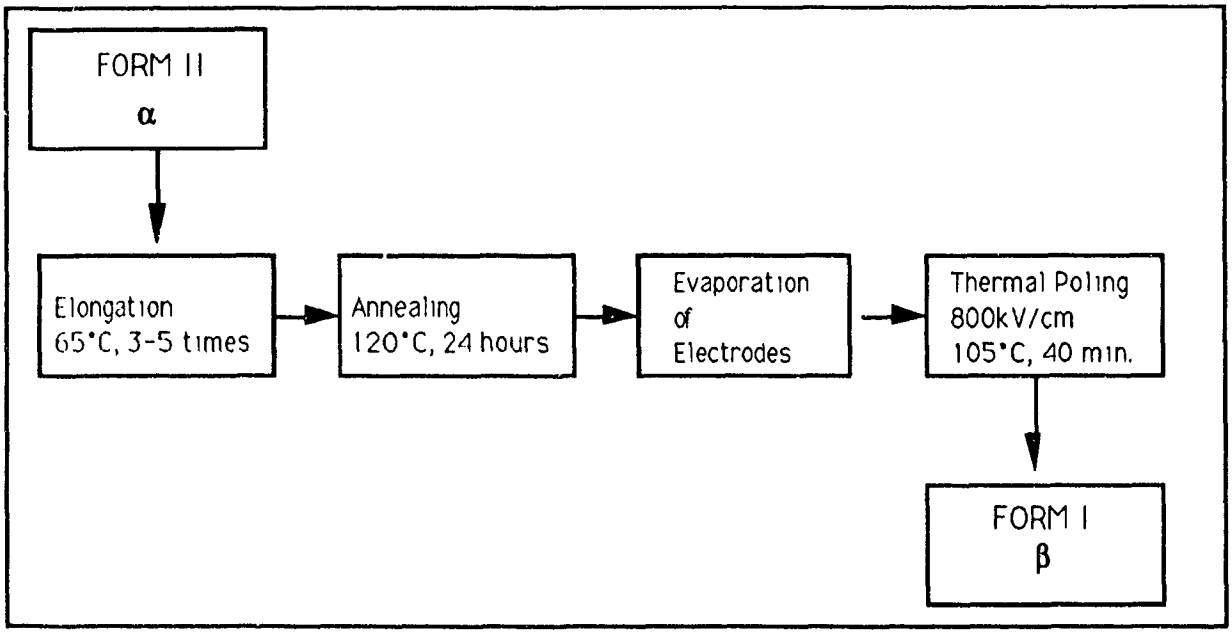

Fig. 2-2: Processing of Non-polar Form II(α) PVDF to Produce Polar Form I(β) [38]

volume of the polarized PVDF film during contraction or elongation changes the net charge distribution within the film. The change in density of the PVDF film appears as a voltage difference between the metallized surfaces (electrodes). Conversely, a voltage difference applied to the film electrodes will cause contraction or elongation of the film. [17] The metallized surfaces of the PVDF film acts as a capacitor able to react in a dynamic manner to changes in mechanical strain. The time constant is dependent on the PVDF film dielectric constant, internal resistance, and impedance of the connected circuits. [37] PVDF film exhibits a flat frequency response over a wide frequency range. The half wavelength resonance (natural resonance frequency) changes with film thickness and can be calculated by:

$fr = vs_3/2t$ [37], where: vs_3 = velocity of sound in the through thickness direction

t = film thickness

The natural resonant frequency for a 28 μm film is 40 MHz and for a 52 μm film, 21.5 MHz. PVDF film exhibits low acoustic impedance, which allows acoustic signals to pass through it with minimal distortion. With a capacitance of 380 pF/cm^2 and a volume (bulk) resistivity of 10^{13} Ωm, the time constant for 28 μm film is, t_c = 1064 seconds. The film is then capable of receiving signals at a frequency of 0.001 Hz (cut off frequency). [17,37]

Piezoelectric materials are anisotropic and therefore, mechanical and electrical responses are axially dependent. The directionality convention is given in Figure 2-3. The polarization axis is 3, through the film thickness. Single subscripts correspond to length (1), width (2), and thickness (3). Double subscripts correspond to axis of applied electrical field (first number) followed by axis of induced mechanical strain (second number). Piezo strain constants (dij), stress constants (gij), and electro-mechanical coupling constants (kij) are given in Table 2-1.

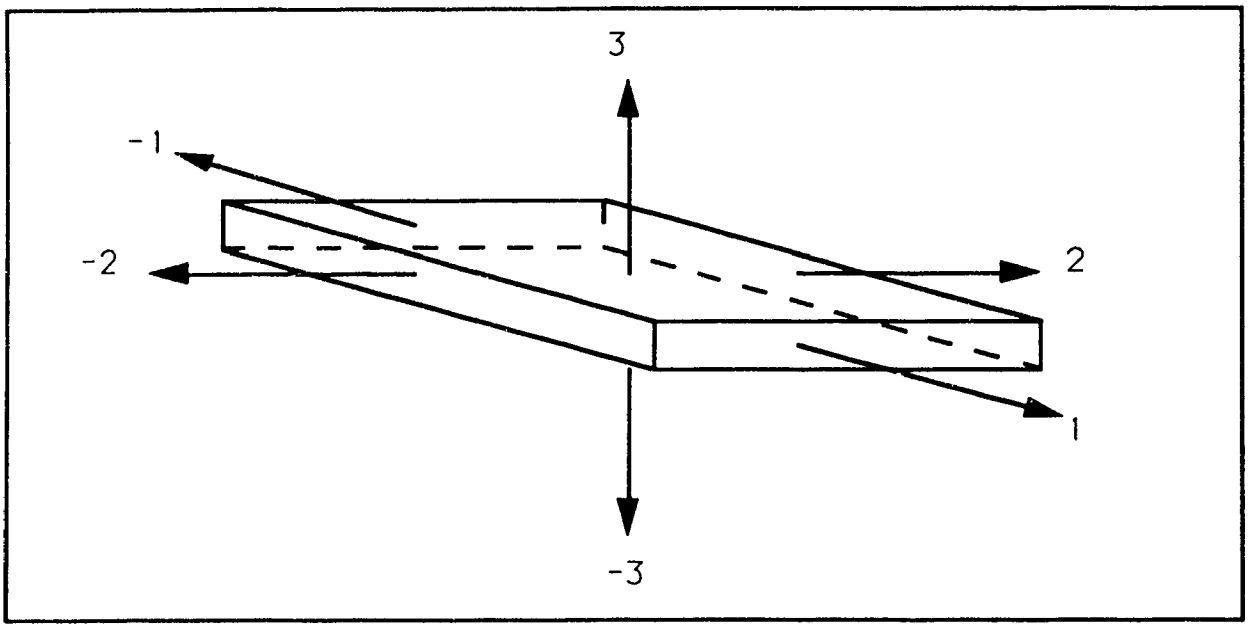

Fig. 2-3: Classification of Axes [37]

Table 2-1: PVDF Film Constants [37]

Piezo Strain Constants	d_{31} = 23	x 10^{-12} m/V or 10^{-12} C/N
	d_{32} = 3	
	d_{33} = -33	
Piezo Stress Constants	g_{31} = 216	x 10^{-3} Vm/N or 10^{-3} m^2/C
	g_{32} = 19	
	g_{33} = -339	
Speed of Sound	vs_3 = 2.2	x 10^3 m/s
	vs_1 = 1.5	
Acoustic Impedance	Za_3 = 3.9	x 10^6 kg/m^2 s

2.4 PVDF Sensor Preparation

The PVDF transducers were prepared in a bi-morph assembly as illustrated in Figure 1-3 b). The bi-morph assembly is formed by folding the PVDF film in half and laminating the inner surfaces, resulting in a two layer structure. The two layer structure forms an electrical shield (ground) around the positive inner electrode. [37] The materials and equipment required for assembly of the PVDF sensors from film sheets (Fig. 2-4) and method of assembly are listed in sections 2.4.1, 2.4.2 and 2.4.3.

2.4.1 Assembly Materials

- PVDF metallized film; 52 μm and 28 μm with NiCu coated surfaces
- protective coating; FEP Teflon Film, C-20, 1 mil, and M-Coat polyurethane
- adhesive; M-Bond 200 Adhesive, cyanoacrylate
- catalyst; M-Bond 200 Catalyst, trichloroethane
- water based conditioner and neutralizer; M-Prep
- tape; 3M brand, double-sided

2.4.2 Assembly Equipment

- cutting surface; plexiglass
- measuring instrument; digital vernier
- cutter; razor edge knife
- glass micro-slides (75 mm x 25 mm)
- pressure clips
- colored markers

2.4.3 Method of Assembly of Sensing Element

Strips of PVDF film of 12.5 mm by 60 mm (0.5 in by 2.4 in) were cut from the two sheets of metallized film using a razor sharp cutting knife on a plexiglass cutting surface. The film was lightly buffed with 400 grit sandpaper. The buffed area was cleaned with a water based conditioner and neutralizer. The PVDF film was then folded to form a two ply area of 12.5 mm by 25 mm (0.5 in by 1 in) with a 12.5 mm by 10 mm (0.5 in by 0.4 in) single ply tab. The width of the 25.4 mm (1 in) long side was

trimmed to 12.7 mm (0.5 in) wide to ensure grounding of the sensor, reducing the effective sensor area to 300 mm^2 (0.5 in^2). Cyanoacrylate adhesive was then applied to one side of the contact surface and catalyst to the opposing side. The two sides of the PVDF film were then pressed together to bond the two ply inner sensor electrode. The outer surface of the PVDF film acts as the sensor ground. The PVDF sensor was then placed between two glass micro-slides and held with pressure clips for a period of 10 minutes to ensure complete curing of the adhesive. Strips of teflon film of 16.5 mm by 54 mm (0.65 in by 2.1 in) were cut from a sheet of one mil thick teflon sheet. The teflon strips were cleaned with a water based conditioner and neutralizer. Double backed adhesive tape was applied to the teflon strips and the assembled PVDF sensing elements were enveloped in the teflon strips. The tab area was not coated in teflon. Adhesively backed colored markers were fixed to the prepared PVDF sensing elements indicating the film thickness used (blue indicates 52 μm, red indicates 28 μm) and ground side of tab (green indicates ground).

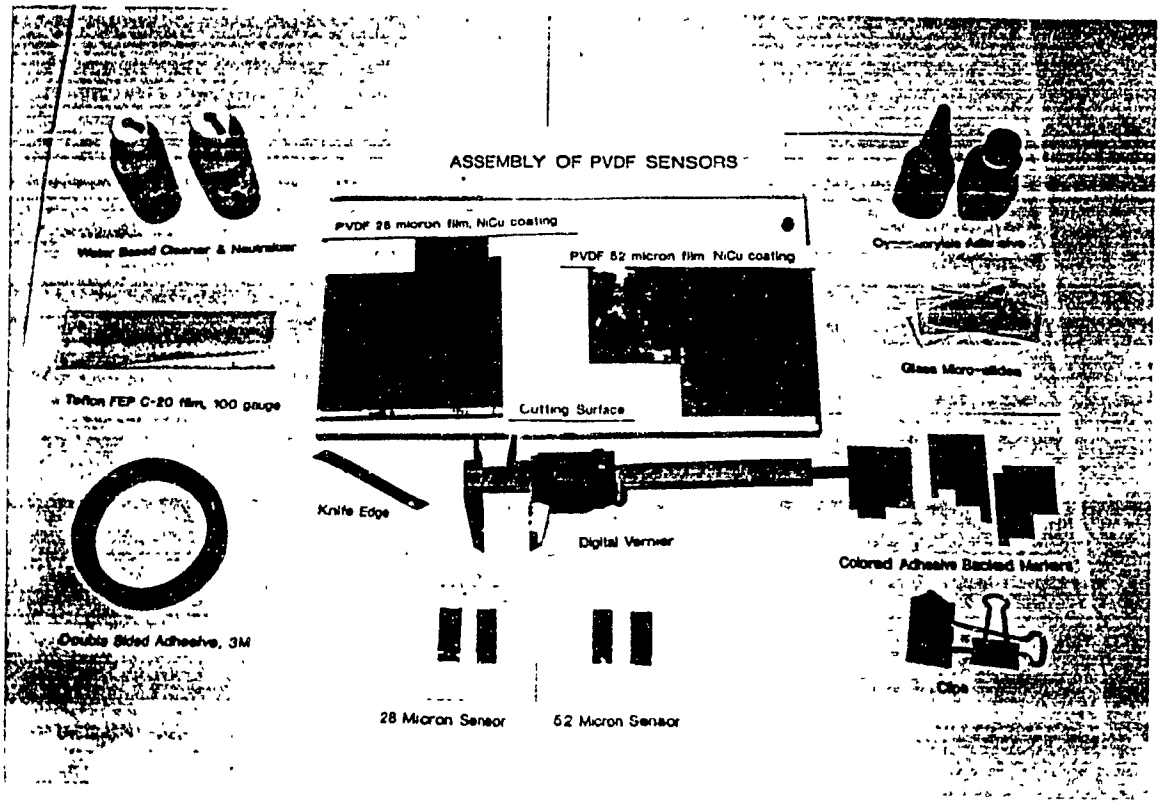

Fig. 2-4: Materials and Equipment Required for Assembly of PVDF Sensors

2.4.4 Lead Attachment to PVDF Sensors

The lead attachment to the sensing elements was accomplished through modification of 14 pin SOIC clips (commonly used to test computer chips) soldered to 24 gauge shielded cables equipped with BNC male connectors. The clips were modified by filing down the edges restricting the hinge mechanism, resulting in a compressive pressure contact between the parallel jaws of the clip. Lead solder was used to connect the metal pin contacts on the inner surfaces of the clip jaws and create a flat contact area for the tab section of the PVDF sensing elements. The resistance of the SOIC clips, 24 gauge shielded cable and BNC connector arrangement was measured with a multimeter and found to be 2 ohms.

2.4.5 Method of Adhesion to Test Piece

The area of attachment on the test piece was lightly sanded with 320 grit abrasive paper and cleaned with water based conditioner and neutralizer. Double backed adhesive tape was applied to the area of attachment on the test piece. The PVDF sensors were attached by pressing the end of the sensor to the tape and smoothing the sensor towards the tab to eliminate entrapped air. [37,39] Adhesion by double backed tape was used in the aluminum block test, and the graphite/epoxy plate tests.

2.5 Pre-Assembled PVDF Sensor Preparation

The pre-assembled PVDF sensors purchased from Pennwalt Corporation required attachment of a male BNC connector to the shielded leads before use.

2.5.1 Male BNC Connector Attachment

The male BNC connectors were soldered to the shielded cable leads using lead solder. The cable shielding was soldered to the steel housing of the BNC connectors to provide a ground.

2.5.2 Method of Adhesion to Test Piece

The aluminum test block was prepared by sanding all surfaces and cleaning with conditioner and neutralizer. The assembled PVDF sensors were adhesively bonded to the aluminum test block with double backed adhesive tape.

2.6 Comparison of PVDF Film with Piezoelectric Materials Used in Ceramic Transducers

PVDF film is characterized by high flexibility, tensile strength, and compliance. The film is also lightweight when compared to ceramic piezoelectric materials, and has low acoustic impedance. [38] A comparison of PVDF film with more commonly used acoustic sensors built from ceramic piezoelectric materials such as lead zirconate titanate (PZT-5) yields values as indicated in Table 2-2. PVDF sensors have low mass, low acoustic impedance, high flexibility and sensitivity compared to ceramic piezoelectric transducers. PVDF film exhibits a compliance ten times greater than ceramics and an achievable maximum strain ten times larger. [37]

Table 2-2: Comparison of PVDF Film and Ceramic PZT Used in Commercial Transducers [21,37]

	PVDF	PZT-5	
Piezo Strain Constant	d_{31} = 23	171	x 10^{-12} m/V or 10^{-12} C/N
Piezo Stress Constant	g_{31} = 216	11.4	x 10^{-3} Vm/N or 10^{-3} m^2/C
Speed of Sound	vs_3 = 2.2	3.2	x 10^3 m/s
Acoustic Impedance	Za_3 = 3.9	24	x 10^6 kg/m^2 s

2.7 Noise Reduction by Common Mode Rejection (CMR) Circuitry

The AU signals were isolated from some of the extraneous noise interference encountered during signal gathering through the use of a common mode rejection circuit. [37] Two identical PVDF sensors were used during each test. One PVDF sensor was coupled to the test piece while the other PVDF sensor was coupled to the test support fixture. The resulting voltage generated by each PVDF sensor during AU testing was input to the circuit in Figure 2-5. Voltages common to both sensors, caused by unwanted vibrations, were cancelled out. The circuit was designed to supply unity gain and an input resistance of 10k ohm. One operational amplifier (JFET) was required for each circuit. The JFET operational amplifier chosen for the CMR circuit of Figure 2-4 has a bandwidth of 4.0 MHz. The CMR circuits were powered by 15 volt external power supplies.

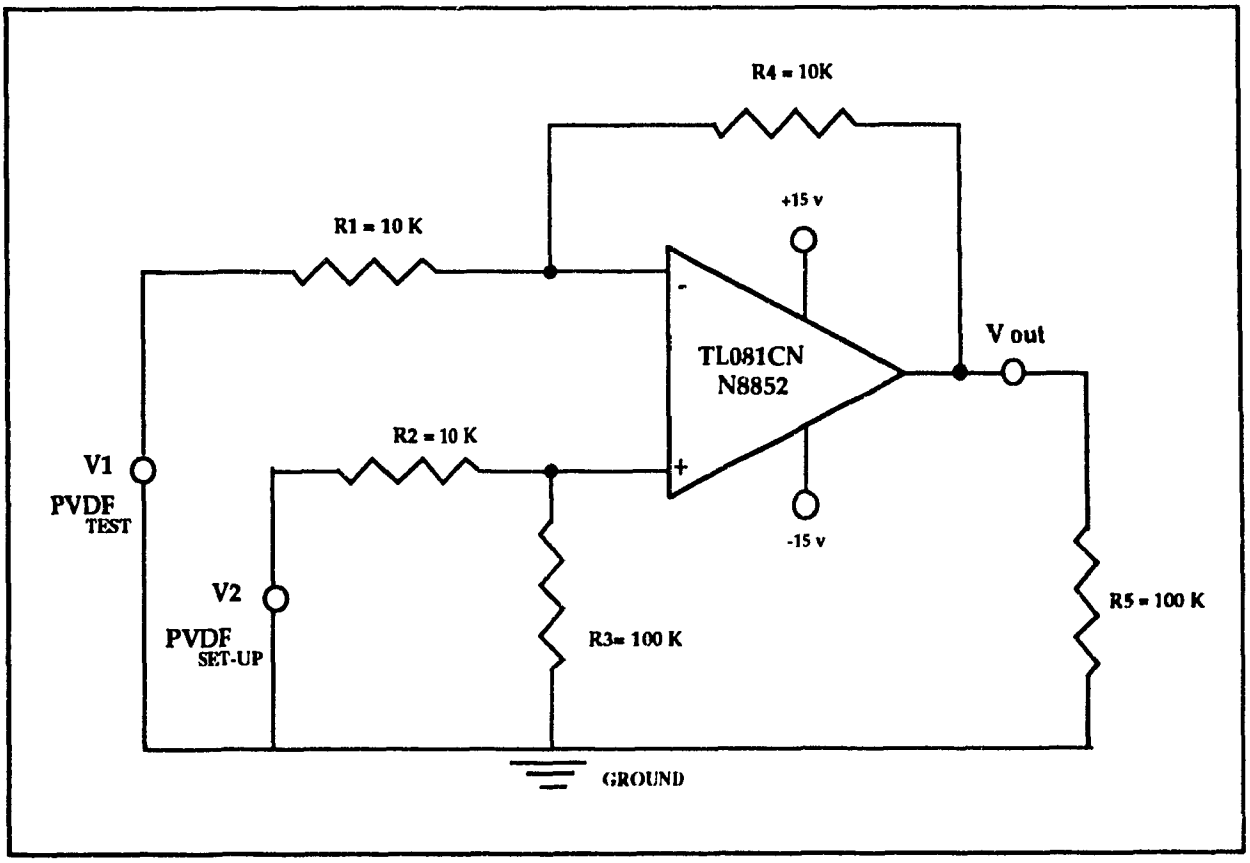

Fig. 2-5: Common Mode Rejection (CMR) Circuit [37]

2.8 Resonant Transducer

The resonant transducer used as a receiver in the aluminum block testing was a Physical Acoustics Corporation, PAC R15, having an operating frequency range of 50 to 200 kHz, and a peak sensitivity of 69 dB (ref. 0 dB = 1V/m/s) at a resonant frequency of 70 kHz. The diameter of the ceramic base of the transducer was 18 mm (0.7 in) and the housing was stainless steel.

2.9 Wideband Transducer

The wideband transducer used as a receiver in aluminum block testing and as a source in graphite/epoxy plate testing was a truncated cone type (point contact), made of PZT (zirconium titanate) encased in a stainless steel housing. The wideband transducer had an approximately flat sensitivity of 0 dB (to within 3 dB) over a 0.2 to 1 MHz frequency range. The outer diameter of the transducer steel housing was 25.4 mm (1 in). The transducer was manufactured by EBL Company, Incorporated, and the voltage-time response and frequency spectrum to a glass capillary break on a steel block is given in Appendix 1.

2.9.1 Lead Attachment to Transducers

Lead attachment to the resonant and wideband transducers was provided by a shielded cable to a male BNC connector. Both transducers were equipped with microdot connectors on the steel housings.

2.9.2 Method of Coupling Transducers to Test Piece

The resonant and wideband transducers were coupled to the aluminum test block and the graphite/epoxy plate with silicone gel, 111 Compound, manufactured by Dow Corning.

3.0 ALUMINUM BLOCK TESTS

Comparison of the response of the assembled PVDF sensors and a commercial resonant and wideband transducer in detecting surface waves was carried out using an aluminum test block. The signal source was provided by a burst of compressed air (air jet). Block dimensions and source locations (S1, S2, S3 and S4) are given in Figure 3-1 and Table 3-1. Waveform signals acquired from receiver locations L1, L2, L3, and L4 were digitized and classified using ICEPAK™ software. The graphs of the voltage-time signal waveforms are given in Appendix 2.

3.1 Acousto-Ultrasonic Test Set-Up

The acousto-ultrasonic test set-up consisted of the aluminum block resting on a sup port fixture and coupled to instrumentation as illustrated in Figures 3-2, 3-3, and 3-4.

3.1.1 Support Fixture

The test support fixture consisted of a wooden platform supported by steel screws with their ends ground to provide point contacts. The wooden platform was 0.9 m by 0.9 m (3 ft by 3 ft) and 12.7 mm (1/2 in) thick. The test fixture rested on a metal bench type lab table with a laminated surface. The aluminum test block (Fig. 3-3) was located in the middle of the wooden platform. Two layers of silicone rubber sheeting 3.2 mm (1/8 in) thick for a total thickness of 6.4 mm (1/4 in) were placed under the test block to dampen extraneous noise (vibration) interference. The air jet signal source was fixed to a height adjustable metal stand equipped with screw clips and a rubber pad under the base. The Lecroy 9400A digital oscilloscope, PC and plotter (Fig. 3-4) were located on a trolley beside the test set-up.

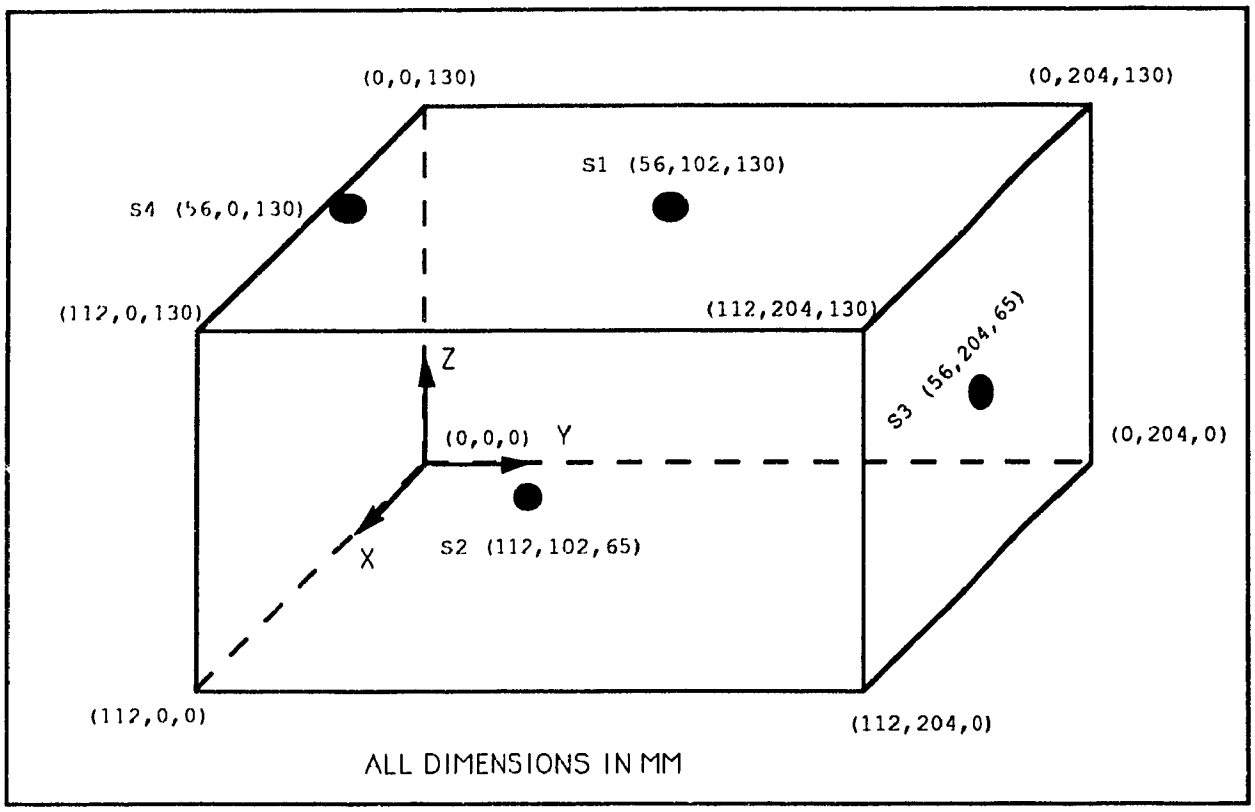

Figure 3-1: Aluminum 6061-T6 Test Block

Table 3-1: Locations of Signal Sources and Receiving Sensors on Aluminum Block

Air Source	Receiver Sensors	
X,Y,Z (mm,mm,mm)	X,Y,Z (mm,mm,mm)	
	Channel 1	Channel 2
S1=56, 102, 130	L1=56, 0, 130	56, 204, 130
S2=112, 102, 65	L2=0, 102, 130	112, 102, 130
S3=56, 204, 65	L3=0, 102, 130	0, 102, 130
S4=56, 0, 130	L4=56, 204, 130	56, 204, 130

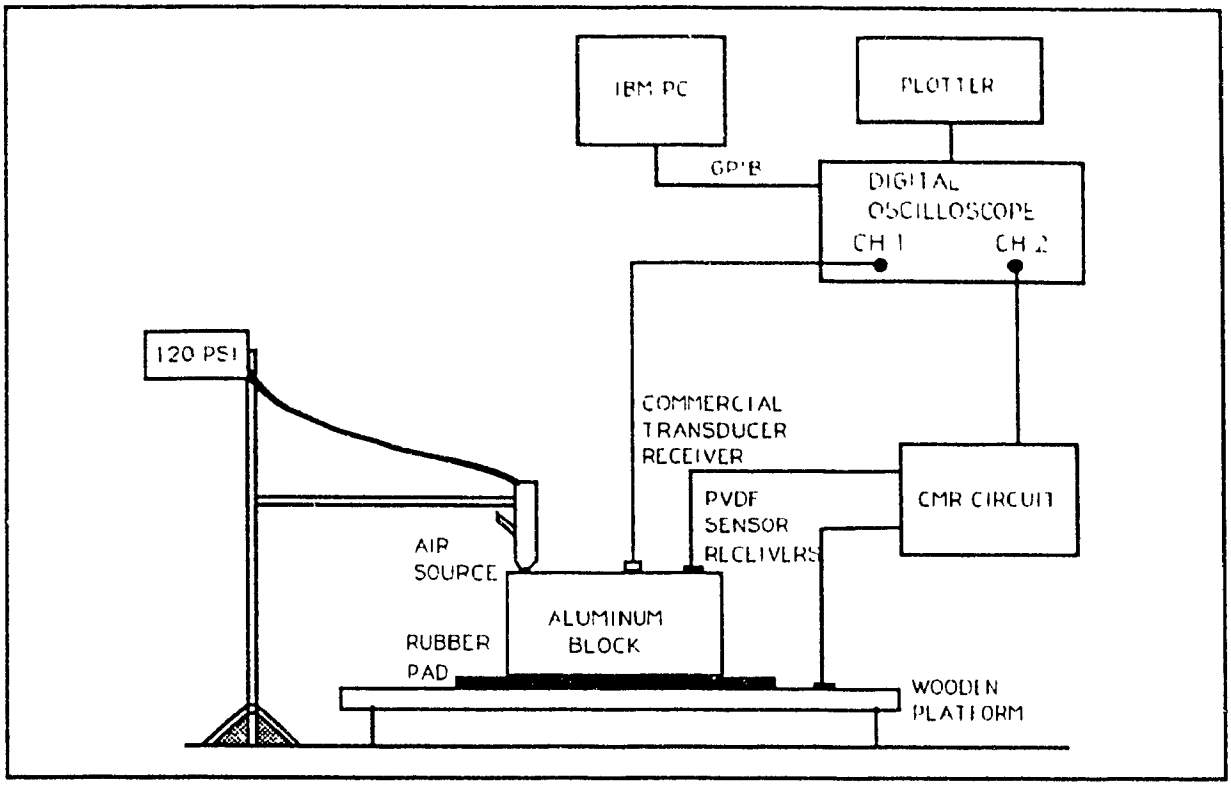

Fig. 3-2: Test Set-Up for Aluminum Block Testing

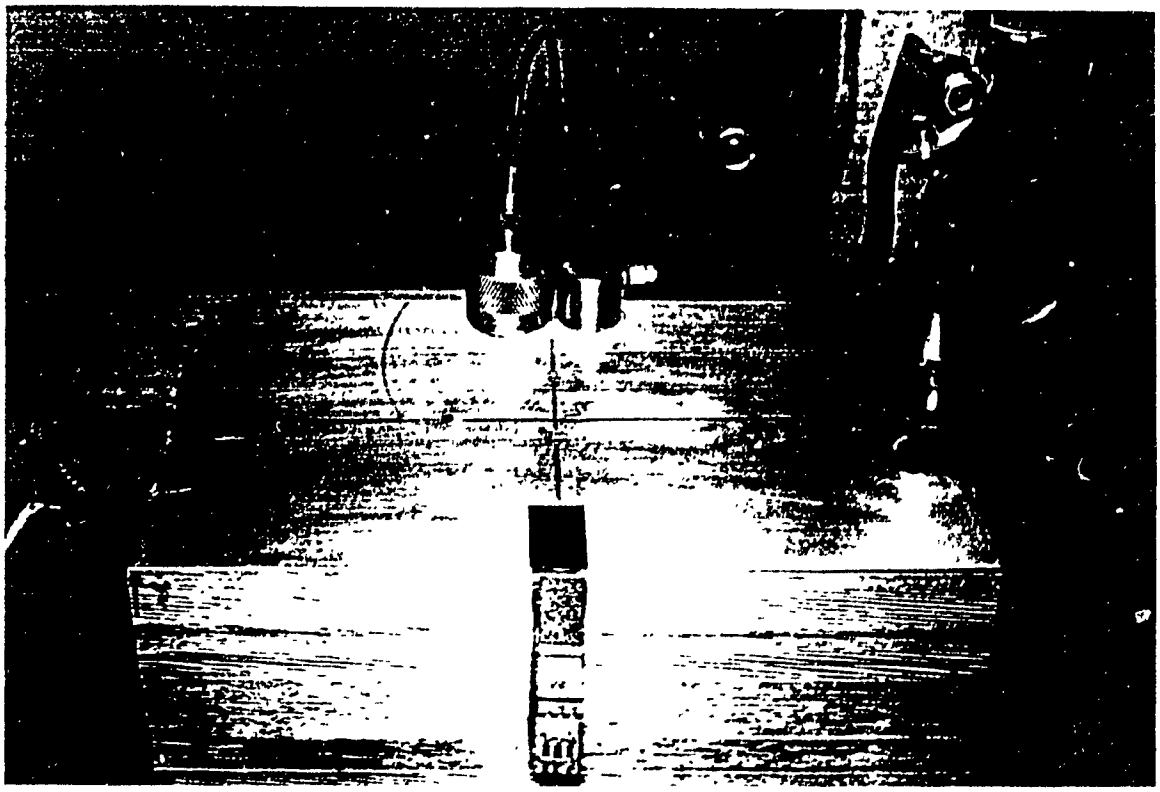

Fig. 3-3: Aluminum Test Block with PVDF Sensors, Wideband and Resonant Transducers, and Compressed Air Source

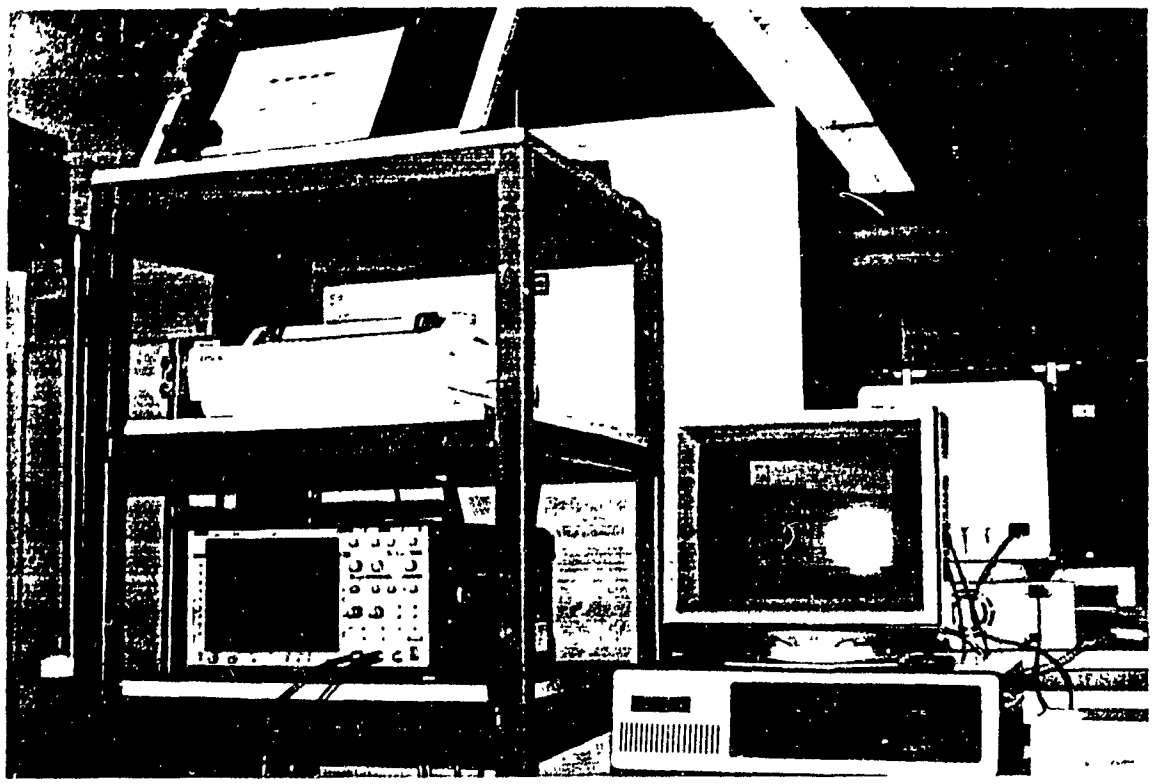

Fig. 3-4: Lecroy 9400A Osilloscope, PC and Plotter Used in AU Signal Gathering

3.1.2 Signal Source

The signal source for the aluminum block testing consisted of an air-hose and nozzle end attachment. The supply pressure was 827 kPa (120 psig). The nozzle end attachment provided a round aperture of 3.2 mm (1/8 in) diameter. The air jet was positioned 6.4 mm (1/4) inch above the surface of the aluminum block. The aluminum block was impacted by a stream of compressed air by pressing a release lever.

3.1.3 Signal Waveform Gathering by Digital Oscilloscope

Time-domain signal waveforms (Appendix 2) were gathered with a two channel Lecroy 9400A digital oscilloscope with data storage capabilities. The digitized waveforms were converted into ASCII files by downloading from the oscilloscope through a GPIB interface into MASP™ software on a micro-computer and then into ASYST™ software. Waveform pattern classification was then performed by reading the ASCII files into ICEPAK™ software located on the same PC and completing waveform feature comparison.

3.1.4 Other Electronics and Connections

A hand-held multi-meter was used to measure cable resistances and supply voltage. All cables used to connect sensors to the CMR circuit and to the digital oscilloscope contained shielded 24 gauge wire and were equipped with male BNC connectors.

3.2 Acousto-Ultrasonic Test Results

The acousto-ultrasonic test results are presented in the form of a comparison of the acoustic signal waveforms received from the PVDF sensors and the ceramic transducers by examination of the voltage-time graphs and by pattern classification of the digitized waveforms.

3.2.1 Comparison of Signal Waveforms

The voltage-time signal waveforms gathered from the aluminum block tests are given in Appendix 2. Graphs 1 to 6 are waveforms of 52 μm PVDF sensors (channels 1 and 2) located the same distance from the source. Graphs 7 to 12 are waveforms of 28 μm PVDF sensors (channels 1 and 2) located the same distance from the source. Graphs 13 to 18 are waveforms of 52 μm PVDF sensor (channel 1) and 28 μm PVDF sensor (channel 2) located the same distance from the source. Graphs 19 to 24 are waveforms of the commercial resonant (channel 1) and the wideband (channel 2) transducers located the same distance from the source (refer to Table 3-1).

Graph numbers 18 and 24 are presented in Figure 3-5. In Figure 3-5 a, the signal waveforms generated by PVDF sensors of 52 μm (channel 1) and 28 μm (channel 2) located at L4 on the aluminum block show extraneous noise interference. In Figure 3-5 b, the signal waveforms generated by the resonant transducer (channel 1) and the wideband transducer (channel 2) show little extraneous noise interference.

The 28 μm sensors demonstrated a slightly greater sensitivity to surface waves (Graphs 13-15) than the 52 μm sensors. The PVDF sensors and the wideband transducer were more sensitive to surface waves than the resonant transducer (Graphs 19-24).

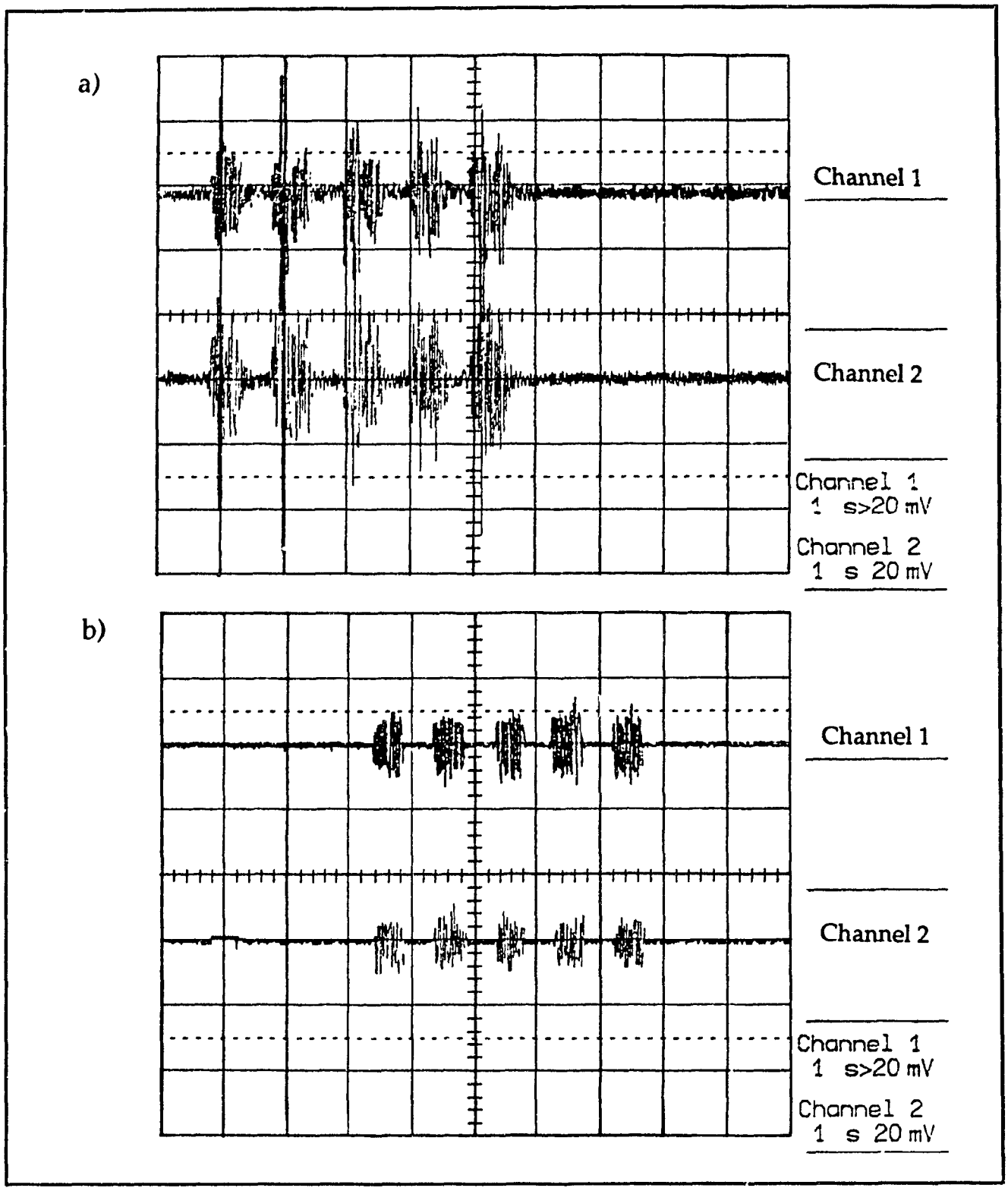

Fig. 3-5: Voltage-Time Waveforms Generated by PVDF Sensors and Commercial Transducers on Aluminum Test Block,
a) PVDF Sensors (52 μm & 28 μm), b) Resonant and Wideband Transducers

3.2.2 Pattern Classification Results

Two class comparisons involve digitized waveforms gathered from the 52 μm and the 28 μm sensors. Three class comparisons involve digitized waveforms gathered from the 52 μm and the 28 μm sensors and either the resonant or the wideband transducer. In Tables 3.2, 3.3, 3.4, and 3.5, signal waveforms acquired during aluminum block tests are classified with respect to receiver sensor type. The receiver signals were classified by comparing; i) PVDF sensors of 52 μm and 28 μm, ii) PVDF sensors of 52 μm, 28 μm, and the resonant transducer, and iii) PVDF sensors of 52 μm, 28 μm, and the wideband transducer. The optimal feature set for each classifier type was determined by selecting the most prominent features in each domain and refining the feature set to contain the minimum number of features corresponding to the maximum training and testing recognition rates.

It is evident from the number of frequency related features chosen in each classifier that primarily frequency related characteristics were used to classify the signal waveforms. Since the resonant transducer had a small frequency band (50 kHz to 200 kHz) when compared to the wideband transducer (200 kHz to 1 MHz) less information can be taken from the signal and fewer features can be extracted.

3.2.2.1 5-Nearest neighbor classifier results are as follows: the classification of the PVDF sensors with respect to foil thickness, resonant, and wideband transducers (Table 3-2) required optimum feature sets containing a majority of frequency related features. Good distinction could be made between the PVDF sensors of different foil thicknesses and the ceramic resonant transducer. The classifier was not able to clearly distinguish between the signals of the PVDF sensors and the wideband transducer during testing due to the similarity of the signal waveforms.

3.2.2.2 Linear discriminant classifier results are as follows: the linear discriminant classifier (Table 3-3) was the most successful in distinguishing between receiver sensors. The optimum feature sets used to identify the PVDF sensors, resonant and wideband transducers relied more heavily on time domain features than the 5NN classifier.

3.2.2.3 Empirical Bayesian classifier results are as follows: the empirical Bayesian classifier (Table 3-4) was the least successful in identifying the signal waveforms. The EB optimal feature sets contained the largest number of features and the majority of features are frequency related. The EB classifier is more sensitive to class size, since it relies on parameters having priori distributions. [23] It is evident that the class sizes were too small to provide good accuracy.

3.2.2.4 Minimum distance classifier results are as follows: the minimum distance classifier (Table 3-5) was only successful in discriminating against the PVDF sensors. The majority of features chosen were from the frequency-domain (stage two of study).

3.3 Discussion of Test Results and Problems Encountered

Assembly of the PVDF sensors was difficult and time consuming. The PVDF sensors were highly sensitive to extraneous noise interference. The extraneous noise interference was attributed to the difficulty in obtaining a properly shielded condition with the SOIC clips as well as an even contact area and a stable contact pressure on the PVDF sensor film.

The linear discriminant algorithm was the most successful in distinguishing sensor type. The number of frequency related features chosen during pattern classification indicate that more information was derived from the frequency-domain than the time-domain.

Based on the difficulty in assembly, the noise interference, and the number of frequency related characteristics used in pattern classification, it was decided to purchase pre-assembled PVDF sensors of 28 μm thickness (40 MHz bandwidth) with shielded leads and use a wideband source transducer for the graphite/plate testing (stage two of study).

Table 3-2: Aluminum Block Classification Results; 5-Nearest Neighbor Function

5-NEAREST NEIGHBOR CLASSIFIER

IDENTITY	CLASS SIZE	SIGNAL RECOGNITION CLASS 1	CLASS 2	CLASS 3	RECOGNITION RATE (%)	FEATURE SET
					TRAINING	
PVDF1, 52	9	9	0	NA	100.00	1 37 38 47
PVDF2, 28	9	0	9	NA	100.00	48 49 53 55
					100.00	56 65 66 68
						71 79 83 84
					TESTING	86 88 96 99
PVDF1, 52	9	8	1	NA	88 89	
PVDF2, 28	9	2	7	NA	77.78	
					83.33	
					TRAINING	
PVDF1, 52	9	9	0	0	100.00	37 38 41 43
PVDF2, 28	9	2	7	0	77.78	65 73 83 86
RESONANT	3	0	0	3	100.00	91
					90.48	
					TESTING	
PVDF1, 52	9	7	2	0	77.78	
PVDF2, 28	9	1	7	1	77.78	
RESONANT	3	0	0	3	100.00	
					80.95	
					TRAINING	
PVDF1, 52	9	9	0	0	100.00	1 37 38 47
PVDF2, 28	9	0	9	0	100.00	48 49 53 55
WIDEBAND	3	0	0	3	100 00	56 65 66 68
					100.00	71 79 83 84
						86 88 96 99
					TESTING	
PVDF1, 52	9	6	3	0	66 67	
PVDF2, 28	9	2	6	1	66 67	
WIDEBAND	3	0	2	1	33 30	
					61.90	

Table 3-3: Aluminum Block Classification Results; Linear Discriminant Function

LINEAR DISCRIMINANT CLASSIFIER

IDENTITY	CLASS SIZE	SIGNAL RECOGNITION CLASS 1	CLASS 2	CLASS 3	RECOGNITION RATE (%)	FEATURE SET
					TRAINING	
PVDF 1, 52	9	8	1	NA	88.89	1 2 10 12
PVDF 2, 28	9	0	9	NA	100.00	17 19 23 26
					94.44	35 36 48 49
						50 51 52 53
					TESTING	54 64 69 71
PVDF 1, 52	9	7	2	NA	77.78	75 82 96 99
PVDF 2, 28	9	2	7	NA	77.78	
					77.78	
					TRAINING	
PVDF 1, 52	9	9	0	0	100.00	1 30 34 41
PVDF 2, 28	9	1	8	0	88.89	44 51 80 83
RESONANT	3	0	0	3	100.00	84 86 88 96
					95.24	99
					TESTING	
PVDF 1, 52	9	6	3	0	66.67	
PVDF 2, 28	9	2	6	1	66.67	
RESONANT	3	0	0	3	100.00	
					71.43	
					TRAINING	
PVDF 1, 52	9	9	0	0	100.00	1 2 4 6 8 10
PVDF 2, 28	9	0	9	0	100.00	15 17 20 23
WIDEBAND	3	0	0	3	100.00	25 26 29 32
					100.00	33 36 40 41
						43 44 46 50
					TESTING	51 55 57 63
PVDF 1, 52	9	8	1	0	88.89	73 79 86 87
PVDF 2, 28	9	1	8	0	88.89	88 91 96 99
WIDEBAND	3	0	0	3	100.00	101
					90.48	

Table 3-4: Aluminum Block Classification Results; Empirical Bayesian Function

EMPIRICAL BAYESIAN CLASSIFIER

IDENTITY	CLASS SIZE	SIGNAL RECOGNITION CLASS 1	CLASS 2	CLASS 3	RECOGNITION RATE (%)	FEATURE SET
					TRAINING	
PVDF 1, 52	9	8	1	NA	88.89	1 2 10 12 17
PVDF2, 28	9	5	4	NA	44.44	19 23 26 35
					66 67	36 50 52 64
						65 66 67 69
					TESTING	71 75 78 82
PVDF 1, 52	9	9	0	NA	100.00	88 96
PVDF2, 28	9	9	0	NA	0 00	99
					50.00	
					TRAINING	
PVDF 1, 52	9	7	1	1	77 78	1 8 19 26 30
PVDF2, 28	9	2	6	1	66.67	34 37 38 41
RESONANT	3	0	1	2	66.67	42 43 44 45
					71 43	48 49 50 51
						53 55 61 62
					TESTING	63 65 66 67
PVDF 1, 52	9	7	0	2	77.78	68 73 74 79
PVDF2, 28	9	7	1	1	11.11	80 81 83 84
RESONANT	3	0	0	3	100 00	86 91 92 99
					52 38	101 105 106
					TRAINING	
PVDF 1, 52	9	6	2	1	66 67	1 2 4 6 8 10
PVDF2, 28	9	2	6	1	66.67	13 15 17 20
WIDEBAND	3	1	0	2	66 67	23 25 26 29
					66 67	30 32 33 36
						40 41 43 44
					TESTING	46 50 51 55
PVDF 1, 52	9	6	0	3	66 67	57 63 73 74
PVDF2, 28	9	6	2	1	22 22	75 79 86 87
WIDEBAND	3	1	0	2	66 67	88 91 96 99
					47.62	101 104

Table 3-5: Aluminum Block Classification Results; Minimum Distance Function

MINIMUM DISTANCE CLASSIFIER

IDENTITY	CLASS SIZE	SIGNAL RECOGNITION CLASS 1	CLASS 2	CLASS 3	RECOGNITION RATE (%)	FEATURE SET
					TRAINING	
PVDF1, 52	9	9	0	NA	100.00	1 2 10 12
PVDF2, 28	9	1	8	NA	88.89	17 19 26 34
					94.44	35 36 41 47
						48 50 51 60
					TESTING	64 68 69 71
PVDF1, 52	9	8	1	NA	88.89	75 78 79 82
PVDF2, 28	9	2	7	NA	77.78	86 88 96 97
					83.33	99 100
					TRAINING	
PVDF1, 52	9	7	1	1	77.78	1 26 30 34
PVDF2, 28	9	0	8	1	88.89	37 38 41 42
RESONANT	3	0	1	2	66.67	43 44 48 50
					80.95	51 53 55 61
						62 65 73 74
					TESTING	80 81 83 84
PVDF1, 52	9	5	2	2	55.56	86 91 92 96
PVDF2, 28	9	2	6	1	66.67	99 100 105
RESONANT	3	0	0	3	100.00	106
					66.67	
					TRAINING	
PVDF1, 52	9	7	1	1	77.78	1 2 4 8 10
PVDF2, 28	9	1	8	0	88.89	15 17 20 23
WIDEBAND	3	0	0	3	100.00	25 26 29 32
					85.71	33 36 40 41
						43 44 46 50
					TESTING	51 55 57 63
PVDF1, 52	9	3	3	3	33.33	79 86 87 88
PVDF2, 28	9	0	8	1	88.89	91 96 99
WIDEBAND	3	1	0	2	66.67	101
					61.90	

4.0 GRAPHITE/EPOXY PLATE TESTS

Testing of the 16 ply unidirectional and cross-ply (±45°) IM7/977-2 graphite/epoxy plates comprised four parts. AU signal gathering, followed by ultrasonic C-Scan, followed by cumulative impact of 3 and 9 hits, and finally compression testing of the impacted and non-impacted areas. The impact sites were confined to a 100 mm (4 inch) by 150 mm (6 inch) center area of the test plate (Figs. 4-1, 4-2, 4-3). The PVDF receiver sensors were positioned within the test grid (Table 4-1) during AU signal gathering.

The sensitivity of the pre-assembled PVDF sensors was verified by fixing each sensor to the aluminum block, used in section 3.0, at the same distance from the ceramic wideband transducer source and comparing the amplitude of the resulting signal waveform displayed on the digital oscilloscope.

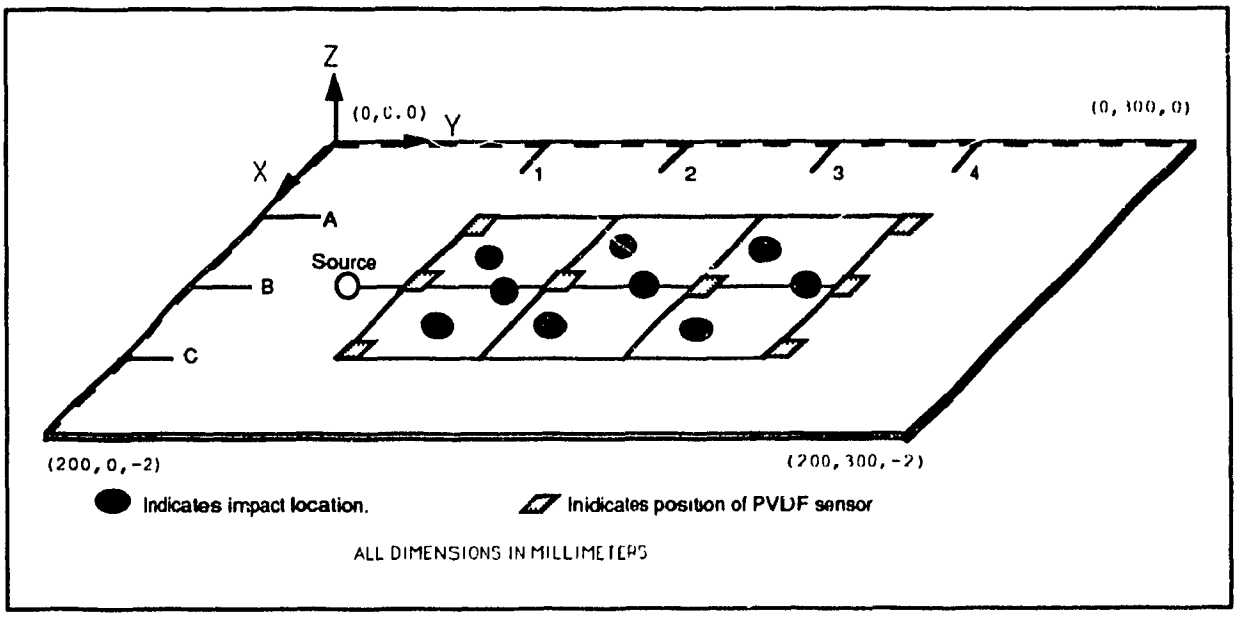

Fig. 4-1: Test Plate Diagram Indicating Position of PVDF Sensors and Impacts in Test Grid

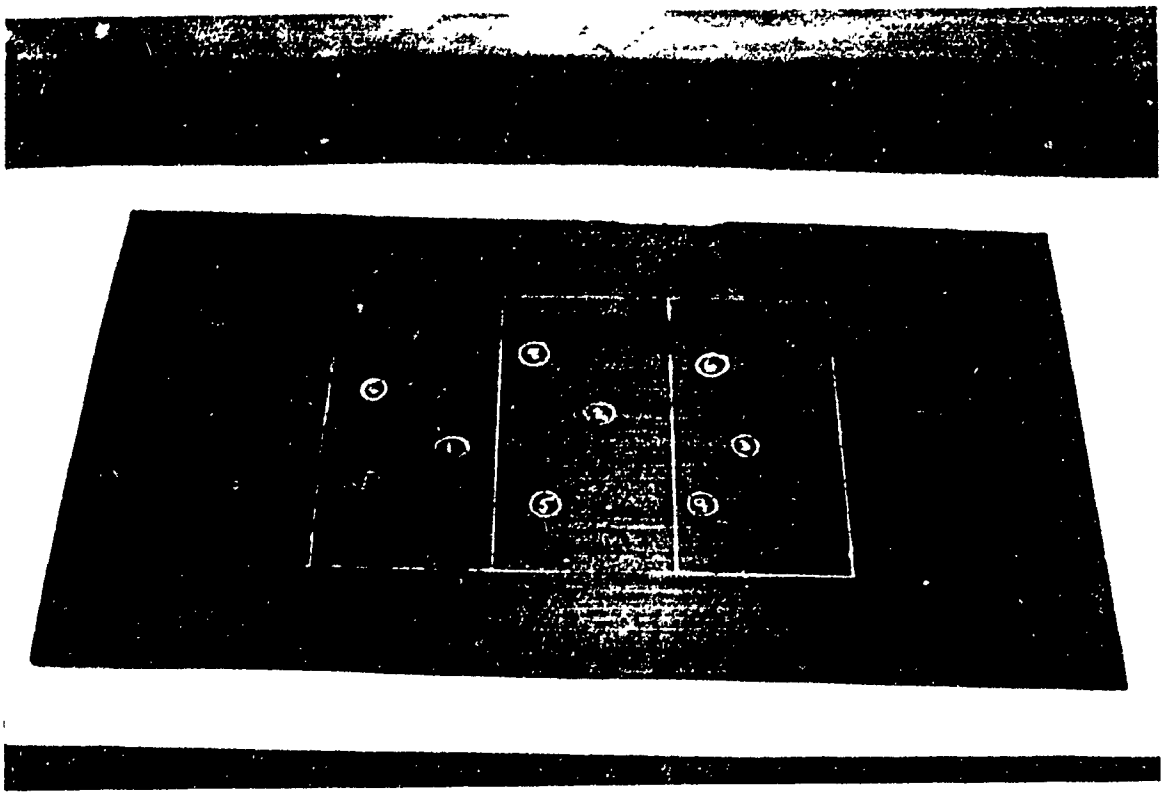

Fig. 4-2: Unidirectional Graphite/Epoxy Plate with Test Grid and Impact Sites Outlined in Silver Ink, Teflon Marker Visible on Lower Left Hand Side

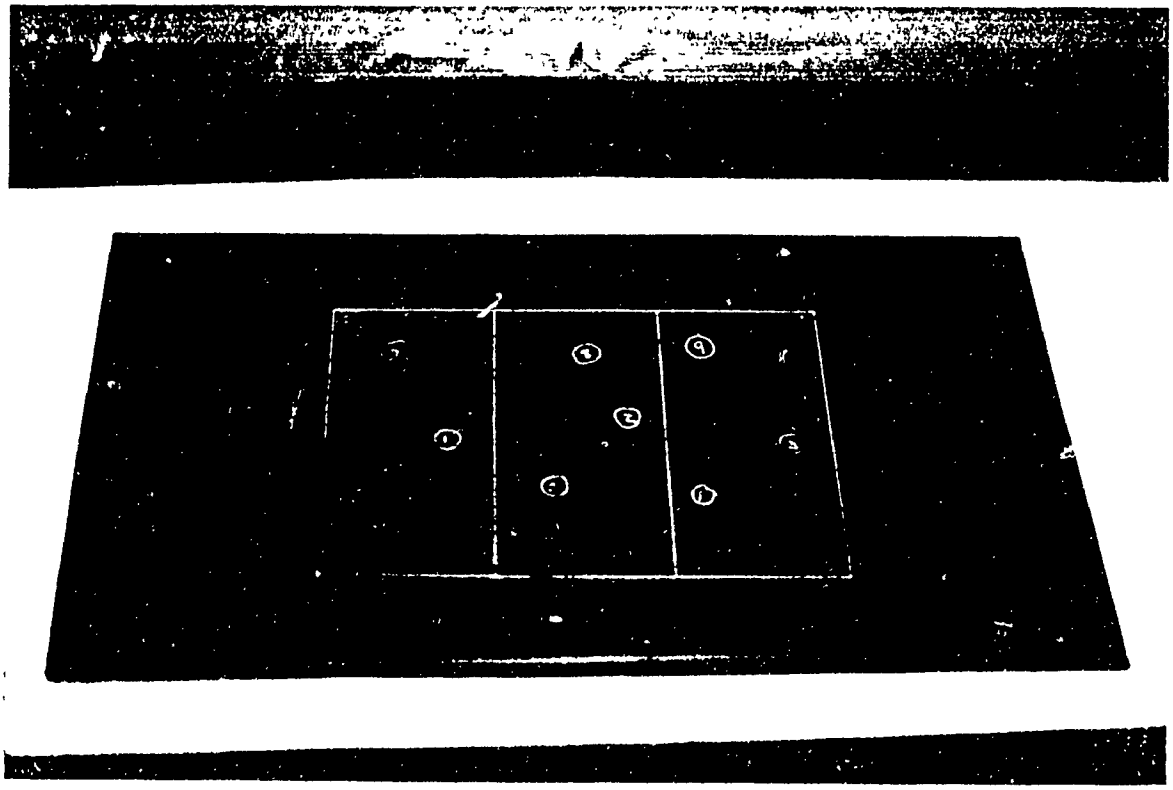

Fig. 4-3: Cross Ply (±45°) Graphite/Epoxy Plate with Test Grid and Impact Sites Outlined in Silver Ink, Teflon Marker Visible on Upper Right Hand Side

Table 4-1: Location of Signal Source and PVDF Sensors on Graphite/Epoxy Plates

Wideband Source Location	PVDF Sensor Locations	
X,Y,Z (mm,mm,mm)	X,Y,Z (mm,mm,mm)	
S = 100, 50, 0	A1 = 50, 75, 0	A4 = 50, 225, 0
	B1 = 100, 75, 0	B2 = 100, 125, 0
	B3 = 100, 175, 0	B4 = 100, 225, 0
	C1 = 150, 75, 0	C4 = 150, 225, 0

4.1 Ultrasonic C-Scan Test Set-Up

C-scan images (signal amplitude versus scanning transducer location) were produced with a MATEC IMT-8000C Ultrasonic Unit and immersion tank coupled to a PC and ink jet printer. The scanning transducer providing and receiving the pulse-echo signals (A-scans) was a 5 MHz broadband type with a 4 inch focal length. A voltage input signal to the scanning transducer was provided by an external Tektronix MP-270 Pulser unit. The reflected signals were amplified with a variable gain MR-106 Receiver unit. Scanning resolution was 1 line/2mm (12.5 lines/inch) with a 2 dB threshold. Two 12.5 mm x 25 mm (1/2 inch by 1 inch) teflon markers were positioned on the surfaces of the test plates. The ±45° plate had two teflon inserts, 6.3 mm (1/4 inch) square located at mid laminate thickness.

The graphite/epoxy plate material velocity was determined to be 2.9 mm/μs from a time delay of 1.44 10^{-6} seconds between front and first back surface echoes and an average plate thickness of 2 mm (0.08 in).

4.2 Acousto-Ultrasonic Test Set-Up

The acousto-ultrasonic signal gathering set-up (Fig. 4-4) consisted of a Lecroy 9400A digital ocilloscope coupled to a PC through a GPIB interface. A input spike voltage of

-100V was provided by a Tektronix MP-270 Pulser to a ceramic wideband source transducer having a truncated cone contact, providing a surface pulse to the test plates as indicated in Figure 1-1. The source transducer had an approximately flat sensitivity of -3 dB over a frequency band of 0.2 to 1 MHz. The source transducer was coupled to the test plates with silicone grease. The four pre-assembled PVDF receiver sensors were 28 μm thick film with Ag ink metallized surfaces, type SDT1-028K distributed by Pennwalt Corporation. The received signals were amplified by 20 dB (gain of 10) using a Tektronix MR-106 Receiver before being captured by the digital oscilloscope. The test plates were placed on a silicone rubber pad of 6.3 mm (1/4 in) thickness mounted on a raised wooden platform with point contacts on a support table. Signal waveforms were plotted using a Roland plotter. The digitized waveforms were downloaded into MASP™ software and converted to ASCII readable files with ASYST™ software. The waveforms were then classified with ICEPAK™ software, with respect to type of plate (0° or ±45°) and number of impacts .

4.2.1 Support Fixture

The test support fixture is the same as that used in the aluminum block testing (refer to section 3.1.1).

4.2.2 Signal Source

The signal source was provided by a ceramic wideband transducer (refer to 2.9) which was used to verify each PVDF sensor sensitivity using the aluminum block prior to signal gathering.

4.2.3 Signal Waveform Gathering by Digital Oscilloscope

Time-domain (voltage-time) signal waveforms were gathered and frequency-domain (amplitude-frequency) information was generated with a Lecroy 9400A digital oscilloscope equipped with data storage and FFT signal processing capabilities. The frequency spectrum was determined through the FFT function available on the Lecroy 9400A. Two memory blocks (identified as C and D on waveform graphs) were used to compare waveforms gathered from various positions in the test plate grids (Table 4-1). The Nyquist limit for FFT processing was 50 MHz.

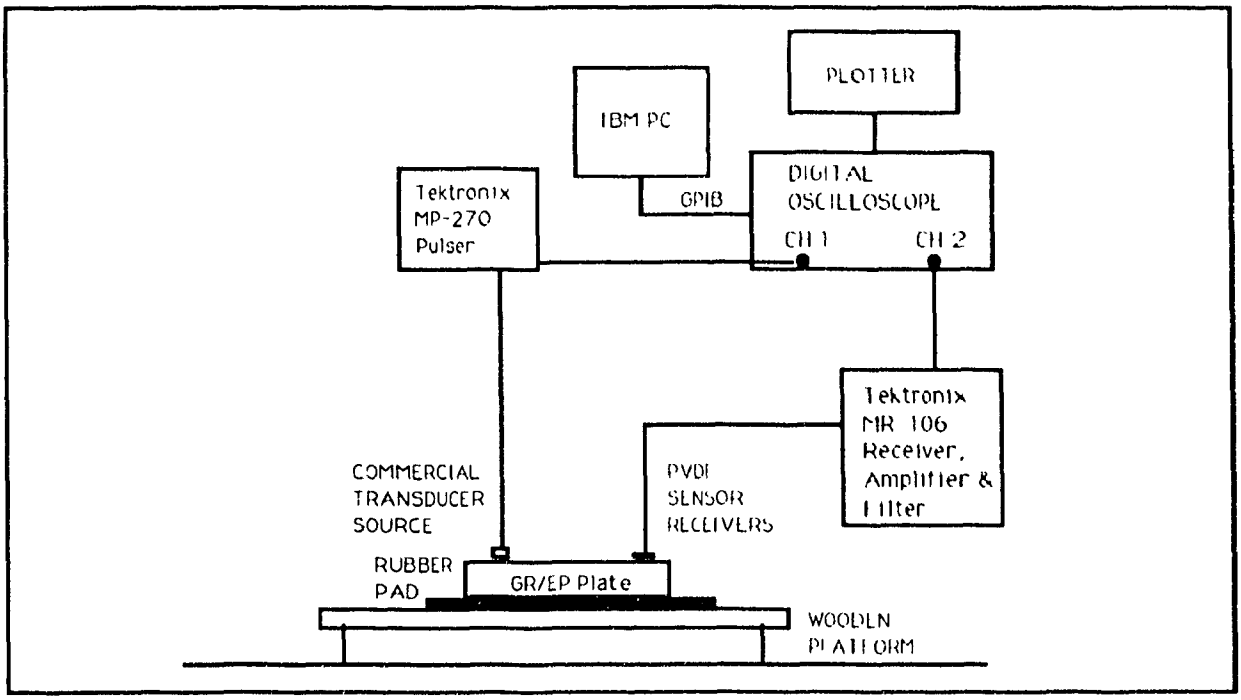

Fig. 4-4: AU Signal Gathering Set-up with Graphite/Epoxy Test Plate

4.3 Impact Test Set-Up

Impact was applied to the test plates in accordance with the procedures as outlined in ASTM D-2444, using impactor design Tup B and flat plate holder design B. The test plates were supported in a picture frame fixture. The impactor mass was 9 kg (20 lbs) and it was dropped through a tube from a height of 30 cm (1 ft), providing an impact energy of 27 joules (20 lb-ft), at an impact velocity of 244 cm/sec (8 ft/sec).

4.4 Compression Test Set-Up

Non-impacted and impacted areas of the test plate were cut into coupons approximately 12 mm wide by 50 mm long (1/2 inch by 2 inch) and tested in quasi-static compression on an MTS-810 using hydraulic grips (Fig. 4-5) and equipped with friction blocks to grip the coupons. The gripping pressure was maintained at 1 MPa. The gauge length of the coupons was approximately 25 mm (1 inch) with the impact site was cen-

tered within the gauge section. The sides of the test coupons were sanded to reduce stress concentrations. T-type (0°/90°) strain gauges of 120 ohm resistance were bonded to the middle of the coupon gauge section and axial and transverse strain data was gathered during testing. The cross-head speed was a constant 0.5 mm/min. Strain and load data were acquired with a Helios data acquisition system equipped with 1/4 arm Wheatstone bridges and coupled to a micro-computer using Labtech Notebook™ software. Data reduction was performed using Quattro-Pro™ software.

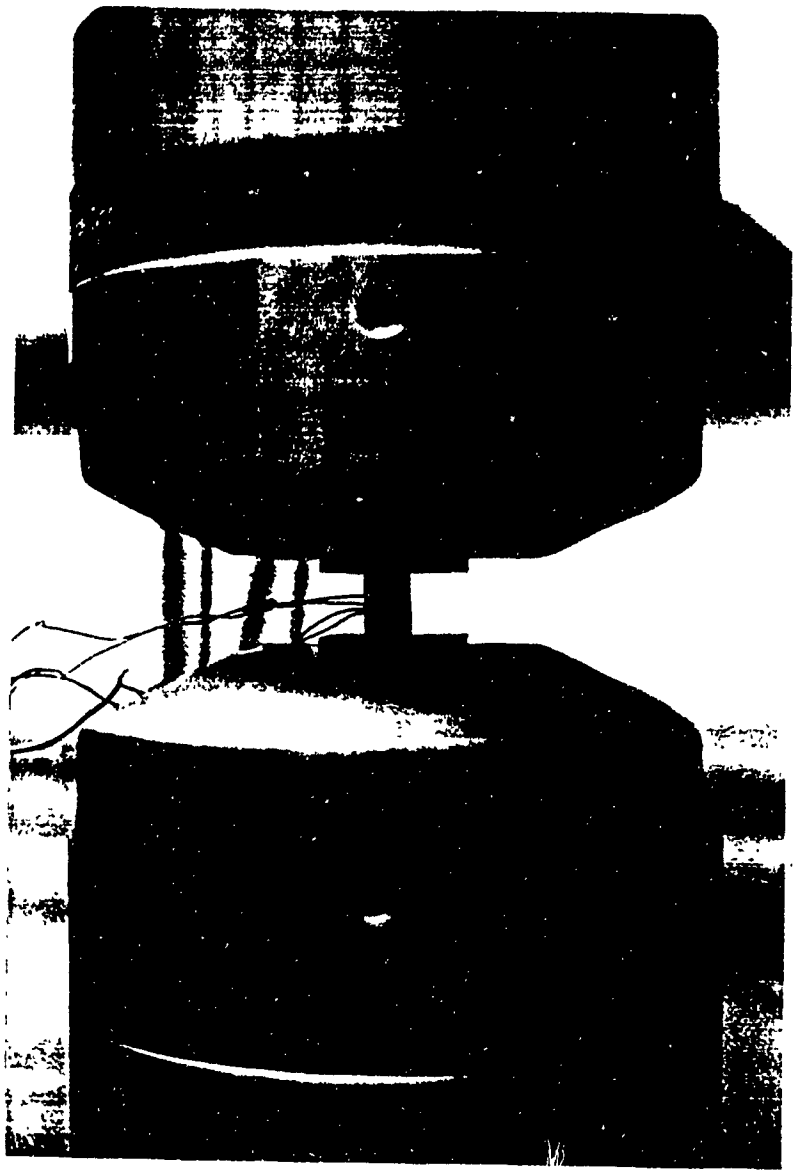

Fig. 4-5: Compression Specimen Mounted in Hydraulic Grips

4.5 Test Results

The test results are presented in the form of comparison of signal waveforms gathered during AU testing with respect to reduction in peak frequency and peak to peak voltage, comparison of ultrasonic C-scan images, correlation of waveform patterns with number of impact hits, and compression test results.

4.5.1 Comparison of AU Signal Waveforms Before and After Impact

The AU signal waveforms gathered from the graphite/epoxy plates are given in Appendix 3. Selected graphs are reproduced in Figures 4-6 to 4-10 to compare the change in the time-domain signal and frequency spectrum for the unidirectional and cross-ply (±45°) plates before and after impact. The selected graphs refer to PVDF sensors positioned at grid locations A4, B2, B3, and C1 (refer to Table 4-1).

In Figure 4-6 a and b, the time-domain and frequency spectrum for signals gathered at grid locations A4 and B2 on the 0° plate at 0 impacts and after 9 impacts are illustrated. At grid location A4 the receiving sensor is 185.4 mm (7.3 in) from the source transducer and at grid position B2 the receiving sensor is 76.4 mm (3 in) from the source transducer. The peak to peak voltage is higher at the B2 position before and after impact due to the closer proximity to the signal source. The frequency spectrum in both cases narrows due to the widening of the time-domain signal.

In Figure 4-7 a and b, the time-domain and frequency spectrum for signals gathered at grid locations B3 and C1 on the 0° plate at 0 impacts and after 9 impacts are illustrated. At grid location B3 the receiving sensor is 127 mm (5 in) from the source transducer and at grid position C1 the receiving sensor is 55.9 mm (2.2 in) from the source transducer. The first peak in the frequency spectrum occurs at a frequency of less than 1 MHz and may be the fundamental frequency of the test plate.

In Figure 4-8 a and b, the time-domain and frequency spectrum for signals gathered at grid locations A4 and B2 on the ±45° plate at 0 impacts and after 9 impacts are illustrated. At grid location A4 the receiving sensor is 185.4 mm (7.3 in) from the source

transducer and at grid position B2 the receiving sensor is 76.4 mm (3 in) from the source transducer. The time-domain waveforms and frequency spectrum are easily distinguished between 0 impacts and 9 impacts. The signal waveform and frequency spectrum after 9 impacts resembles those of the 0° plate.

In Figure 4-9 a and b, the time-domain and frequency spectrum for signals gathered at grid locations B3 and C1 on the ±45° plate at 0 impacts and after 9 impacts are illustrated. At grid location B3 the receiving sensor is 127 mm (5 in) from the source transducer and at grid position C1 the receiving sensor is 55.9 mm (2.2 in) from the source transducer. The peak to peak voltage of the signal acquired at the C1 grid position is higher due to its closer proximity to the signal source.

In Figure 4-10 a and b, the time-domain and frequency spectrum for signals gathered at grid location B2 on the 0° and ±45° plate at 0 impacts and after 9 impacts are illustrated. At grid position B2 the receiving sensor is 76.4 mm (3 in) from the source transducer. The signal waveforms of the undamaged plates are distinctive in shape. The signal waveforms and frequency spectrum after accumulated damage are similar in shape and amplitude.

In Appendix 3, the waveforms gathered from all eight grid positions are presented. The signal waveforms are compared by evaluating two shape parameters, peak to peak voltage, and the frequency at which the peak amplitude occurs (peak frequency) in Figures 4-11 to 4-14.

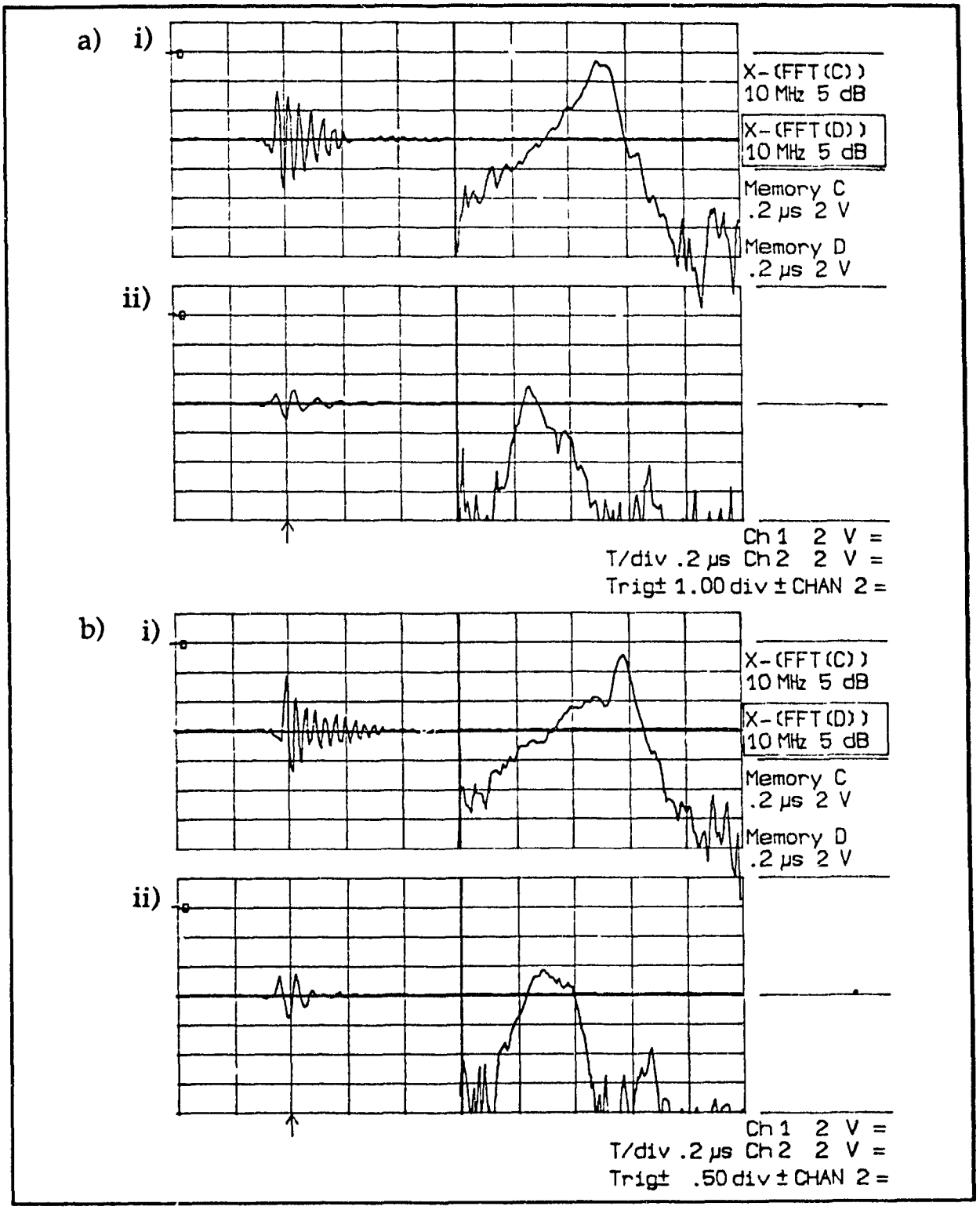

Fig. 4-6: Time and Frequency Domain Plots of PVDF Sensor Response;
a) Grid Location A4, i) 0° Plate, 0 Impacts, ii) 0° Plate, 9 Impacts,
b) Grid Location B2, i) 0° Plate, 0 Impacts, ii) 0° Plate, 9 Impacts,

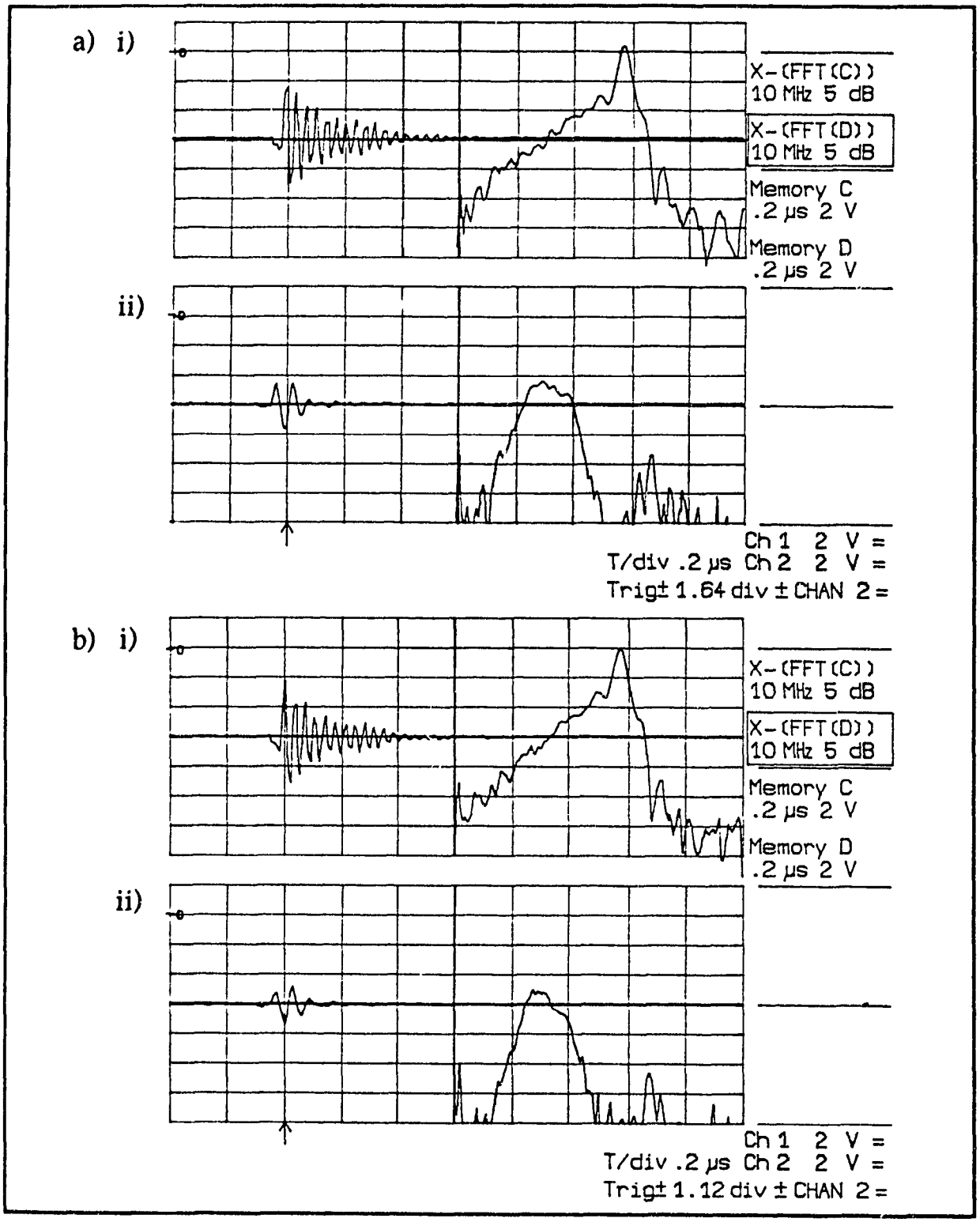

Fig. 4-7: Time and Frequency Domain Plots of PVDF Sensor Response;
a) Grid Location B3, i) 0° Plate, 0 Impacts, ii) 0° Plate, 9 Impacts,
b) Grid Location C1, i) 0° Plate, 0 Impacts, ii) 0° Plate, 9 Impacts,

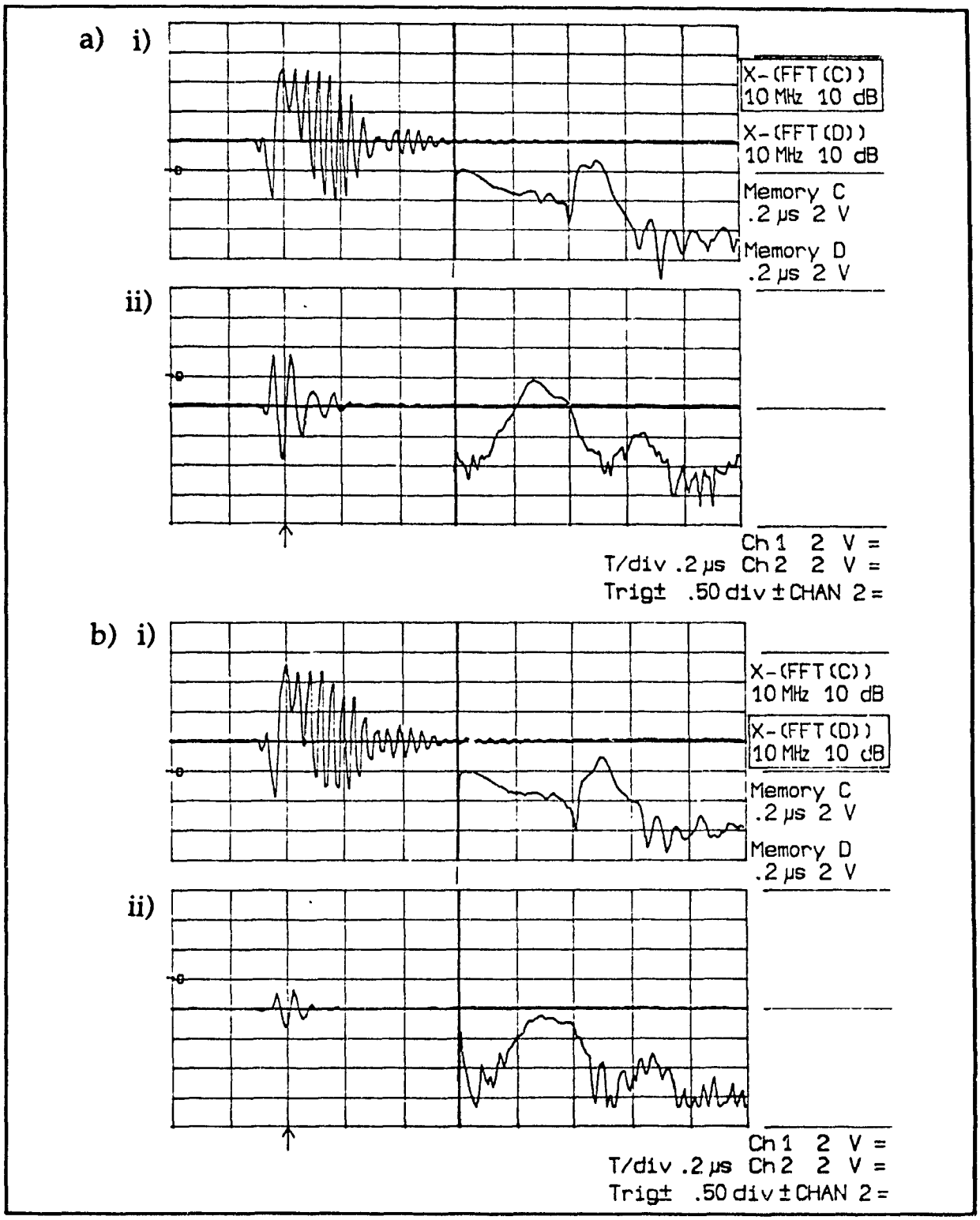

Fig. 4-8: Time and Frequency Domain Plots of PVDF Sensor Response;
a) Grid Location A4, i) ±45° Plate, 0 Impacts, ii) ±45° Plate, 9 Impacts,
b) Grid Location B2, i) ±45° Plate, 0 Impacts, ii) ±45° Plate, 9 Impacts,

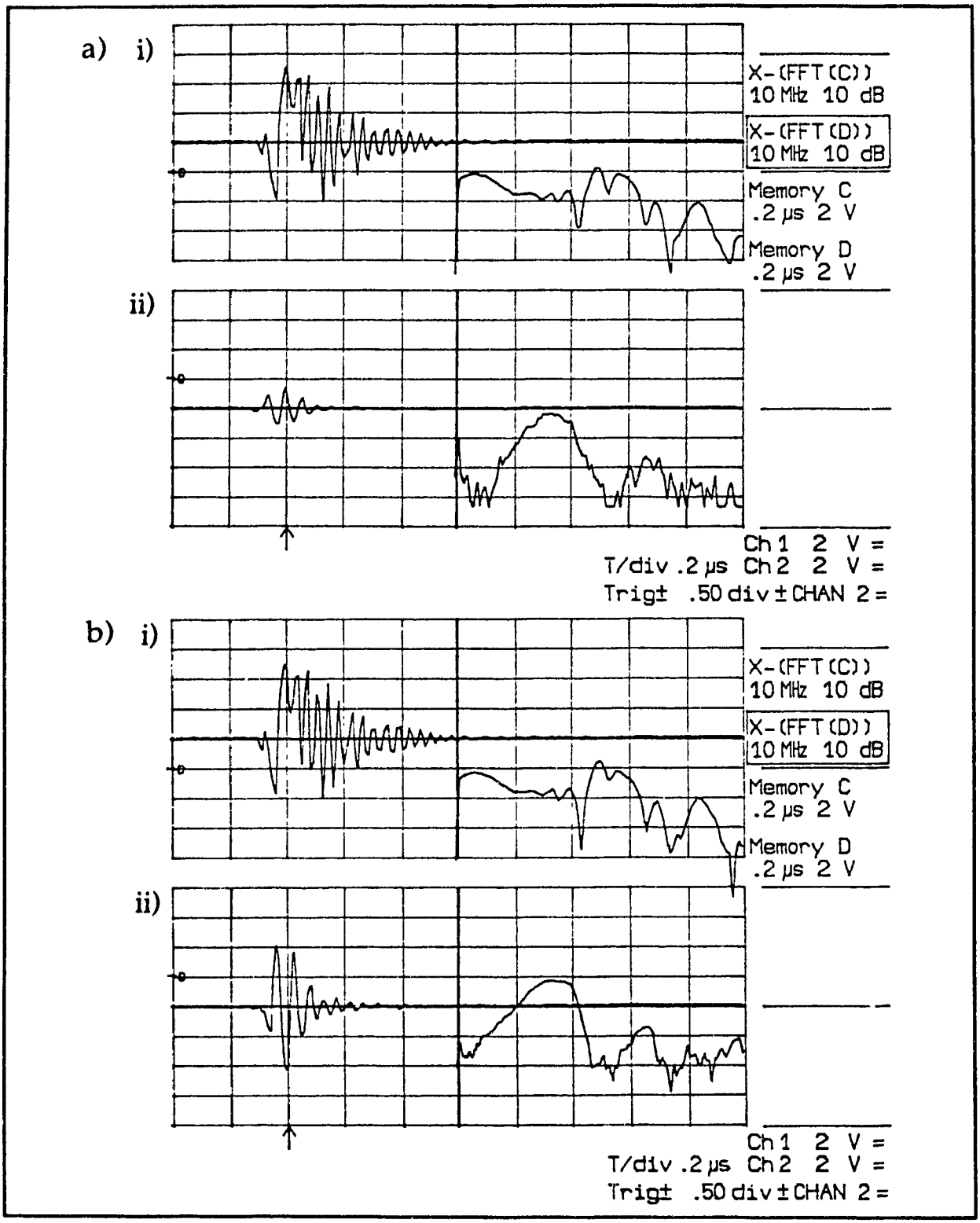

Fig. 4-9: Time and Frequency Domain Plots of PVDF Sensor Response;
a) Grid Location B3, i) ±45° Plate, 0 Impacts, ii) ±45° Plate, 9 Impacts,
b) Grid Location C1, i) ±45° Plate, 0 Impacts, ii) ±45° Plate, 9 Impacts,

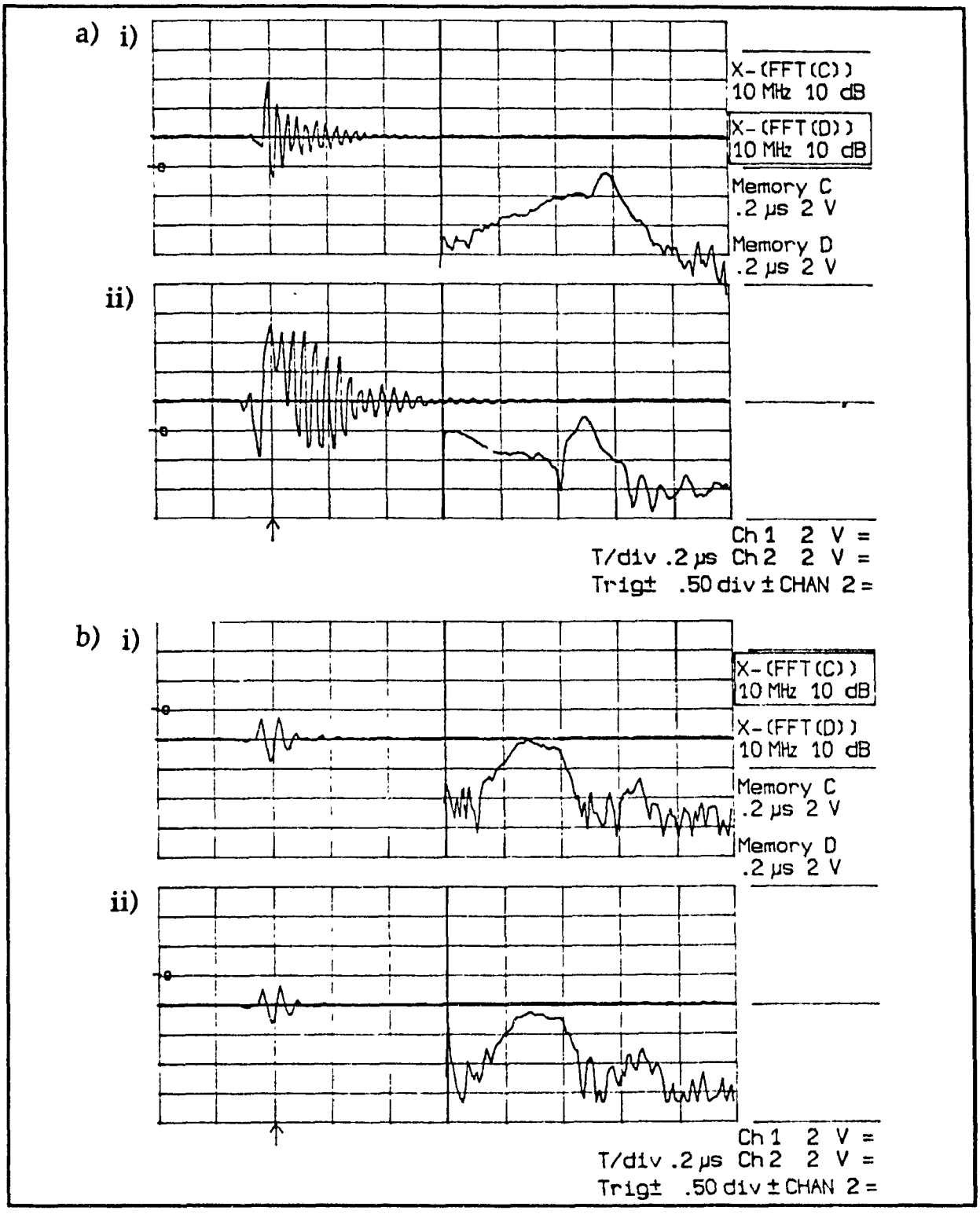

Fig. 4-10: Time and Frequency Domain Plots of PVDF Sensor Response;
a) Grid Location B2, i) 0° Plate, 0 Impacts, ii) ±45° Plate, 0 Impacts,
b) Grid Location B2, i) 0° Plate, 9 Impacts, ii) ±45° Plate, 9 Impacts.

The peak frequency of the signals gathered from both the 0° and the ±45° plate decreased with cumulative impact damage (Fig. 4-11 and 4-12). The results are presented in tabular form in Table 4-2. There was scatter of results from signals gathered at the A1 and C1 grid positions. This is likely due to the fact that those grid positions are oriented almost 90° from the source with respect to the fiber direction. This causes greater signal scattering due to interference with the fiber. The decrease in peak frequency of the 0° plate was greater than the ±45° plate. The average peak frequency of the 0° plate dropped from 27.5 MHz (0 impacts) to 11.5 MHz (9 impacts) an overall change of 16 MHz. The peak frequency of the ±45° plate dropped from an average of 25 MHz (0 impacts) to 15 MHz (9 impacts) an overall change of 10 MHz.

The initial peak to peak voltage of the 0° plate (Fig. 4-13) remained at 7.5 volts for 0, 3, and 9 impacts until a transition at the A1 and C1 grid positions 56 mm (2.2 in) from the source signal. The average peak to peak voltage then became 7.5 volts (0 impacts) and 2.5 volts (9 impacts), a reduction of 5 volts due to impact damage. The average peak to peak voltage values of the ±45° plate (Fig. 4-14) after the transition point was 9 volts (0 impacts) and 2 volts (9 impacts), a reduction of 7 volts due to impact damage.

Table 4-2: Decrease in Peak Frequency and Peak to Peak Voltage Due to Impact Damage

	0 Impacts	3 Impacts	9 Impacts	Max Decrease Due to Impact
Peak Frequency	MHz	MHz	MHz	%
0° Plate	27.5	22.5	11.5	58
±45° Plate	25.0	21.0	15.0	40
Peak to Peak Voltage	V	V	V	
0° Plate	7.5	5.5	2.5	67
±45° Plate	9.0	7.0	3.5	61

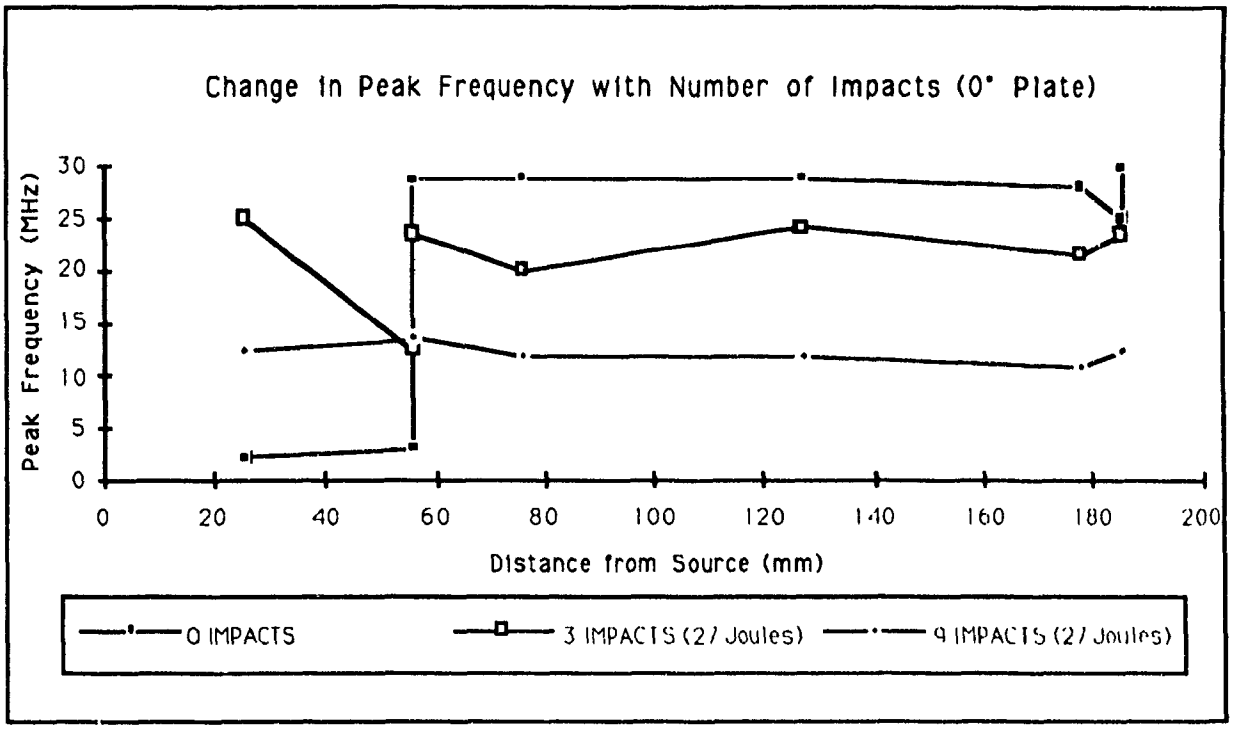

Fig. 4-11: Change in Peak Frequency with Number of Impacts; 0° Plate

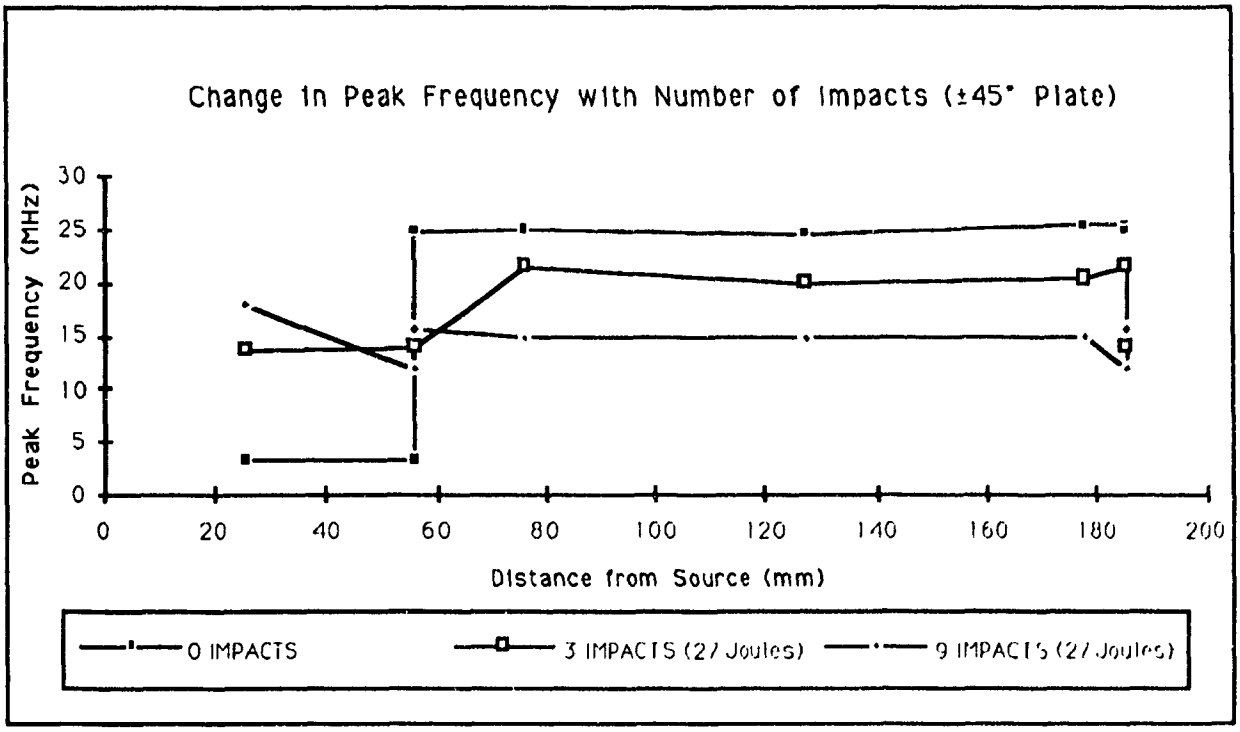

Fig. 4-12: Change in Peak Frequency with Number of Impacts; ±45° Plate

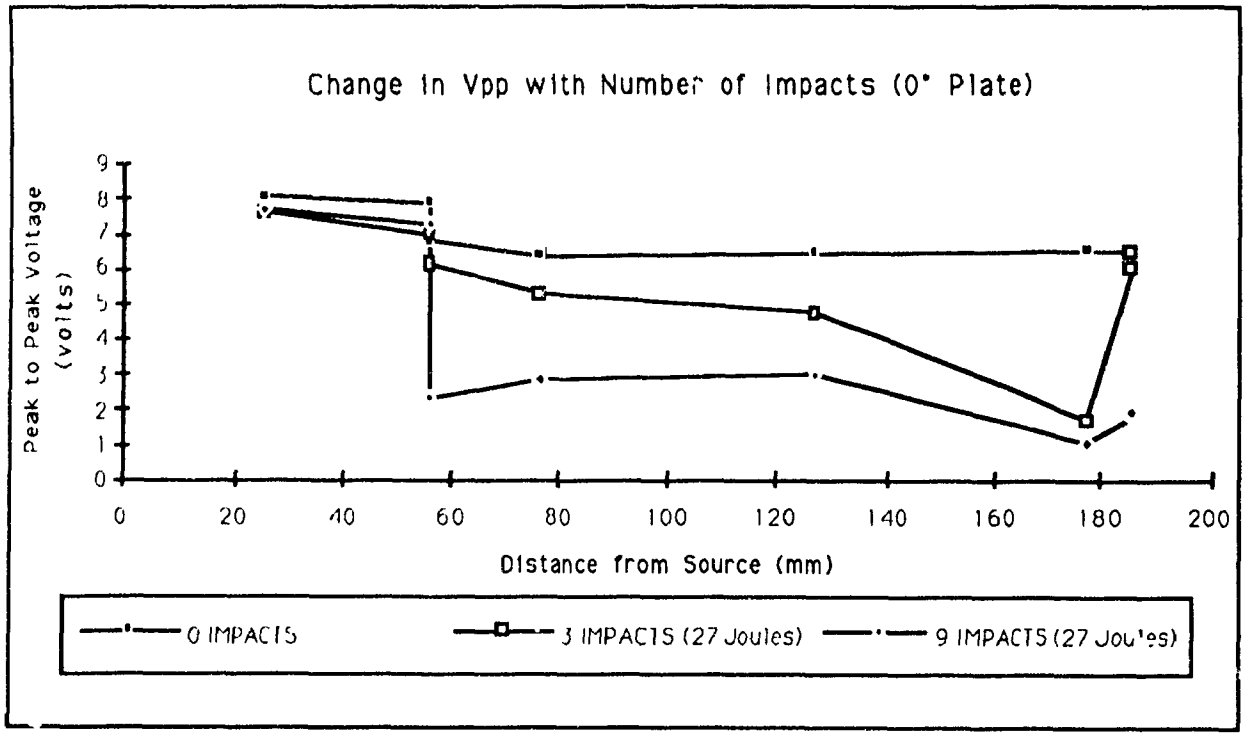

Fig. 4-13: Change in Peak to Peak Voltage with Number of Impacts; 0° Plate

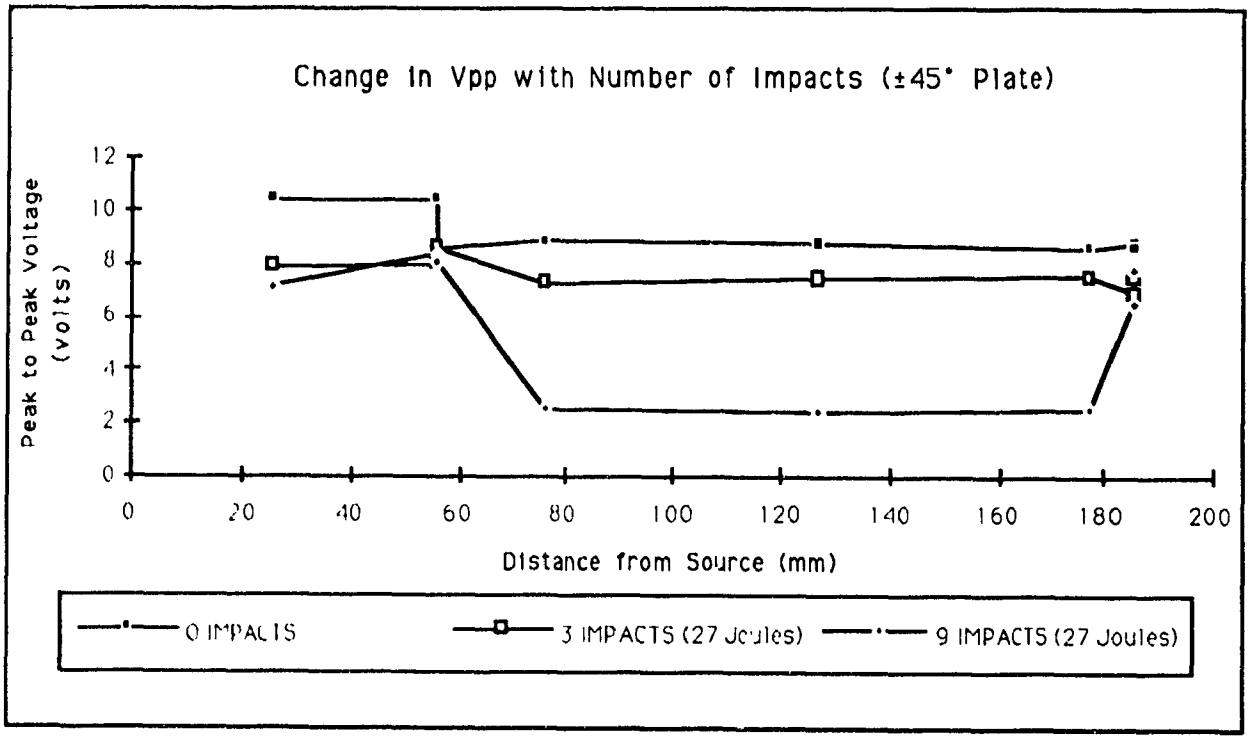

Fig. 4-14: Change in Peak to Peak Voltage with Number of Impacts; ±45° Plate

4.5.2 Ultrasonic C-Scan Results

Ultrasonic C-scan images are given in Appendix 4 for 0° and ±45° plates subjected to 0 impacts and 9 impacts. C-scan images are displayed in terms of signal amplitude versus scanning transducer position and are presented in 2-D (plan view) in Appendix 4 and 3-D (rotated) format in Figures 4-15 to 4-18. The color legend indicates signal amplitude.

Through examination of the C-scan images, the location of impact hits and extent of impact damage is not readily identifiable Some loss of signal was indicated at the center of the plates, probably due to some permanent deformation of the plates (bending) due to impact in the center plate region.

In Figure 4-15 and 4-16, the 3-D image of the 0° plate with 0 impacts and 9 impacts is presented. One piece of teflon tape was placed at the top and the bottom surface of the plate and is clearly indicated on the 3-D image in Figure 4-15. Black indicates bottom surface and white indicates top surface. The black areas at each end of the plate are the supports in the immersion tank. The fiber direction is clearly indicated by the lines running from end to end through the plate. There are no indications of voids or delaminations. In Figure 4-16, the same plate after 9 impacts has been C-scanned. Both teflon tapes were placed on the side of the plate subjected to impact. The lines running down the plate are more pronounced and may indicate bending (permanent deformation). There are no indications of delaminations due to impact.

In Figure 4-17 and 4-18, the 3-D image of the ±45° plate with 0 impacts and 9 impacts is presented. The two pieces of teflon tape fixed to the top surface of the plate and the two teflon inserts situated at mid-laminate of the plate are readily apparent. The black area at the base of the plate is the support in the immersion tank. No areas of voids or delaminations are apparent. There is some signal change from one corner of the plate diagonally across to the opposite side. This is probably due to the plate not resting parallel to the indexing transducer in the immersion tank. In Figure 4-18, the same plate after 9 impacts has been C-scanned. The teflon inserts and one tape on the bottom surface is apparent. No delamination due to impact damage can be discerned.

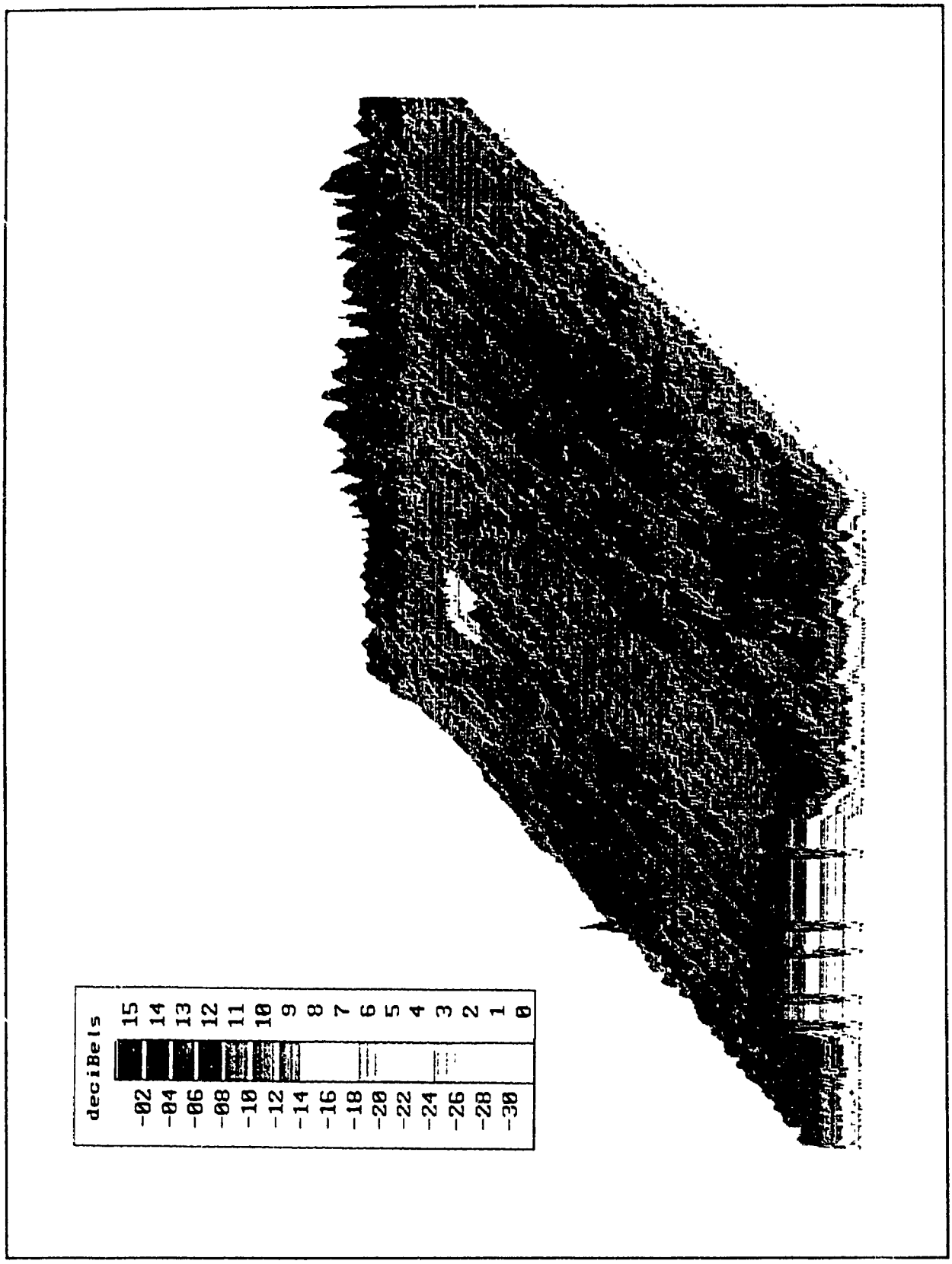

Fig 4-15: Ultrasonic C-Scan Image of 0° Plate, 0 Impacts

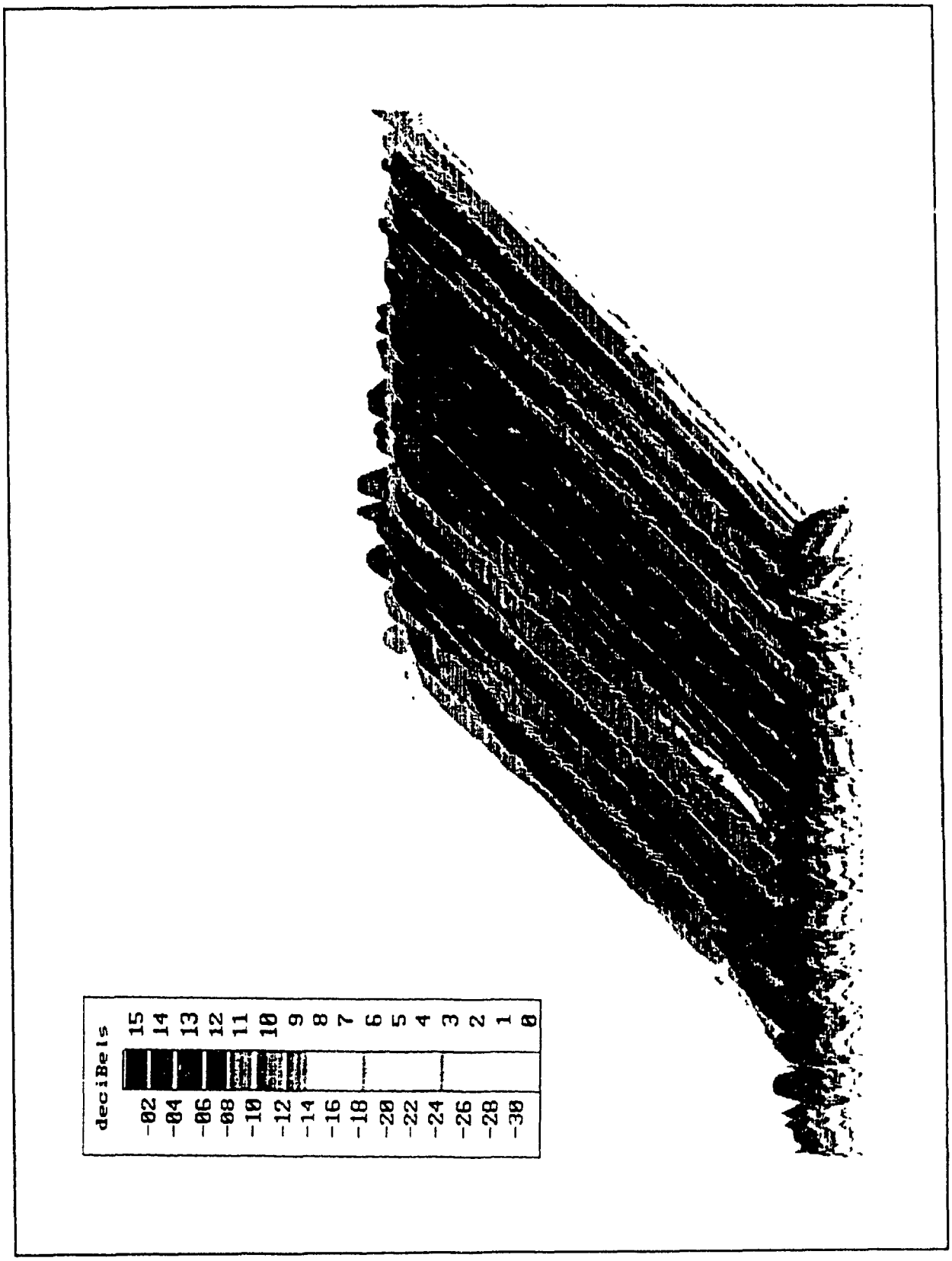

Fig 4-16: Ultrasonic C-Scan Image of 0° Plate, 9 Impacts

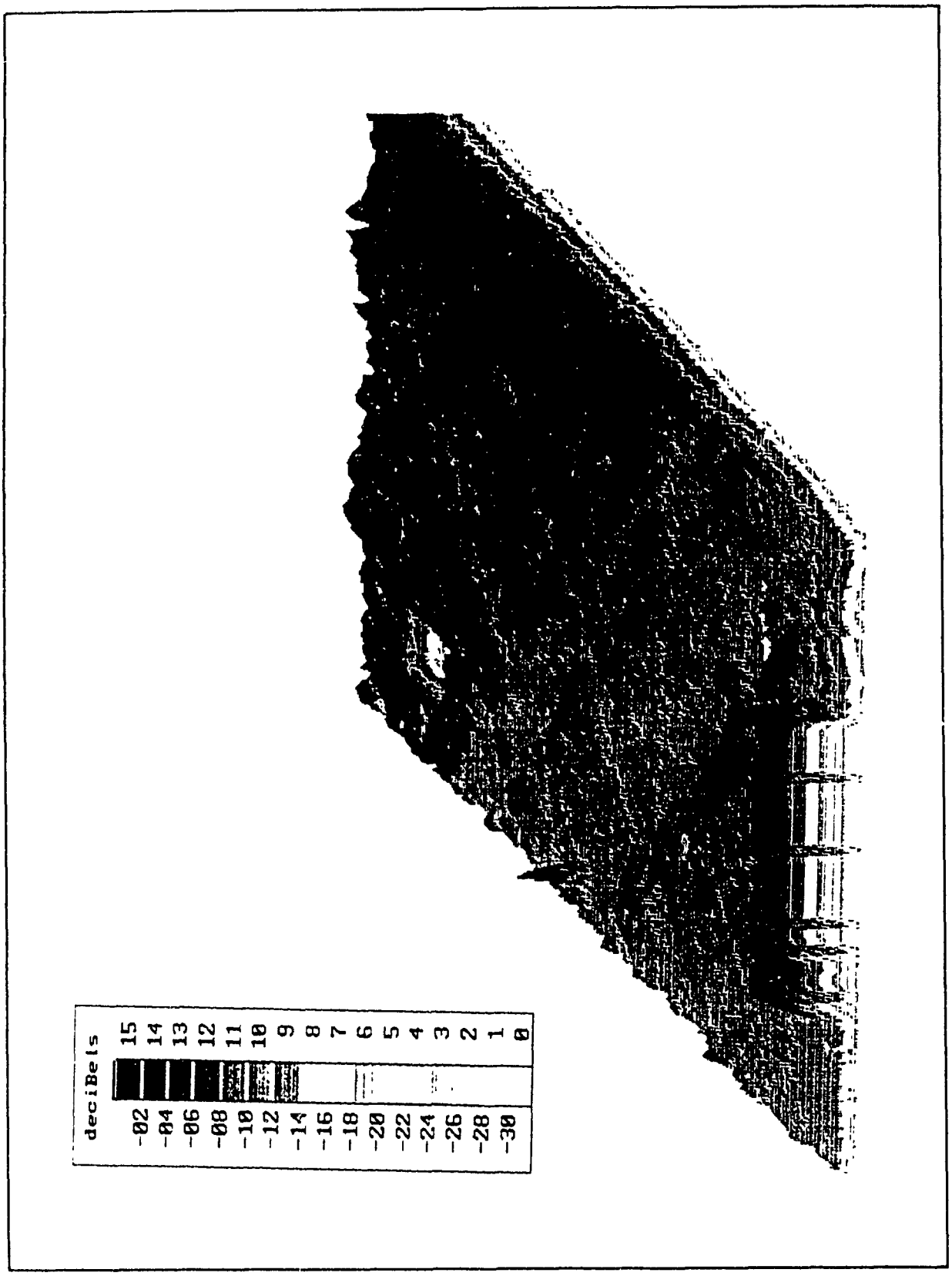

Fig 4-17: Ultrasonic C-Scan Image of ±45° Plate, 0 Impacts

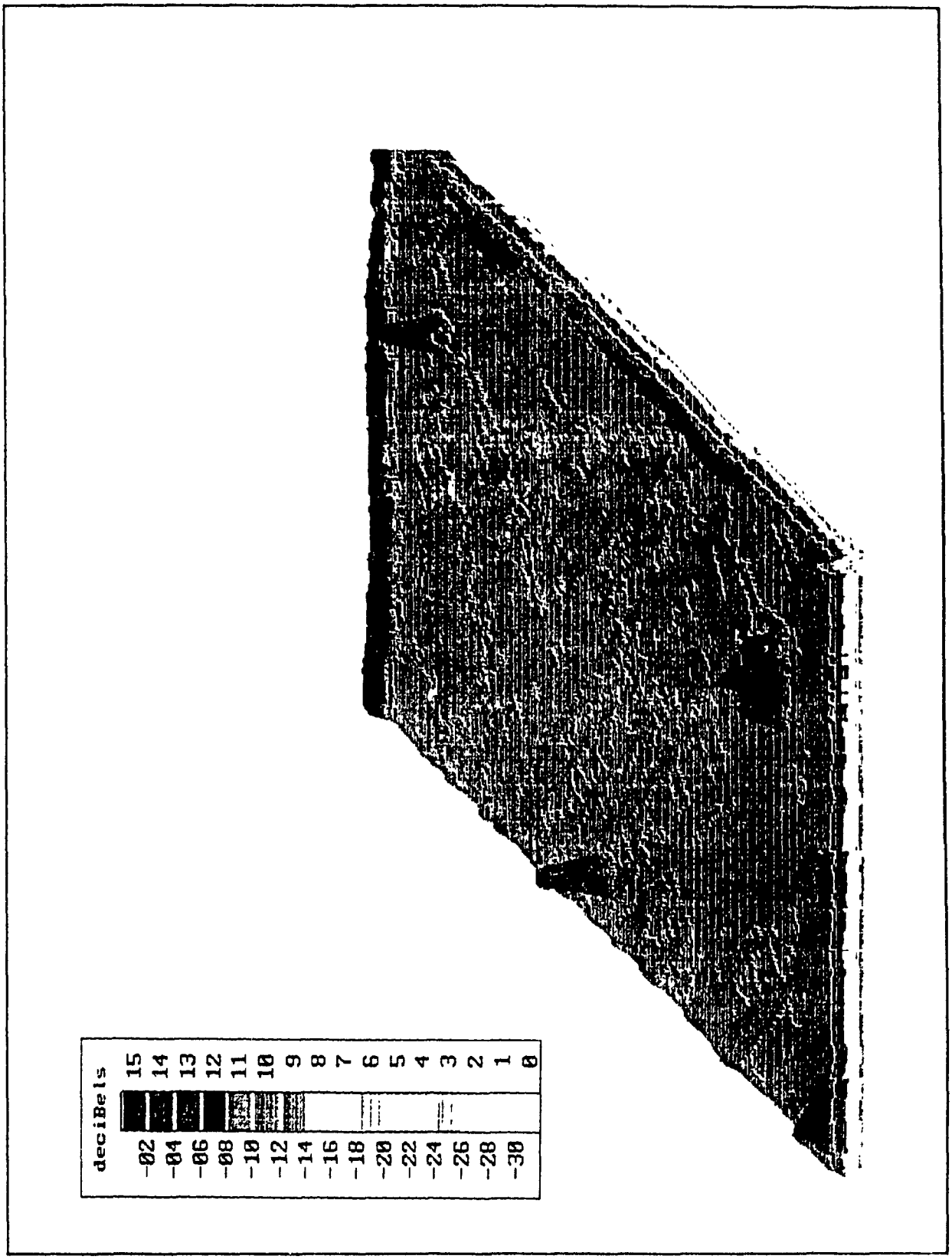

Fig 4-18: Ultrasonic C-Scan Image of ±45° Plate, 9 Impacts

4.5.3 Pattern Classification Results

The classification results for the 0° and ±45° plates (Table 4-3) including non-impacted and impacted (3 hits) signal files demonstrated training values of 93.75% and testing values of 75.00%. Each of the four classifiers was able to correctly distinguish the signals as coming from the 0° or ±45° plate respectively within an average acceptable recognition testing rate of 75%.

In Table 4-4, the 5-Nearest Neighbour Function Classifier was able to distinguish signals as coming from the 0° or ±45° plate after 0, 3, and 9 impacts respectively (three classes) with 45% confidence. When reduced to a two class problem of 0 and 3, and 0 and 9 impacts, the classification was more successful providing testing values of 71%.

In Table 4-5, the Linear Discriminant Function Classifier provided an average testing value of 75% for the three class problem of the 0° plate signals. The ±45° plate classification provided a confidence level of 55%. The two class problems of 0 and 3 impacts, provided a testing recognition rate of 62% for both the 0° and the ±45° plates. The two class problem 0 and 9 impacts, provided a testing recognition rate of 86% and 71% respectively for the 0° and ±45° plates.

In Table 4-6, the Empirical Bayesian Function Classifier provided a testing recognition rate of 73% for the three class problem with the 0° plate signals. The classification of the three class problem using the ±45° plate signals provided a testing recognition rate of 45%. The two class problem of 0 and 3 impacts provided a testing recognition rate of 88% for both plates. The two class problem of 0 and 9 impacts provided a testing recognition rate of 86% for the 0° plate and 71% for the ±45° plate.

In Table 4-7, the Minimum Distance Function Classifier was able to classify the three class and two class problems with testing recognition percentages of 75%, 88%, and 86% for the 0° plate signals. Classification of the ±45° plate signals for the three class and two class problems provided recognition rates of 45%, 50% and 71%.

Table 4-3: Pattern Classification Results of 0° and ±45° Plates (0 Impact and 3 Impact Signal Data Files)

PLATE IDENTITY	CLASS SIZE	SIGNAL RECOGNITION CLASS 1	SIGNAL RECOGNITION CLASS 2	RECOGNITION RATE (%)	FEATURE SET
5-NEAREST NEIGHBOR CLASSIFIER					
				TRAINING	
0° Plate	8	8	0	100 00	40 51 53 58
±45° Plate	8	1	7	87 50	64 66 77 79
				93 75	89 101 102
					103 104 106
				TESTING	
0° Plate	8	6	2	75 00	
±45° Plate	8	2	6	75 00	
				75 00	
LINEAR DISCRIMINANT FUNCTION CLASSIFIER					
				TRAINING	
0° Plate	8	8	0	100 00	40 51 53 56
±45° Plate	8	0	8	100 00	58 64 66 77
				100 00	79 85 89 91
					92 94 95 97
				TESTING	101 102 106
0° Plate	8	5	3	62 50	
±45° Plate	8	1	7	87 50	
				75 00	
EMPIRICAL BAYESIAN CLASSIFIER					
				TRAINING	
0° Plate	8	8	0	100 00	35 36 40 51
±45° Plate	8	1	7	87 50	53 56 58 61
				93 75	64 66 77 79
					85 92 94 95
				TESTING	101 102 106
0° Plate	8	7	1	87 50	
±45° Plate	8	3	5	62 50	
				75 00	
MINIMUM DISTANCE CLASSIFIER					
				TRAINING	
0° Plate	8	7	1	87 50	40 51 53 56
±45° Plate	8	0	8	100 00	58 64 66 77
				93 75	79 85 95 97
					106
				TESTING	
0° Plate	8	5	3	62 50	
±45° Plate	8	1	7	87 50	
				75 00	

Table 4-4: 5-Nearest Neighbor Function Classification Results; 0, 3, and 9 Impacts

5-NEAREST NEIGHBOR FUNCTION CLASSIFIER

Number of Impacts	CLASS SIZE	SIGNAL RECOGNITION CLASS 1	CLASS 2	CLASS 3	RECOGN RATE (%)	FEATURE SET	CLASS SIZE	SIGNAL RECOGNITION CLASS 1	CLASS 2	CLASS 3	RECOGN RATE (%)	FEATURE SET
	0° PLATE						±45° PLATE					
					TRAINING						TRAINING	
0 Impacts	4	4	0	0	100 00	19 42 59	4	4	0	0	100 00	45 50 52
3 Impacts	4	0	4	0	100 00	60 61 72	4	1	3	0	75 00	55 57 58
9 Impacts	3	0	2	1	33 33	77 87 90	3	1	0	2	66 67	59 60 64
					81 82	91 98 100 101					81 82	71 77 78 79 83 87
					TESTING	102					TESTING	94 106
0 Impacts	4	2	1	1	50 00		4	3	1	0	75 00	
3 Impacts	4	0	3	1	75 00		3	1	1	1	33 33	
9 Impacts	3	1	2	0	0 00		3	0	1	2	66 70	
					45 45						60 00	
					TRAINING						TRAINING	
0 Impacts	4	4	0	NA	100 00	3 6 8 15	4	4	0	NA	100 00	38 39 40
3 Impacts	4	0	4	NA	100 00	43 83 90	4	0	4	NA	100 00	45 50 51
					100 00	91 95 97 98 102					100 00	57 59 64 66 71 77
					TESTING						TESTING	79 94
0 Impacts	4	3	1	NA	75 00		4	3	1	NA	75 00	101
3 Impacts	4	2	2	NA	50 00		4	1	3	NA	75 00	
					62 50						75 00	
					TRAINING						TRAINING	
0 Impacts	4	4	0	NA	100 00	87 91	4	4	0	NA	100 00	59 60 83
9 Impacts	3	1	2	NA	66 67	101 102	4	0	4	NA	100 00	87 88
					85 71						100 00	106
					TESTING						TESTING	
0 Impacts	4	3	1	NA	75 00		4	3	1	NA	75 00	
9 Impacts	3	1	2	NA	66 67		3	1	2	NA	66 67	
					71 43						71 43	

Table 4-5: Linear Discriminant Function Classification Results; 0, 3, and 9 Impacts

LINEAR DISCRIMINANT FUNCTION CLASSIFIER

Number of IMPACTS	CLASS SIZE	SIGNAL RECOGNITION CLASS 1	CLASS 2	CLASS 3	RECOGN RATE (%)	FEATURE SET	CLASS SIZE	SIGNAL RECOGNITION CLASS 1	CLASS 2	CLASS 3	RECOGN RATE (%)	FEATURE SET
	0° PLATE						±45° PLATE					
					TRAINING						TRAINING	
0-Impacts	4	4	0	0	100 00	3 4 19	4	4	0	0	100 00	4 17 18
3-Impacts	4	0	4	0	100 00	27 42 52	4	0	4	0	100 00	39 45 49
9-Impacts	3	0	0	3	100 00	56 69 86	3	0	0	3	100 00	48 49 52
					100 00	90 102					100 00	55 56 57 58 59 60
					TESTING						TESTING	69 77 78
0-Impacts	4	3	0	1	75 00		4	4	0	0	100 00	83 86 87
3-Impacts	4	1	3	0	75 00		4	2	0	2	0 00	91 92 93
9-Impacts	3	0	1	2	66 67		3	0	1	2	66 67	94 105
					75 00						54 55	104 108
					TRAINING						TRAINING	
0-Impacts	4	4	0	NA	100 00	3 7 1 75	4	4	0	NA	100 00	4 60 77
3-Impacts	4	0	4	NA	100 00		4	0	4	NA	100 00	79 88 91
					100 00						100 00	92 93 94
					TESTING						TESTING	
0-Impacts	4	3	1	NA	75 00		4	4	0	NA	100 00	
3-Impacts	4	2	2	NA	50 00		4	3	1	NA	25 00	
					62 50						62 50	
					TRAINING						TRAINING	
0-Impacts	4	4	0	NA	100 00	19 27 28	4	4	0	NA	100 00	55 88
9-Impacts	3	0	3	NA	100 00	52 56 57	4	0	4	NA	100 00	
					100 00	59 61 77 99 100					100 00	
					TESTING						TESTING	
0-Impacts	4	4	0	NA	100 00		4	3	1	NA	75 00	
9-Impacts	3	1	2	NA	66 67		3	1	2	NA	66 67	
					85 71						71 43	

Table 4-6: Empirical Bayesian Function Classification Results; 0, 3, and 9 Impacts

EMPIRICAL BAYESIAN FUNCTION CLASSIFIER

Number of IMPACTS/PLATE	CLASS SIZE	SIGNAL RECOGNITION CLASS 1	CLASS 2	CLASS 3	RECOGN RATE (%)	FEATURE SET	CLASS SIZE	SIGNAL RECOGNITION CLASS 1	CLASS 2	CLASS 3	RECOGN RATE (%)	FEATURE SET
	0° PLATE						±45° PLATE					
					TRAINING						TRAINING	
0 Impacts	4	3	1	0	75 00	3 42 50	4	3	0	1	75 00	4 41 43
3 Impacts	4	0	4	0	100 00	61 66 67	4	0	4	0	100 00	44 45 48
9 Impacts	3	0	0	3	100 00	70 77 79	3	0	0	3	100 00	49 53 55
					90 91	82 86 87					90 91	56 58 59
						90 105						60 64 65
					TESTING						TESTING	66 68 69
0 Impacts	4	3	1	0	75 00		4	2	0	2	50 00	71 74 78
3 Impacts	4	0	3	1	75 00		4	0	0	4	0 00	83 86 87
9 Impacts	3	0	1	2	66 67		3	0	0	3	100 00	88 89 91
					72 73						45 45	92 93 94
												101 103
												104 107
					TRAINING						TRAINING	
0 Impacts	4	4	0	NA	100 00	43 45 52	4	4	0	NA	100 00	4 39 41
3 Impacts	4	0	4	NA	100 00	80 82 86	3	0	3	NA	100 00	49 53 57
					100 00	87 102					100 00	65 70 71
						105 106						73 74 82
					TESTING	108					TESTING	83 86 88
0 Impacts	4	4	0	NA	100 00		4	3	1	NA	75 00	92 93
3 Impacts	4	1	3	NA	75 00		4	0	4	NA	100 00	
					87 50						87 50	
					TRAINING						TRAINING	
0 Impacts	4	4	0	NA	100 00	3 19 45	4	4	0	NA	100 00	48 54 64
9 Impacts	3	0	3	NA	100 00	50 52 55	3	0	3	NA	100 00	87 107
					100 00	66 72 86					100 00	
						87 102						
					TESTING	105 106					TESTING	
0 Impacts	4	3	1	NA	75 00	108	4	3	1	NA	75 00	
9 Impacts	3	0	3	NA	100 00		3	1	2	NA	66 67	
					85 71						71 43	

Table 4-7: Minimum Distance Function Classification Results; 0, 3, and 9 Impacts

MINIMUM DISTANCE FUNCTION CLASSIFIER

Number of IMPACTS	CLASS SIZE	SIGNAL RECOGNITION CLASS 1	CLASS 2	CLASS 3	RECOGN RATE (%)	FEATURE SET	CLASS SIZE	SIGNAL RECOGNITION CLASS 1	CLASS 2	CLASS 3	RECOGN RATE (%)	FEATURE SET
	0° PLATE						±45° PLATE					
					TRAINING						TRAINING	
0-Impacts	4	4	0	0	100 00	2 3 66	4	4	0	0	100 00	52 59 60
3-Impacts	4	0	4	0	100 00	69 72 74	4	0	4	0	100 00	79 89 90
9-Impacts	3	1	0	2	66 67	75 76 77	3	1	0	2	66 67	94 102
					90 91	80 83 86 87 90					90 91	103 104 106 108
					TESTING						TESTING	
0-Impacts	4	3	1	0	75 00		4	2	2	0	50 00	
3-Impacts	4	2	2	0	50 00		4	0	2	2	50 00	
9-Impacts	3	1	0	2	66 67		3	0	2	1	33 33	
					75 00						45 45	
					TRAINING						TRAINING	
0-Impacts	4	4	0	NA	100 00	80 83 86	4	4	0	NA	100 00	57 70 71
3-Impacts	3	0	3	NA	100 00	87 102	3	0	3	NA	100 00	108
					100 00	103					100 00	
					TESTING						TESTING	
0-Impacts	4	4	0	NA	100 00		4	2	2	NA	50 00	
3-Impacts	4	1	3	NA	75 00		4	2	2	NA	50 00	
					87 50						50 00	
					TRAINING						TRAINING	
0-Impacts	4	4	0	NA	100 00	55 56 72	4	4	0	NA	100 00	57 80 88
9-Impacts	3	0	3	NA	100 00	86 102	3	0	3	NA	100 00	91 104
					100 00	102					100 00	106 107
					TESTING						TESTING	
0-Impacts	4	3	1	NA	75 00		4	4	0	NA	100 00	
9-Impacts	3	0	3	NA	100 00		3	2	1	NA	33 33	
					85 71						71 43	

4.5.4 Compression Test Results

The compression test results indicate a change in stiffness (modulus) due to the 27 J (20 lb-ft) impact from 155.8 GPa to 128.3 GPa for the 0° coupons and from 17.6 GPa to 15.7 GPa for the ±45° coupons, a reduction of 17.7% and 10.8% respectively. The modulus values given in Table 4-8 compare suppliers values [40], and test values for non-impacted and impacted coupons. Refer to Appendix 5 for load/strain curves.

The unidirectional coupons failed due to matrix buckling (32) and cracking in the axial direction following by out of plane buckling. The coupons split in half lengthwise (Fig. 4-19) along the fiber direction before ultimate failure, therefore a value of ultimate strength could not be ascertained.

The cross-ply (±45°) coupons failed due to local shearing in the gauge sections followed by out of plane buckling. Failure did not occur due to shear and therefore ultimate strength could not be ascertained.

Table 4-8: Compression Test Results for Non-Impacted and Impacted Coupons

	Suppler Modulus		No Impacts Modulus		Impacted Modulus	
Coupons	GPa	Msi	GPa	Msi	GPa	Msi
0° Plate						
AVG	158 5	23 0	155 8	22 6	128 3	18 6
STD DEV	6 5	0 9	1 8	0 3	3 3	0 5
±45° Plate						
*AVG	16 5	2 4	17 6	2 6	15 7	2 3
STD DEV	NA	NA	0 3	0 0	0 3	0 0

* Determined using laminate theory, refer to reference 41.

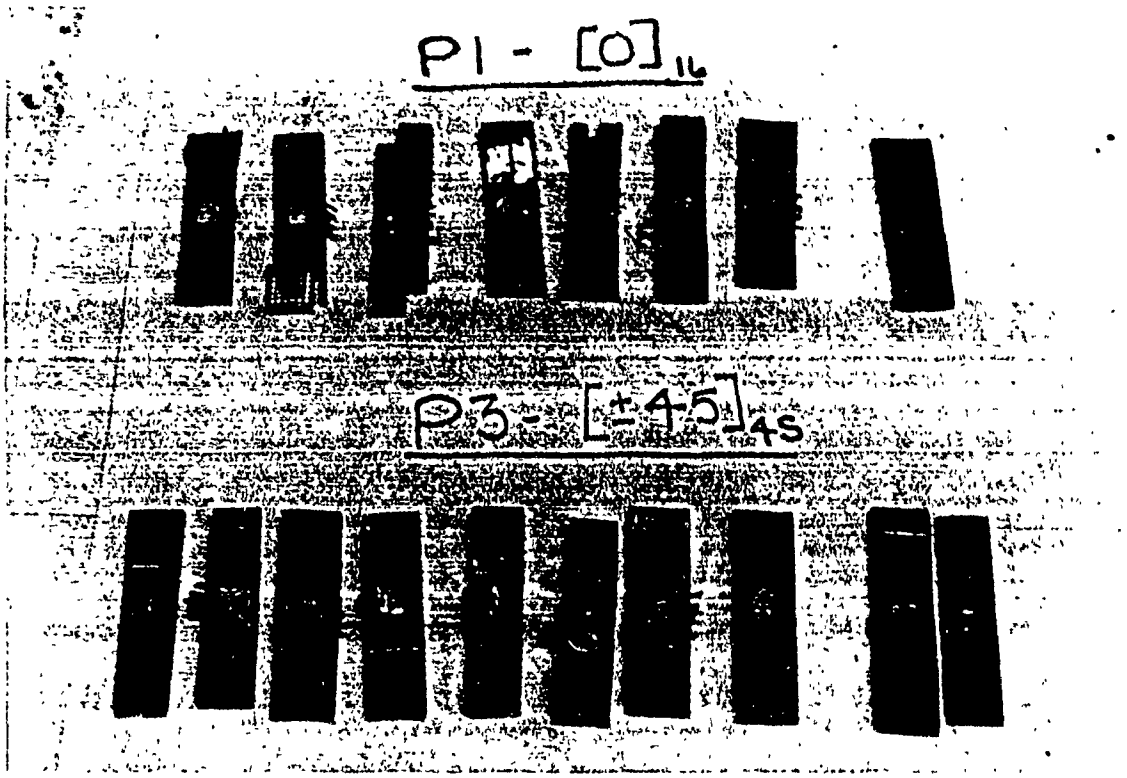

Fig. 4-19: Unidirectional and ±45° Coupons after Quasi-Static Compression Testing

4.6 Discussion of Test Results and Problems Encountered

The problem of noise interference experienced during aluminum block testing was overcome using the pre-assembled PVDF sensors.

The trend in reduction in peak frequency and peak to peak voltage is evident from Figures 4-11 to 4-14. The initial parts of the graphs include some scatter due to the position of the A1 and C1 grid positions with respect to the fiber direction and the trend does not become evident until a distance of 56 mm from the source transducer. Scatter is also indicated at the maximum sensor position. The fact that the A1, A4, B1, B4, C1 and C4 grid positions are close to the ends of the test plates may have resulted in edge conditions becoming a factor. The A4 and C4 positions are also not aligned with the source transducer and the axial fiber direction. Also, the ±45° plate had two teflon inserts which may have contributed to signal scatter. The fundamental frequency and the second harmonic frequency for the graphite/epoxy test plates could not be de-

rived from the frequency spectrum. Due to the magnitude of the peak frequency, it is likely that the frequency of the test system as a whole was included in the frequency spectrum. This would include the input from the electronics, the silicone rubber underpad and the wooden support structure. In retrospect, front-ended signal filtering (low pass) may have been useful in obtaining the true harmonics of the test plates and subsequently the signal velocity.

The method of adhesion of the PVDF sensors to the test plates created some problems which may have affected the results. The double backed tape provided some non-uniform adhesion of the PVDF sensors to the test plates. Some pieces of tape (taken from the same roll) provided uniform contact of the PVDF sensors to the test surface, whereas other pieces of tape allowed edges and centers of the sensors to disbond from the test surface. This disbonding could have been due to contamination of the tape by dust. High humidity in the test area may have also affected the efficiency of the adhesive.

The ultrasonic C-scan imaging system used was not set up to provide B-prime images. B-prime imaging would have provided an end-view through wall perspective along one scanner stroke (width of the test plate). The end-view through-the-thickness images may have indicated the extent of impact damage at the impact sites.

The compression testing was successful in determining comparative change in modulus but ultimate strength values could not be obtained due to pre-mature failure of the coupons. Edge guides would have been useful in restricting out of plane failure of the specimens and providing ultimate strength values. More data points (a faster acquisition rate) during initial loading would have resulted in better graphs and perhaps more accurate modulus values.

5.0 CONCLUSIONS

The trend in reduction of peak frequency and peak to peak voltage due to impact damage has been determined using the AU technique and PVDF sensors for graphite/epoxy composite plates subjected to repeated impacts. The graphite/epoxy plates have been ultrasonically C-scanned in an attempt to determine impact damage. The AU signals have been classified with respect to number of impacts. The non-impacted and impacted areas of the test plates have been tested in compression and the reduction in modulus has been determined.

Based on the findings, it is apparent that impact damage can be assessed through acousto-ultrasonic means with PVDF sensors. Use of pre-assembled shielded sensors greatly reduces extraneous noise interference. Impact damage is indicated by a lowering in the frequency at which the peak amplitude occurs in the frequency spectrum and a lowering in the peak to peak voltage of the time-domain signal.

Ultrasonic C-scan is limited in determining low velocity impact damage when interlaminar delamination does not occur. Through-the-thickness B-scan imaging may provide a better method of determining the extent and depth of matrix/fiber damage.

More signal gathering is required at each stage in the assessment process to ensure a larger statistical data base with which to produce acceptable pattern classification results.

Low velocity impact damage lowers compression modulus in both 0° and ±45° graphite/epoxy laminations. Unidirectional graphite/epoxy plates are more severely affected by low velocity impact damage. Guide planes are required to provide edge support to test coupons during compression testing.

Future work should focus on methods to isolate the frequency spectrum of the plates from the test system and create a data base of signal waveforms from various plates made of high and low modulus fibers, epoxy and PEEK resins, and various ply orientations. It is important to establish a criteria for the minimum number of waveforms required for confidence in pattern classification and to establish tolerancing to identify what is an acceptable testing percentage result. Better methods of bonding the PVDF sensors to the test objects need to be evaluated.

In conclusion, the handling and performance of the pre-assembled PVDF sensors was above expectations. Due to their geometry and low mass they were much less awkward to handle than the ceramic transducers in the steel housings. They proved to be quite resilient and able to withstand a number of bondings and removals with double backed tape without tearing. They provided an excellent means to gather time-domain signals. The Lecroy 9400A digital oscilloscope with built-in signal processing capabilities proved to be user friendly and versatile. It contained many functions able to derive information from signal waveforms and was an excellent tool to digitize and to evaluate the signal waveforms. The true power of the ICEPAK™ software was not demonstrated in this study. Proper signal classification requires more sampling of waveforms. ICEPAK™ offers a tremendous potential to create a data base of waveform features corresponding to damage in various materials.

REFERENCES

1. Vary, A., "Acousto-Ultrasonic Characterization of Fiber Reinforced Composites", *Materials Evaluation*, Vol. 40, May 1982, pp. 650-654 & 662.

2. Vary, A., "Acousto-Ultrasonics: Retrospective Exhortation with Bibliography", *Materials Evaluation*, ,Vol. 49, May 1991, pp. 581-591.

3. Tang, B. and E. G. Henneke, II, "Lamb-Wave Monitoring of Axial Stiffness Reduction of Laminated Composite Plates", *Materials Evaluation*, Vol. 47, Aug. 1989, pp. 928-934.

4. Williams, Jr., J.H. and B. Doll, "A Simple Wave Propagation Analysis of Piezoceramic Ultrasonic Transducer Response", *Materials Evaluation*, Vol. 40, Dec. 1982, pp. 1374-1381.

5. Kiernan, M.T., and J.C. Duke, Jr., "Acousto-Ultrasonics as a Monitor of Material Anisotrpy", *Materials Evaluation*, Vol. 46, July 1988, pp. 1105-1113.

6. Smith, I.C., and S.V. Hoa, "Utilization of PVDF Sensors to Determine Impact Damage in Graphite/Epoxy Plates by Acousto-Ultrasonic Technique", *Proceedings of the 4th Intl. Symp. on Acoustic Emission from Composite Materials*, Seattle, Washington, July 1992.

7. Bunsell, A.R., "The Monitoring of Damage in Carbon Fibre Composite Structures by Acoustic Emission", in *Proceedings, Second International Conference on Composite Structures*, Sept. 1983, pp. 1-20, Paisley College of Technology, Scotland.

8. Poon. C., T. Benak and R. Gould, "Assessment of Impact Damage in Toughened Resin Composites", *Theoretical and Applied Fracture Mechanics*, Vol. 13, 1990, pp. 81-97.

9. *Nondestructive Testing Handbook; Volume 5, Acoustic Emission Testing*, 2nd Edition, R. K. Miller, Ed., P. McIntrie, Ed., 1986, pp. 96, 122, 428, 435, 436.

10. Campbell, C., *Surface Acoustic Wave Devices and Their Processing Applications*, Academic Press, Inc., London, 1989, pp. 10, 11, 23.

11. Wu, K., P.B. Nagy, and L. Adler, "Far Field radiation of a Vibrating Point Source in Anisotropic Media", *Journal of Nondestructive Evaluation*, Vol. 10, No. 2, 1991, pp. 71-78.

12. Chedid-Helou, F.A., and J.H. Hemann, "Mathematical Modelling of Wave Propagation in Anisotropic Media", *Materials Evaluation*, Vol. 49, June 1991, pp. 708-715.

13. Kiernan, M.T., and J.C. Duke, Jr., "PC Analysis of an Acousto-Ultrasonic Signal", *Materials Evaluation*, Vol. 46, Sept. 1988, pp. 1344-1352.

14. Bhatt, M., and P.J. Hogg, "Test Conditions in Stress Wave Factor Measurements for Fibre-Reinforced Composites and Laminates", *NDT International*, Vol. 21, No. 1, Feb. 1988, pp. 3-10.

15. Williams, Jr., J.H., and N.R. Lampert, "Ultrasonic Evaluation of Impact-Damaged Graphite Fiber Composite", *Materials Evaluation*, Vol. 38, Dec. 1980, pp. 68-72.

16. Williams, Jr., J.H., H. Karaguille and S.S. Lee, "Ultrasonic Input-Output for Transmitting and Receiving Longitudinal Transducers Coupled to Same Face of Isotropic Elastic Plate", *Materials Evaluation*, Vol. 40, May 1982, pp. 655-662.

17. Carlisle, B.H., "Piezoelectric Plastics Promise New Sensors", *Machine Design*, Oct. 1986, Penton Publishing Inc., Cleveland, Ohio.

18. Kynar Piezo Film Product Summary and Price List, Pennwalt Corporation, May 1990.

19. Stiffler, R., and E. G. Henneke, II, "The Application of Polyvinylidene Fluoride as an Acoustic Emission Transducer for Fibrous Composite Materials", *Materials Evaluation*, Vol. 41, July 1983, pp. 956-960.

20. Mattiocco, F., E. Dieulesaint, and D. Royer, "PVF2 Transducers for Rayleigh Waves", *Electronics Letters*, Vol. 16, No. 7, March 1980, pp. 250-251.

21. Shiwa, M., H. Inaba, S.H. Carpenter, and T. Kishi, "Development of High-Sensitivity and Low Noise Integrated Acoustic Emission Sensor", *Materials Evaluation*, Vol. 50, July 1992, pp. 868-874.

22. English, L.K., "Listen and Learn: AE Testing of Composites", *Materials Engineering*, May 1987, pp. 38-41.

23. Kautz, H.E., and B.A. Lerch, "Preliminary Investigation of Acousto-Ultrasonic Evaluation of Metal-Matix Composite Specimens", *Materials Evaluation*, Vol. 49, May 1991, pp. 607-612.

24. Hosten, B., "High-Precision Measurement Using Digital Oscilloscopy", *Materials Evaluation*, Vol. 48, Nov. 1990, pp. 1416-1422.

25. Lecroy 1990 Catalog, Reference Guide to Digital Waveform Instruments, Lecroy Corporation, N.Y., pp. I27-I36, IV14-IV47.

26. McRae, K.I., "Deconvolution Techniques for Ultrasonic Imaging of Adhesive Joints", *Materials Evaluation*, Vol. 48, Nov. 1990, pp. 1380-1384.

27. Karpur, P., "Split-Spectrum Technique as a Preprocessor for Enhanced Reliability in Ultrasonic Signal Analyses, *Materials Evaluation*, Vol. 50, June 1992, pp. 793-797.

28. Intelligent Classifier Engineering Package (ICEPAK), User's Manual, Version 3.00, 1989, Tektrend International Inc., Montreal, Québec.

29. Hoa, S.V., and I.C. Smith, "Acoustic Emission Signal Classification of Graphite/ Polyphenylene Sulfide Composite Subjected to Mode II Fracture", *Proceedings of the 3rd Intl. Conf. on Acoustic Emission for Composite Materials*, Paris, France 1989.

30. Hay, D.R., R.W.Y. Chan, D. Sharp and K.J. Siddiqui, "Classification of Acoustic Emission Signals from Deformation Mechanisms in Aluminum Alloys", *Journal of Acoustic Emission*, Vol. 3, No. 2, 1984, pp. 118-129.

31. Ohtsu, M. and K. Ono, "Pattern Recognition Analysis of Acoustic Emission from Unidirectional Carbon Fiber-Epoxy Composites by Using Autoregressive Modeling", *Journal of Acoustic Emission*, Vol. 6, No. 1, 1987, pp. 61-71.

32. Bergmann, H.W., et al., *Mechanical Properties and Damage Mechanisms of Carbon fiber-Reinforced Composites Compression Loading*, Institut für Strukturmechanik, Braunschweig, August 1988.

33. Hahn, H.T., and J.G. Williams, "Compression Failure Mechanisms in Unidirectional Composites", *Proceedings from the Seventh Conference on Composite Materials: Testing and Design*, ASTM STP 893, 1986, pp. 115-139.

34. *Interlaminar Response of Composite Materials*, N.J. Pagano, ed., Elsevier Science Publishing Co., New York, N.Y., 1989, pp. 166.

35. Hart-Smith, L.J., "Making Better Coupons, Part 1", *Aerospace Composites & Materials*, Vol. 3, No. 3, May/June 1991, pp. 26-30, & 58.

36. Hart-Smith, L.J., "Making Better Coupons, Part 2", *Aerospace Composites & Materials*, Vol. 3, No. 4, July/Aug. 1991, pp. 13-17.

37. Kynar Piezo Film Technical Manual, Pennwalt Corporation, Valley Forge, PA, 1987, pp. 9, 5-15.

38. Sessler, G.M., "Piezoelectricity in Polyvinyldenefluoride", *J. Acoustical Society of America*, Vol. 70, No. 6, Dec. 1981, pp. 1595-1608.

39. Piezo Film Sensors (PFS), Product Data Sheet Number 9, Pennwalt Corporation, Valley Forge, PA, 1987.

40. ICI Fiberite, Materials Handbook, ICI Fiberite, Tempe, AZ, March 1989, pg. V. b-53.

41. Tsai, S.W and H.T. Hahn, *Introduction to Composite Materials*, Technomic Publishing Co., Lancaster, PA, 1980, pp. 36 to 57

Appendix 1: Wideband Source Transducer Voltage-Time Response and Frequency Spectrum to Glass Capillary Break on Steel Block

(supplied by ELB Incorporated, Cincinnati)

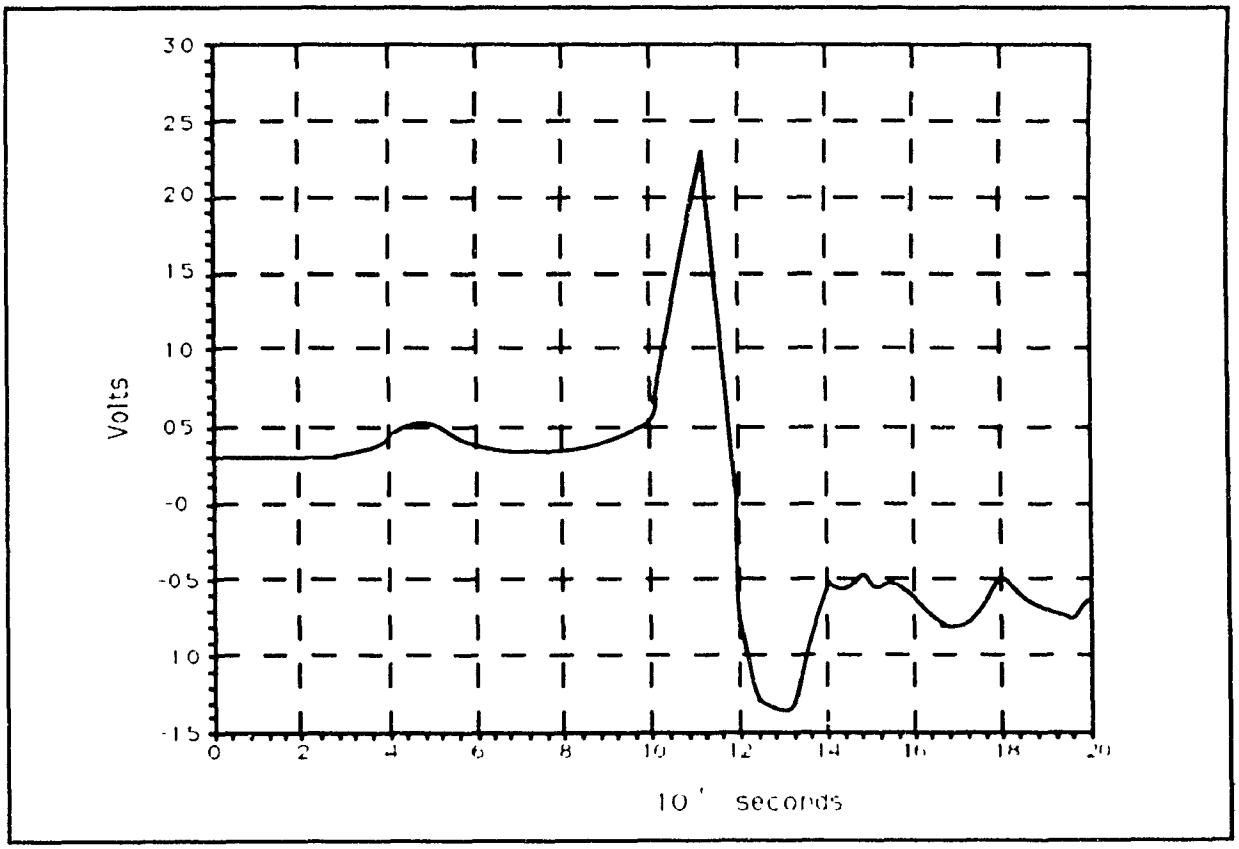
30
25
20
15
10
05
-0
-05
10
-15
Volts
0
2
4
6
8
10
12
14
16
18
20
10 ' seconds

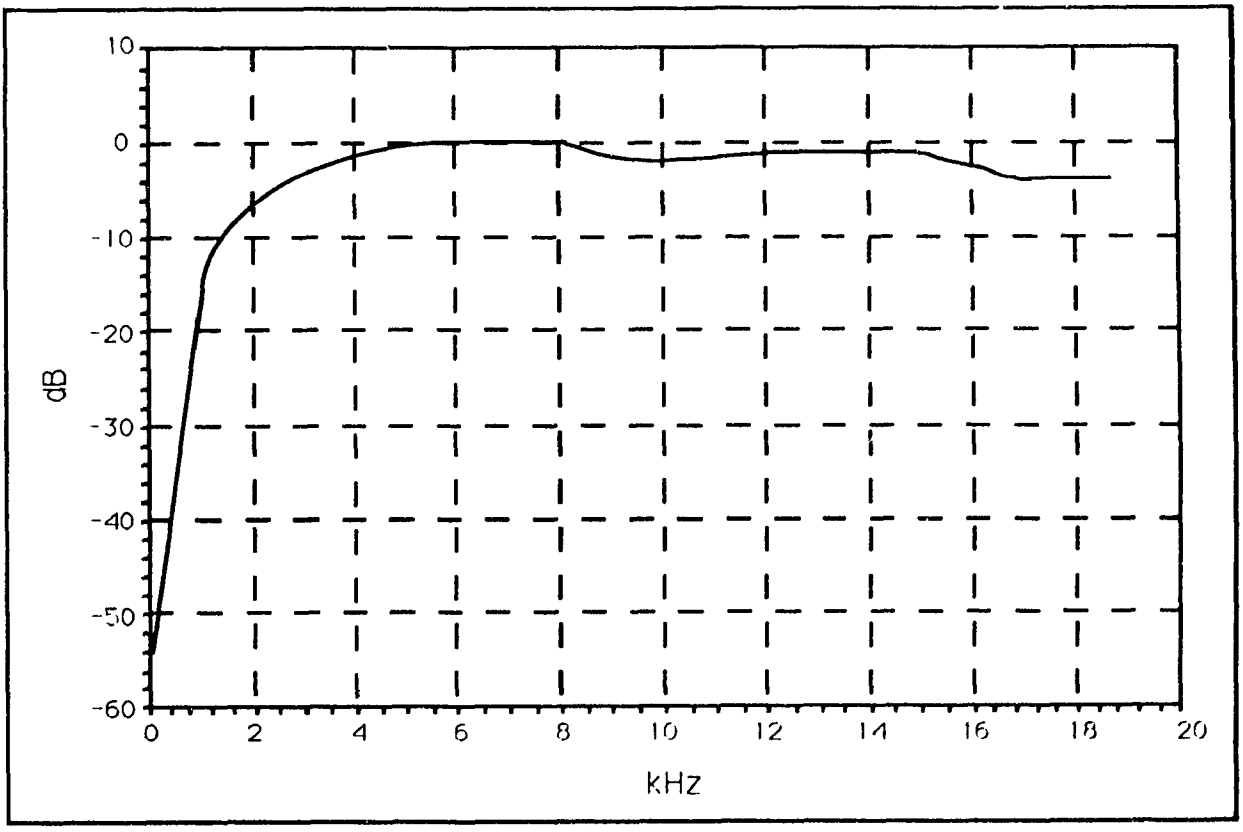
10
0
-10
-20
-30
-40
-50
-60
dB
0
2
4
6
8
10
12
14
16
18
20
kHz

Appendix 2: Graphs of Voltage-Time Signal Waveforms Acquired in Aluminum Block Testing

Graph #1
Test Piece: Aluminum Block
Source Location: S1
Sensor Pair Location: L1
Channel 1: PVDF 52 μm
Channel 2: PVDF 52 μm

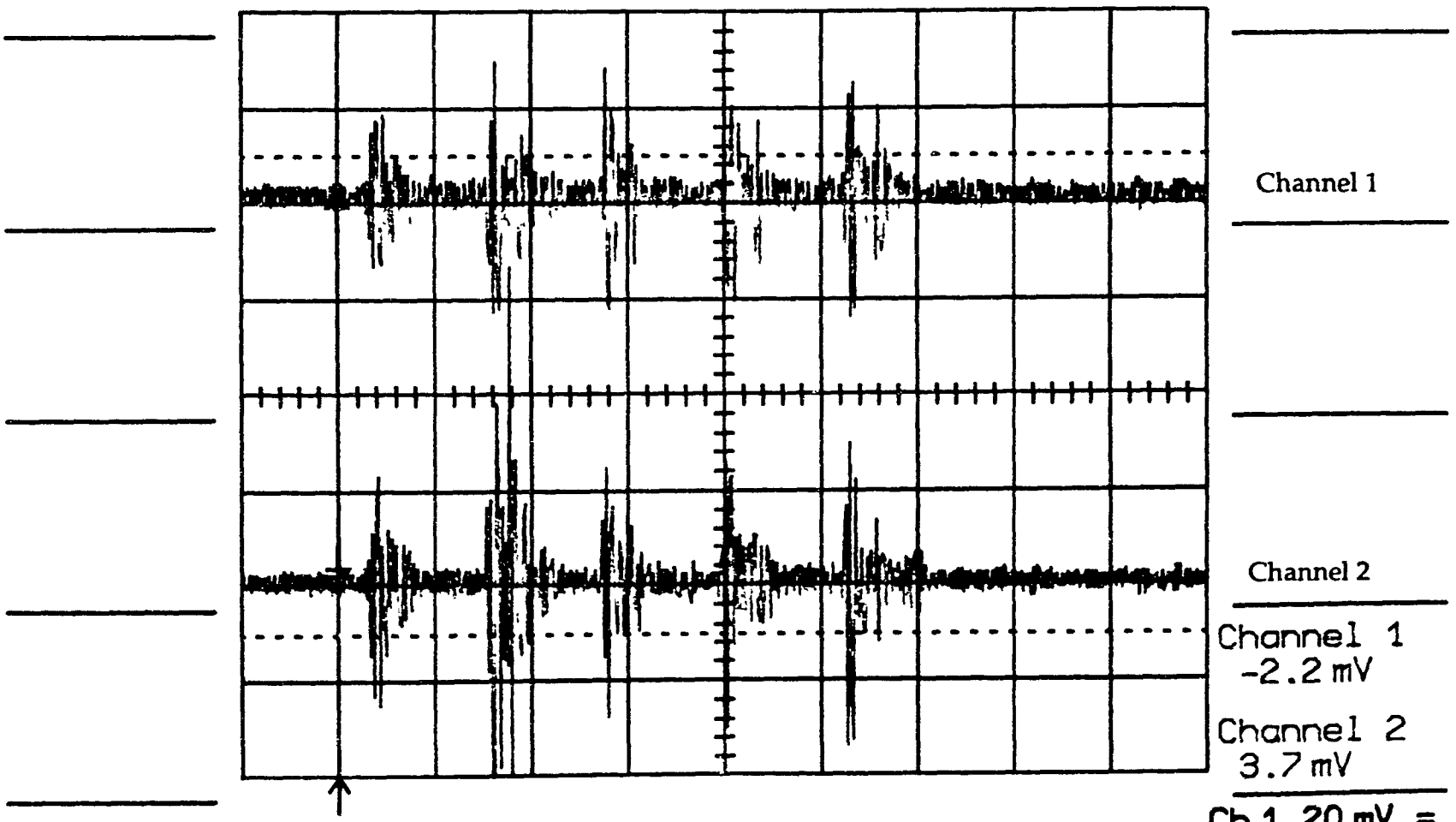

Graph #2
Test Piece: Aluminum Block
Source Location: S1
Sensor Pair Location: 1.2
Channel 1: PVDF 52 µm
Channel 2: PVDF 52 µm

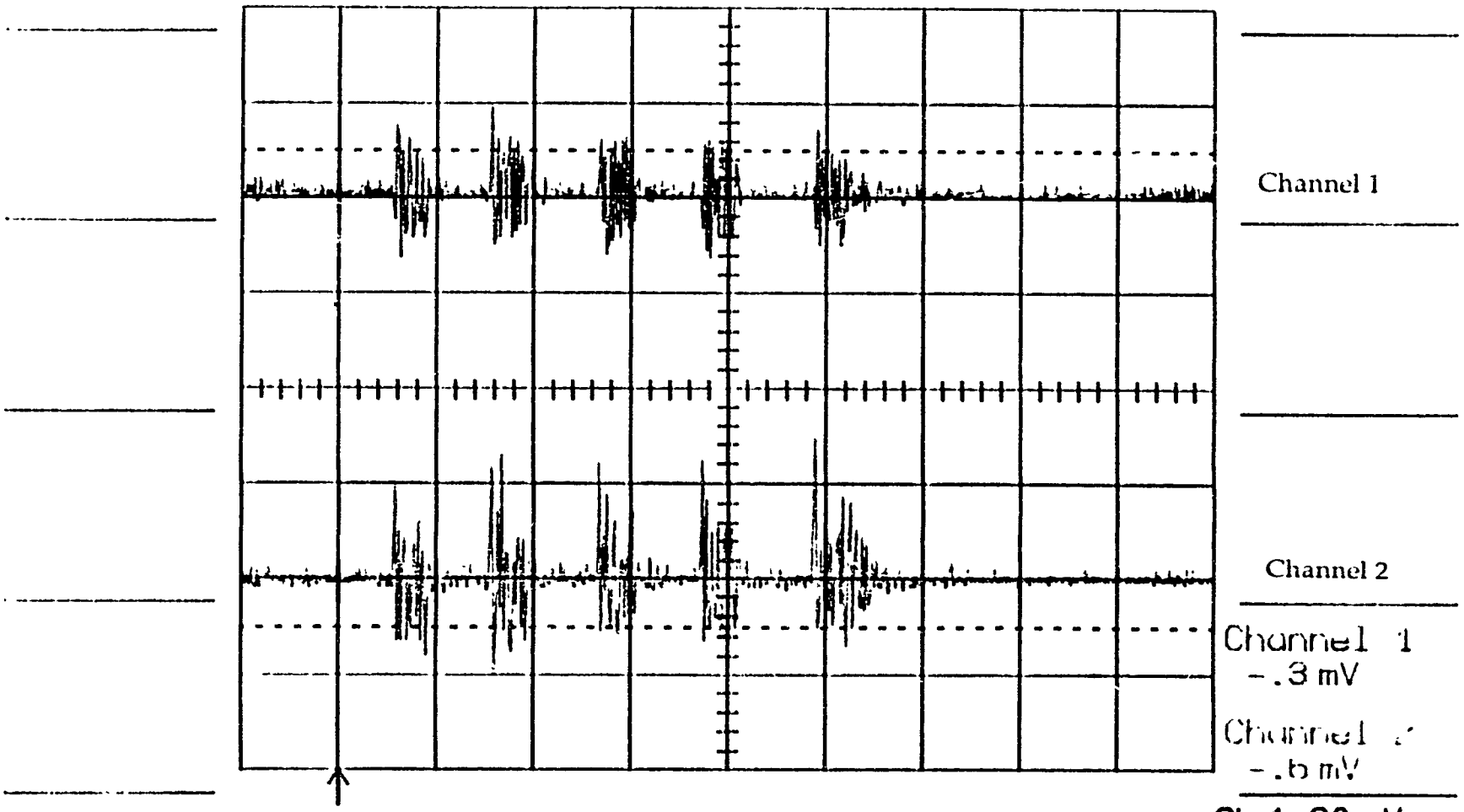

Graph #3
Test Piece: Aluminum Block
Source Location: S2
Sensor Pair Location: 1.1
Channel 1: PVDF 52 µm
Channel 2: PVDF 52 µm

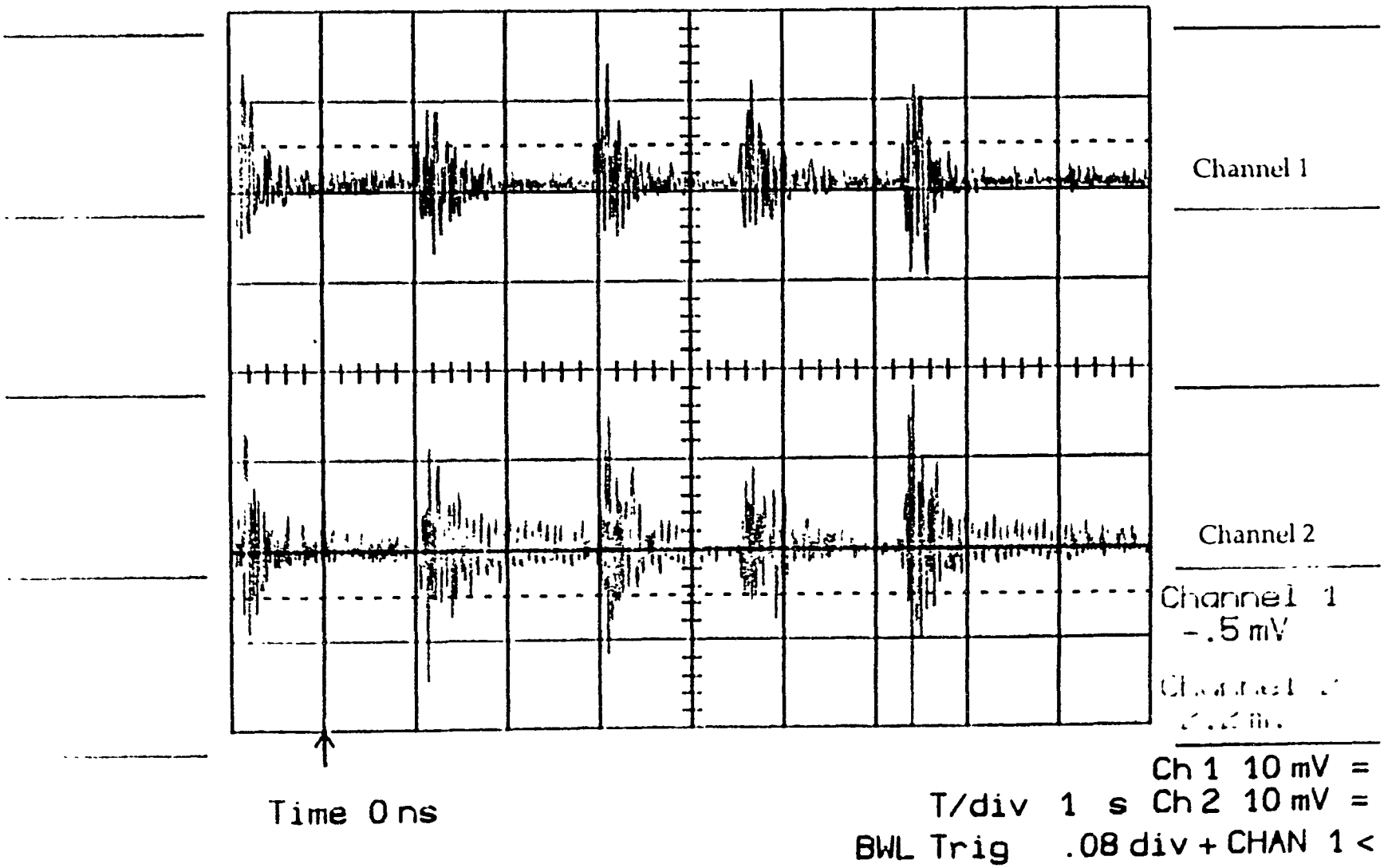

Graph #4
Test Piece: Aluminum Block
Source Location: S2
Sensor Pair Location: 1 3
Channel 1: PVDF 52 µm
Channel 2: PVDF 52 µm

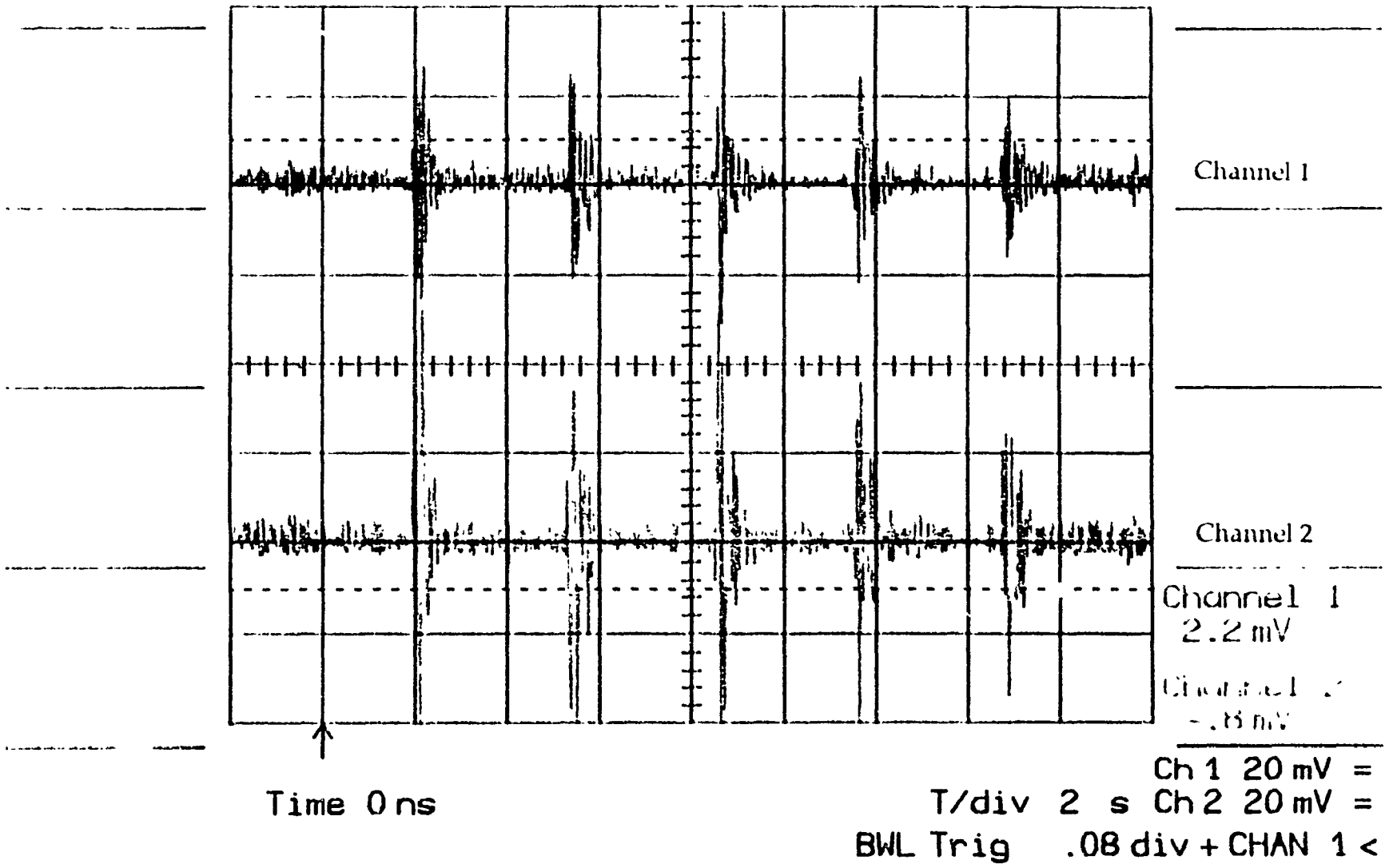

Graph #5
Test Piece: Aluminum Block
Source Location: S3
Sensor Pair Location: L4
Channel 1: PVDF 52 µm
Channel 2: PVDF 52 µm

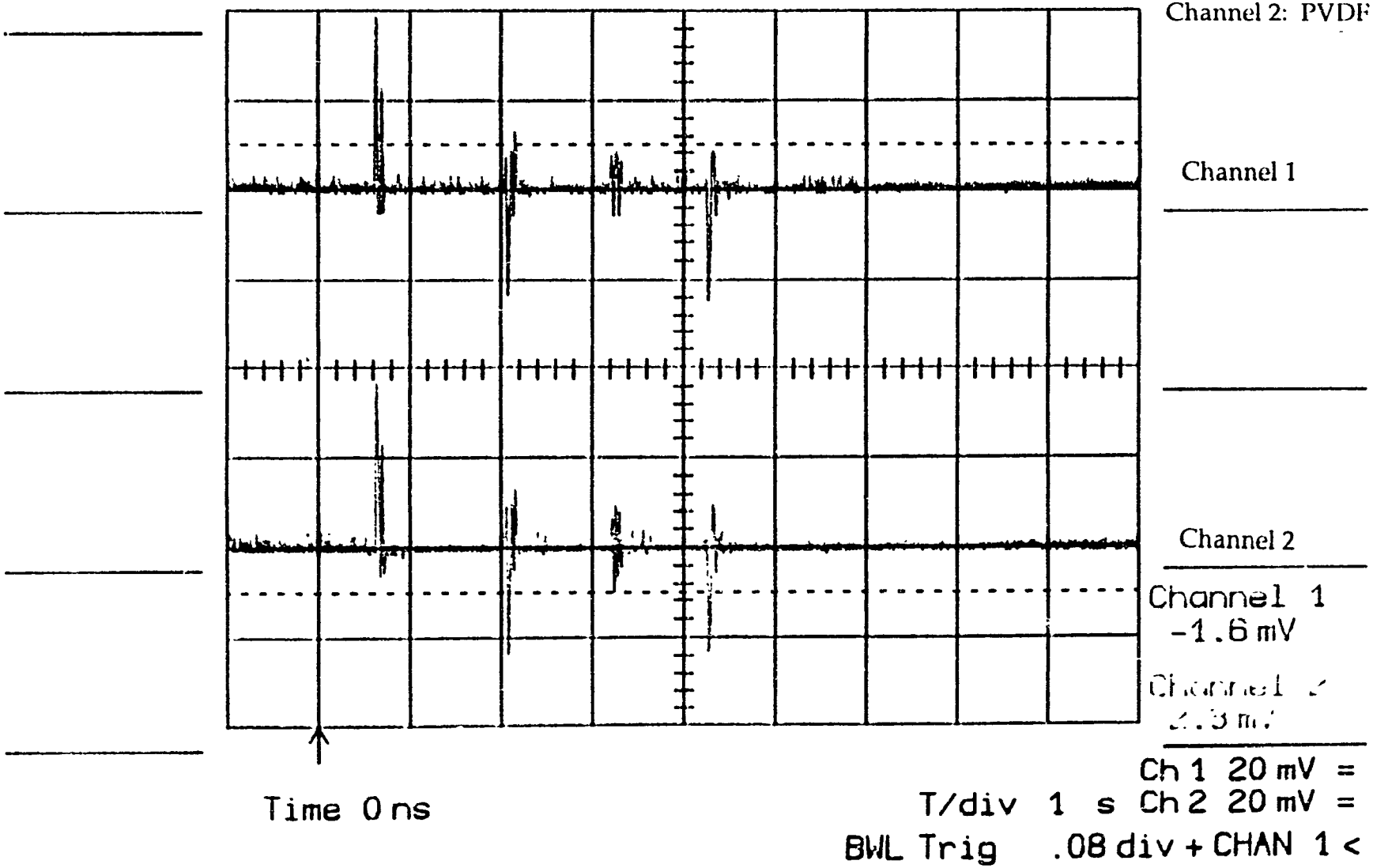

Graph #6
Test Piece: Aluminum Block
Source Location: S4
Sensor Pair Location: 1.4
Channel 1: PVDF 52 μm
Channel 2: PVDF 52 μm

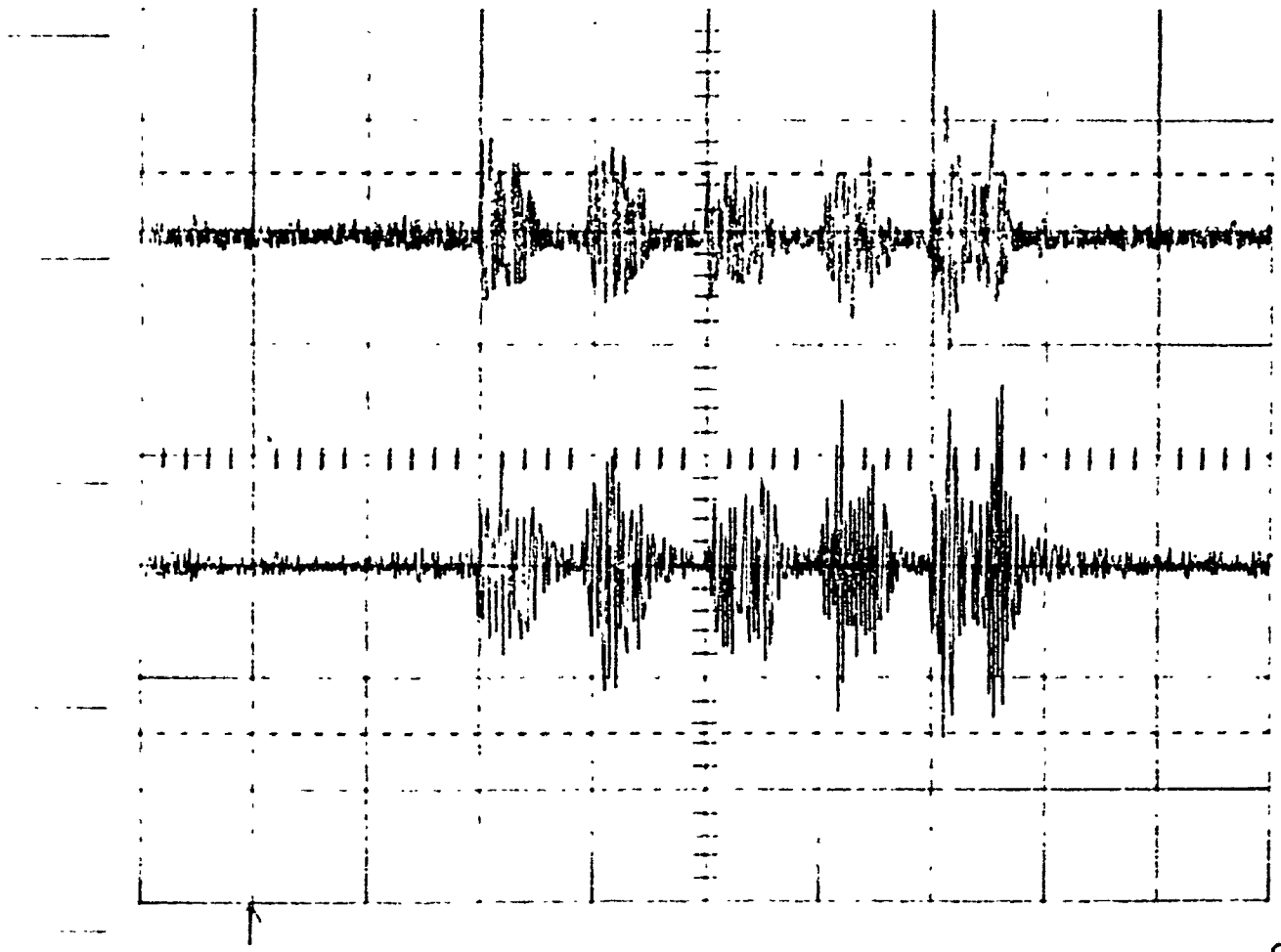

Graph #7
Test Piece: Aluminum Block
Source Location: S1
Sensor Pair Location: L1
Channel 1: PVDF 28 μm
Channel 2: PVDF 28 μm

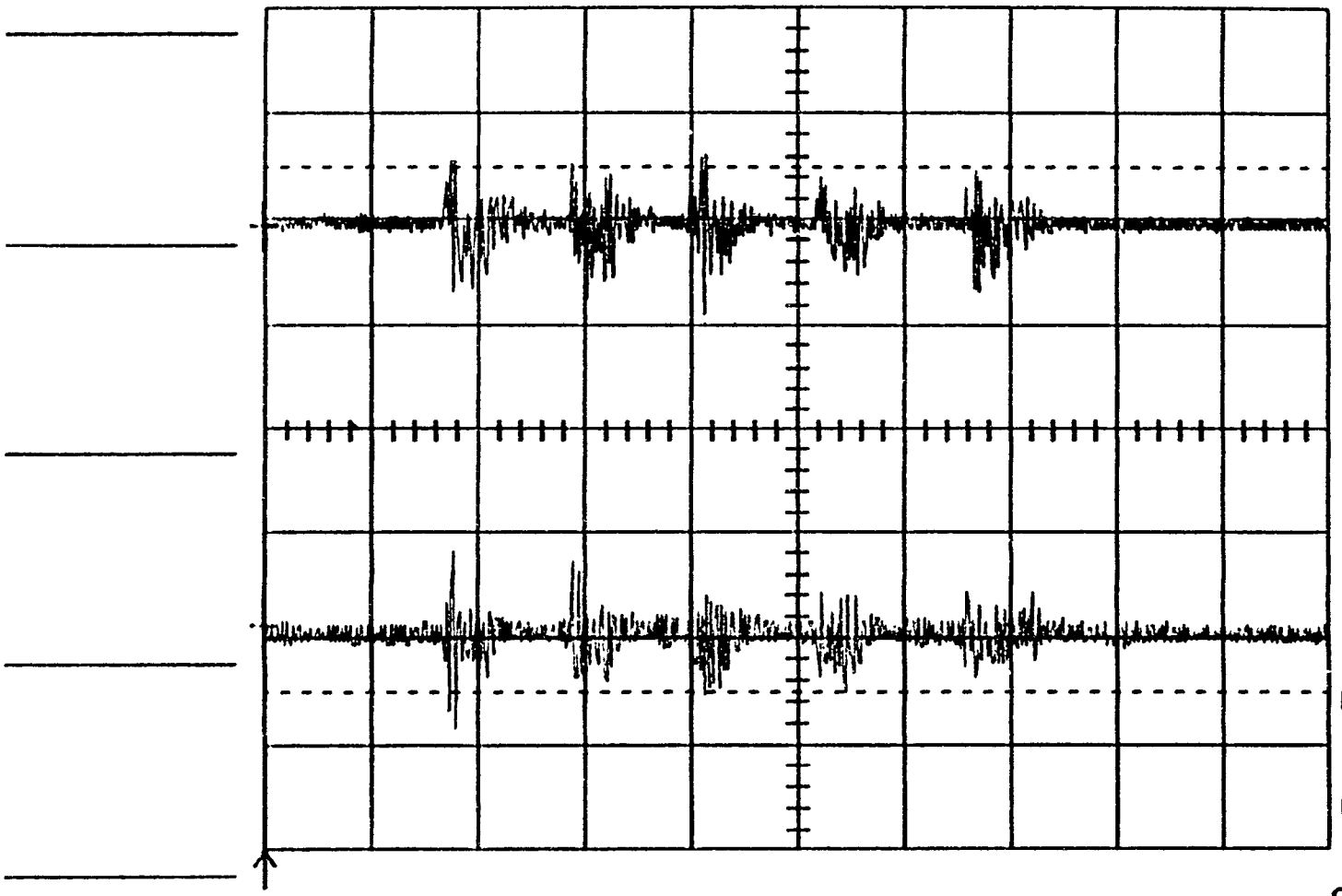

Graph #8
Test Piece. Aluminum Block
Source Location: S1
Sensor Pair Location: L2
Channel 1: PVDF 28 µm
Channel 2: PVDF 28 µm

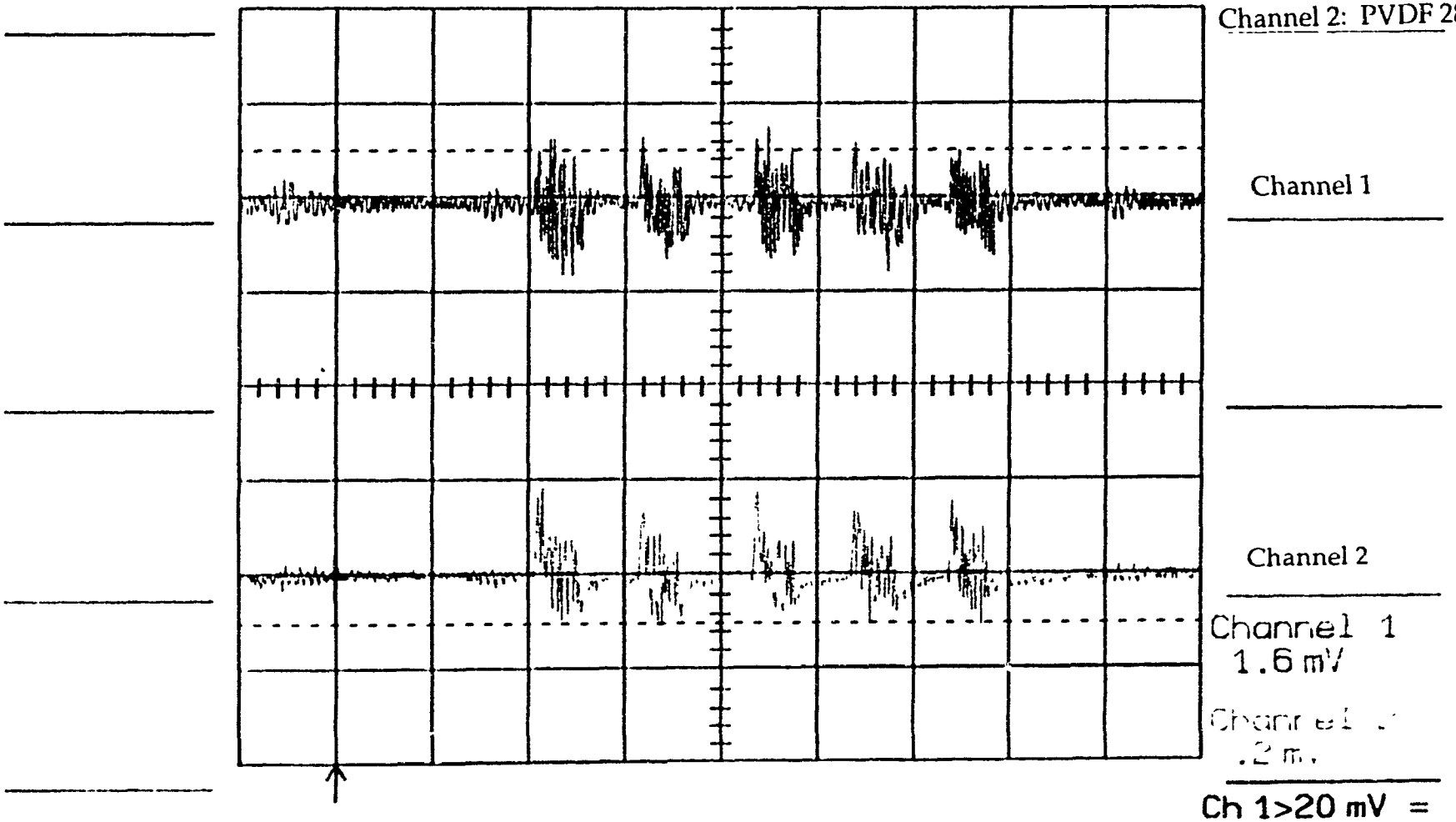

Graph #9
Test Piece: Aluminum Block
Source Location: S2
Sensor Pair Location: L1
Channel 1: PVDF 28 µm
Channel 2: PVDF 28 µm

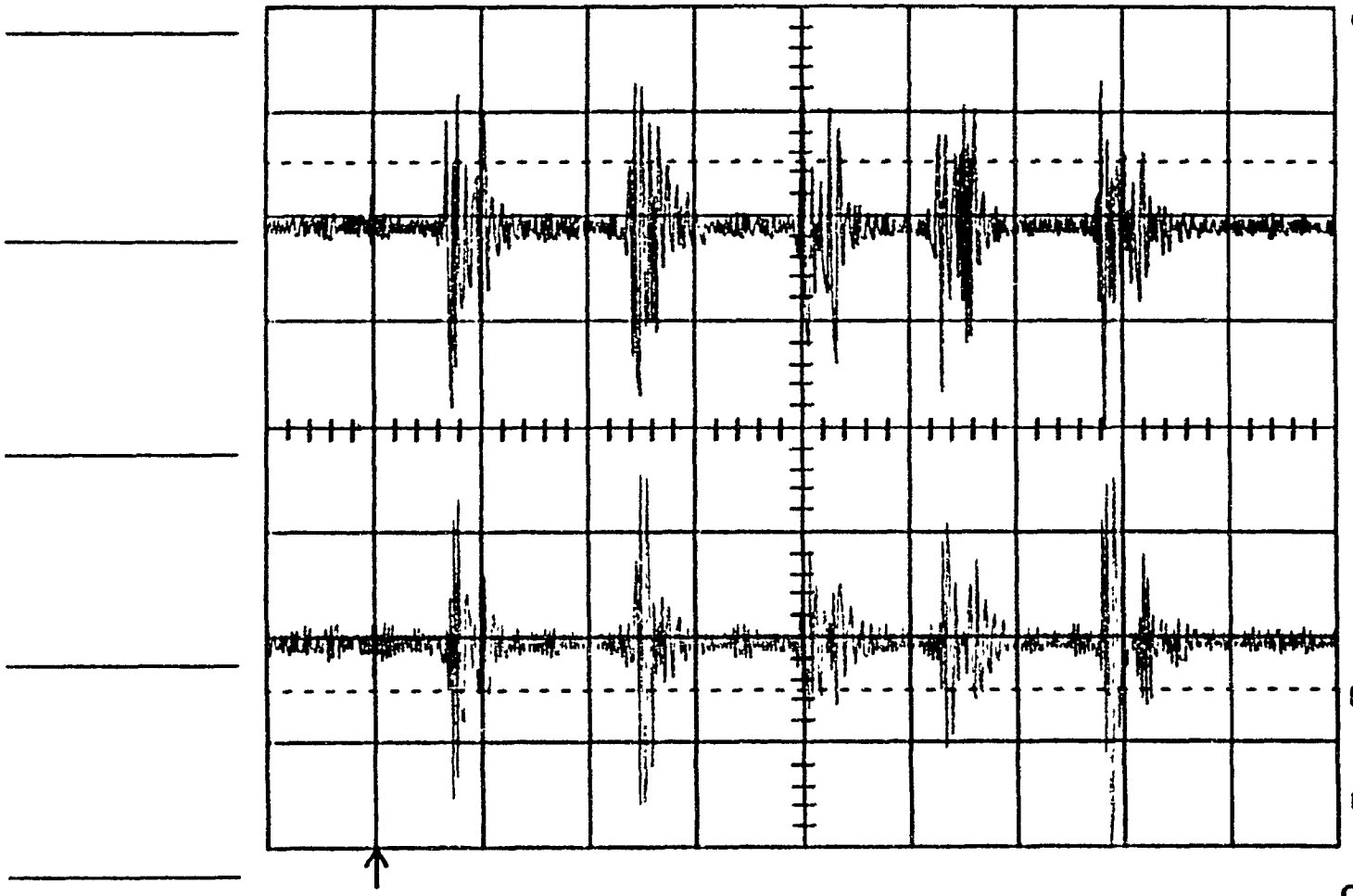

Graph #10
Test Piece: Aluminum Block
Source Location: S2
Sensor Pair Location: I3
Channel 1: PVDF 28 μm
Channel 2: PVDF 28 μm

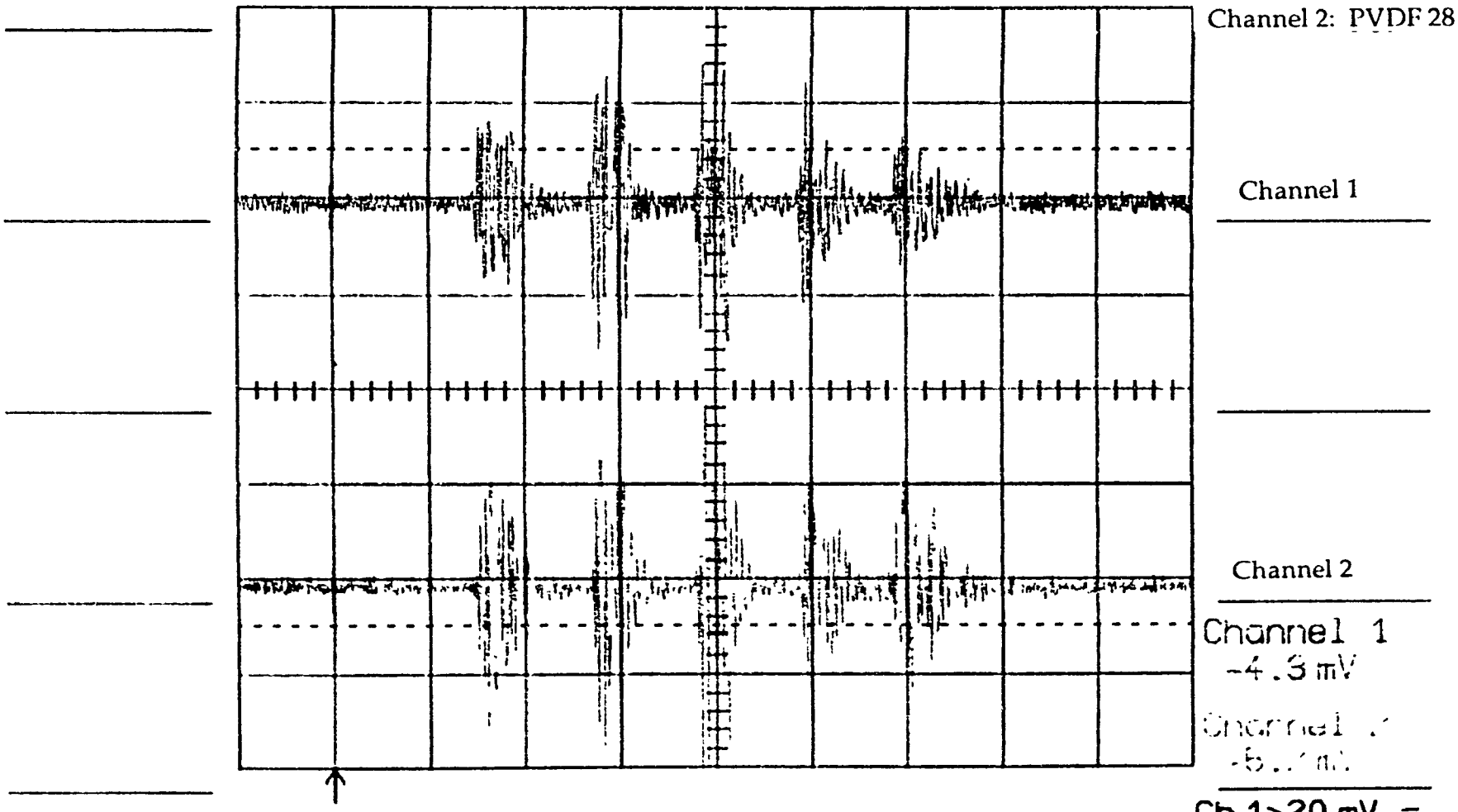

Graph #11
Test Piece: Aluminum Block
Source Location: S3
Sensor Pair Location: L4
Channel 1: PVDF 28 µm
Channel 2: PVDF 28 µm

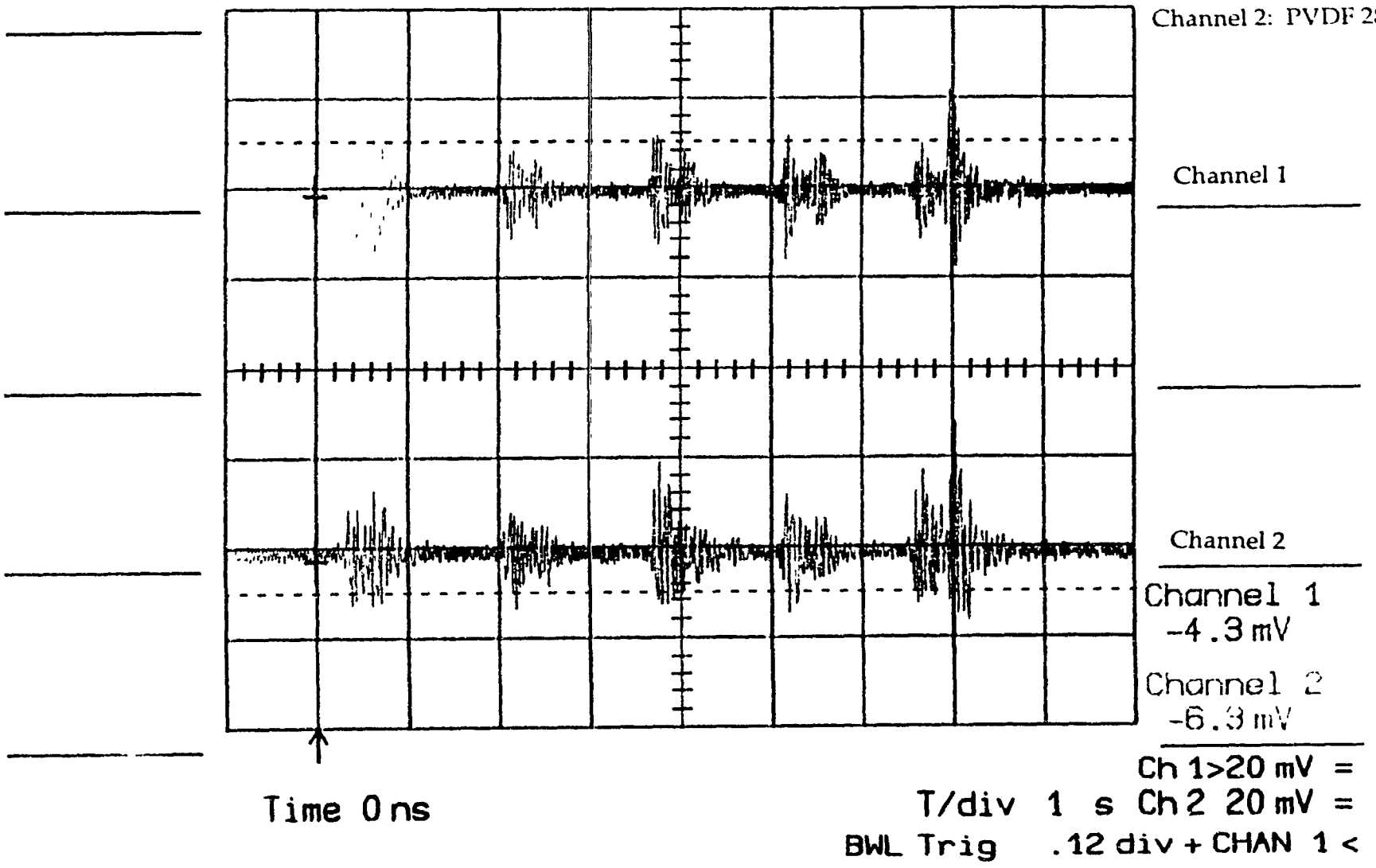

Graph #12
Test Piece: Aluminum Block
Source Location: S4
Sensor Pair Location: L4
Channel 1: PVDF 28 µm
Channel 2: PVDF 28 µm

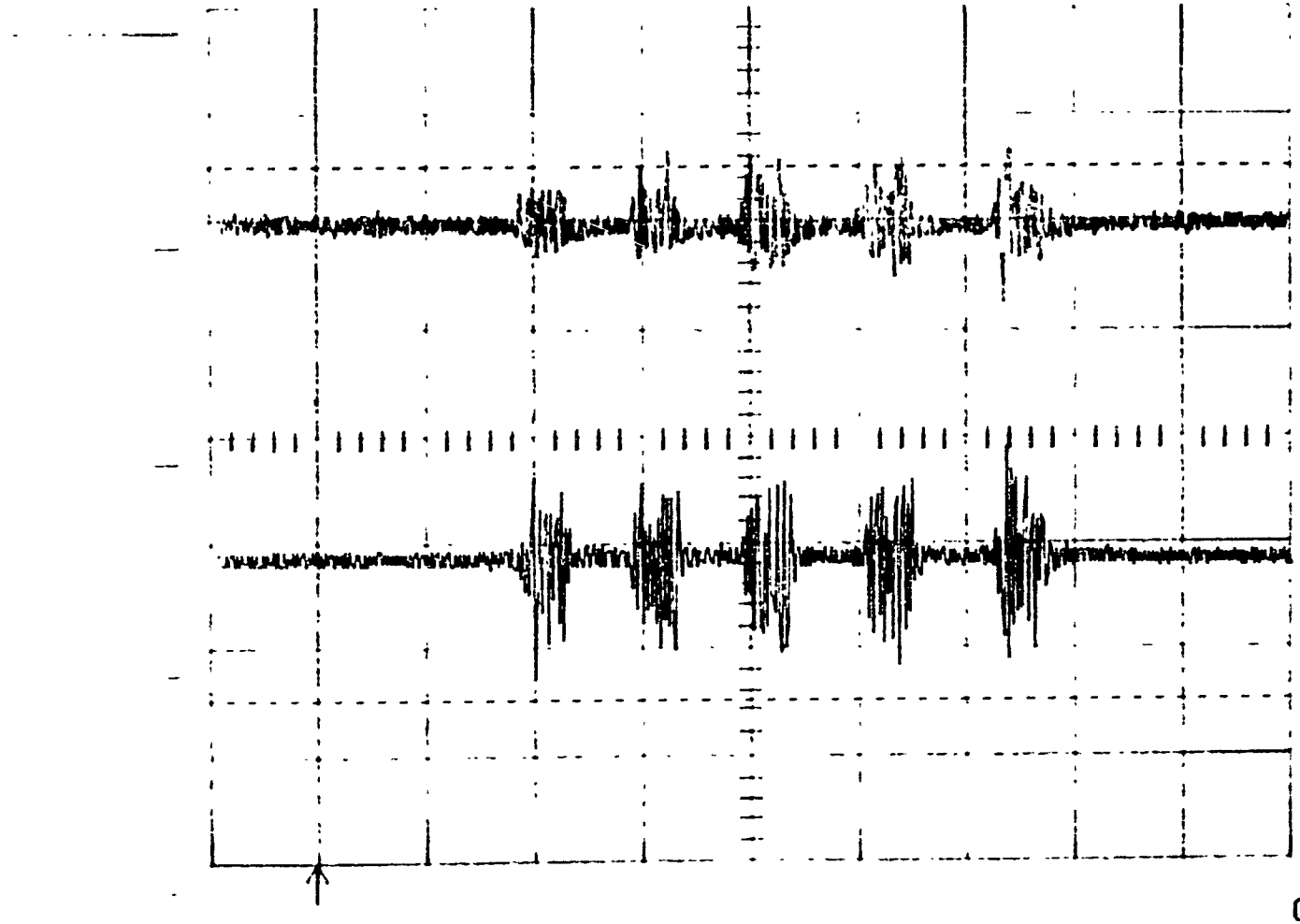

Graph #13
Test Piece: Aluminum Block
Source Location: S1
Sensor Pair Location: I 1
Channel 1: PVDF 52 μm
Channel 2: PVDF 28 μm

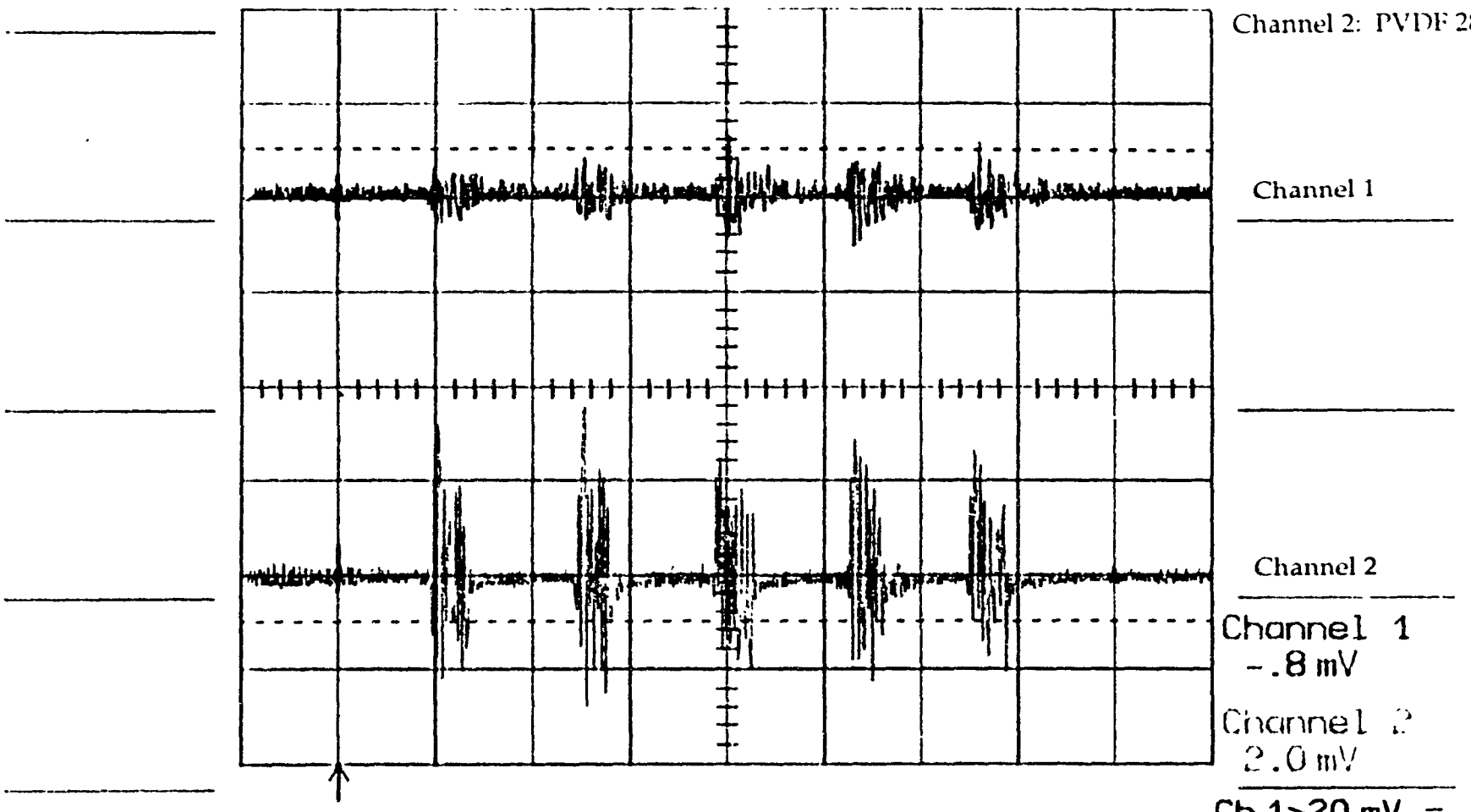

Graph #14
Test Piece: Aluminum Block
Source Location: S1
Sensor Pair Location: L2
Channel 1: PVDF 52 µm
Channel 2: PVDF 28 µm

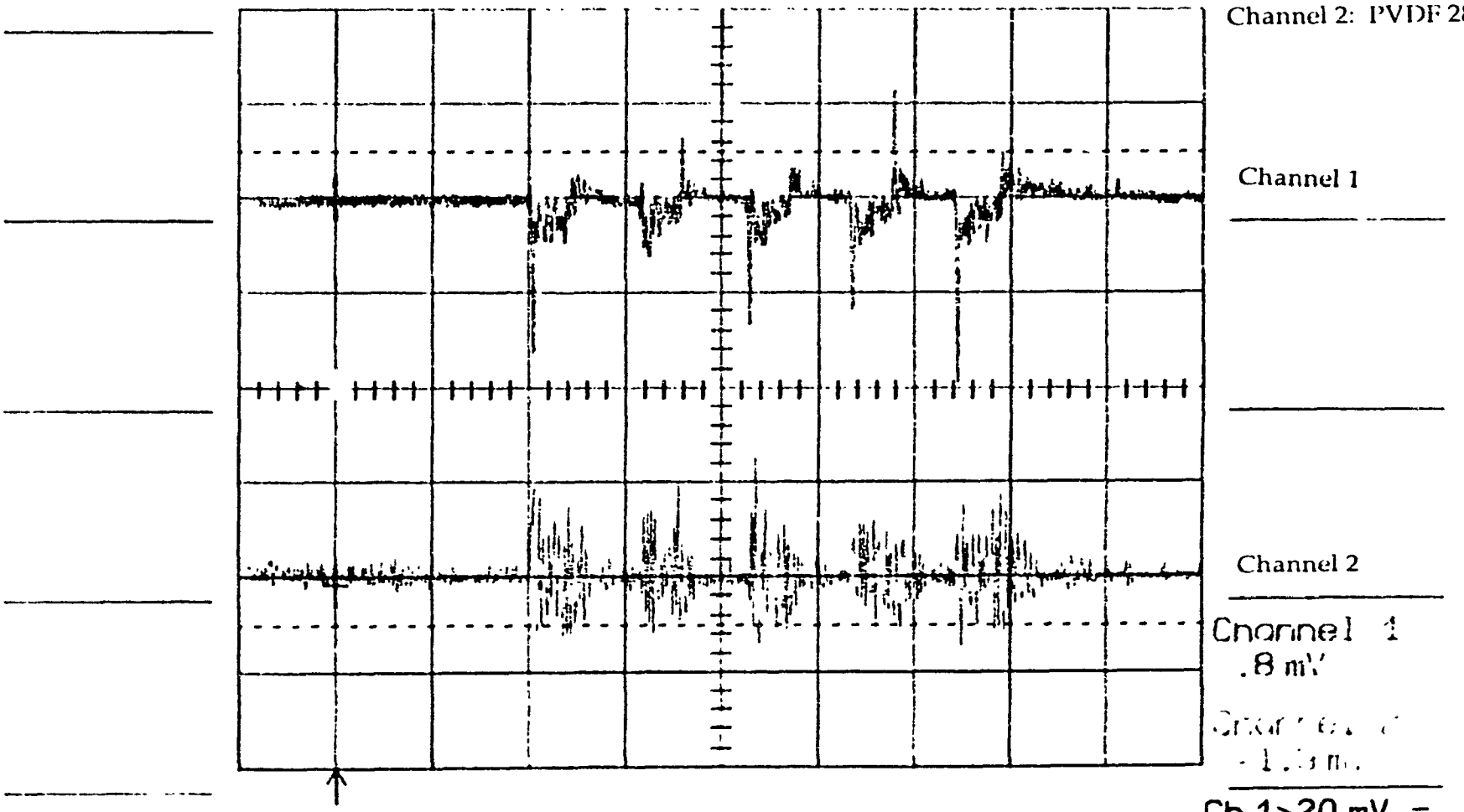

Graph #15
Test Piece. Aluminum Block
Source Location: S2
Sensor Pair Location: 1.1
Channel 1: PVDF 52 µm
Channel 2: PVDF 28 µm

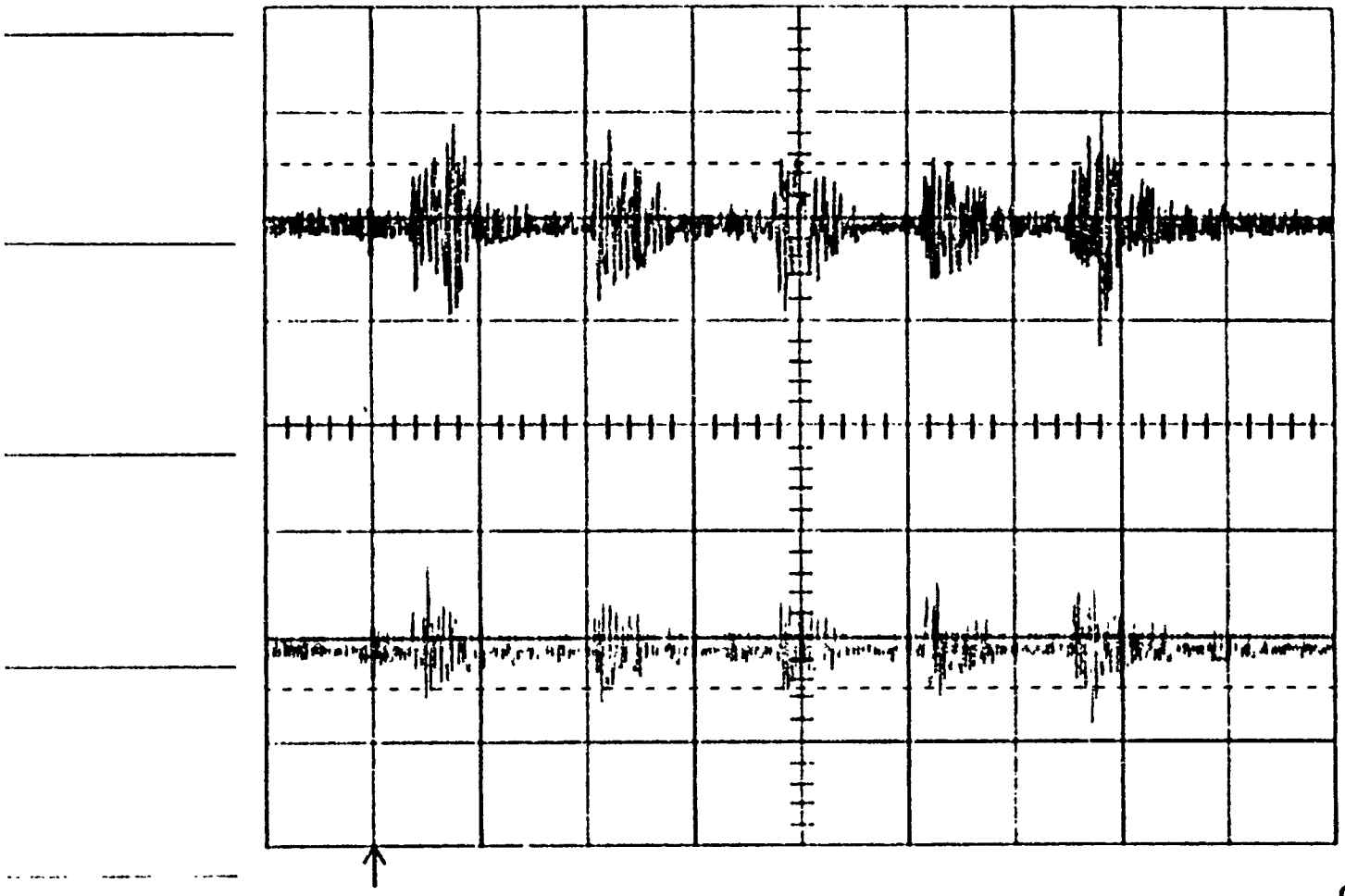

Graph #16
Test Piece: Aluminum Block
Source Location: S2
Sensor Pair Location: L3
Channel 1: PVDF 52 µm
Channel 2: PVDF 28 µm

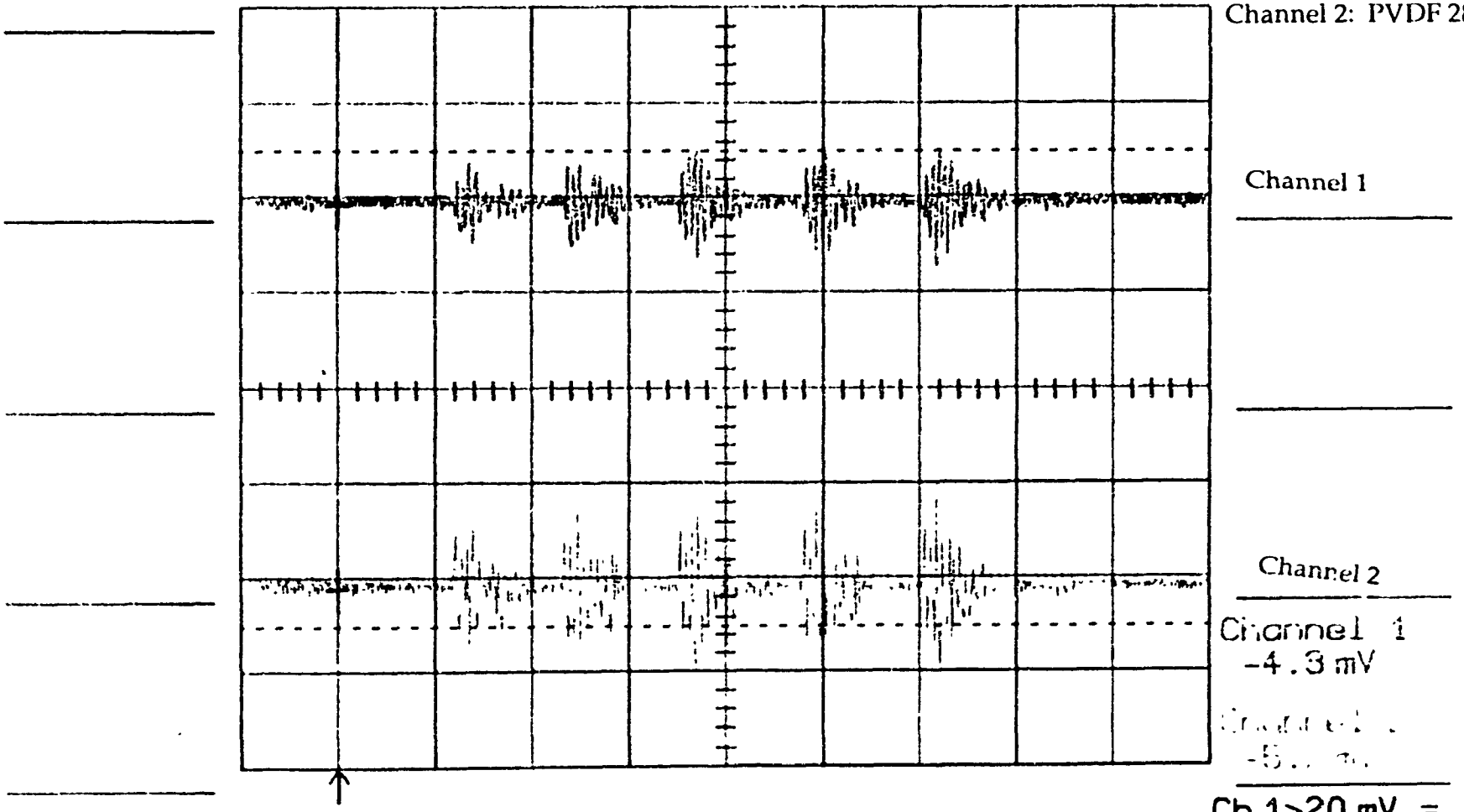

Graph #17
Test Piece: Aluminum Block
Source Location: S3
Sensor Pair Location: 1.4
Channel 1: PVDF 52 µm
Channel 2: PVDF 28 µm

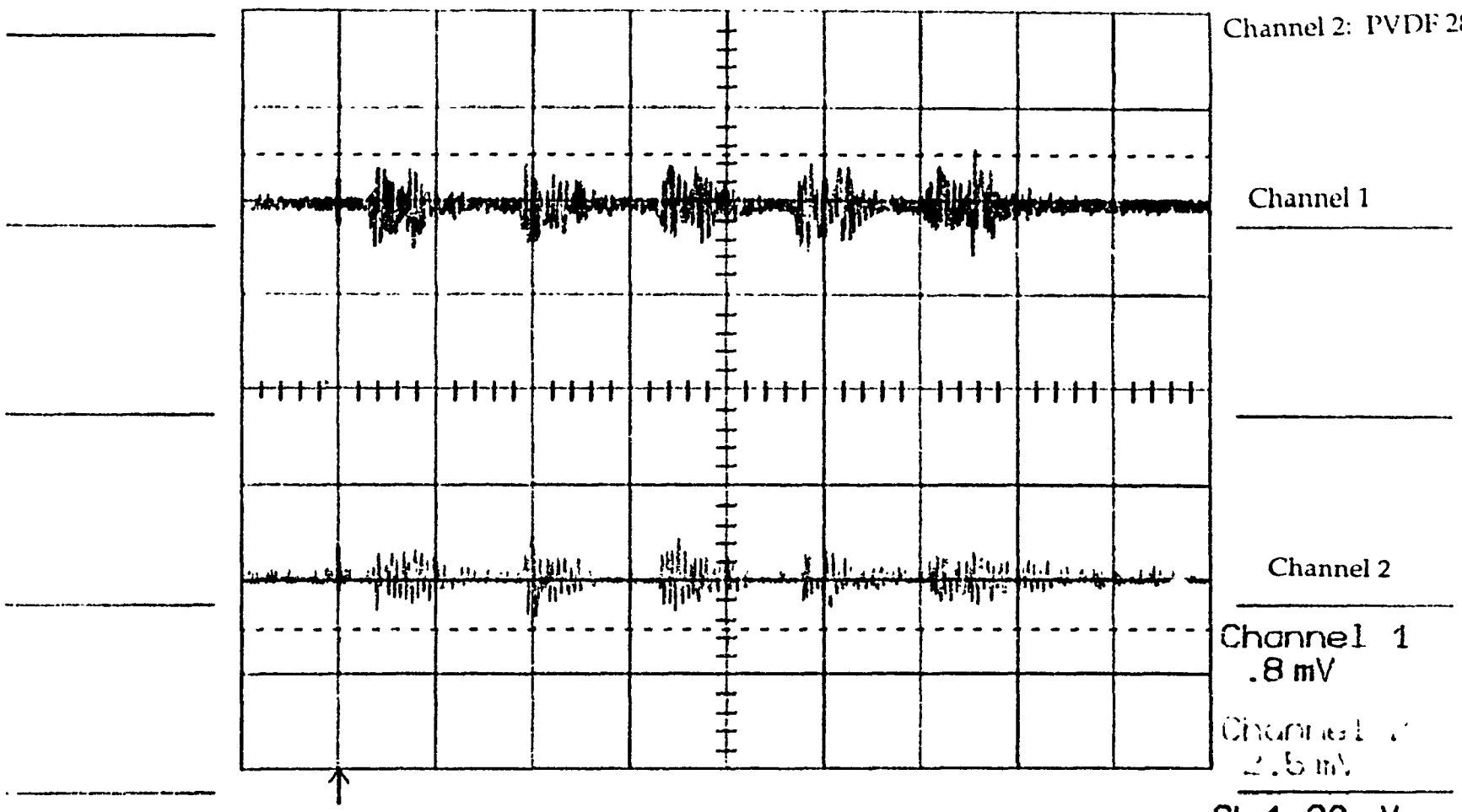

Graph #18
Test Piece: Aluminum Block
Source Location: S4
Sensor Pair Location: L4
Channel 1: PVDF 52 µm
Channel 2: PVDF 28 µm

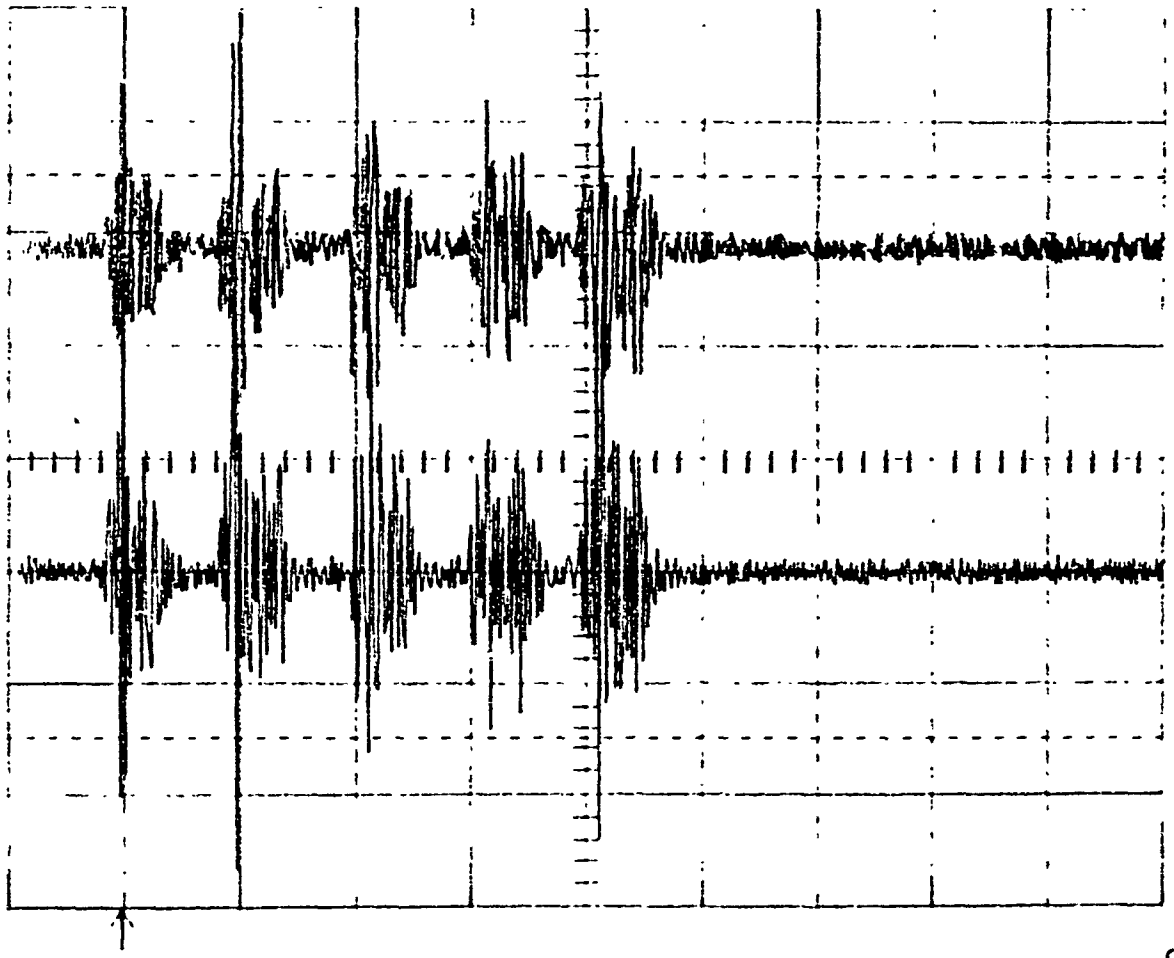

Graph #19
Test Piece: Aluminum Block
Source Location: S1
Sensor Pair Location: L1
Channel 1: Resonant
Channel 2: Wideband

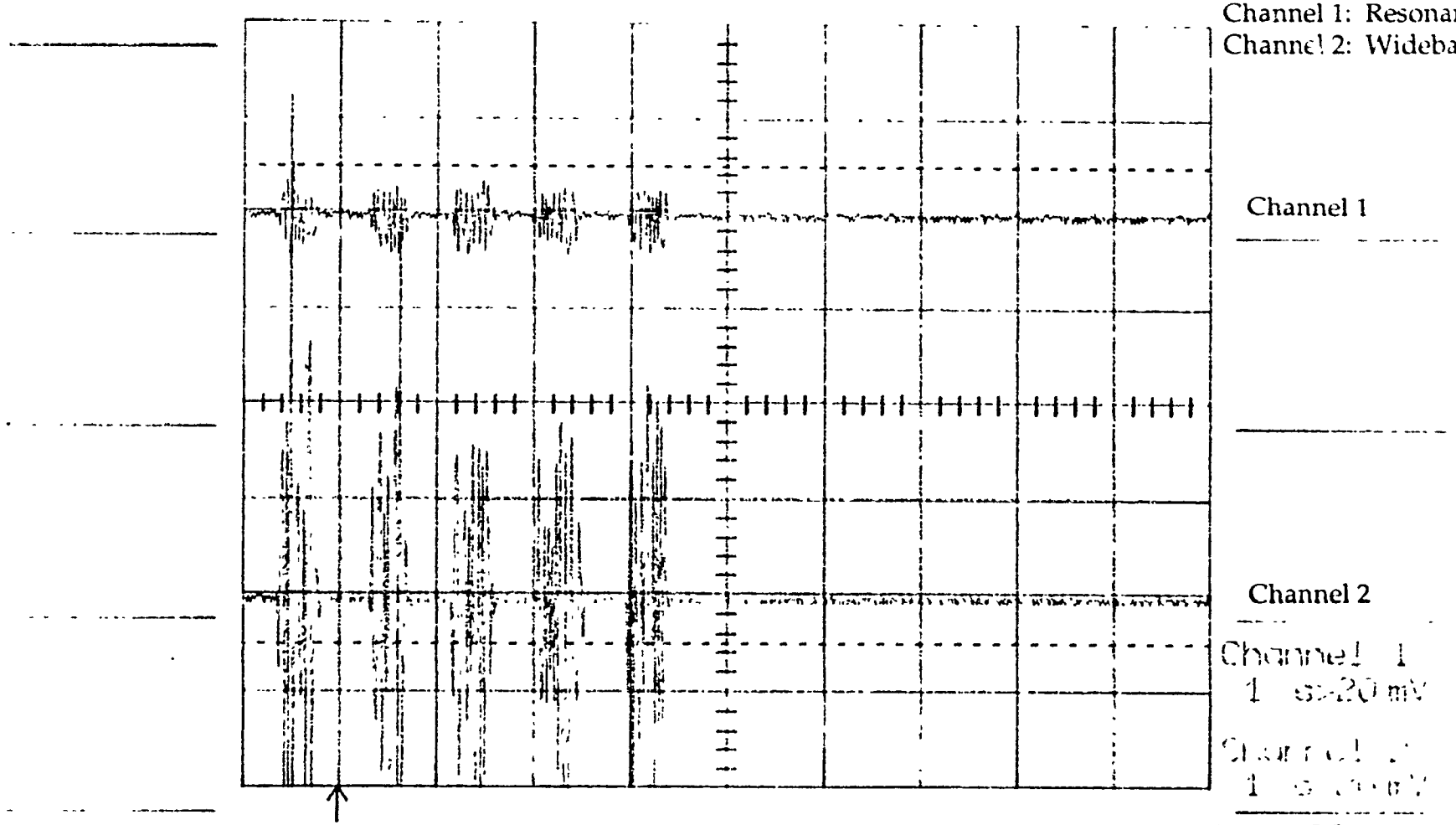

Graph #20
Test Piece: Aluminum Block
Source Location: S1
Sensor Pair Location: L2
Channel 1: Resonant
Channel 2: Wideband

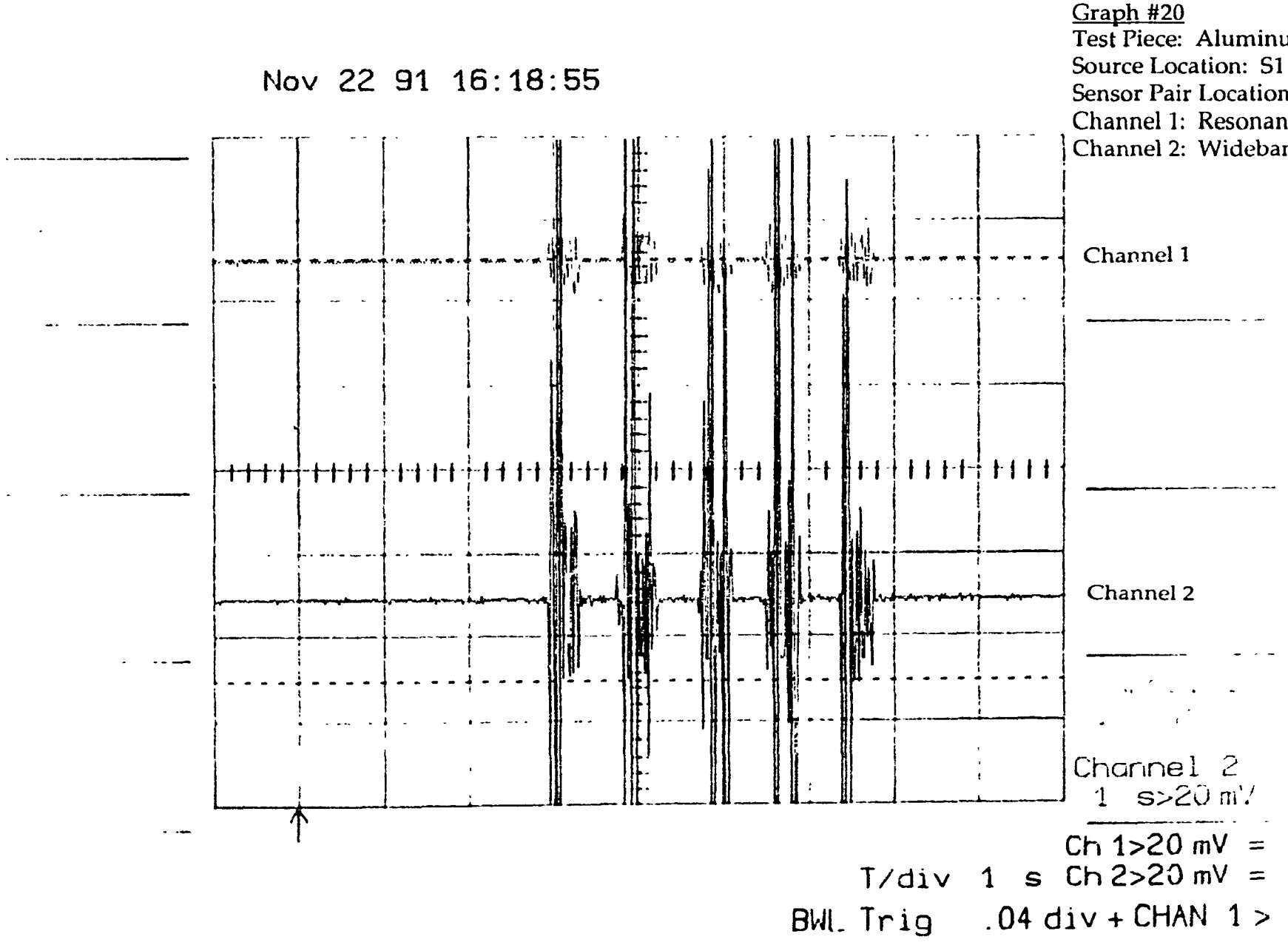

Graph #21
Test Piece: Aluminum Block
Source Location: S2
Sensor Pair Location: L1
Channel 1: Resonant
Channel 2: Wideband

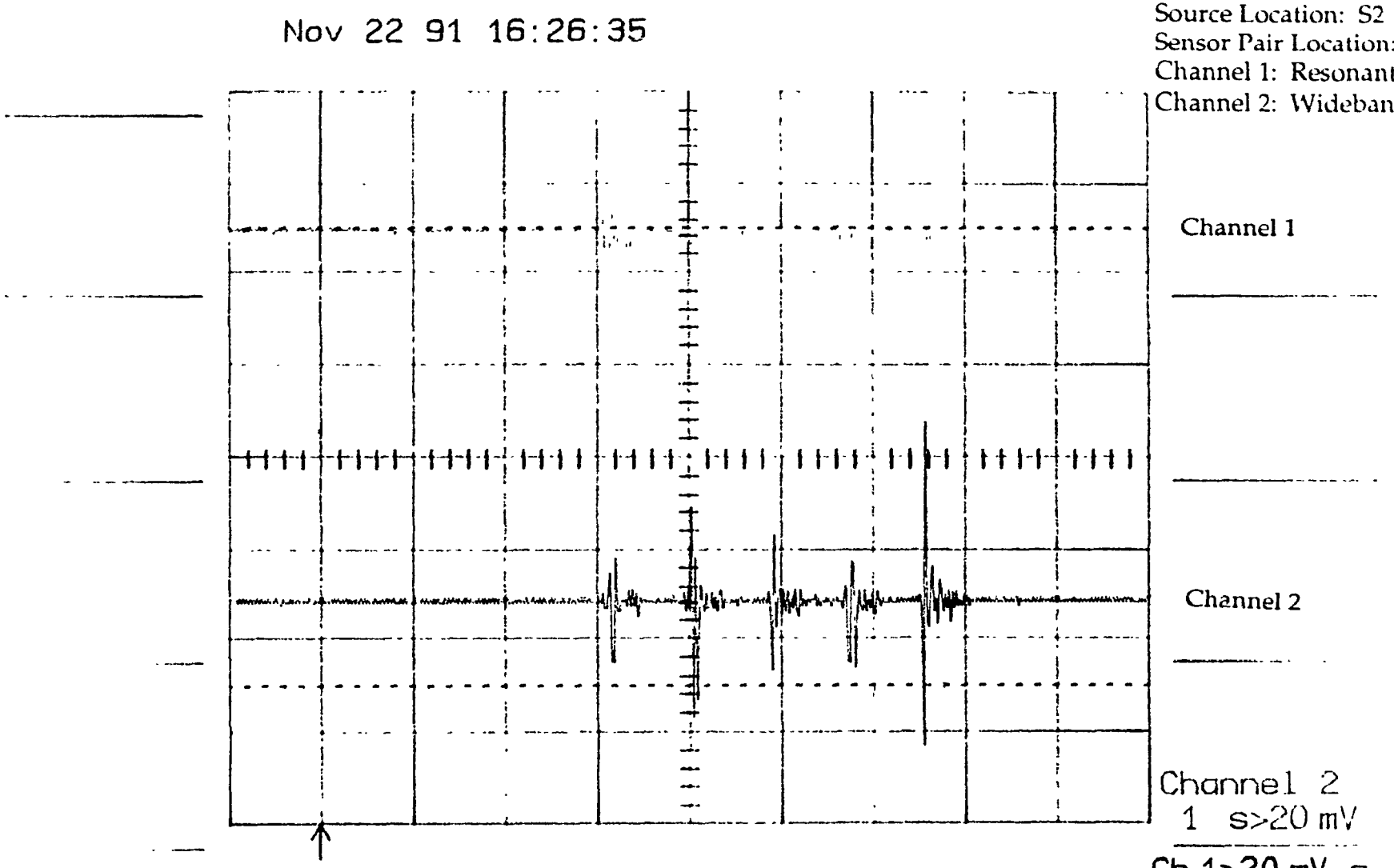

Graph #22
Test Piece: Aluminum Block
Source Location: S2
Sensor Pair Location: L3
Channel 1: Resonant
Channel 2: Wideband

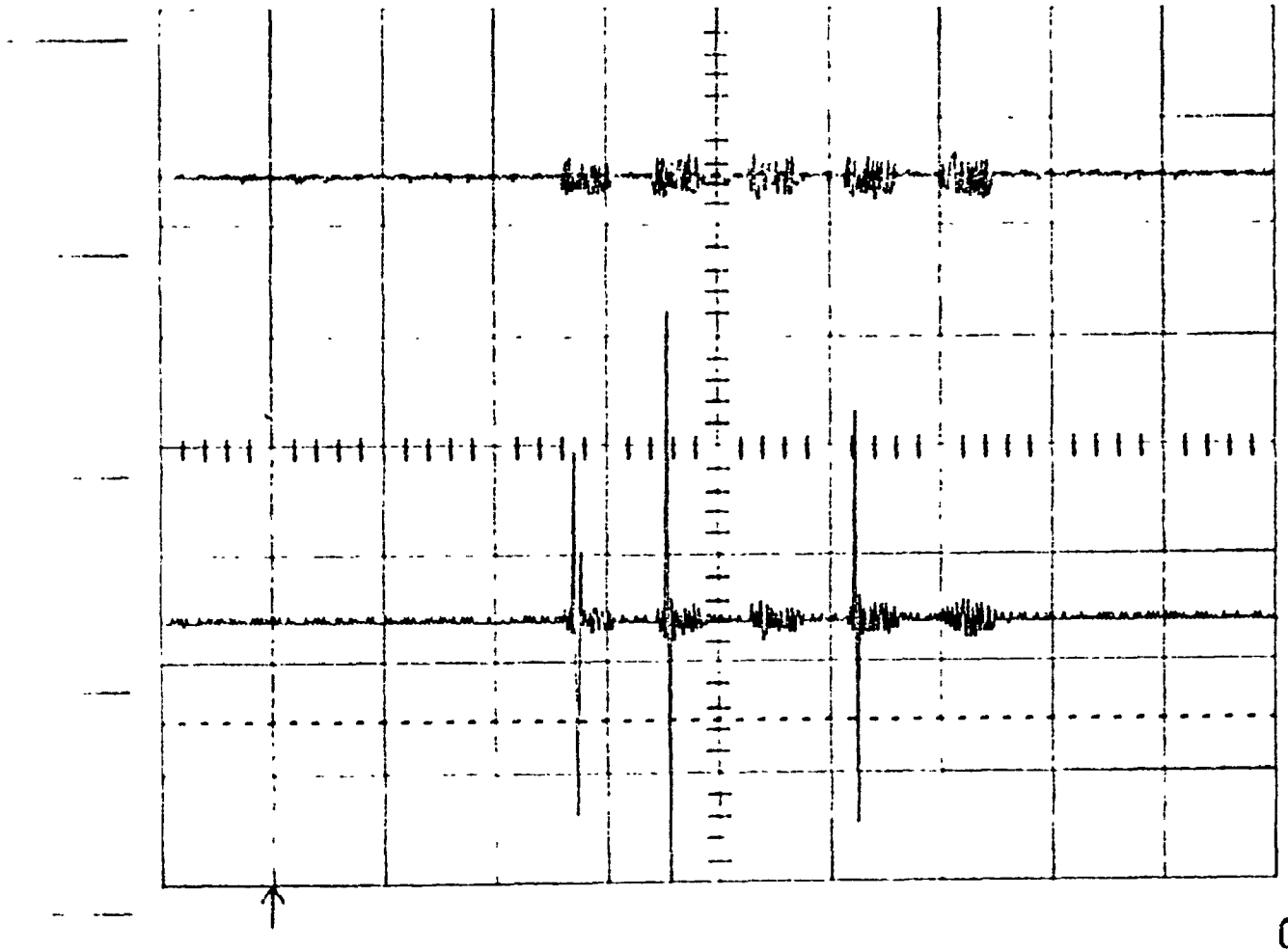

Graph #23
Test Piece: Aluminum Block
Source Location: S3
Sensor Pair Location: L4
Channel 1: Resonant
Channel 2: Wideband

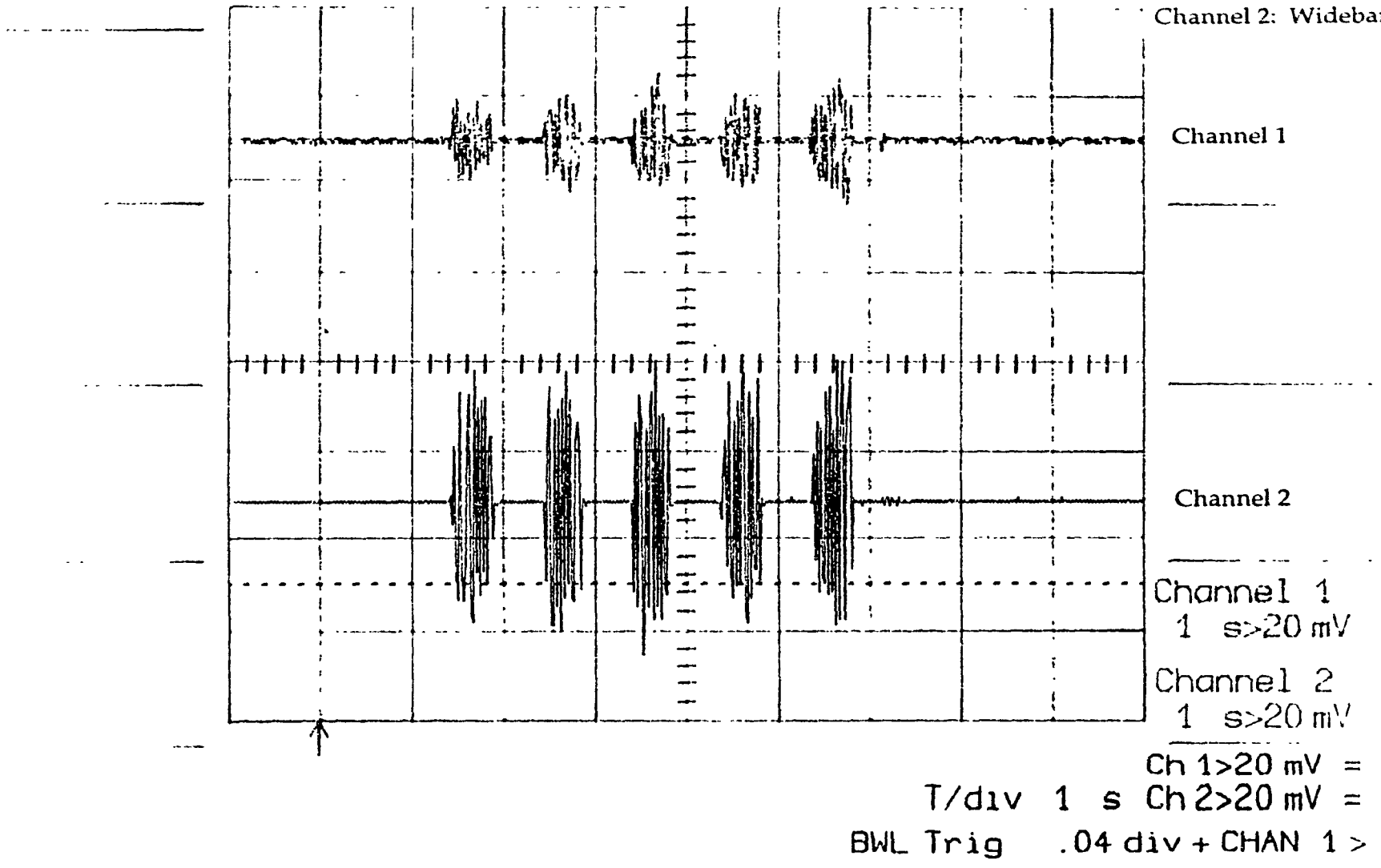

Graph #24
Test Piece: Aluminum Block
Source Location: S4
Sensor Pair Location: L4
Channel 1: Resonant
Channel 2: Wideband

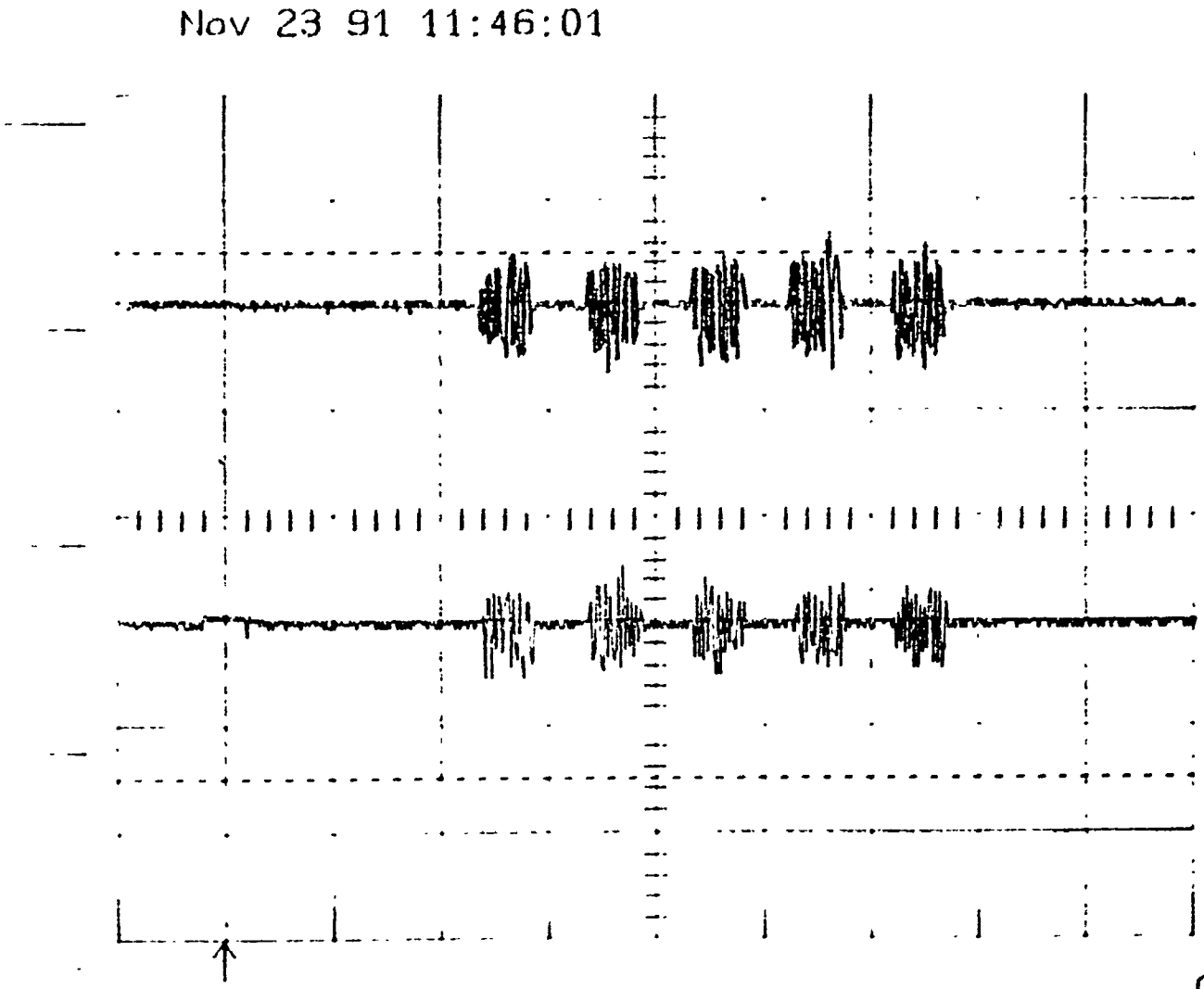

Appendix 3: Graphs of Voltage-Time Signal Waveforms and Frequency Spectrum Acquired in Graphite/Epoxy Plate Testing

Graph #25
Test Piece: Graphite/Epoxy [0°]
Impacts: 0
Sensors: Pre-Assembled PVDF 28 µm
Memory C: waveform recieved from sensor #1 at grid location A1
Vpp = 7.86 volts Fpeak= 3.0 MHz, Amplitude= -7.0 dB
Memory D: waveform received from sensor #4 at grid location A4
Vpp = 6.50 volts Fpeak= 25.0 MHz, Amplitude= -1.4 dB

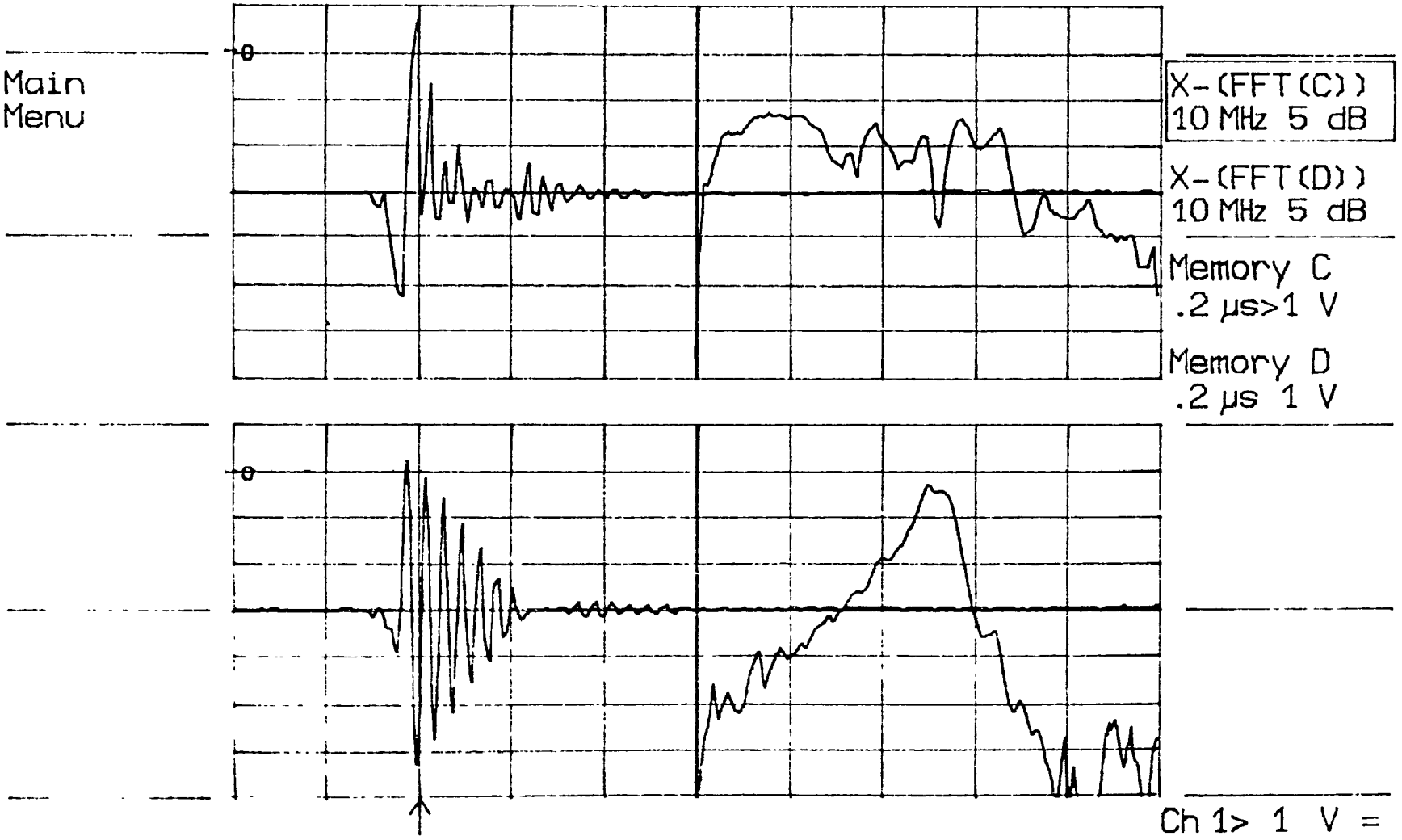

Graph #26
Test Piece: Graphite/Epoxy [0°]
Impacts: 0
Sensors: Pre-Assembled PVDF 28 µm
Memory C: waveform recieved from sensor #1 at grid location B1
Vpp = 8.06 volts Fpeak= 2.2 MHz, Amplitude= -6.1 dB
Memory D: waveform received from sensor #4 at grid location B4
Vpp = 6.50 volts Fpeak= 28 MHz, Amplitude= 1.5 dB

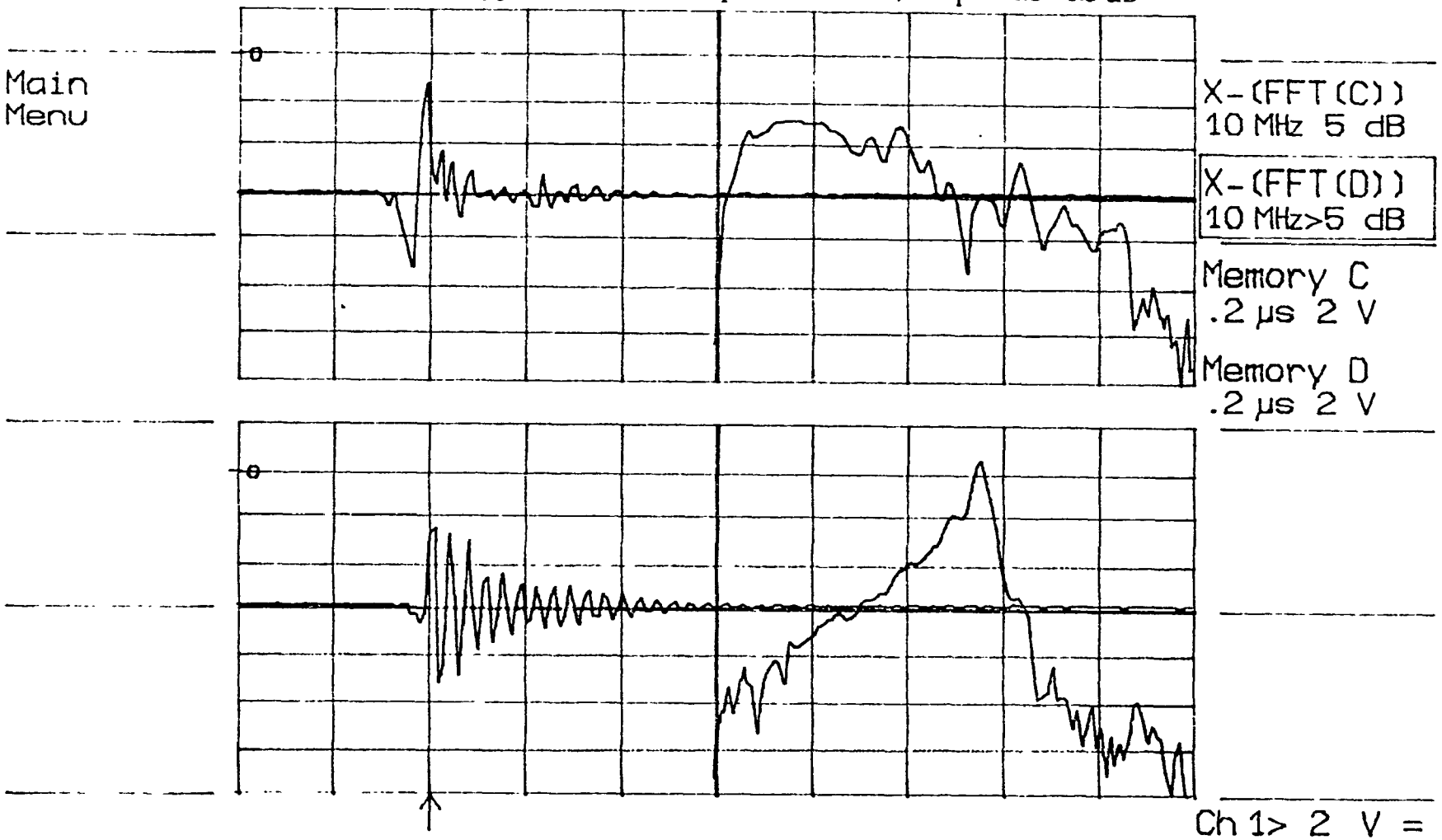

Graph #27
Test Piece: Graphite/Epoxy [0°]
Impacts: 0
Sensors: Pre-Assembled PVDF 28 μm
Memory C: waveform recieved from sensor #2 at grid location B2
Vpp = 6.36 volts Fpeak= 28.8 MHz, Amplitude= -2.6 dB
Memory D: waveform received from sensor #3 at grid location B3
Vpp = 6.46 volts Fpeak= 28.8 MHz, Amplitude= 1.0 dB

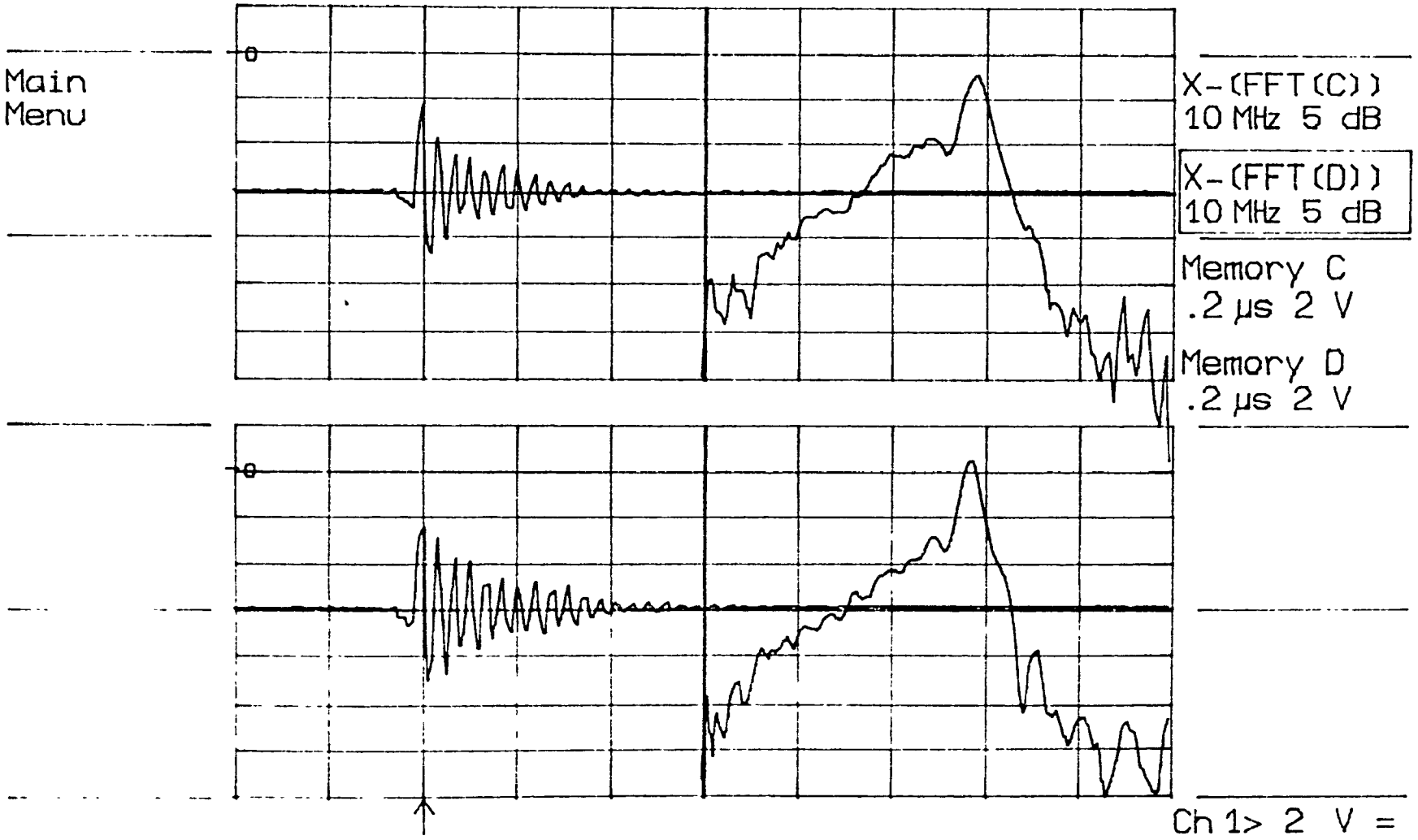

Graph #28
Test Piece: Graphite/Epoxy [0°]
Impacts: 0
Sensors: Pre-Assembled PVDF 28 µm
Memory C: waveform recieved from sensor #1 at grid location C1
Vpp = 6.80 volts Fpeak= 28.6 MHz, Amplitude= 0 dB
Memory D: waveform received from sensor #4 at grid location C4
Vpp = 6.06 volts Fpeak= 30.0 MHz, Amplitude= -2.0 dB

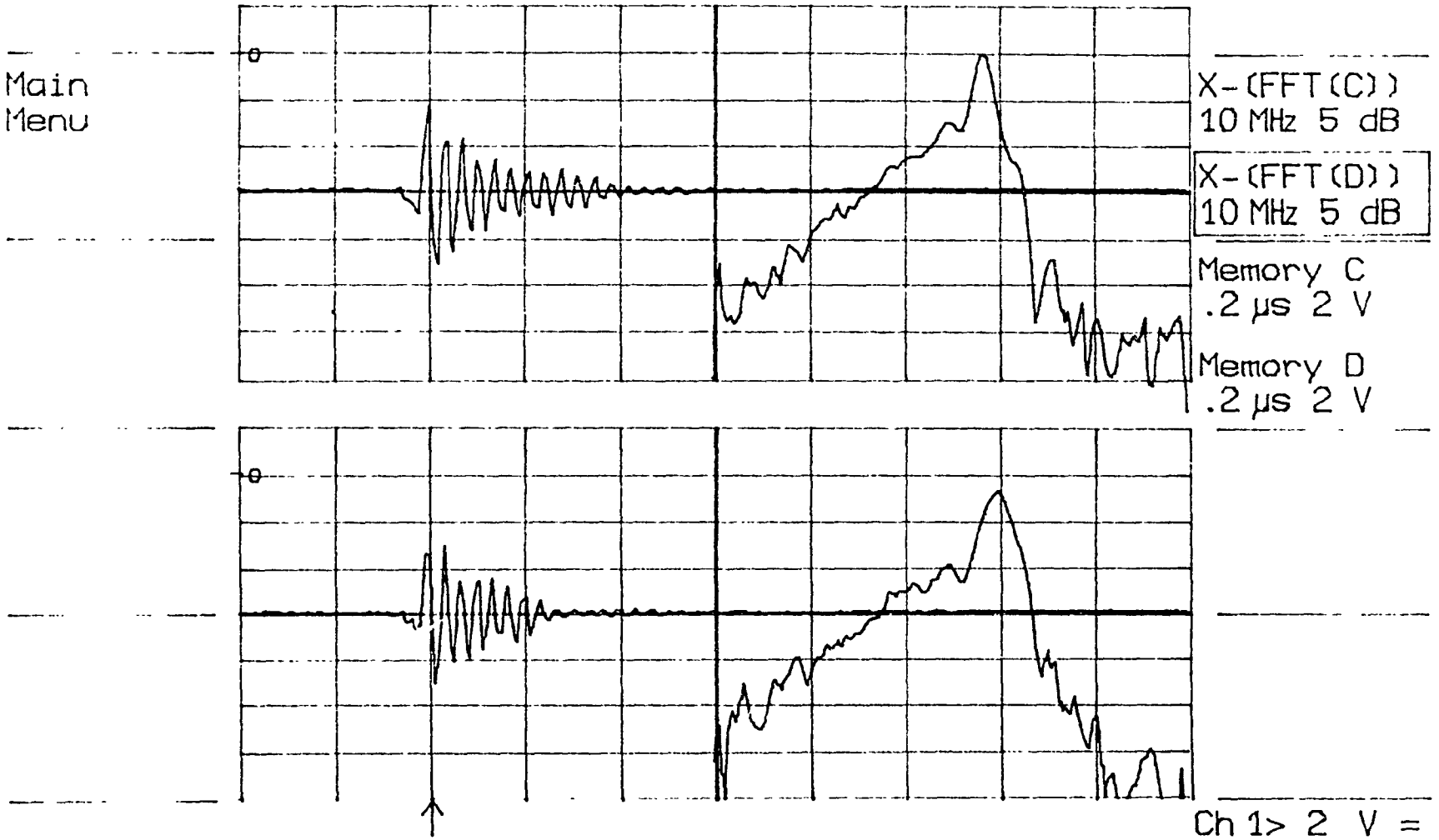

Graph #29
Test Piece: Graphite/Epoxy [±45°]
Impacts: 0
Sensors: Pre-Assembled PVDF 28 μm
Memory C: waveform recieved from sensor #1 at grid location A1
Vpp = 10.46 volts Fpeak= 3.4 MHz, Amplitude= 4.2 dB
Memory D: waveform received from sensor #4 at grid location A4
Vpp = 8.74 volts Fpeak= 25.0 MHz, Amplitude= 4.7 dB

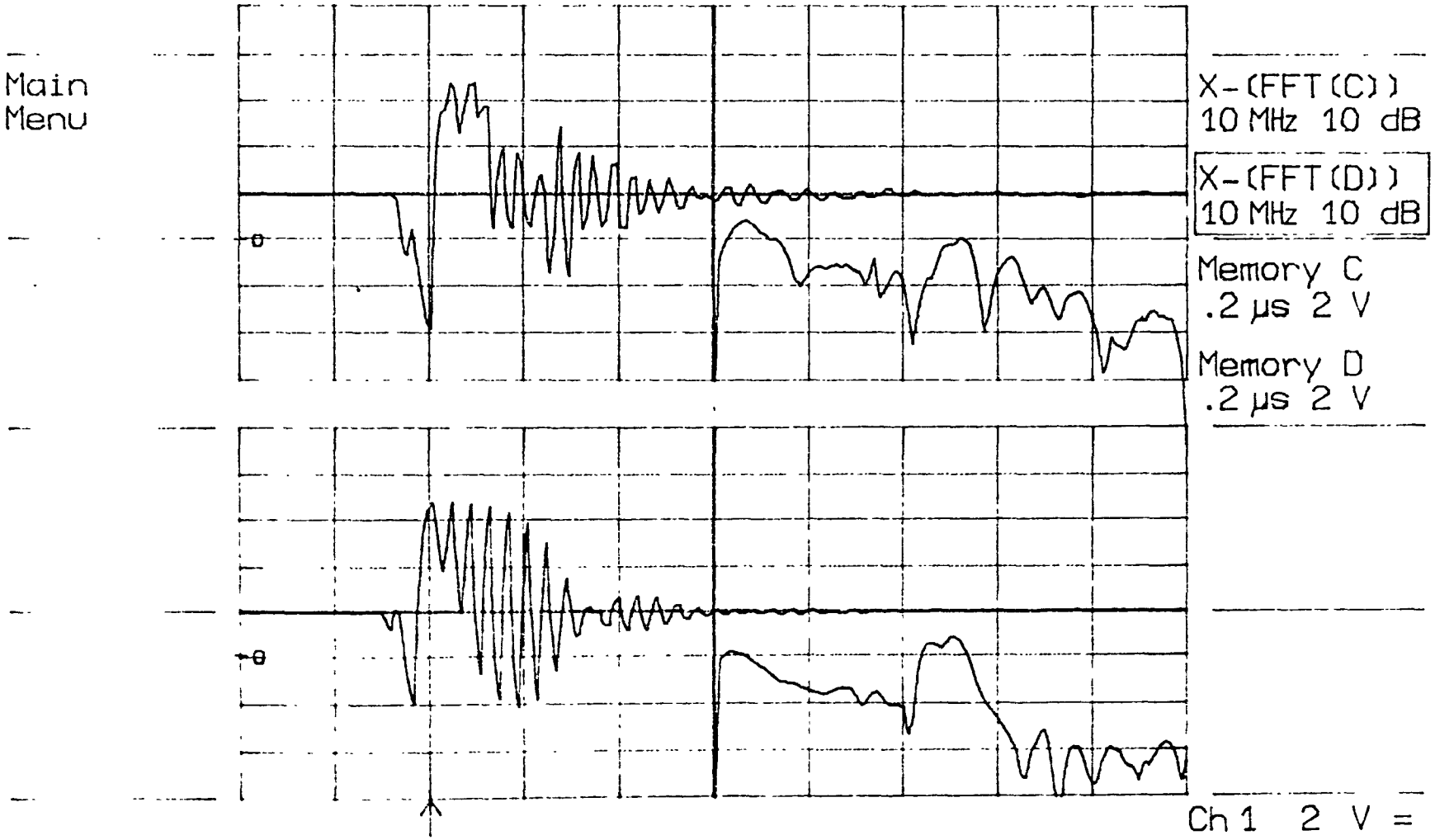

Graph #30
Test Piece: Graphite/Epoxy [±45°]
Impacts: 0
Sensors: Pre-Assembled PVDF 28 μm
Memory C: waveform recieved from sensor #1 at grid location B1
Vpp = 10.46 volts Fpeak= 3.4 MHz, Amplitude= 3.8 dB
Memory D: waveform received from sensor #4 at grid location B4
Vpp = 8.62 volts Fpeak= 25.4 MHz, Amplitude= 4.4 dB

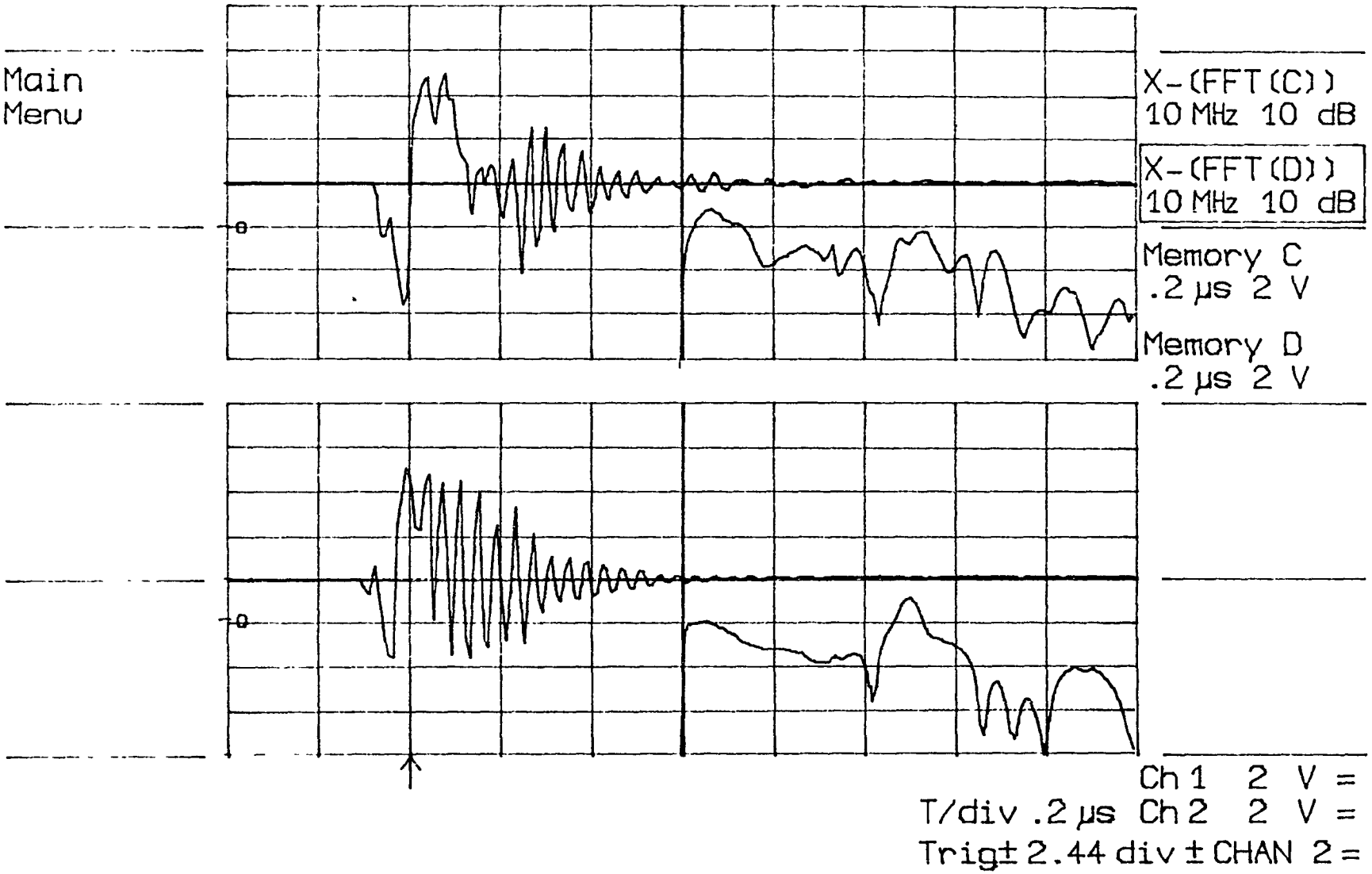

Graph #31
Test Piece: Graphite/Epoxy [±45°]
Impacts: 0
Sensors: Pre-Assembled PVDF 28 µm
Memory C: waveform recieved from sensor #2 at grid location B2
Vpp = 8.84 volts Fpeak= 25.0 MHz, Amplitude= 5.0 dB
Memory D: waveform received from sensor #3 at grid location B3
Vpp = 8.80 volts Fpeak= 24.5 MHz, Amplitude= 0.8 dB

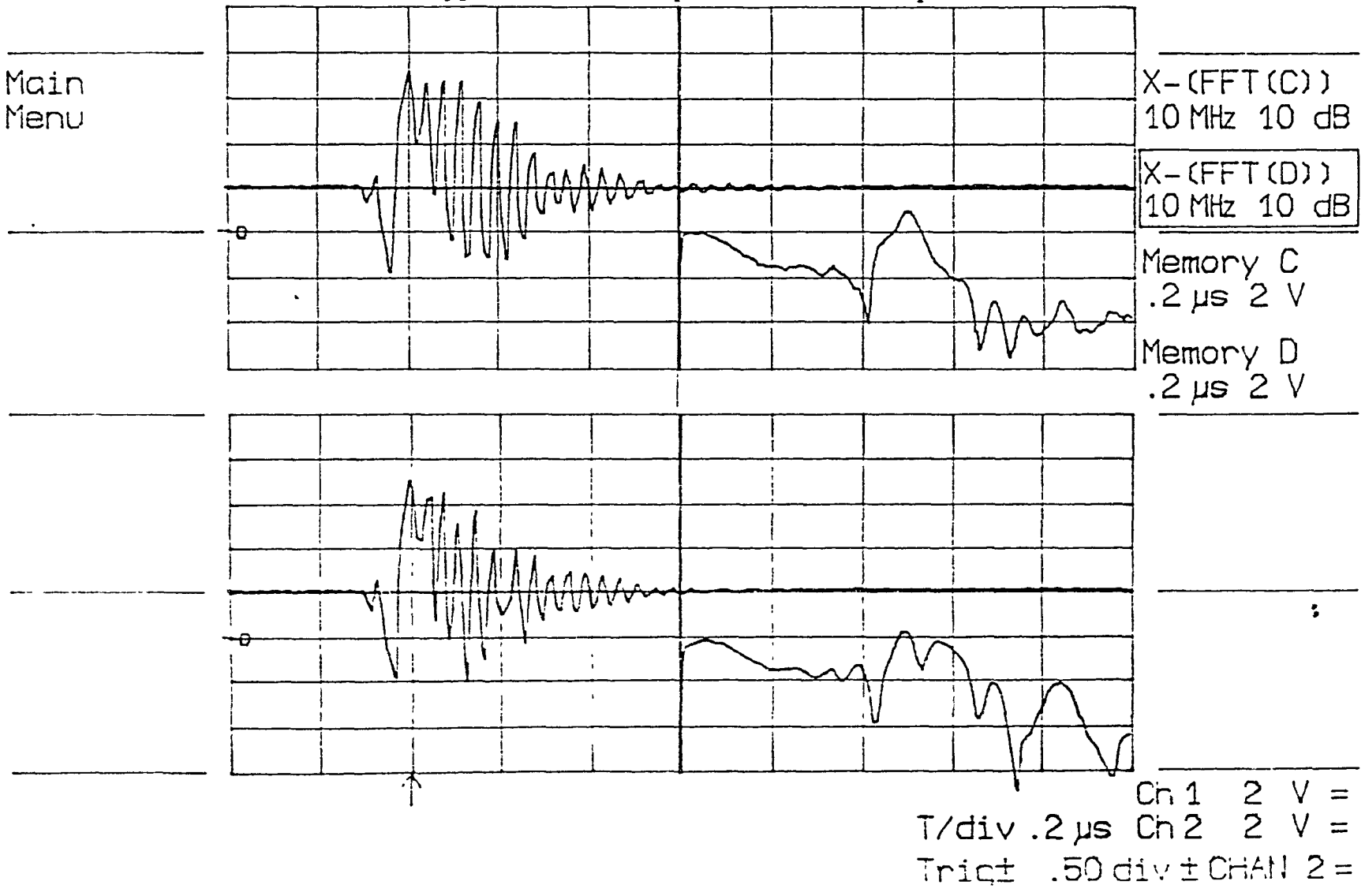

Graph #32
Test Piece: Graphite/Epoxy [±45°]
Impacts: 0
Sensors: Pre-Assembled PVDF 28 μm
Memory C: waveform recieved from sensor #1 at grid location C1
Vpp = 8.62 volts Fpeak= 25.0 MHz, Amplitude= 0 dB
Memory D: waveform received from sensor #4 at grid location C4
Vpp = 8.58 volts Fpeak= 25.0 MHz, Amplitude= 4.2 dB

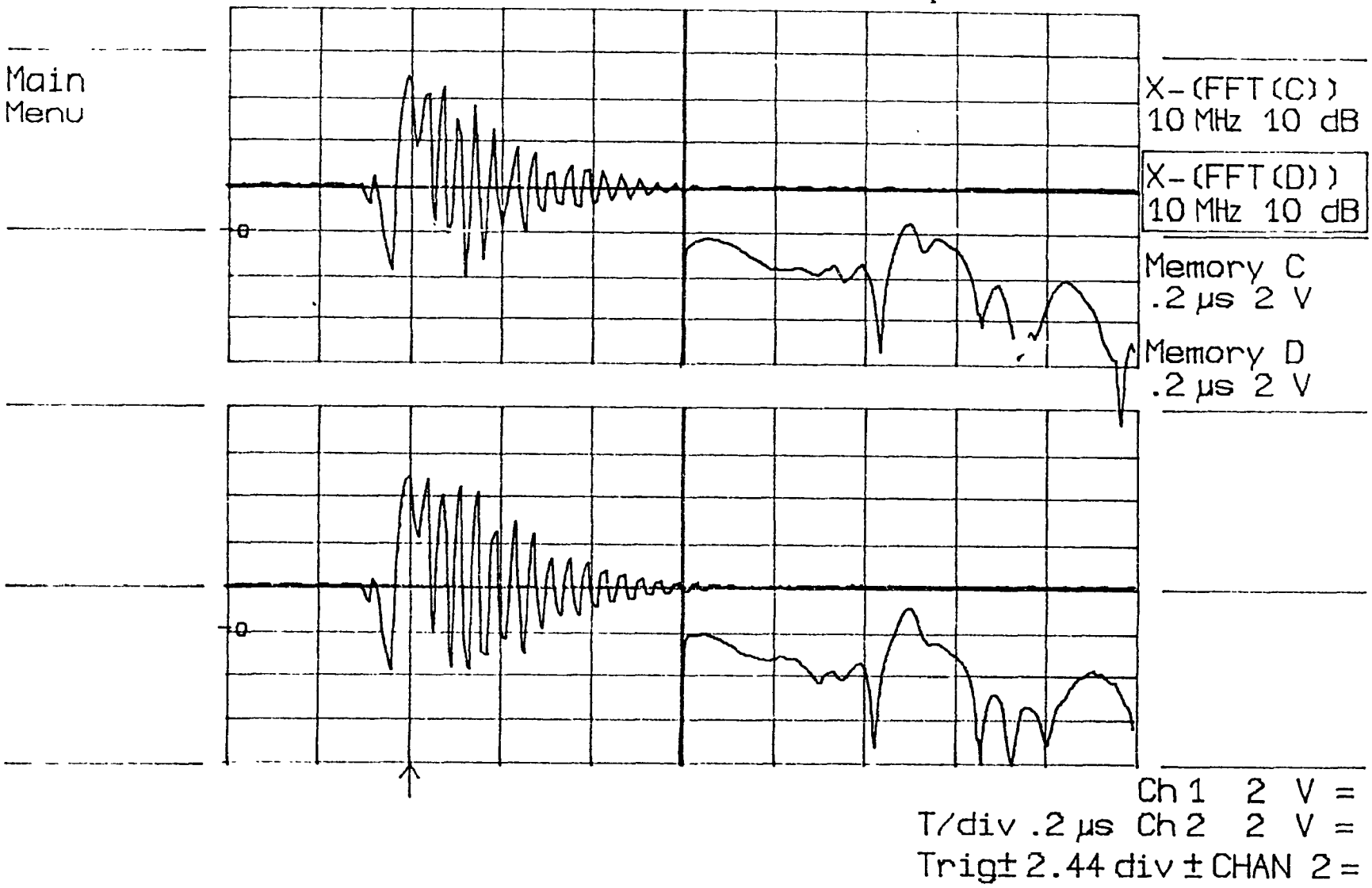

Graph #33
Test Piece: Graphite/Epoxy [0°]
Impacts: 3
Sensors: Pre-Assembled PVDF 28 µm
Memory C: waveform recieved from sensor #1 at grid location A1
Vpp = 7.00 volts Fpeak= 12.5 MHz, Amplitude= 4.0 dB
Memory D: waveform received from sensor #4 at grid location A4
Vpp = 6.02 volts Fpeak= 23.5 MHz, Amplitude= -0.5 dB

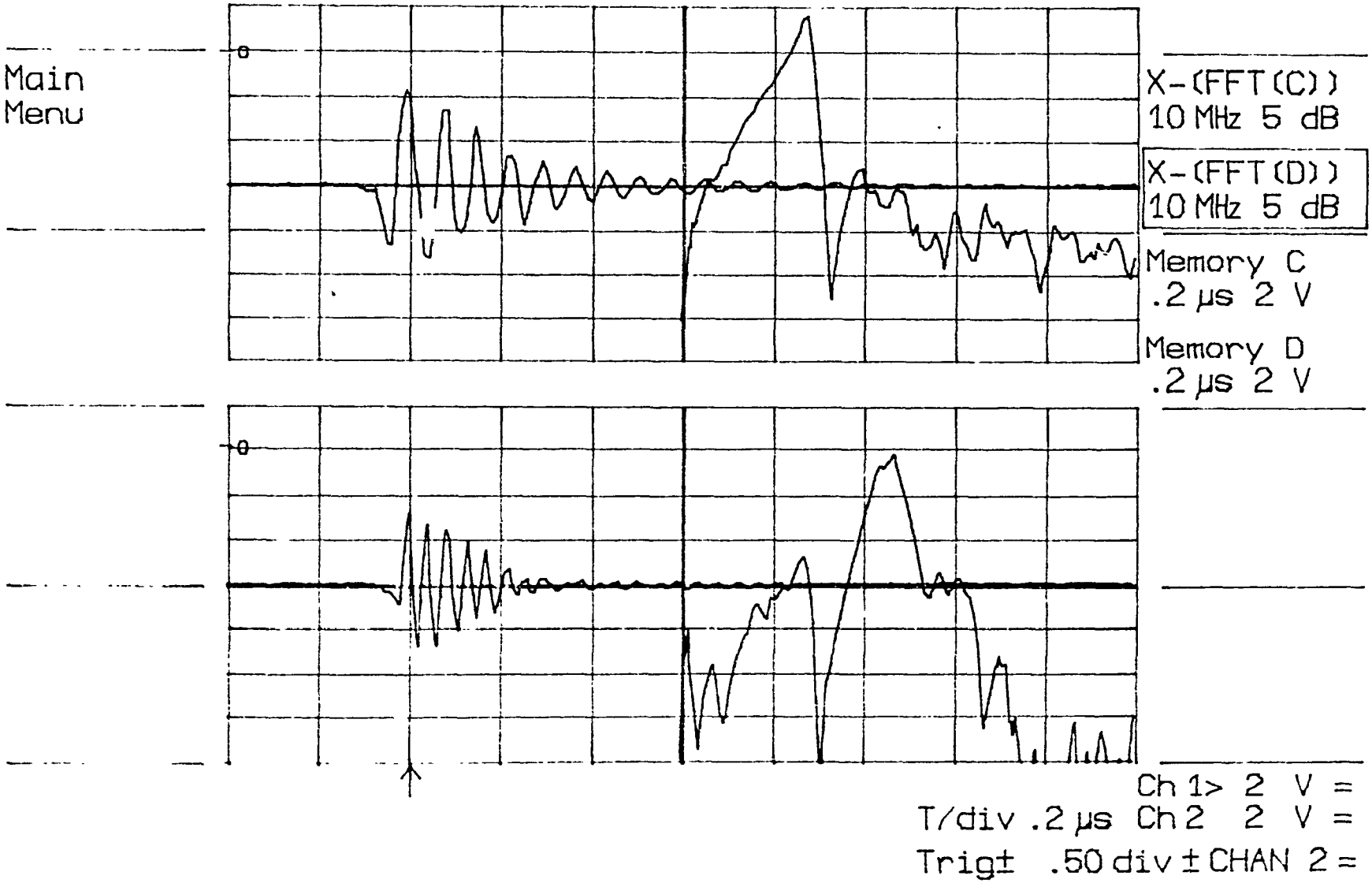

Graph #34
Test Piece: Graphite/Epoxy [0°]
Impacts: 3
Sensors: Pre-Assembled PVDF 28 µm
Memory C: waveform recieved from sensor #1 at grid location B1
Vpp =7.64 volts Fpeak= 25.0 MHz, Amplitude= 0 dB
Memory D: waveform received from sensor #4 at grid location B4
Vpp = 1.68 volts Fpeak= 21.6 MHz, Amplitude= -14.2 dB

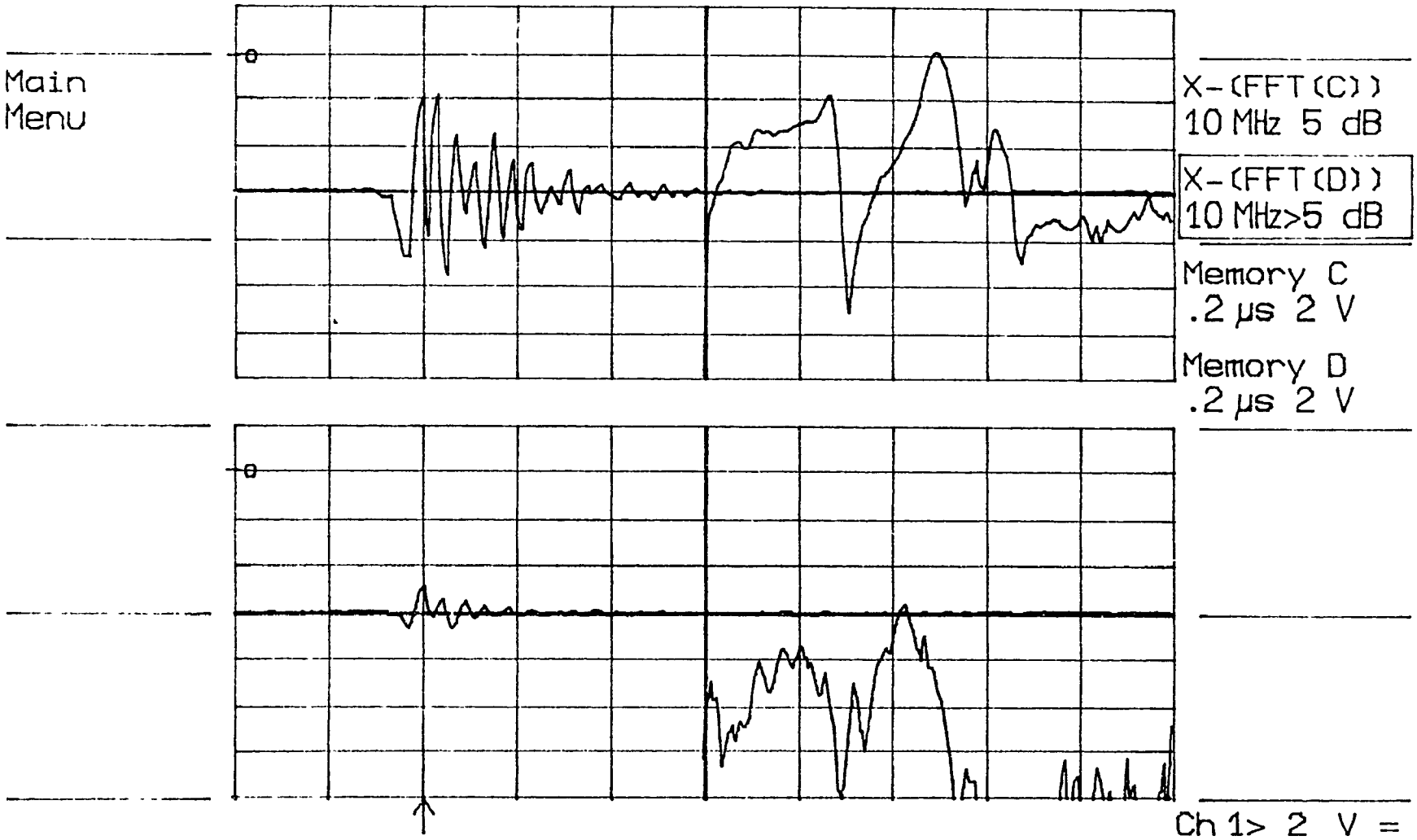

Graph #35
Test Piece: Graphite/Epoxy [0°]
Impacts: 3
Sensors: Pre-Assembled PVDF 28 µm
Memory C: waveform recieved from sensor #2 at grid location B2
Vpp = 5.30 volts Fpeak= 20.0 MHz, Amplitude= -2.5 dB
Memory D: waveform received from sensor #3 at grid location B3
Vpp = 4.78 volts Fpeak= 24.0 MHz, Amplitude= -7.5 dB

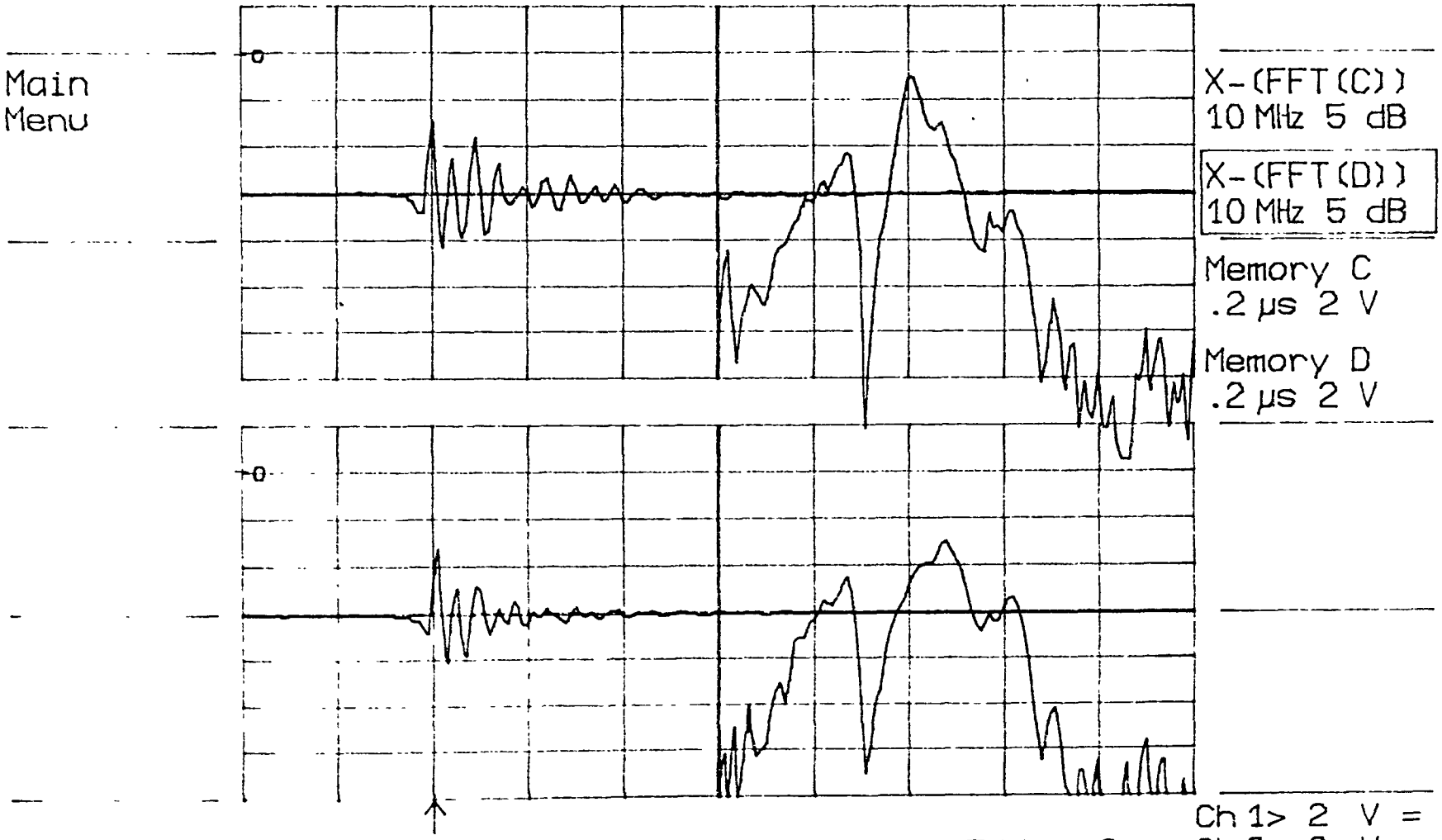

Graph #36
Test Piece: Graphite/Epoxy [0°]
Impacts: 3
Sensors: Pre-Assembled PVDF 28 μm
Memory C: waveform recieved from sensor #1 at grid location C1
Vpp = 6.14 volts Fpeak= 23.5 MHz, Amplitude= 3.0 dB
Memory D: waveform received from sensor #4 at grid location C4
Vpp = 6.42 volts Fpeak= 23.5 MHz, Amplitude= 6.0 dB

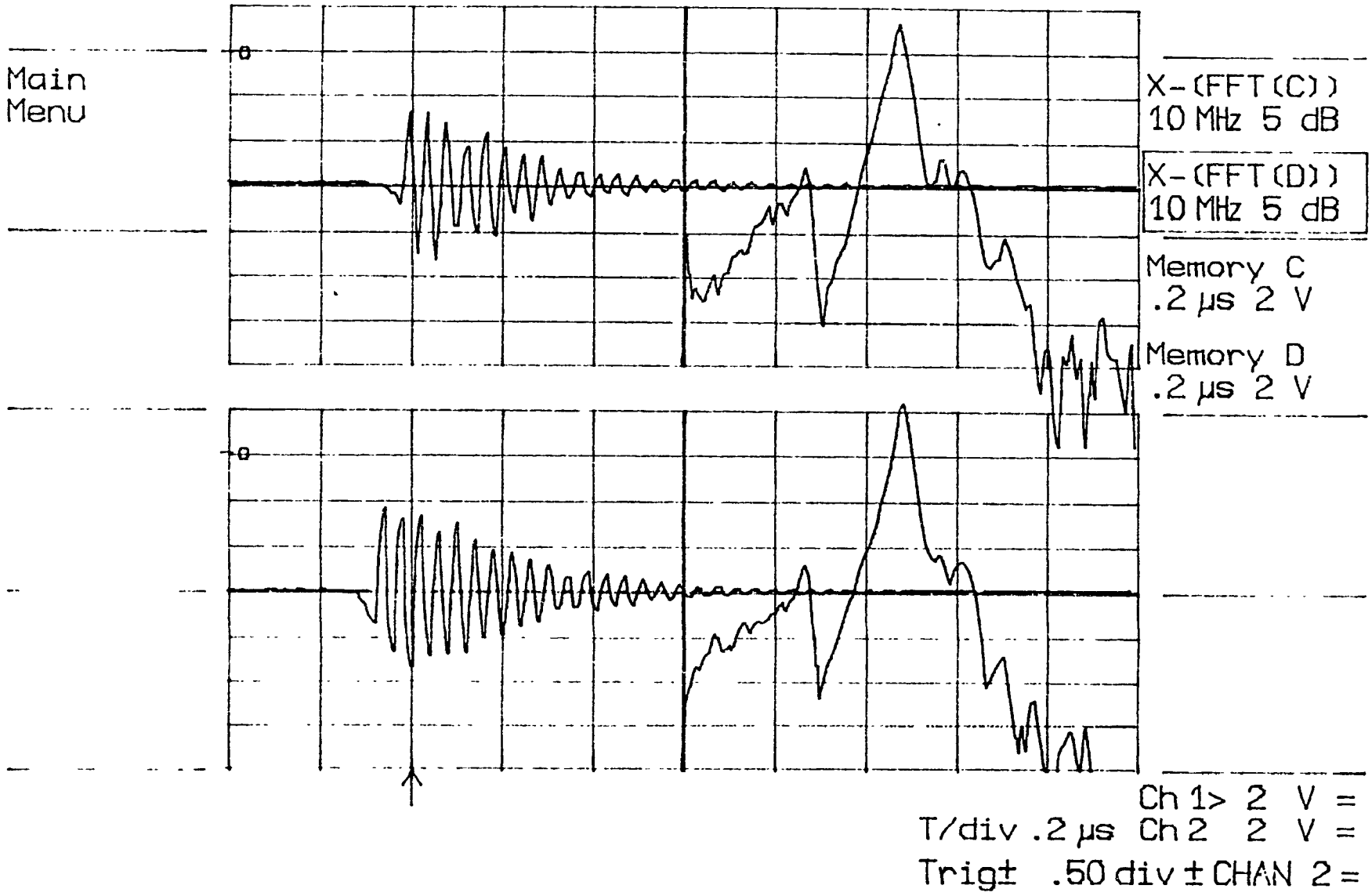

Graph #37
Test Piece: Graphite/Epoxy [±45°]
Impacts: 3
Sensors: Pre-Assembled PVDF 28 μm
Memory C: waveform recieved from sensor #1 at grid location A1
Vpp = 8.00 volts Fpeak= 14.0 MHz, Amplitude= 6.7 dB
Memory D: waveform received from sensor #4 at grid location A4
Vpp = 6.96 volts Fpeak= 21.5 MHz, Amplitude= 6.7 dB

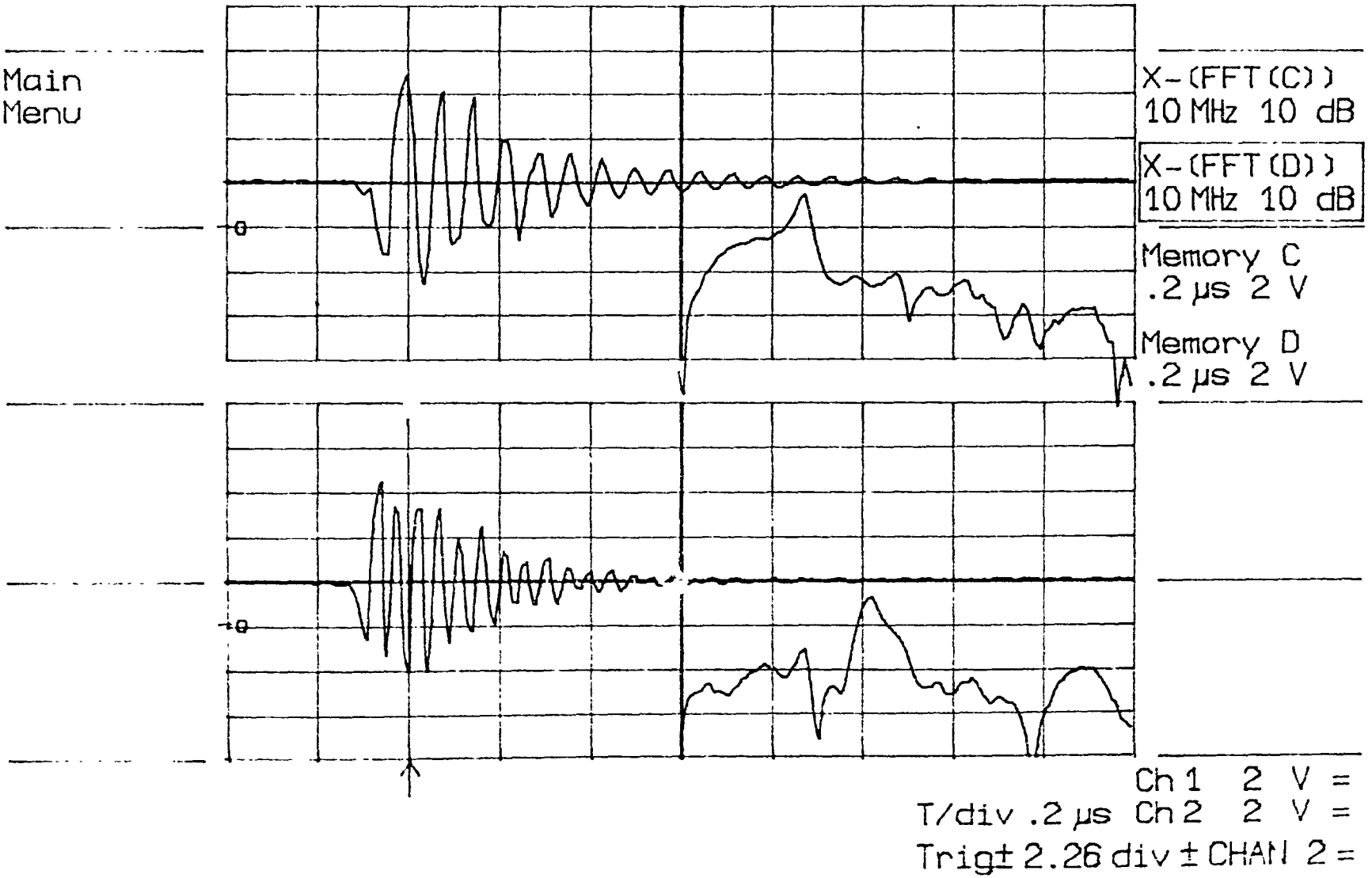

Graph #38
Test Piece: Graphite/Epoxy [±45°]
Impacts: 3
Sensors: Pre-Assembled PVDF 28 μm
Memory C: waveform recieved from sensor #1 at grid location B1
Vpp = 7.92 volts Fpeak= 13.8 MHz, Amplitude= 4.1 dB
Memory D: waveform received from sensor #4 at grid location B4
Vpp = 7.56 volts Fpeak= 20.4 MHz, Amplitude= 5.7 dB

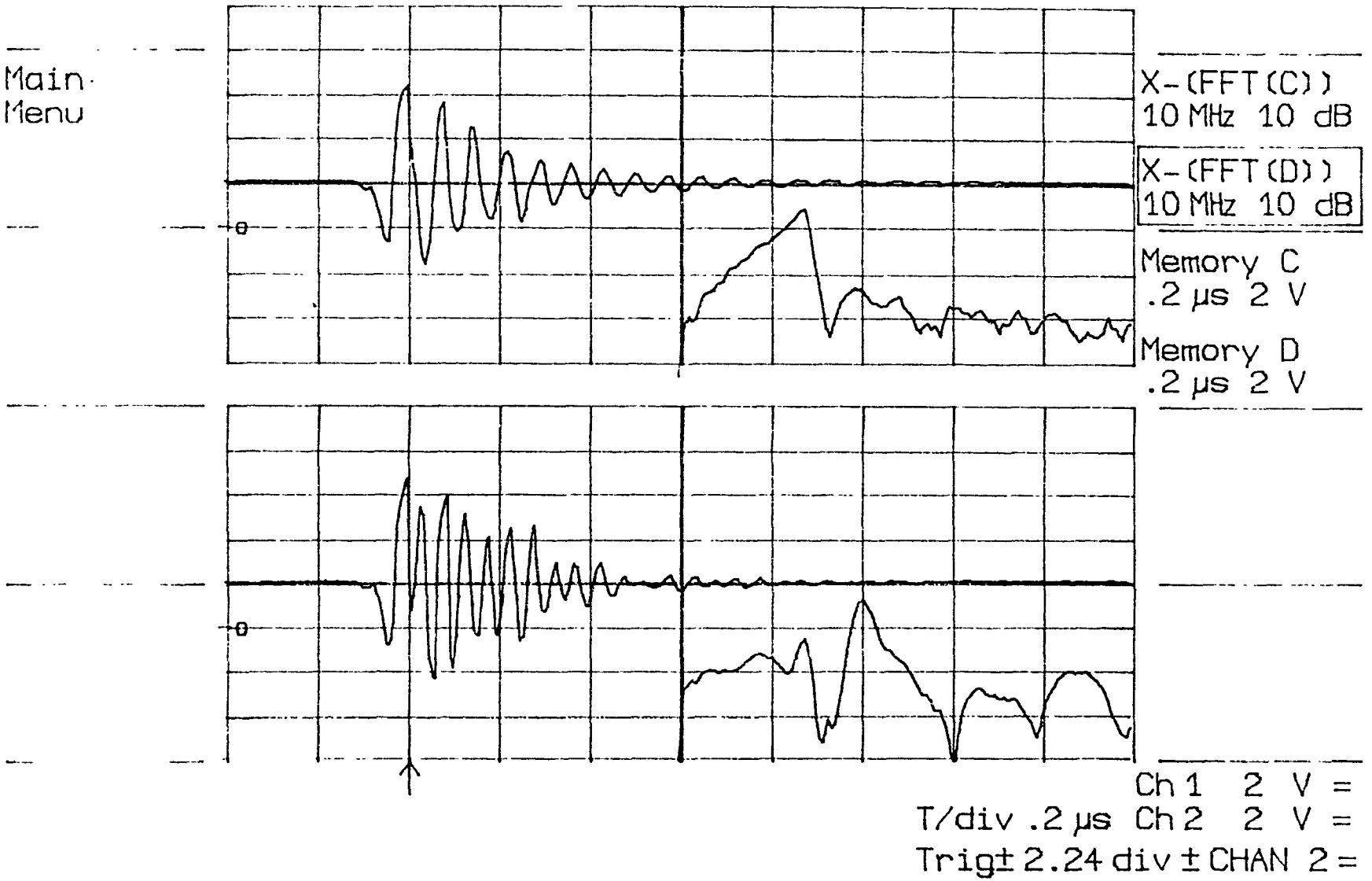

Graph #39
Test Piece: Graphite/Epoxy [±45°]
Impacts: 3
Sensors: Pre-Assembled PVDF 28 µm
Memory C: waveform recieved from sensor #2 at grid location B2
Vpp = 7.34 volts Fpeak= 21.5 MHz, Amplitude= 5.0 dB
Memory D: waveform received from sensor #3 at grid location B3
Vpp = 7.44 volts Fpeak= 20.4 MHz, Amplitude= 5.7 dB

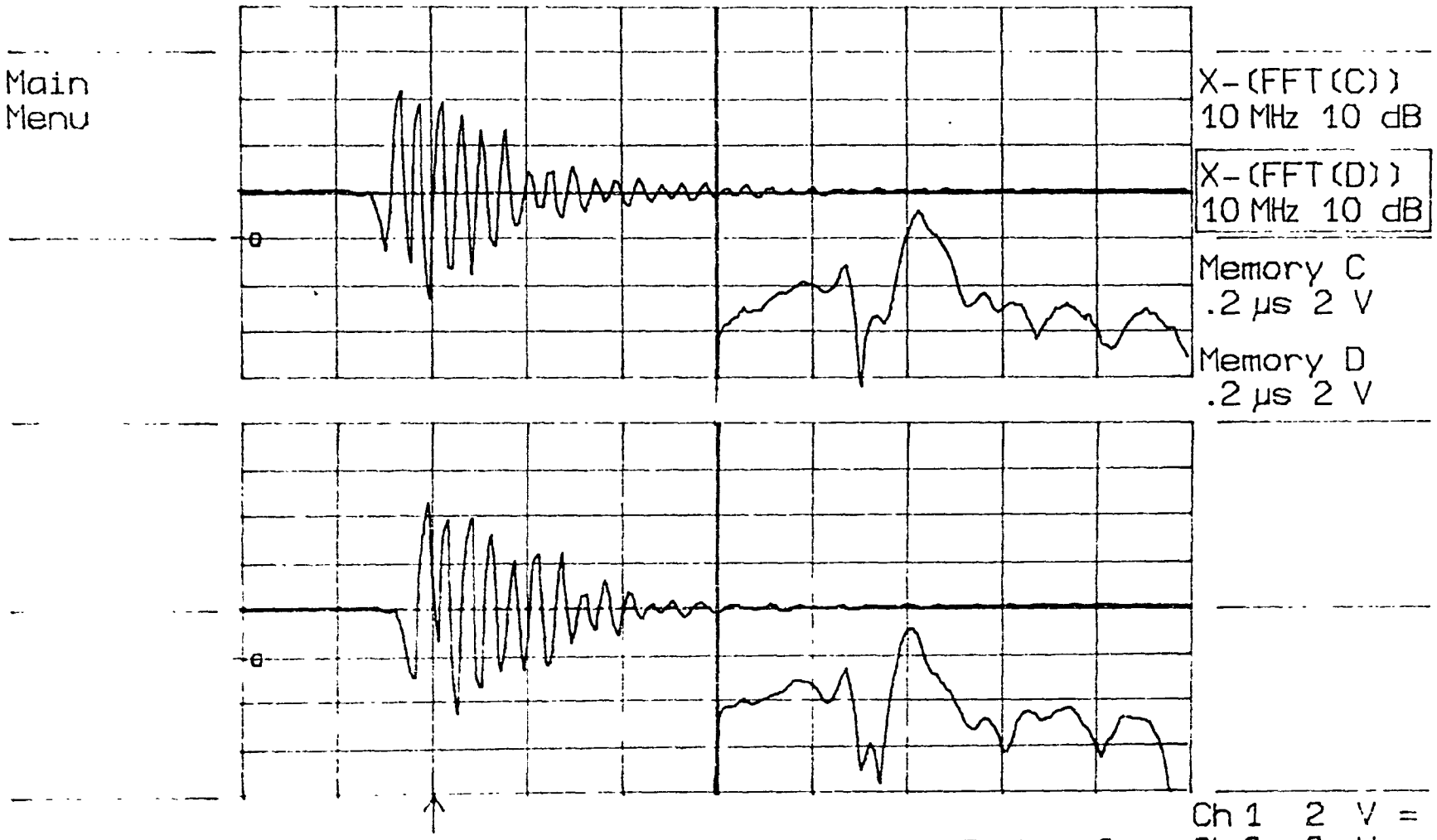

Graph #40
Test Piece: Graphite/Epoxy [±45°]
Impacts: 3
Sensors: Pre-Assembled PVDF 28 µm
Memory C: waveform recieved from sensor #1 at grid location C1
Vpp = 8.58 volts Fpeak= 14.0 MHz, Amplitude= 6.7 dB
Memory D: waveform received from sensor #4 at grid location C4
Vpp = 7.56 volts Fpeak= 14.0 MHz, Amplitude= 5.7 dB

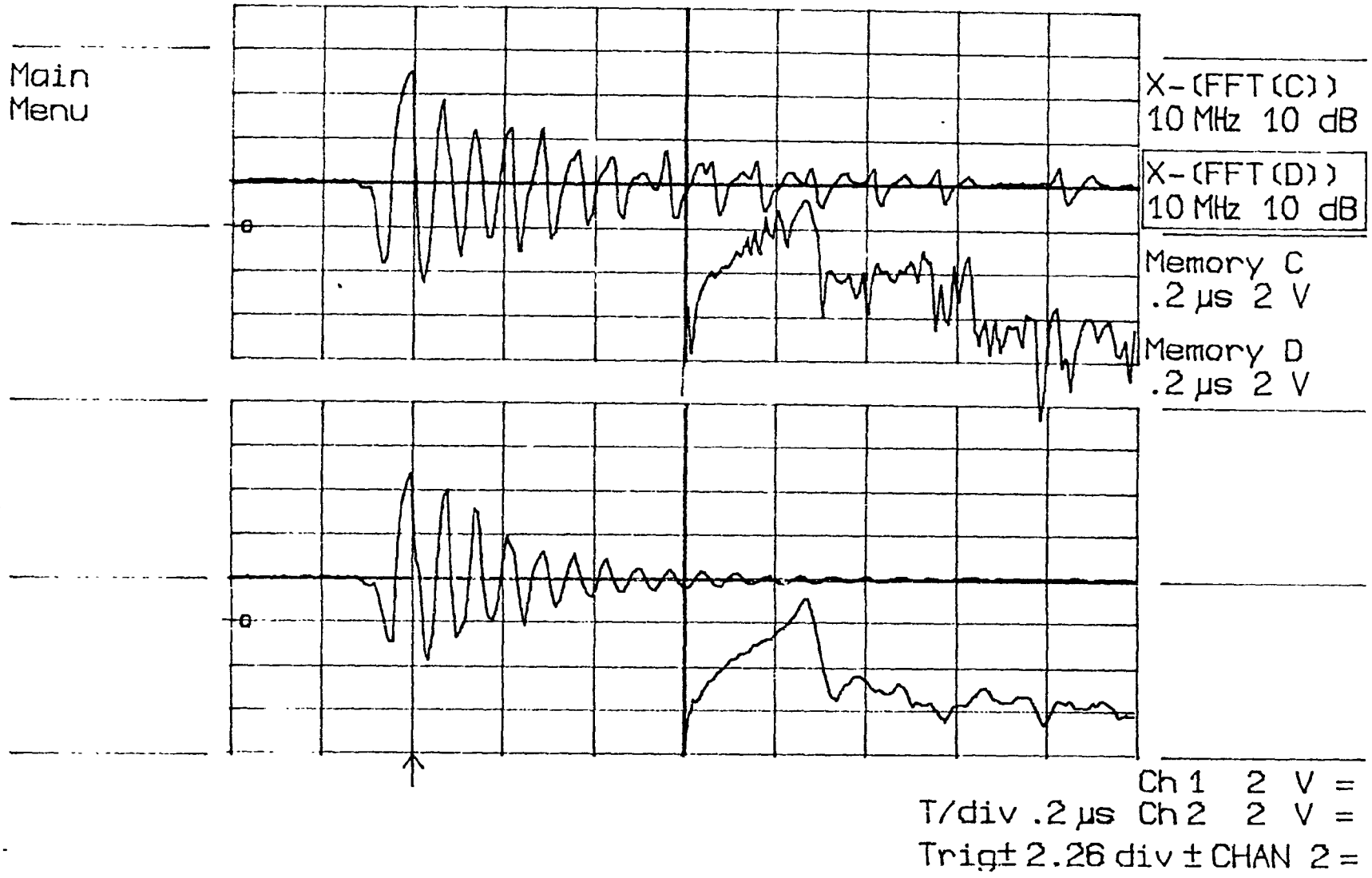

Graph #41
Test Piece: Graphite/Epoxy [0°]
Impacts: 9
Sensors: Pre-Assembled PVDF 28 μm
Memory C: waveform recieved from sensor #1 at grid location A1
Vpp = 7.30 volts Fpeak= 13.5 MHz, Amplitude= -4.0 dB
Memory D: waveform received from sensor #4 at grid location A4
Vpp = 1.84 volts Fpeak= 12.5 MHz, Amplitude= -12.0 dB

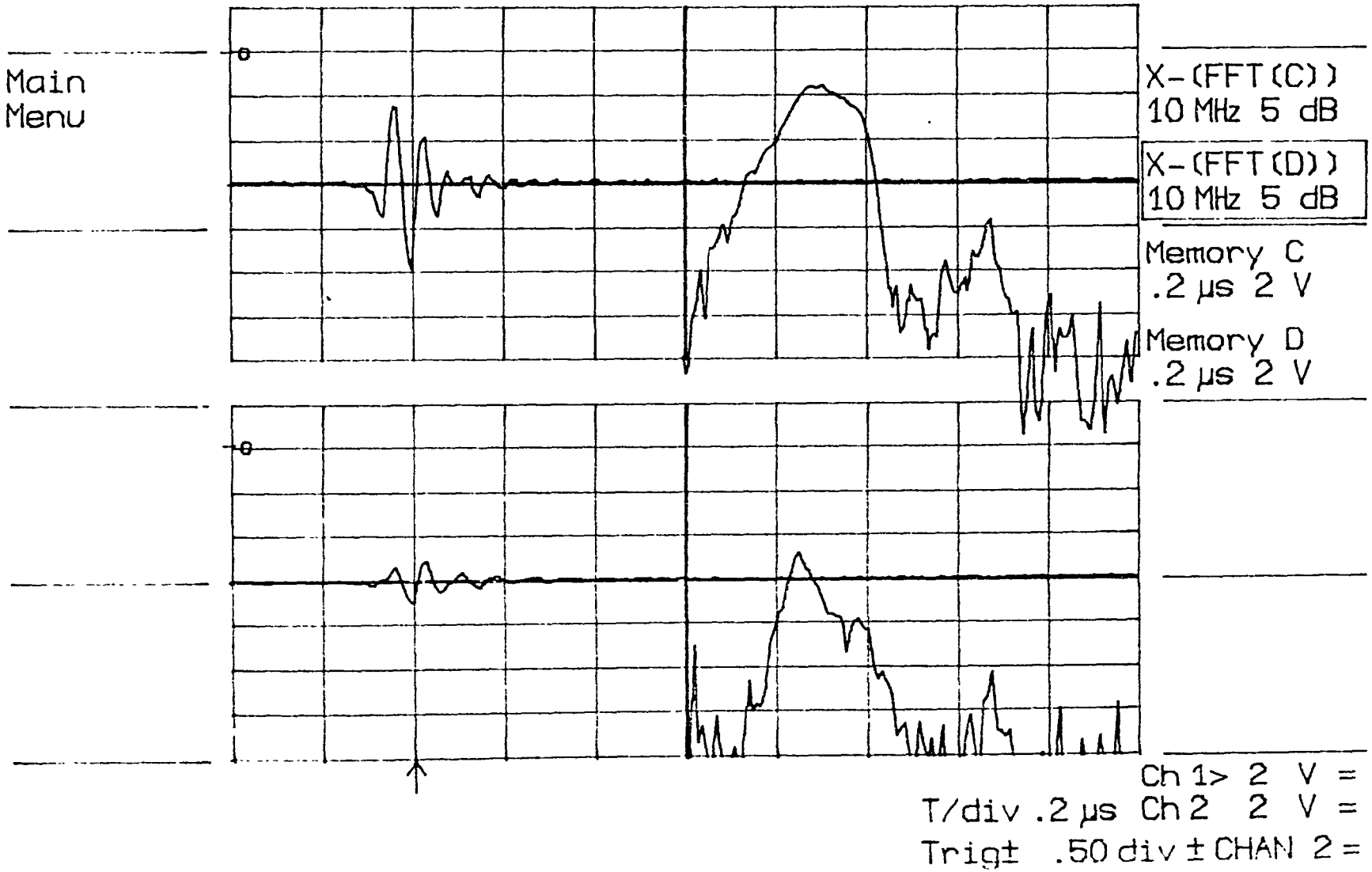

Graph #42
Test Piece: Graphite/Epoxy [0°]
Impacts: 9
Sensors: Pre-Assembled PVDF 28 µm
Memory C: waveform recieved from sensor #1 at grid location B1
Vpp = 7.70 volts Fpeak= 12.5 MHz, Amplitude= -3.5 dB
Memory D: waveform received from sensor #3 at grid location B3
Vpp = 3.00 volts Fpeak= 12.5 MHz, Amplitude= -11.3 dB

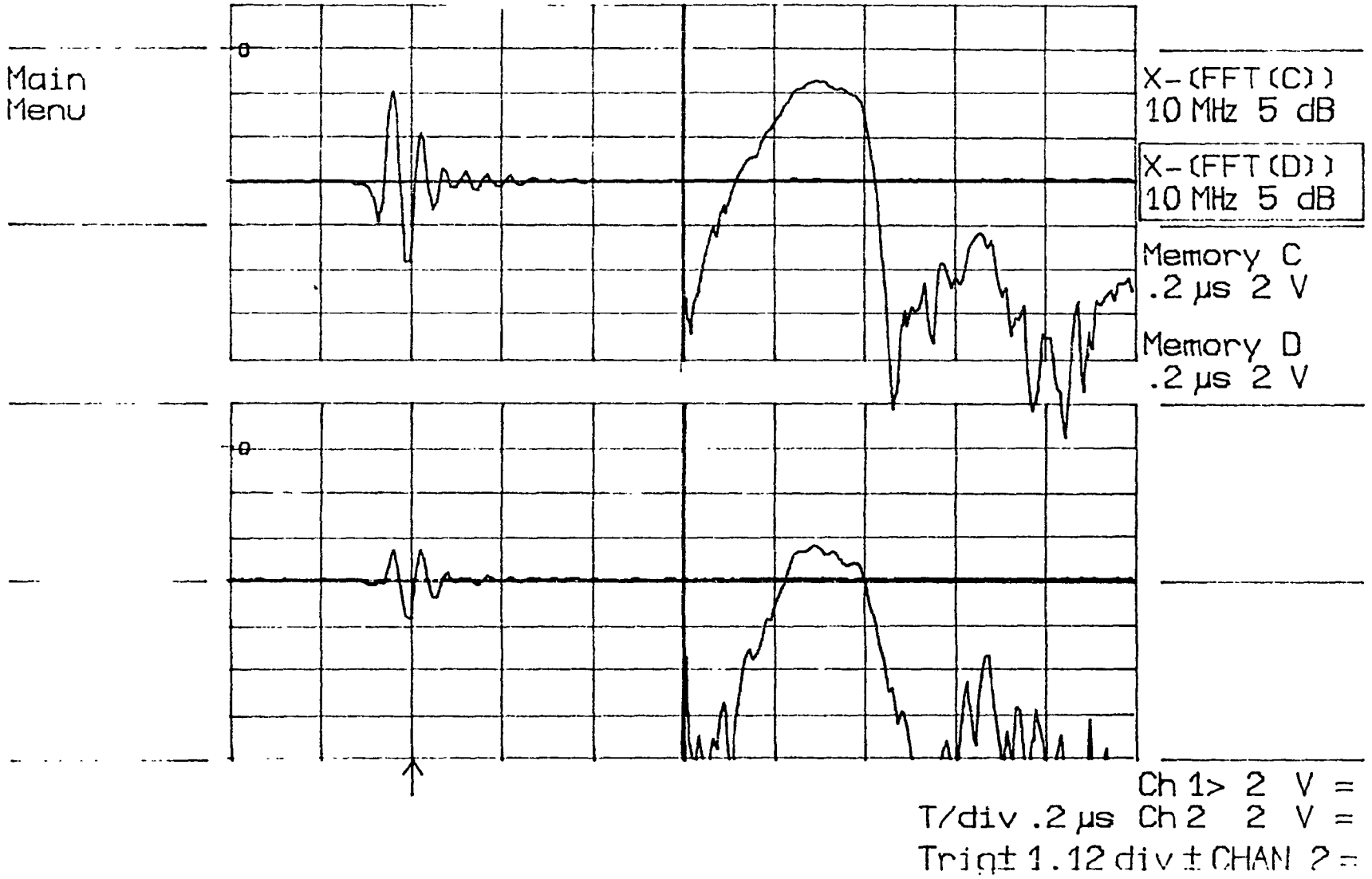

Graph #43
Test Piece: Graphite/Epoxy [0°]
Impacts: 9
Sensors: Pre-Assembled PVDF 28 µm
Memory C: waveform recieved from sensor #2 at grid location B2
Vpp = 2.86 volts Fpeak= 12.0 MHz, Amplitude= -11.2 dB
Memory D: waveform received from sensor #3 at grid location B3
Vpp = 3.00 volts Fpeak= 12.0 MHz, Amplitude= -11.3 dB

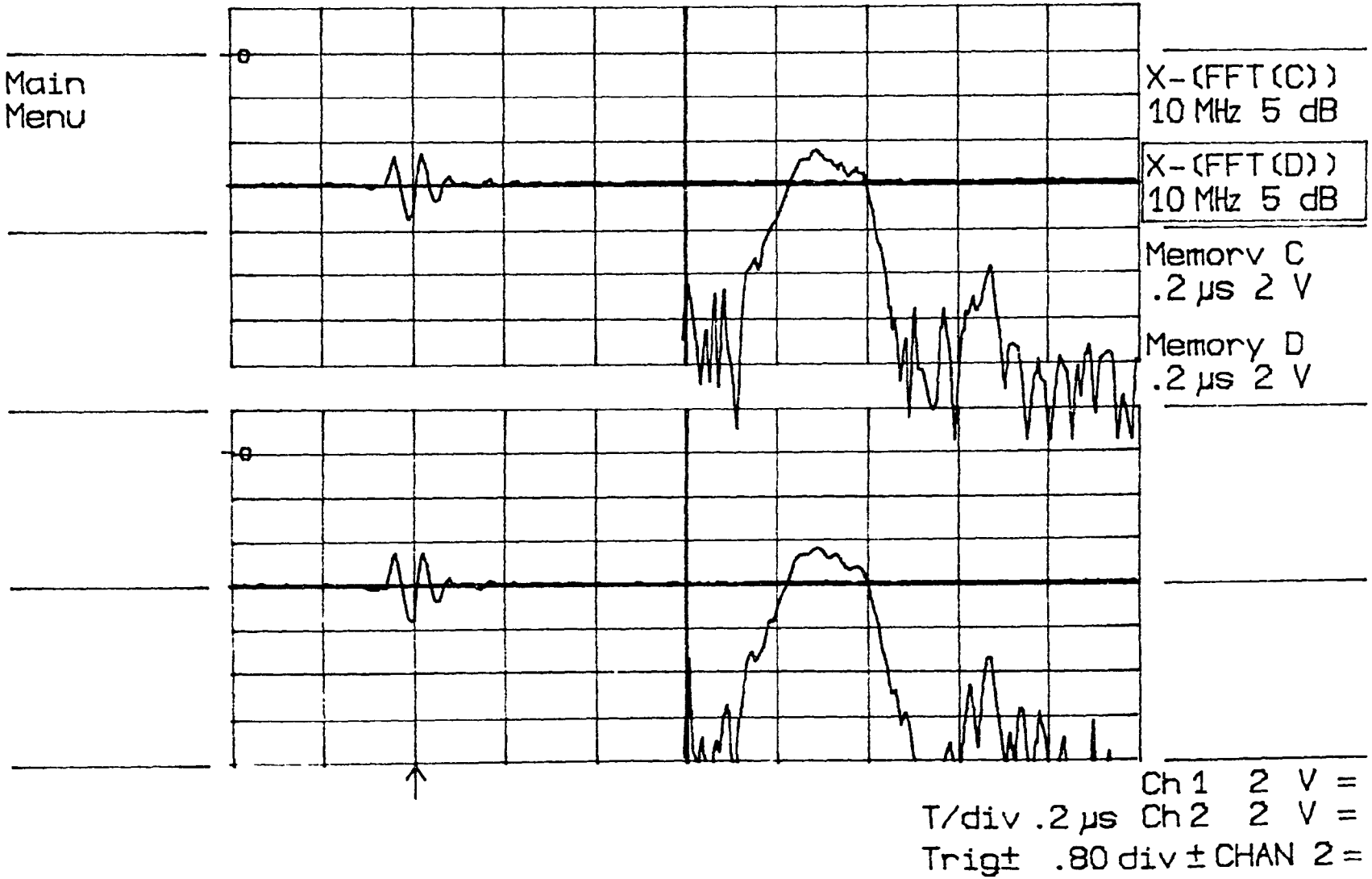

Graph #44
Test Piece: Graphite/Epoxy [0°]
Impacts: 9
Sensors: Pre-Assembled PVDF 28 µm
Memory C: waveform recieved from sensor #1 at grid location C1
Vpp = 2.36 volts Fpeak= 13.6 MHz, Amplitude= -12.7 dB

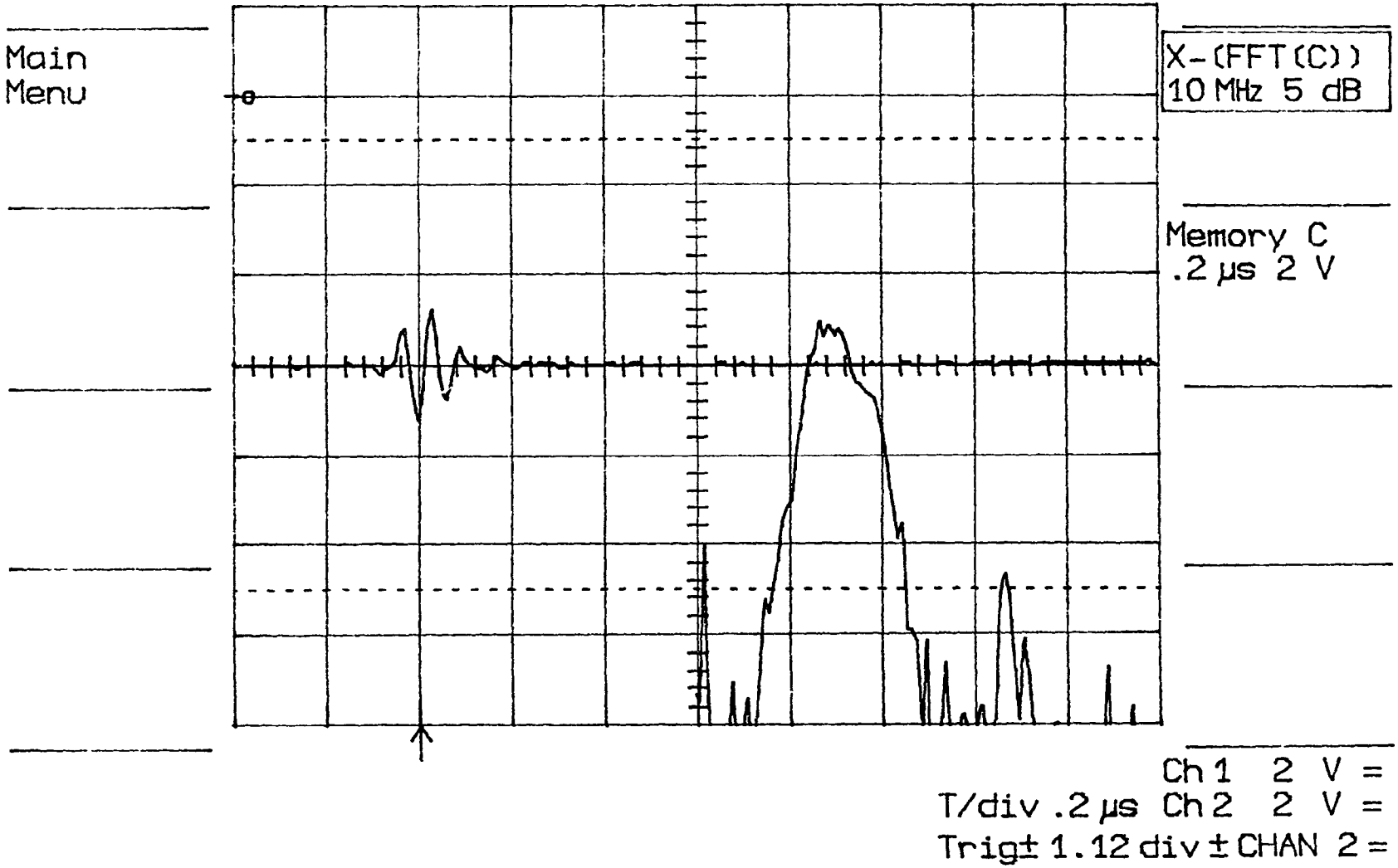

Graph #45
Test Piece: Graphite/Epoxy [±45°]
Impacts: 9
Sensors: Pre-Assembled PVDF 28 μm
Memory C: waveform recieved from sensor #1 at grid location A1
Vpp = 8.30 volts Fpeak= 12.0 MHz, Amplitude= 1.8 dB
Memory D: waveform received from sensor #3 at grid location A4
Vpp = 7.20 volts Fpeak= 12.0 MHz, Amplitude= -1.8 dB

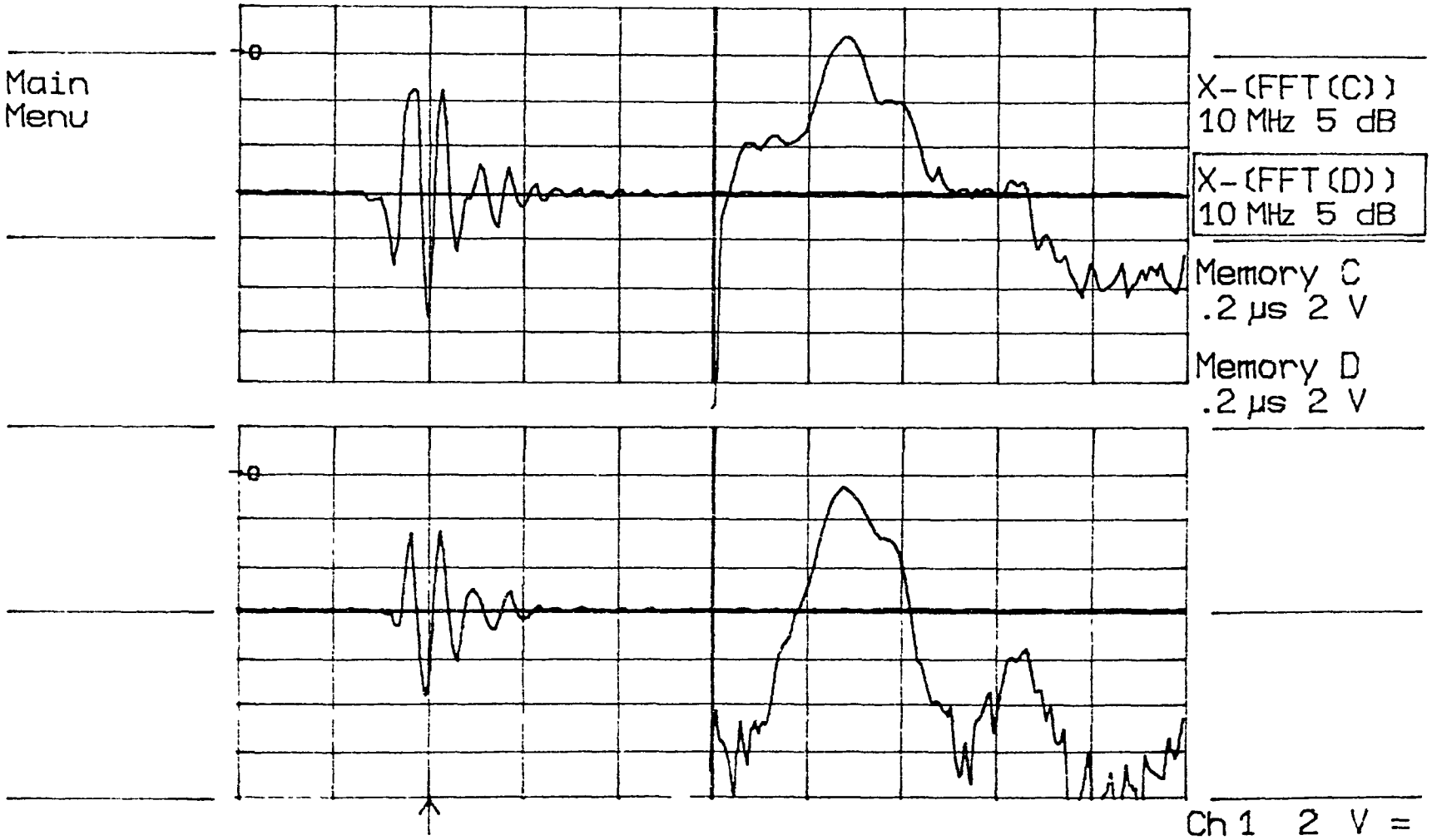

Graph #46
Test Piece: Graphite/Epoxy [±45°]
Impacts: 9
Sensors: Pre-Assembled PVDF 28 µm
Memory C: waveform recieved from sensor #1 at grid location B1
Vpp = 7.14 volts Fpeak= 18.0 MHz, Amplitude= -2.0 dB
Memory D: waveform received from sensor #3 at grid location B3
Vpp = 2.46 volts Fpeak= 14.8 MHz, Amplitude= -12.2 dB

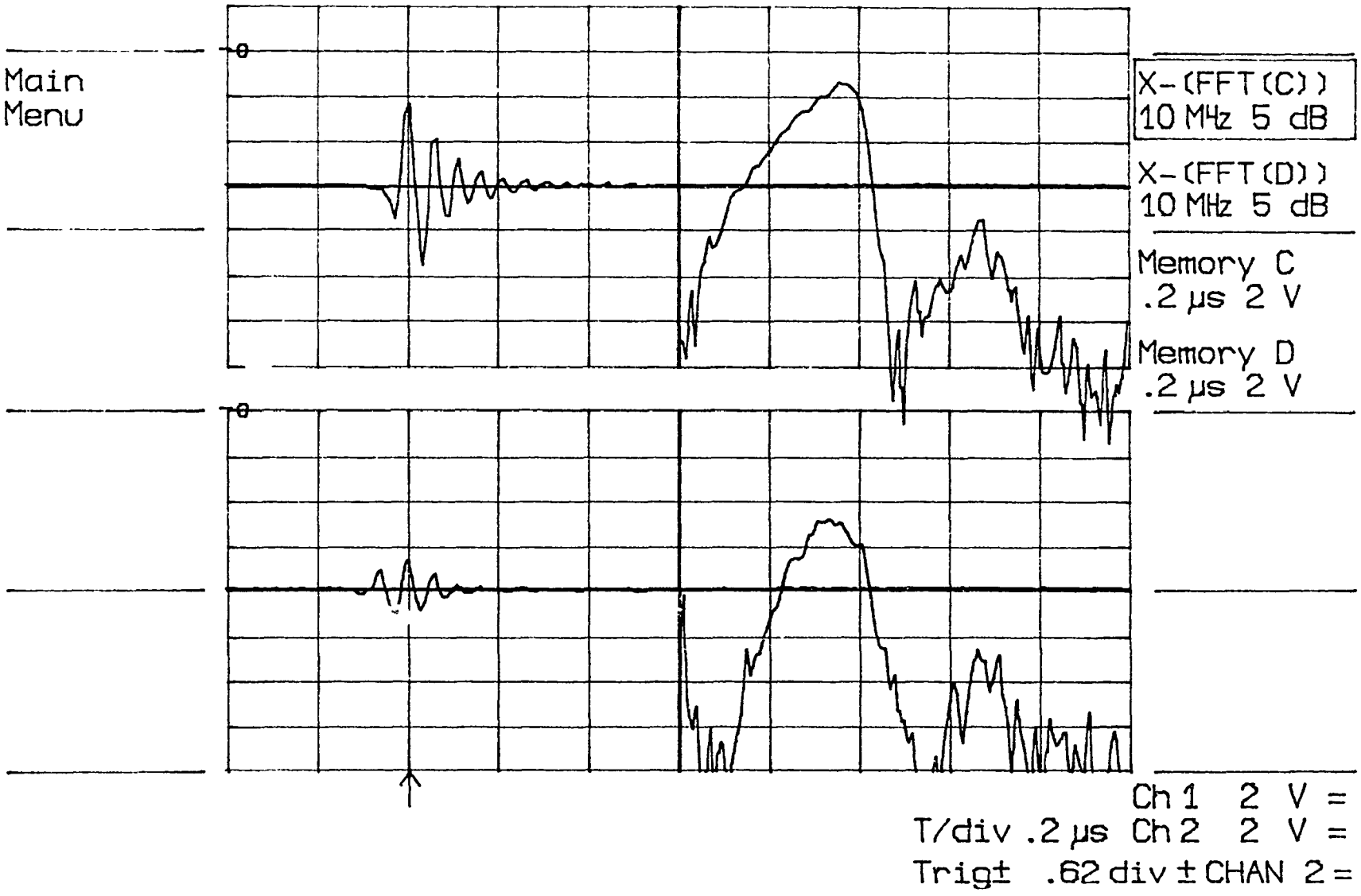

Graph #47
Test Piece: Graphite/Epoxy [±45°]
Impacts: 9
Sensors: Pre-Assembled PVDF 28 µm
Memory C: waveform recieved from sensor #2 at grid location B2
Vpp = 2.50 volts Fpeak= 14.8 MHz, Amplitude= -13.0 dB
Memory D: waveform received from sensor #3 at grid location B3
Vpp = 2.46 volts Fpeak= 14.8 MHz, Amplitude= -12.5 dB

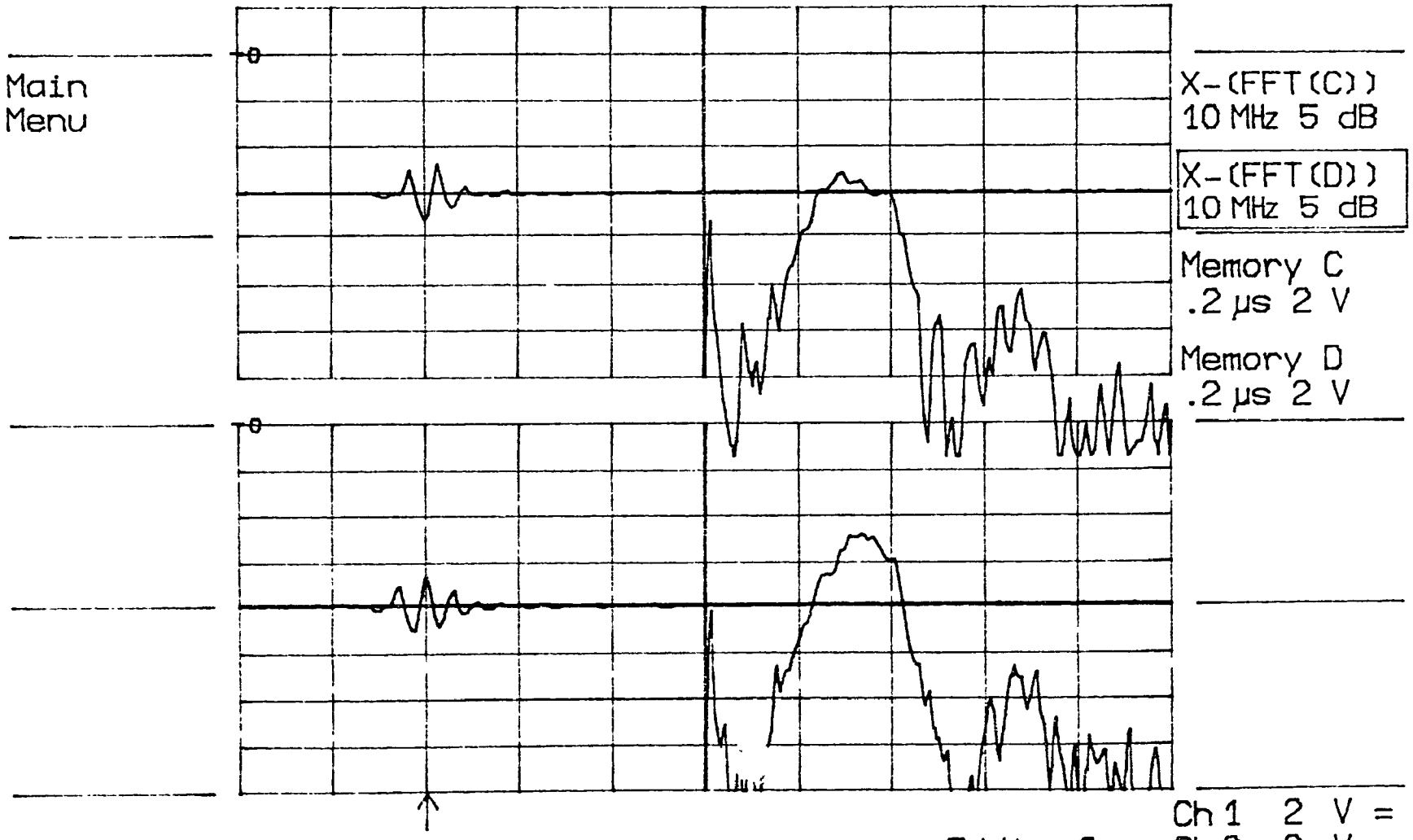

Graph #48
Test Piece: Graphite/Epoxy [±45°]
Impacts: 9
Sensors: Pre-Assembled PVDF 28 μm
Memory C: waveform recieved from sensor #1 at grid location C1
Vpp = 8.08 volts Fpeak= 15.6 MHz, Amplitude= -2.1 dB
Memory D: waveform received from sensor #4 at grid location C4
Vpp = 7.85 volts Fpeak= 15.6 MHz, Amplitude= -1.0 dB

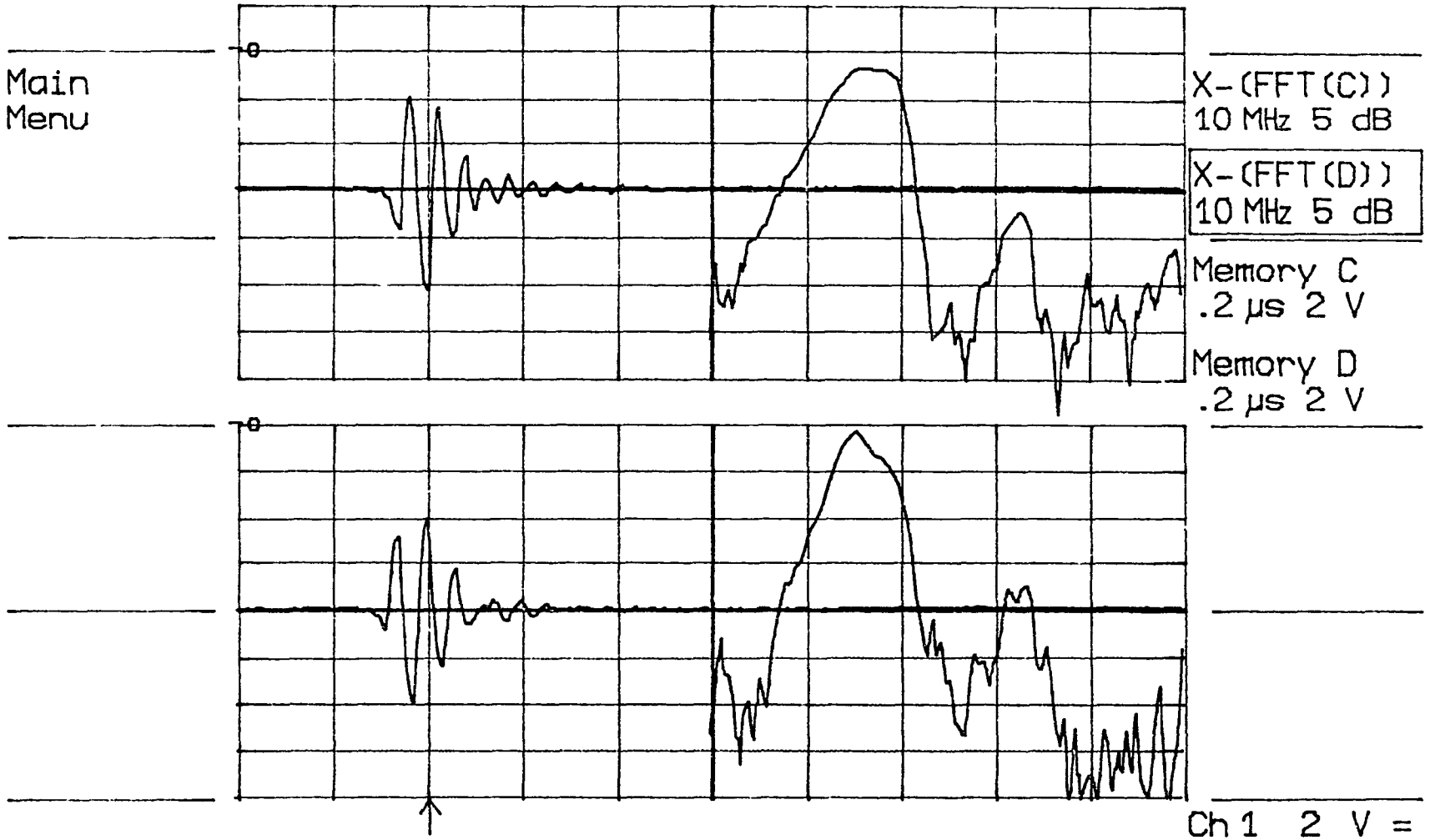

Appendix 4: Ultrasonic C-Scan Images of Graphite/Epoxy Plates Before and After Impact

C-SCAN PLOT COLLECTED ON: Sat Apr 11 13:24:14 1992

PART I.D. Number:	Plate #1, 16 ply	PART TYPE:	IM7/977-2, 0 Deg.
Operator:	C. Smith	Transducer Type:	Wideband
Transducer S/N:		Transducer Mfr:	
Nominal Cntr Freq:	5 MHz	Attenuation:	
Energy:		Damping:	MP-270 Pul., 50 dB
Gain:	MR-106 Rec., 17 dB	HP Filter:	Highpass 5 MHz
Comment1:	2 Marker, 0 Insert	Comment 2:	Sampling = 50
Comment3:	0 Impacts	Comment 4:	Increment = 0.08 in
External Trigger:	FG 504 40 MHz Fn. Generator, Lin Sweep 0.1ms duration.		
MP-270 Pulser:	maximum pulse amplitude, low pulse width.		

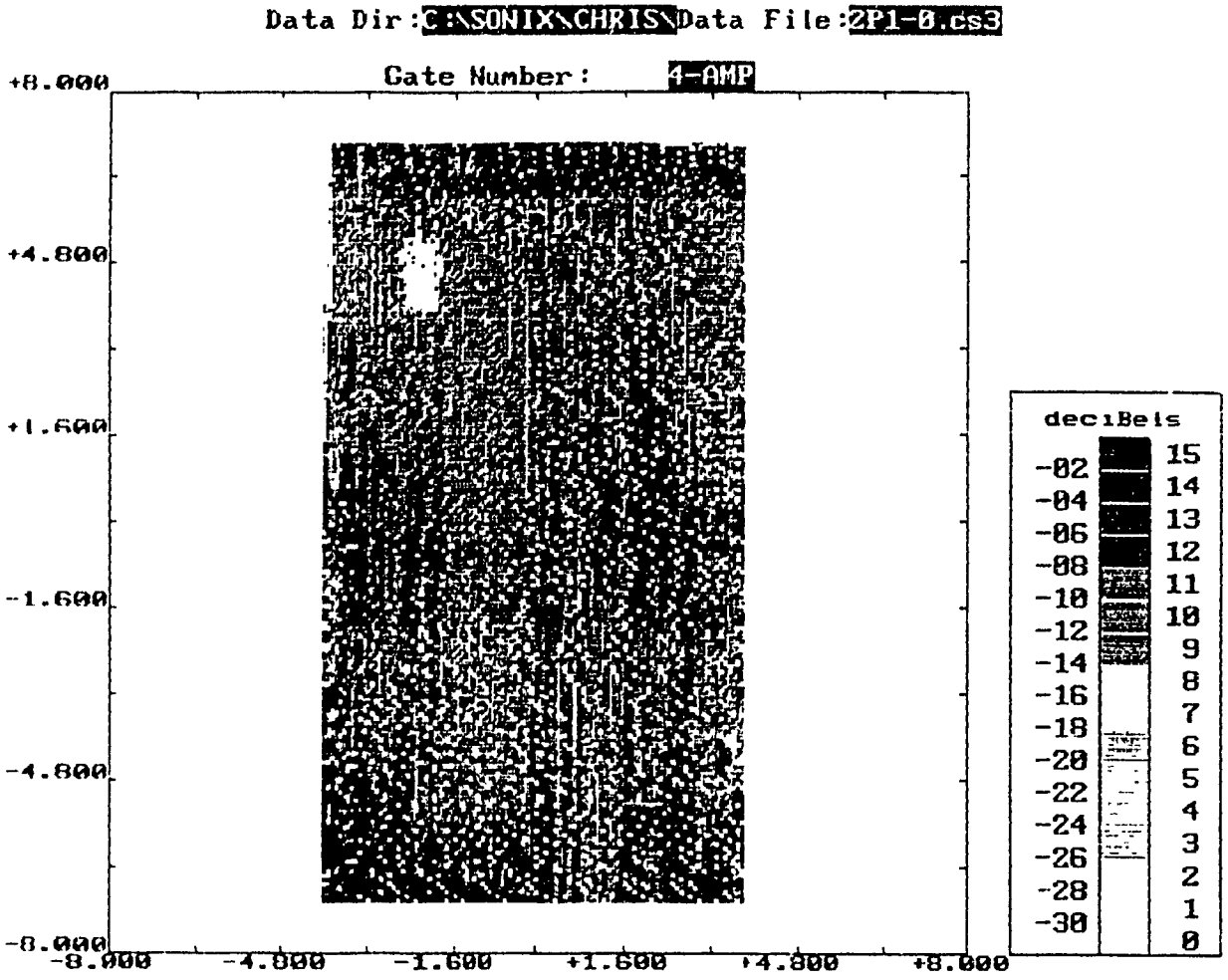

C-SCAN PLOT COLLECTED ON: Mon May 11 7:39:274 1992

PART I.D. Number:	Plate #1, 16 ply	PART TYPE:	IM7/977-2, 0 Deg.
Operator:	C. Smith	Transducer Type:	Wideband
Transducer S/N:		Transducer Mfr:	
Nominal Cntr Freq:	5 MHz	Attenuation:	
Energy:		Damping:	MP-270 Pul., 50 dB
Gain:	MR-106 Rec., 18 dB	HP Filter:	Highpass 5 MHz
Comment1:	2 Marker, 0 Insert	Comment 2:	Sampling = 50
Comment3:	9 Impacts, 27 Joule	Comment 4:	Increment = 0.08 in
External Trigger:	MP-270 Pulser, maximum pulse rate, 25% amplitude, low pulse width.		

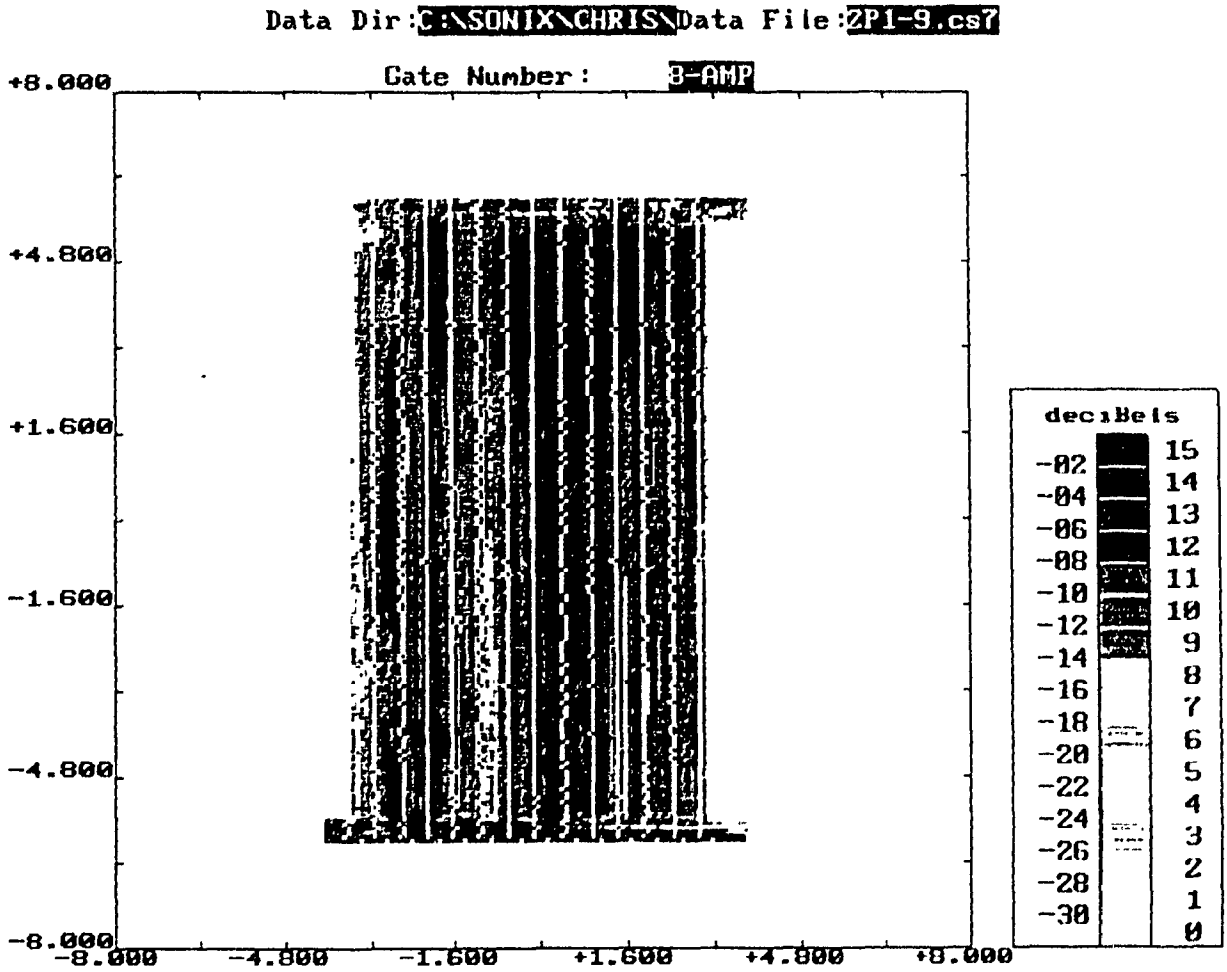

C-SCAN PLOT COLLECTED ON: Sat Apr 11 14:04:15 1992

PART I.D. Number:	Plate #3, 16 ply	PART TYPE:	IM7/977-2, ±45 Deg.
Operator:	C. Smith	Transducer Type:	Wideband
Transducer S/N:		Transducer Mfr:	
Nominal Cntr Freq:	5 MHz	Attenuation:	
Energy:		Damping:	MP-270 Pul., 50 dB
Gain:	MR-106 Rec., 20 dB	HP Filter:	Highpass 5 MHz
Comment1:	2 Marker, 2 Insert	Comment 2:	Sampling = 50
Comment3:	0 Impacts	Comment 4:	Increment = 0.08 in
External Trigger:	FG 504 40 MHz Fn. Generator, Lin Sweep 0.1ms duration. MP-270 Pulser, MR-106 Receiver, one marker on top surface, one marker on bottom surface.		

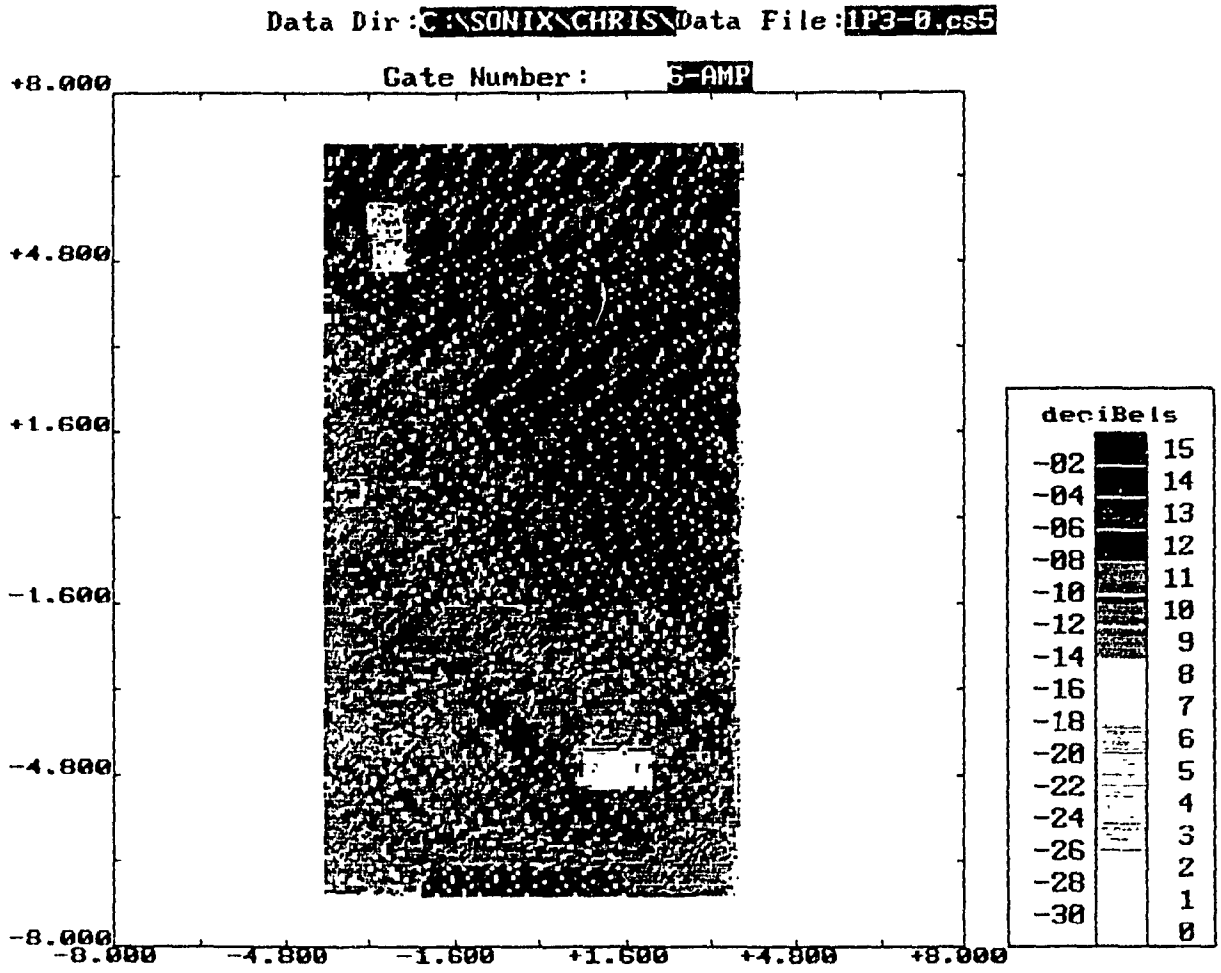

C-SCAN PLOT COLLECTED ON: Tue June 23 14:04:29 1992

PART I.D. Number:	Plate #3, 16 ply	PART TYPE:	IM7/977-2, ±45 Deg.
Operator:	C. Smith	Transducer Type:	Wideband
Transducer S/N:		Transducer Mfr:	
Nominal Cntr Freq:	5 MHz	Attenuation:	
Energy:		Damping:	MP-270 Pul., 50 dB
Gain:	MR-106 Rec., 19 dB	HP Filter:	Highpass 5 MHz
Comment1:	2 Marker, 2 Insert	Comment 2:	Sampling = 50
Comment3:	9 Impacts x 27 Joule	Comment 4:	Impacts bottom surf.
External Trigger:	MP-270 Pulser, MR-106 Receiver, one marker on bottom surface.		

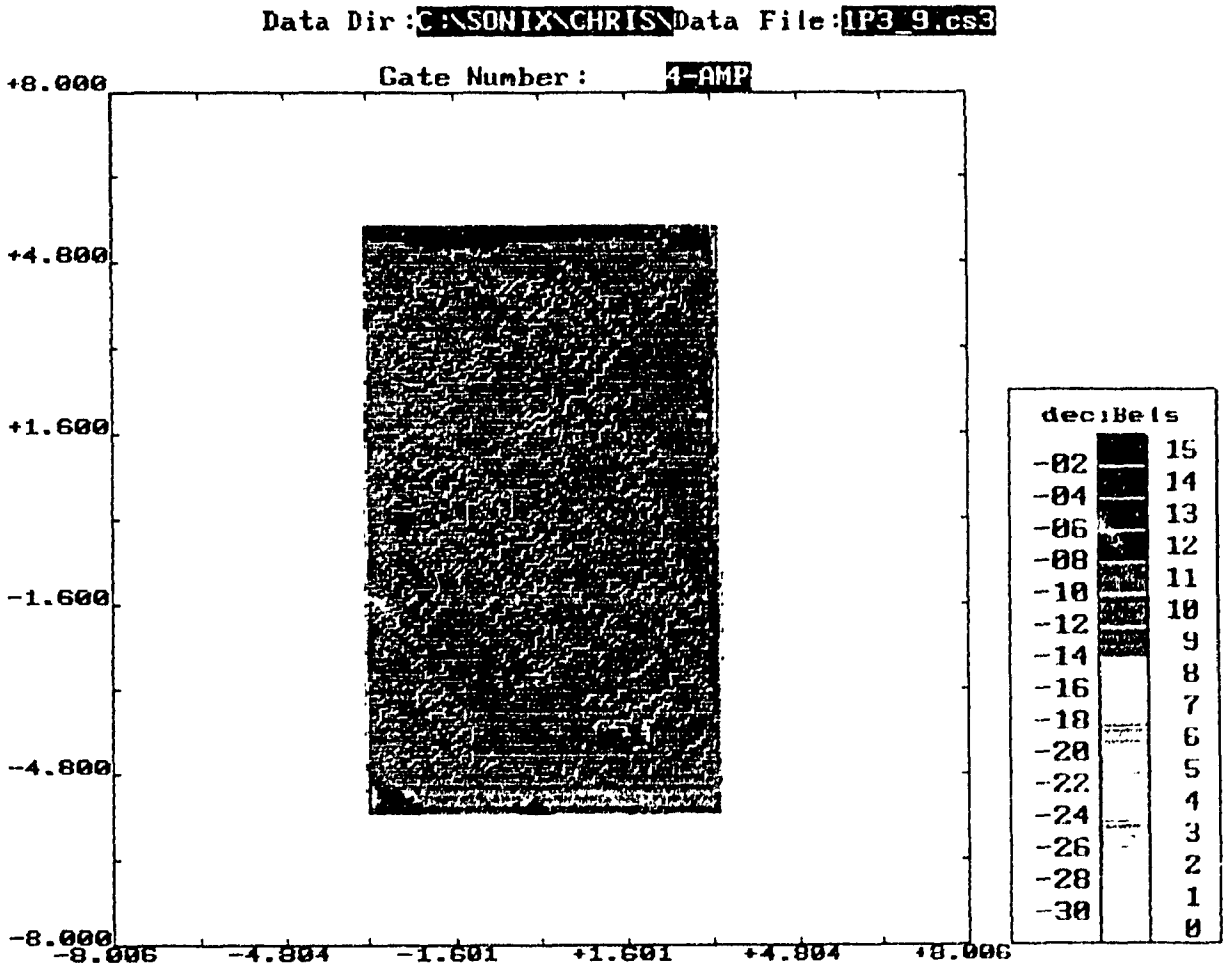

Appendix 5: Compression Test Load/Strain Curves

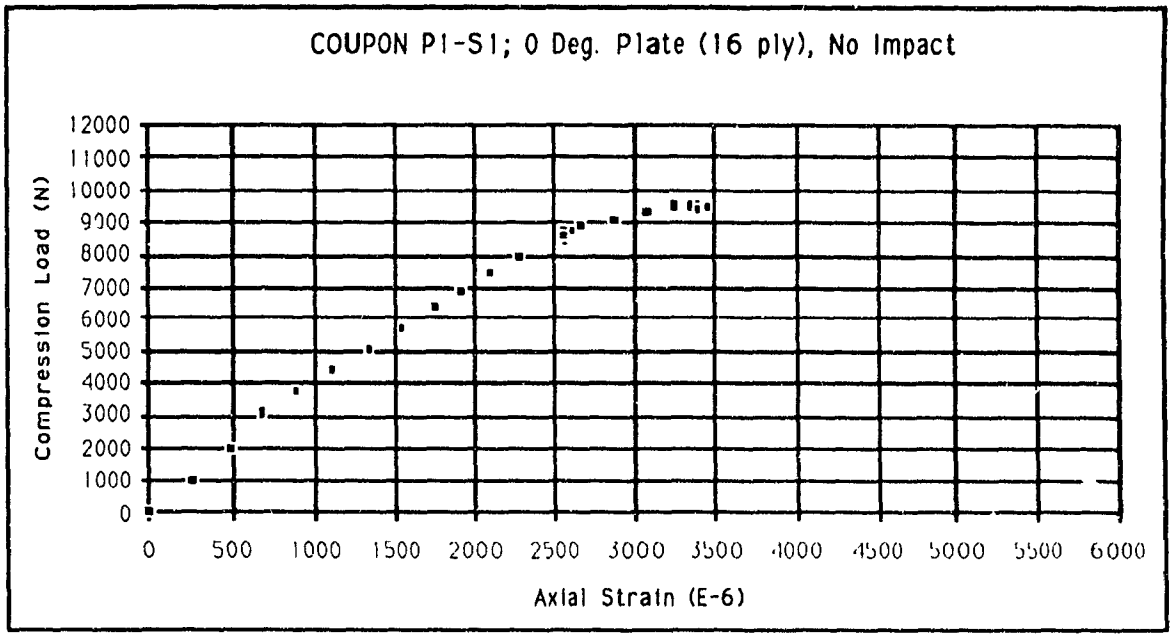

$w = 11.98$ mm

$t = 2.01$ mm

$$E = \frac{\Delta P / (w \bullet t)}{\Delta \varepsilon_a}$$

$\Delta P = (4750\text{-}1000)$ N

$\Delta \varepsilon_a = (1250\text{-}250) \times 10^{-6}$

$E = 155.7$ GPa

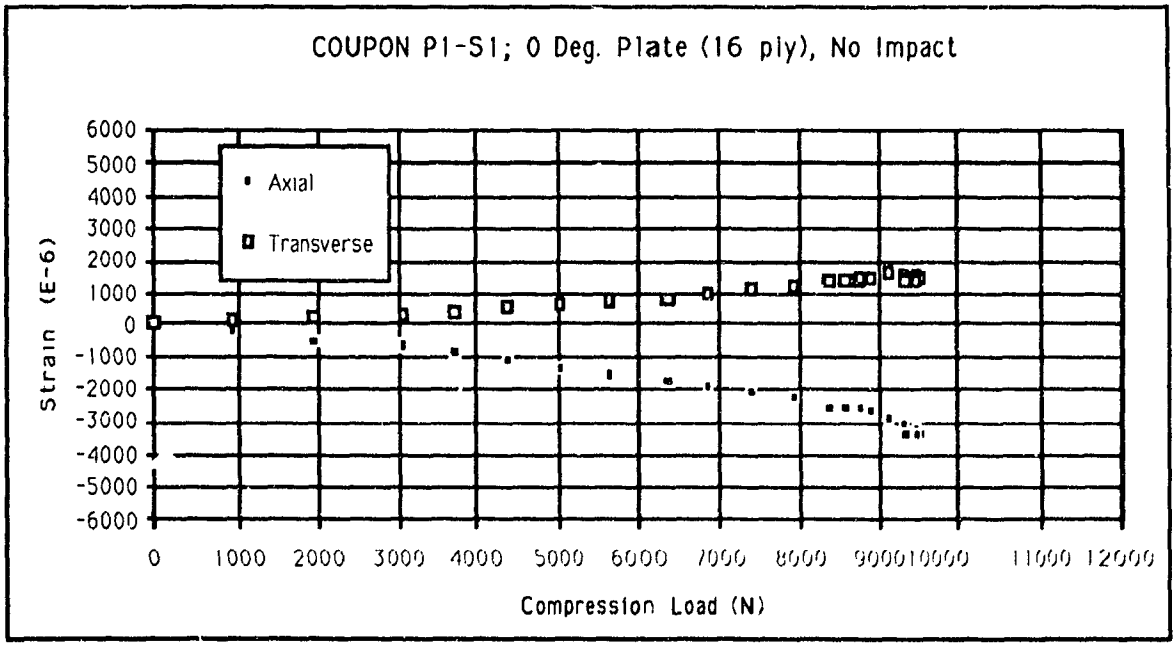

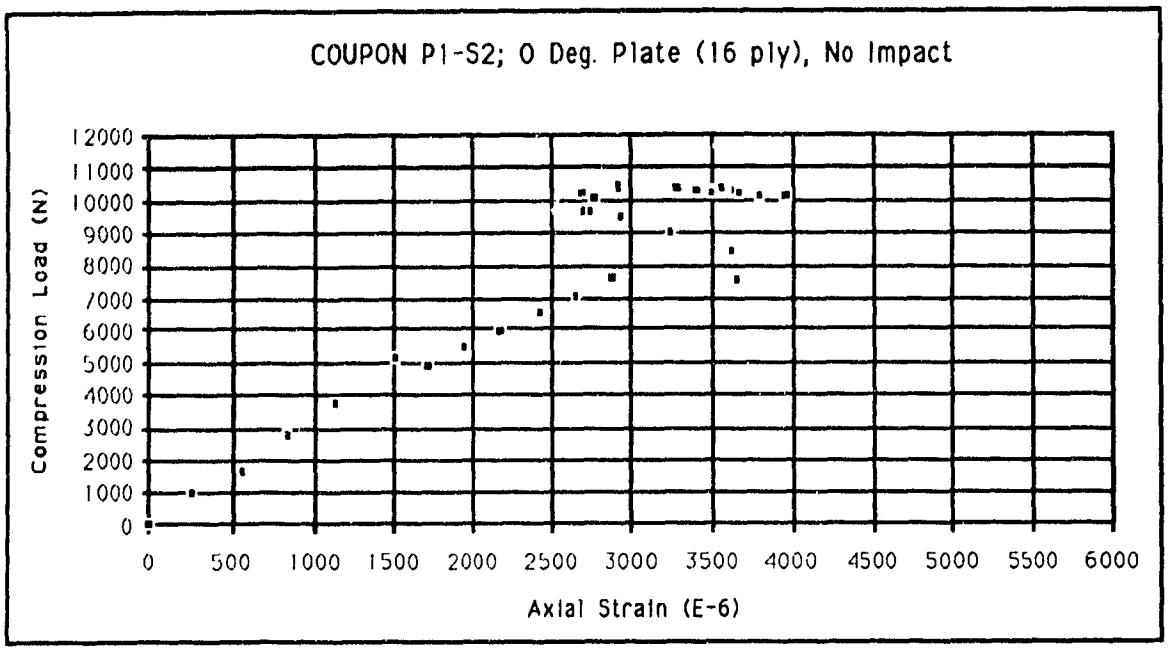

w = 10.82 mm
t = 2.01 mm

$$E = \frac{\Delta P / (w \bullet t)}{\Delta \varepsilon_a}$$

$\Delta P = (4250 - 900)$ N

$\Delta \varepsilon_a = (1250\text{-}250) \times 10^{-6}$

E = 154.1 GPa

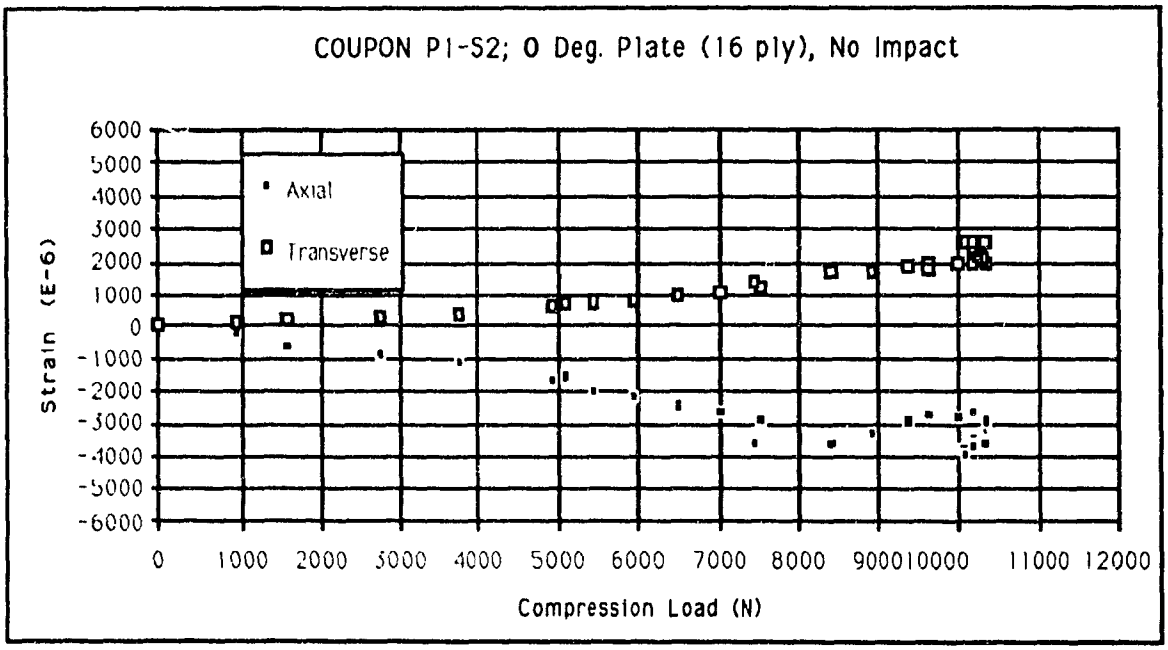

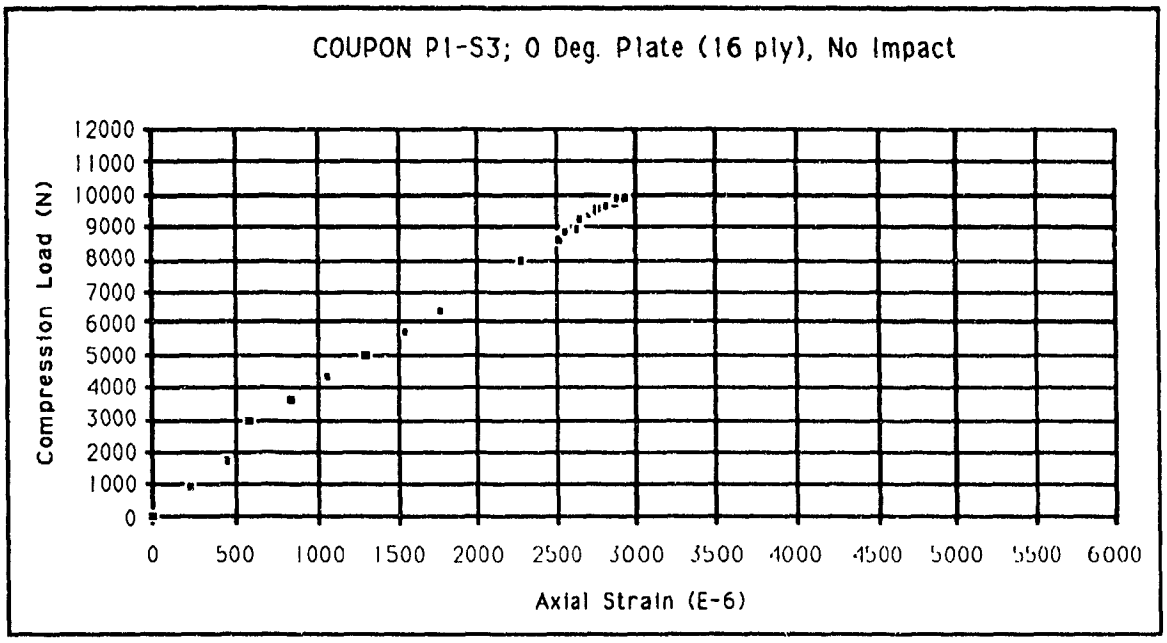

w = 12.86 mm
t = 2.01 mm

$$E = \frac{\Delta P / (w \bullet t)}{\Delta \varepsilon_a}$$

$\Delta P = (5075 - 1000)$ N

$\Delta \varepsilon_a = (1250-250) \times 10^{-6}$

$E = 157.6$ GPa

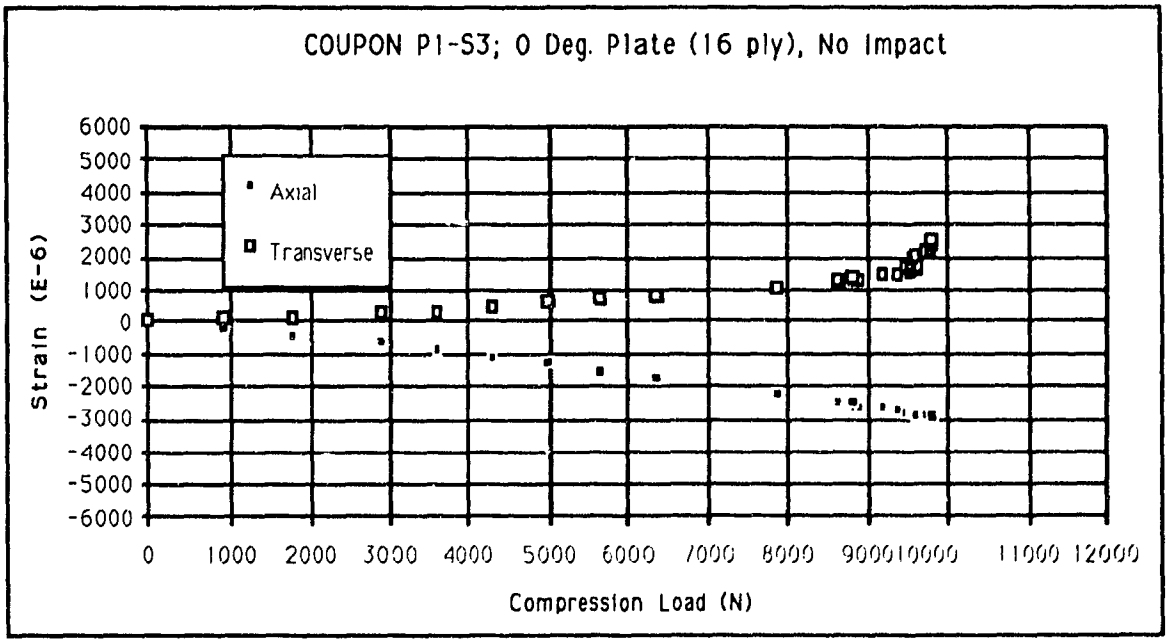

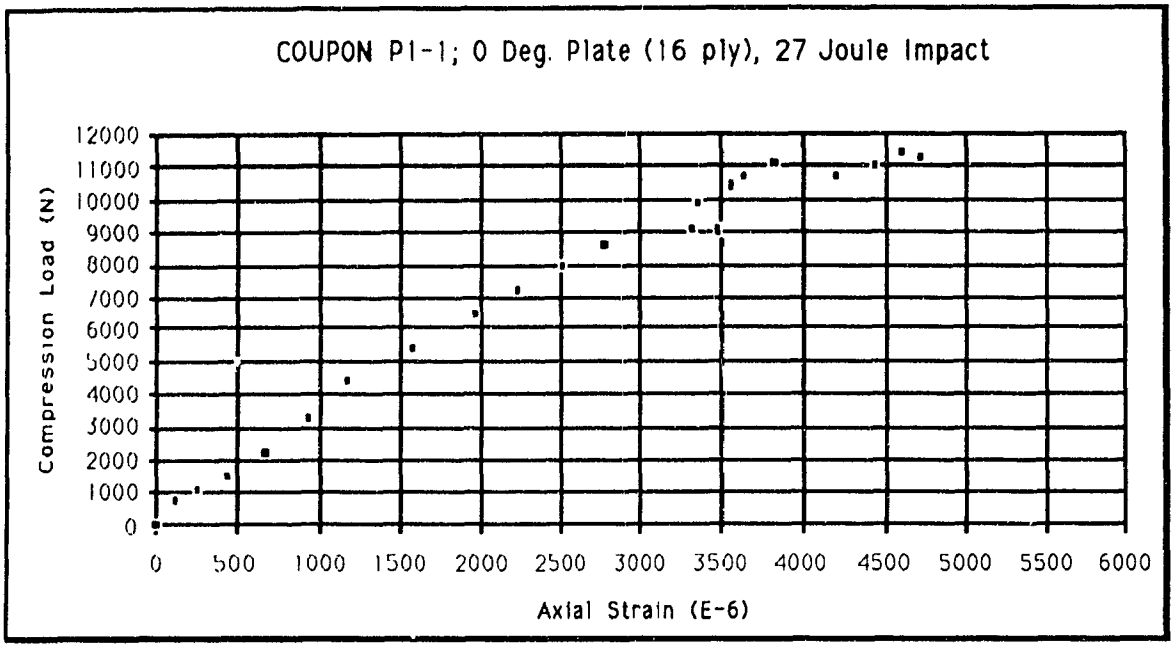

w = 12.74 mm

t = 2.01 mm

$$E = \frac{\Delta P / (w \bullet t)}{\Delta \varepsilon_a}$$

$\Delta P = (4250 - 950)$ N

$\Delta \varepsilon_a = (1250\text{-}250) \times 10^{-6}$

$E = 128.9$ GPa

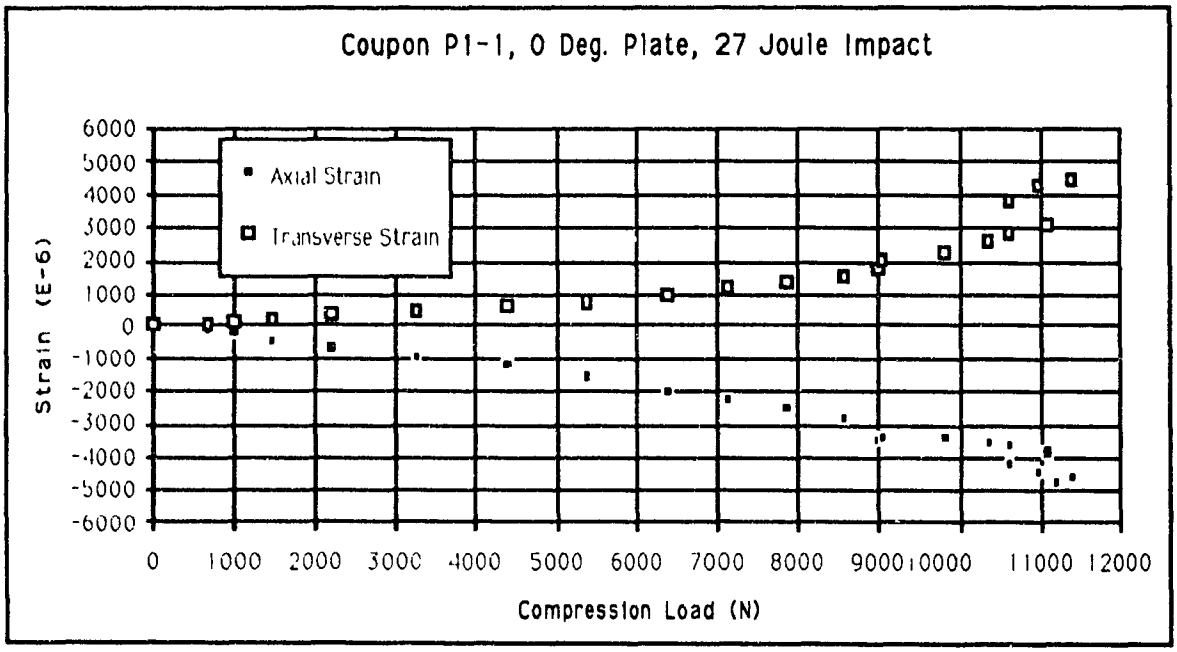

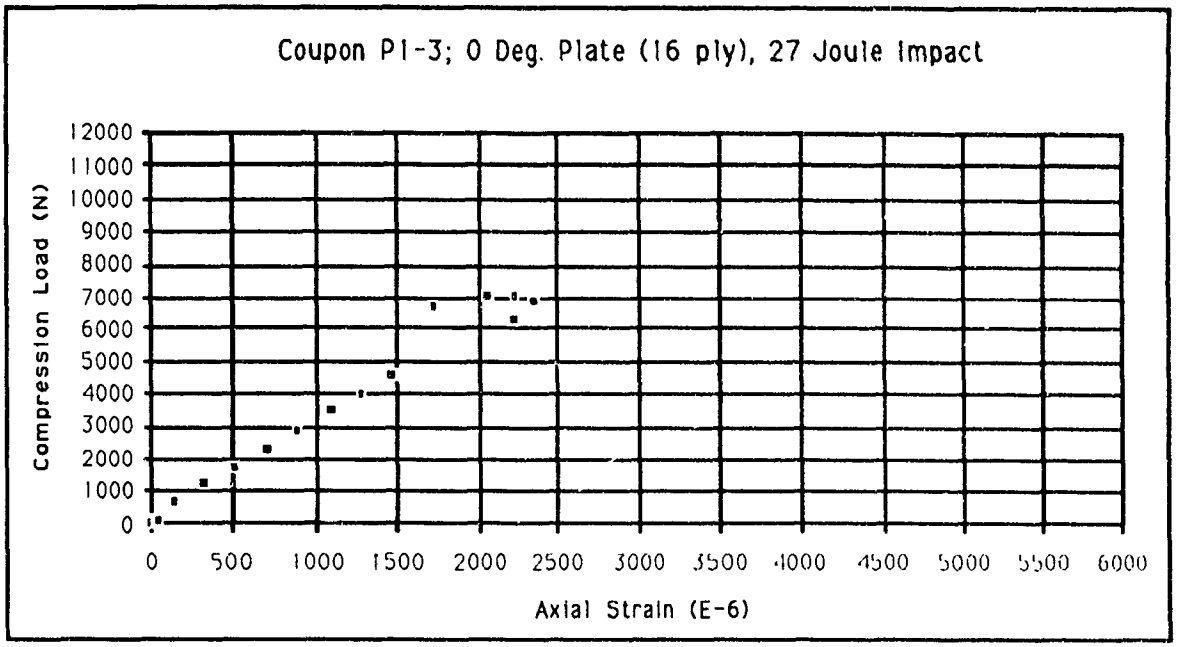

$w = 11.78$ mm

$t = 2.01$ mm

$$E = \frac{\Delta P / (w \bullet t)}{\Delta \varepsilon_a}$$

$\Delta P = (4000\text{-}1000)$ N

$\Delta \varepsilon_a = (1250\text{-}250) \times 10^{-6}$

$E = 126.7$ GPa

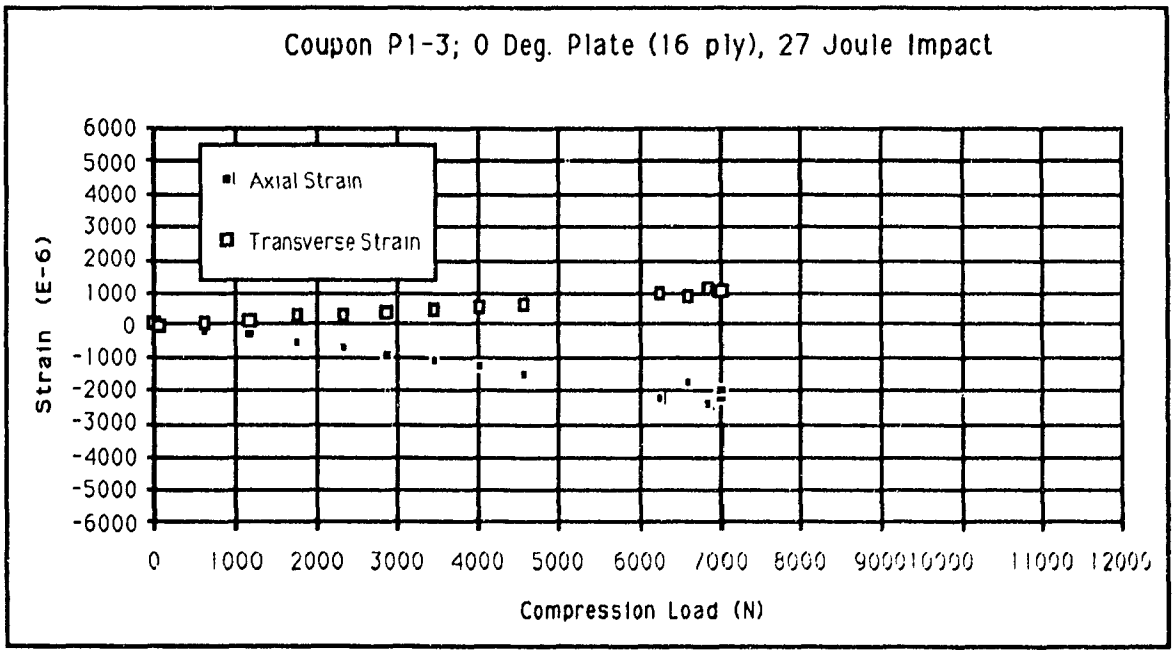

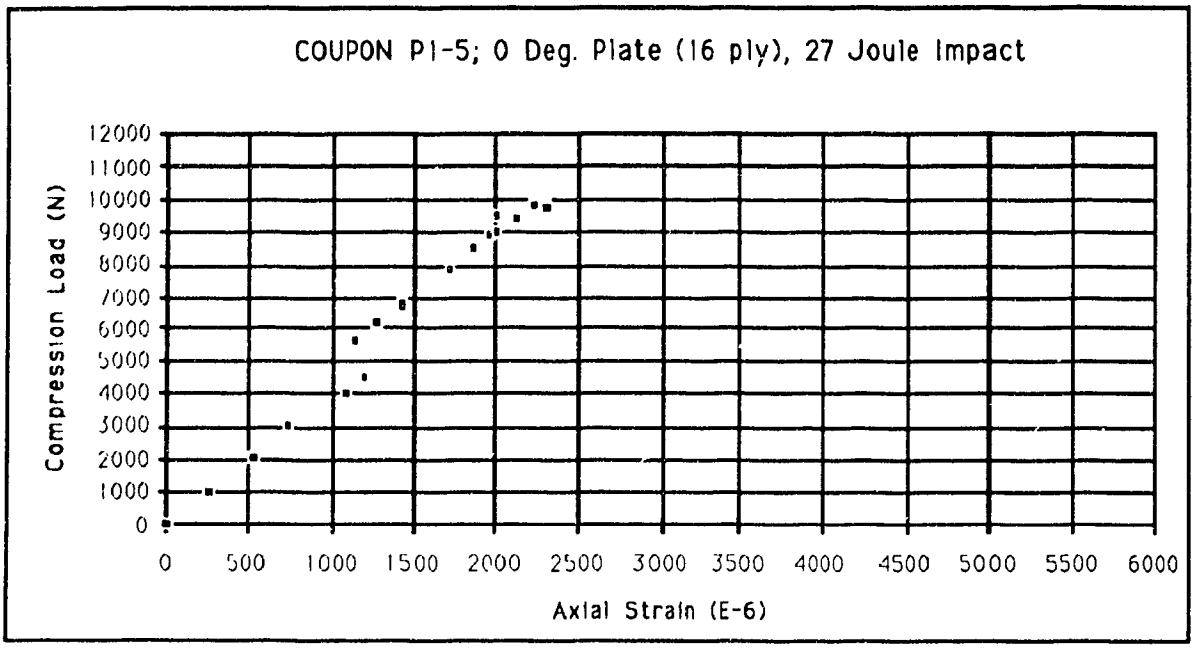

w = 13.89 mm
t = 2.01 mm

$$E = \frac{\Delta P / (w \bullet t)}{\Delta \varepsilon_a}$$

$\Delta P = (4700 - 1000)$ N

$\Delta \varepsilon_a = (1250\text{-}250) \times 10^{-6}$

$E = 132.5$ GPa

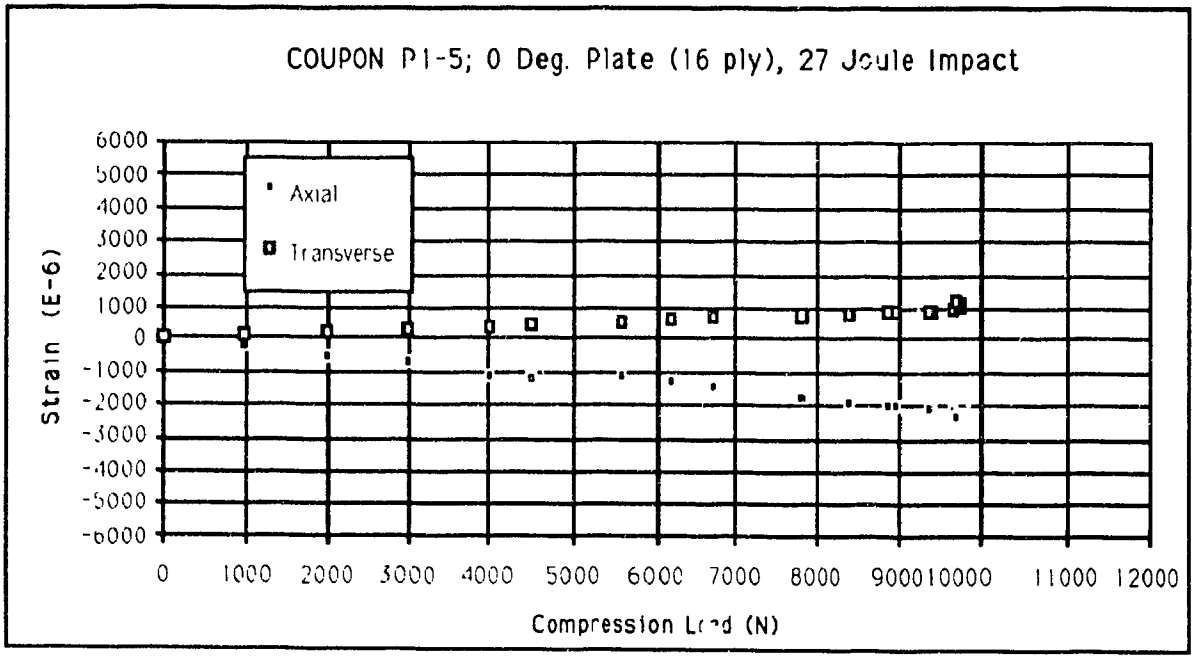

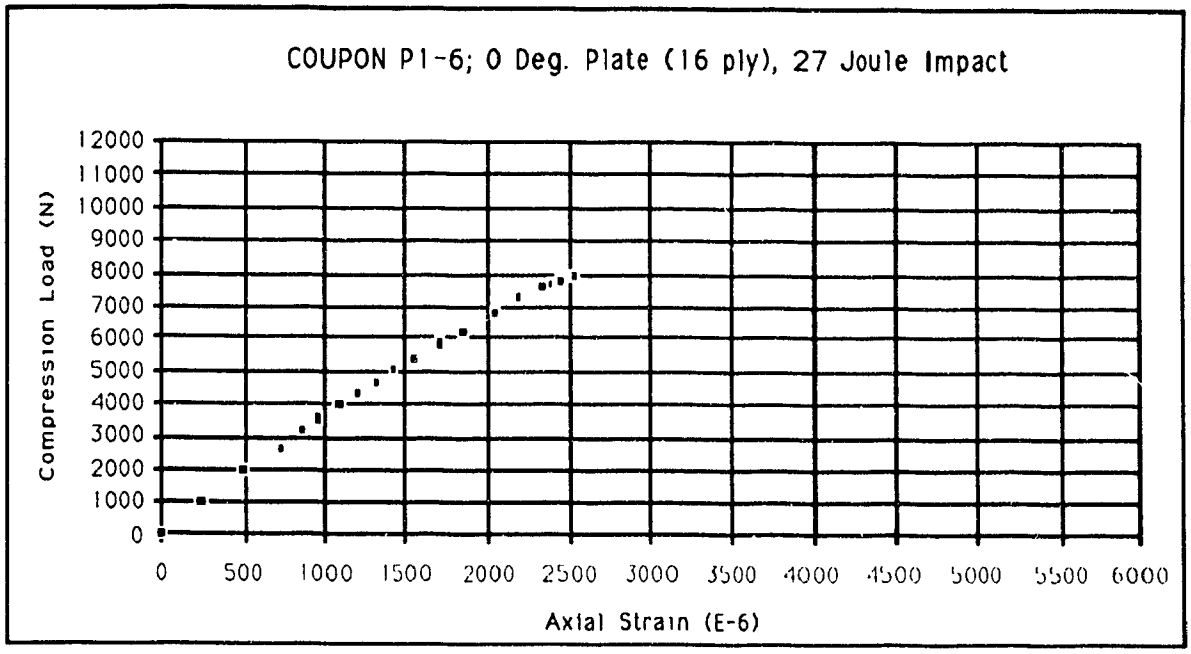

w = 13.05 mm
t = 2.01 mm

$$E = \frac{\Delta P / (w \bullet t)}{\Delta \varepsilon_a}$$

$\Delta P = (4400 - 1000)$ N

$\Delta \varepsilon_a = (1250\text{-}250) \times 10^{-6}$

$E = 129.6$ GPa

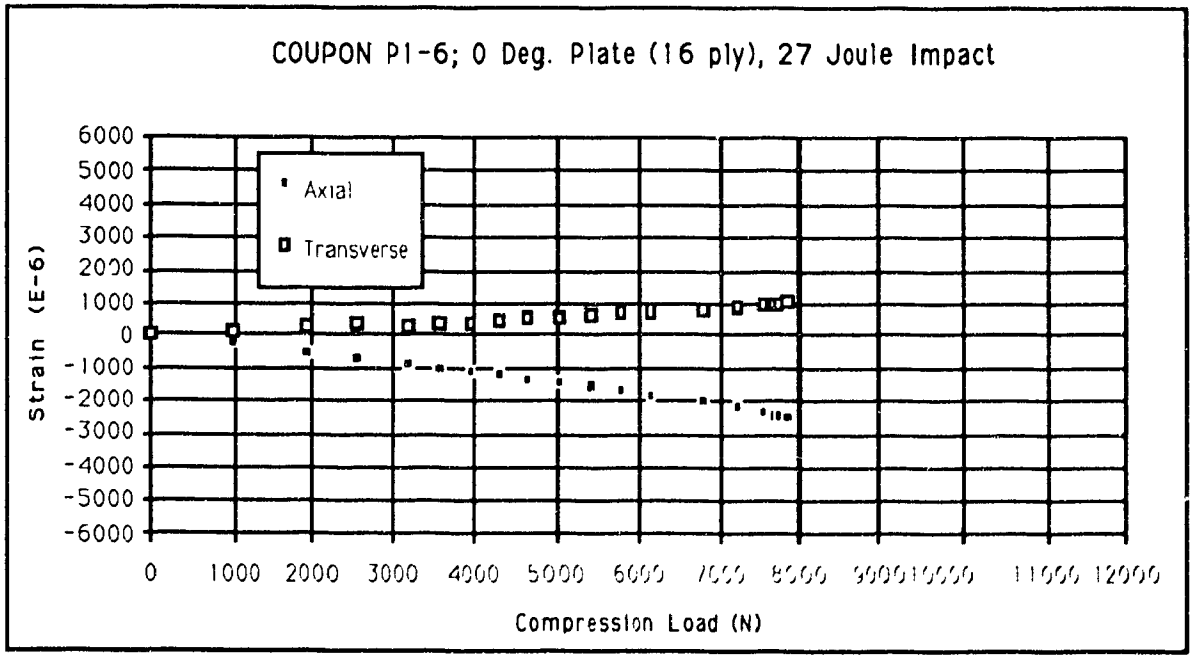

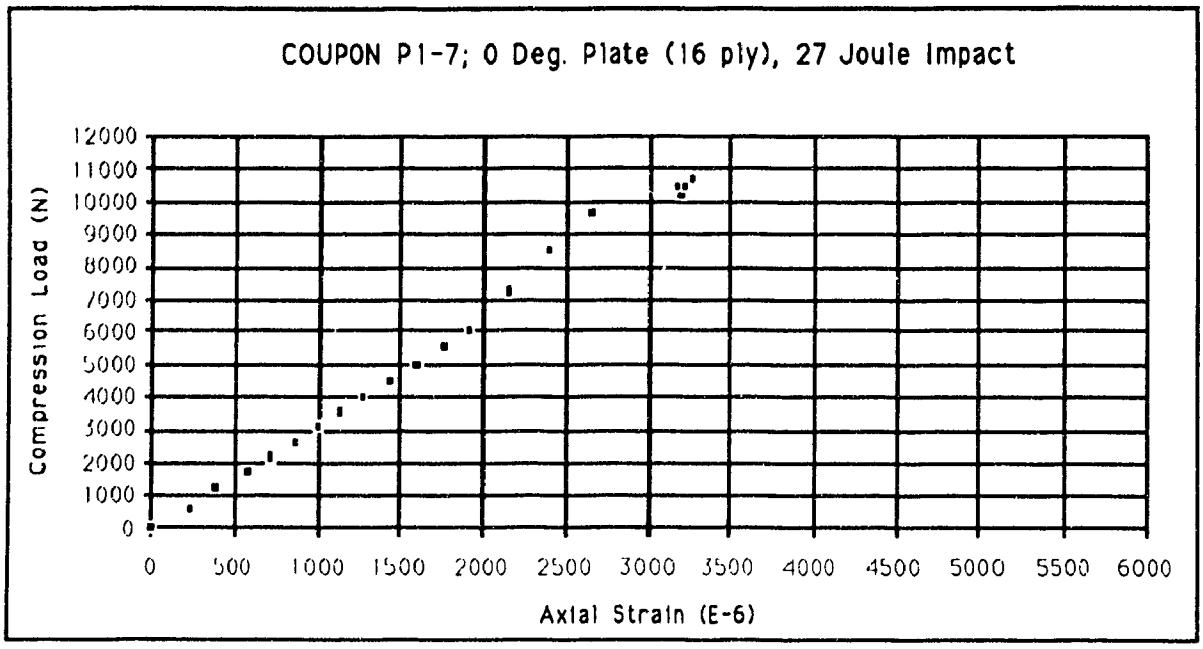

w = 12.31 mm
t = 2.01 mm

$$E = \frac{\Delta P / (w \bullet t)}{\Delta \varepsilon_a}$$

$\Delta P = (3950 - 800)$ N

$\Delta \varepsilon_a = (1250 - 250) \times 10^{-6}$

$E = 127.3$ GPa

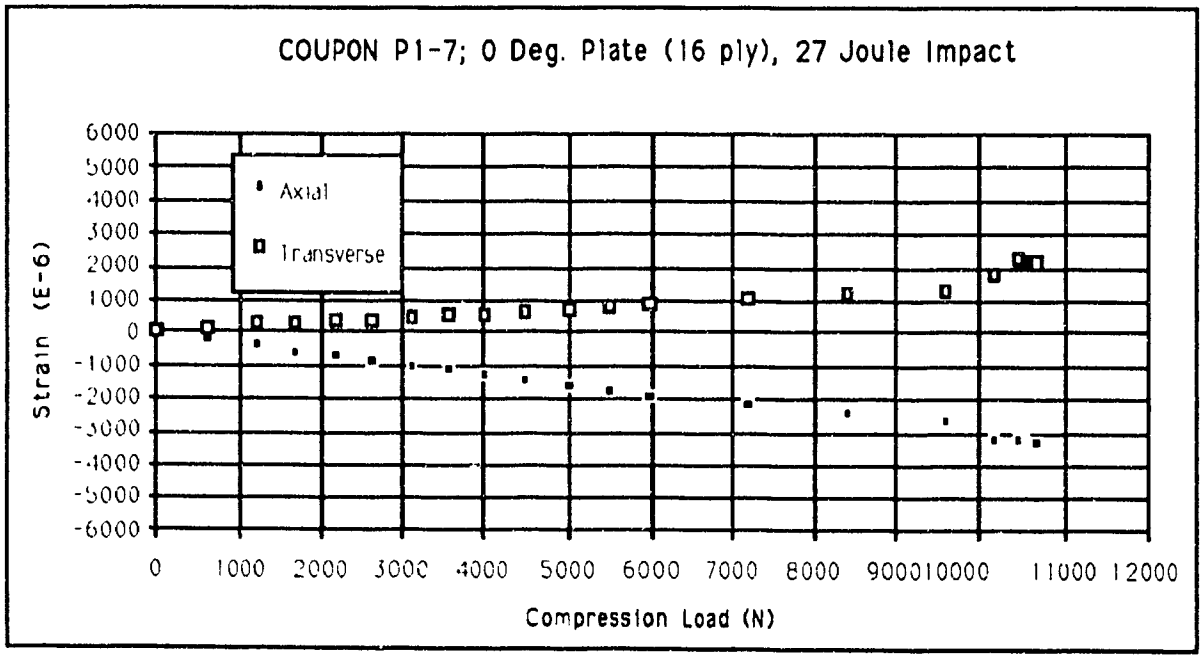

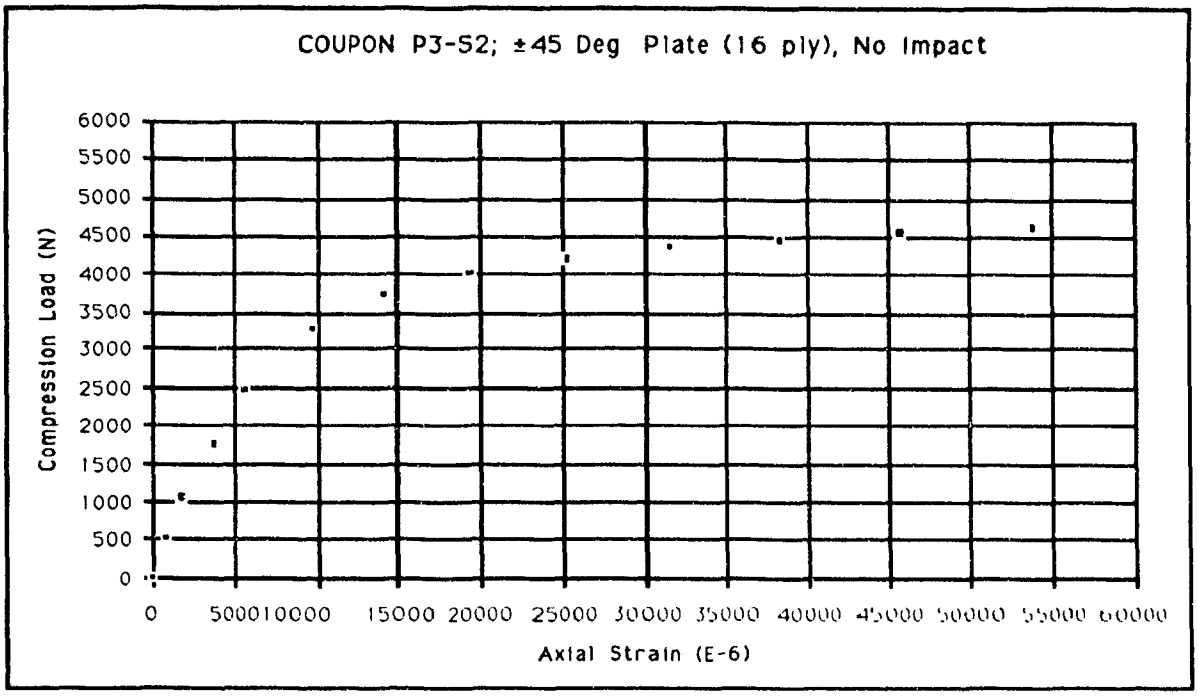

w = 13.01 mm
t = 2.04 mm

$$E = \frac{\Delta P / (w \bullet t)}{\Delta \varepsilon_a}$$

$\Delta P = (2375\text{-}0)$ N

$\Delta \varepsilon_a = (5000\text{-}0) \times 10^{-6}$

$E = 17.9$ GPa

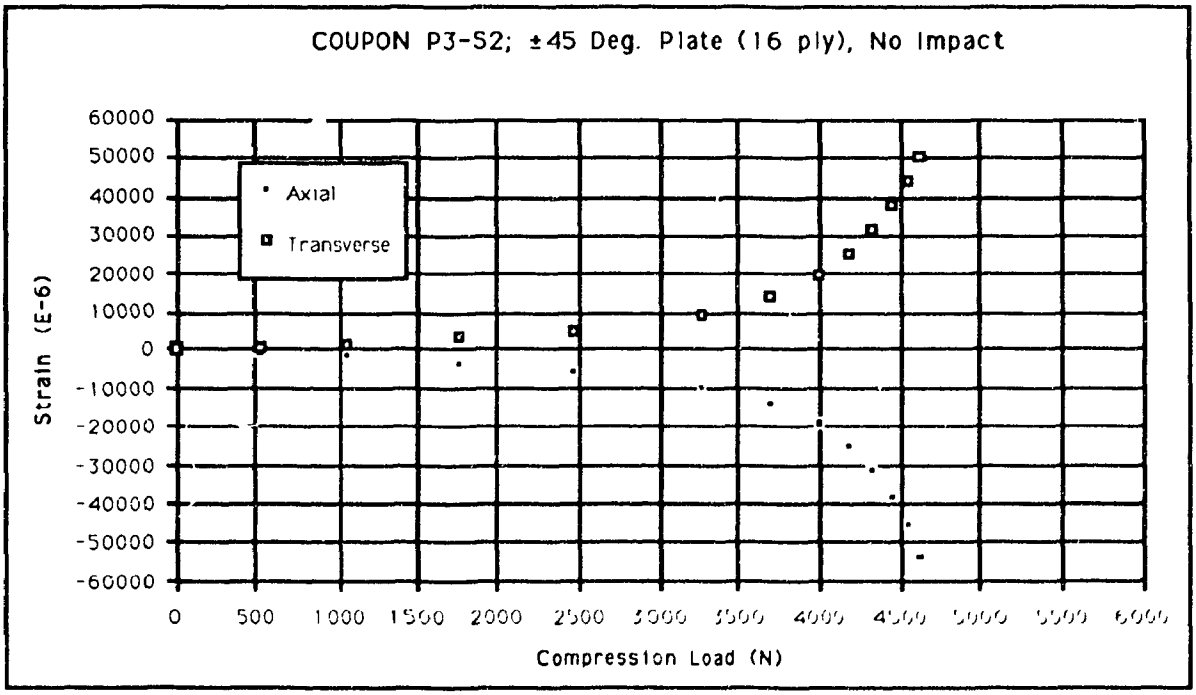

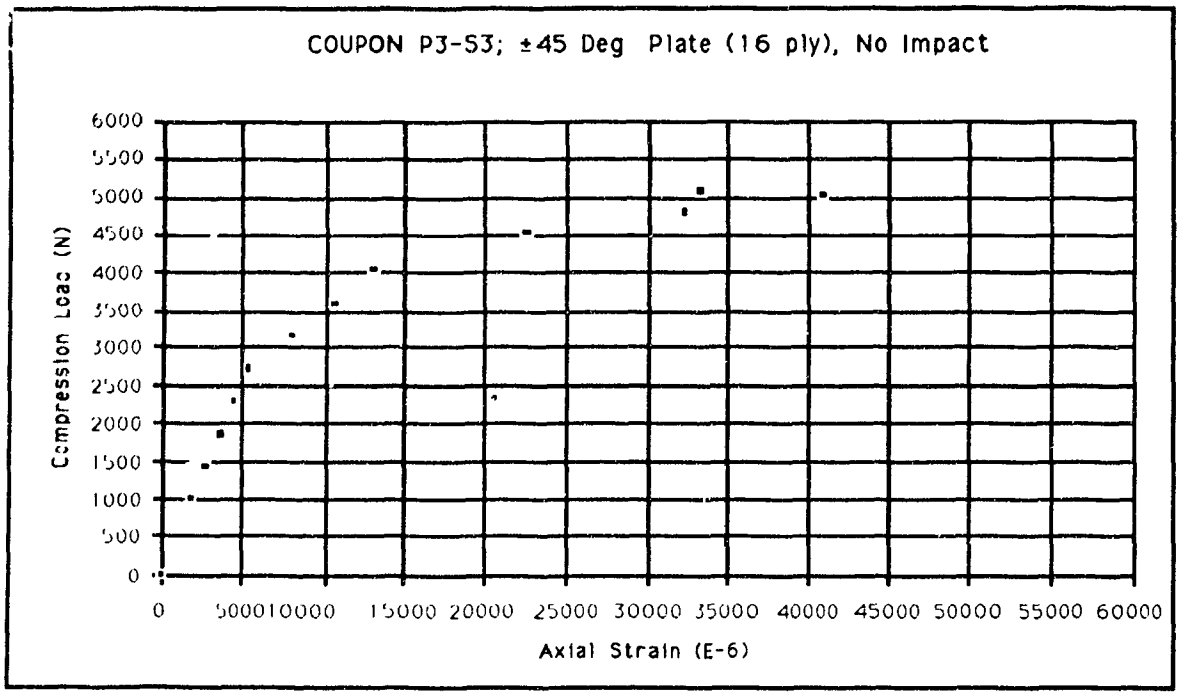

$w = 13.25\ mm$

$t = 2.04\ mm$

$$E = \frac{\Delta P / (w \bullet t)}{\Delta \varepsilon_a}$$

$$\Delta P = (2375\text{-}0)\ N$$

$$\Delta \varepsilon_a = (5000\text{-}0) \times 10^{-6}$$

$$E = 17.6\ GPa$$

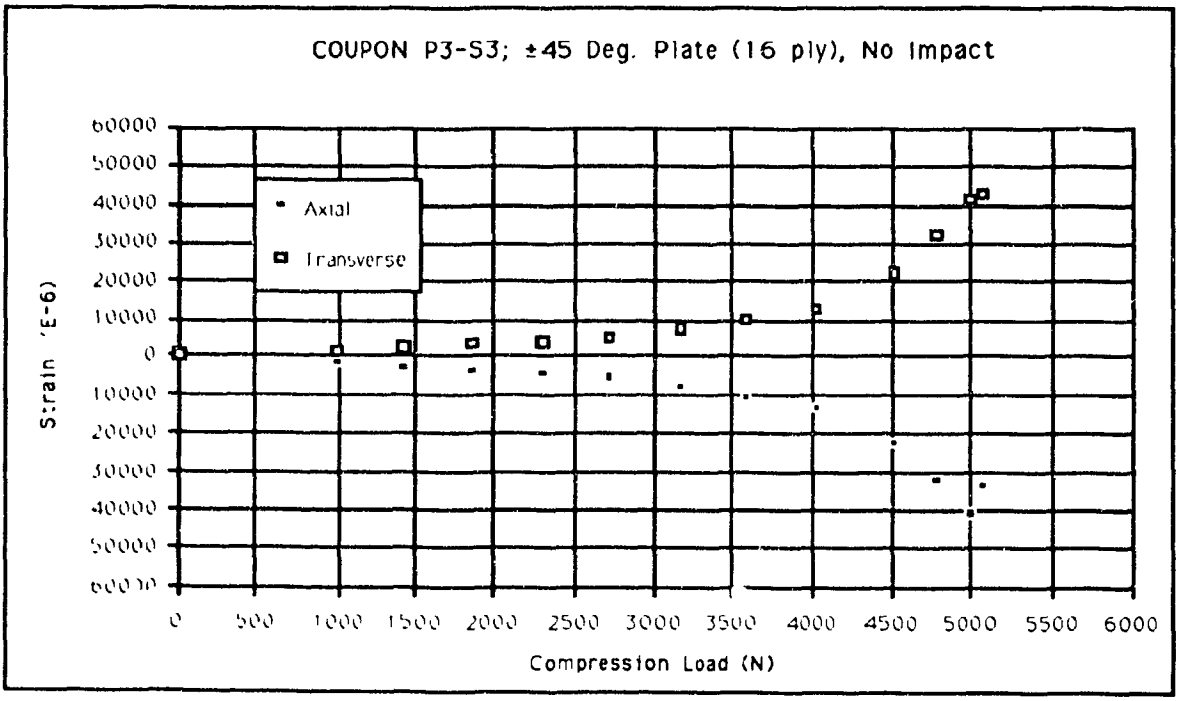

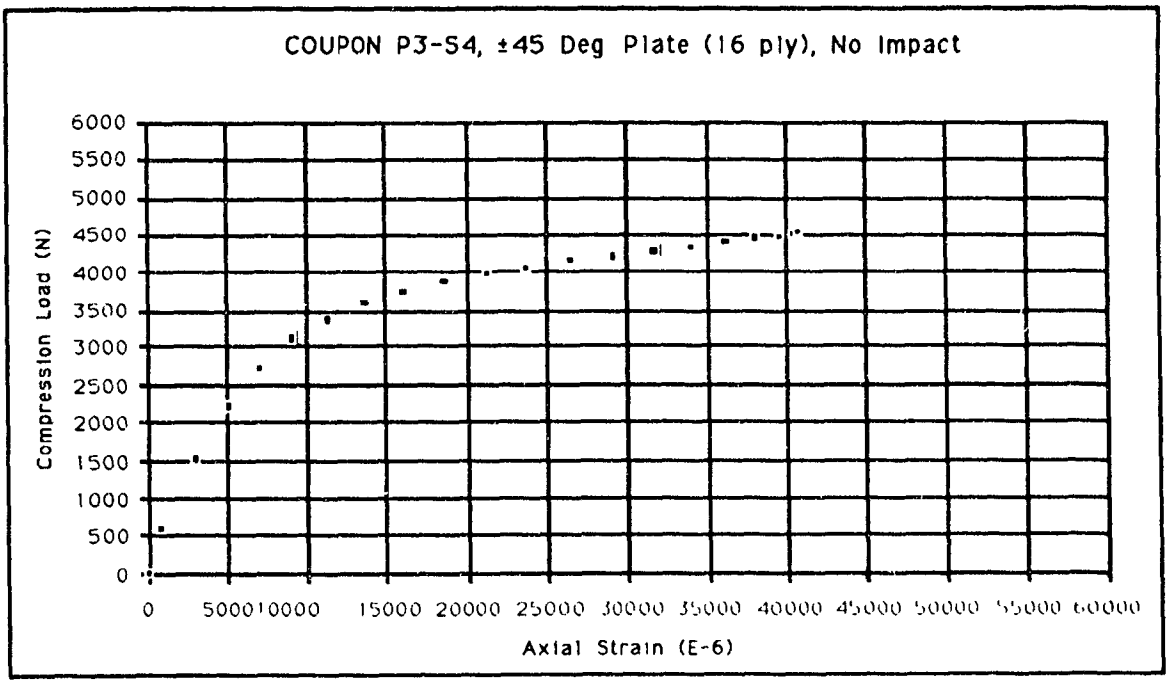

w = 12.98 mm

t = 2.04 mm

$$E = \frac{\Delta P / (w \bullet t)}{\Delta \varepsilon_a}$$

$\Delta P = (2300\text{-}0)$ N

$\Delta \varepsilon_a = (5000\text{-}0) \times 10^{-6}$

$E = 17.4$ GPa

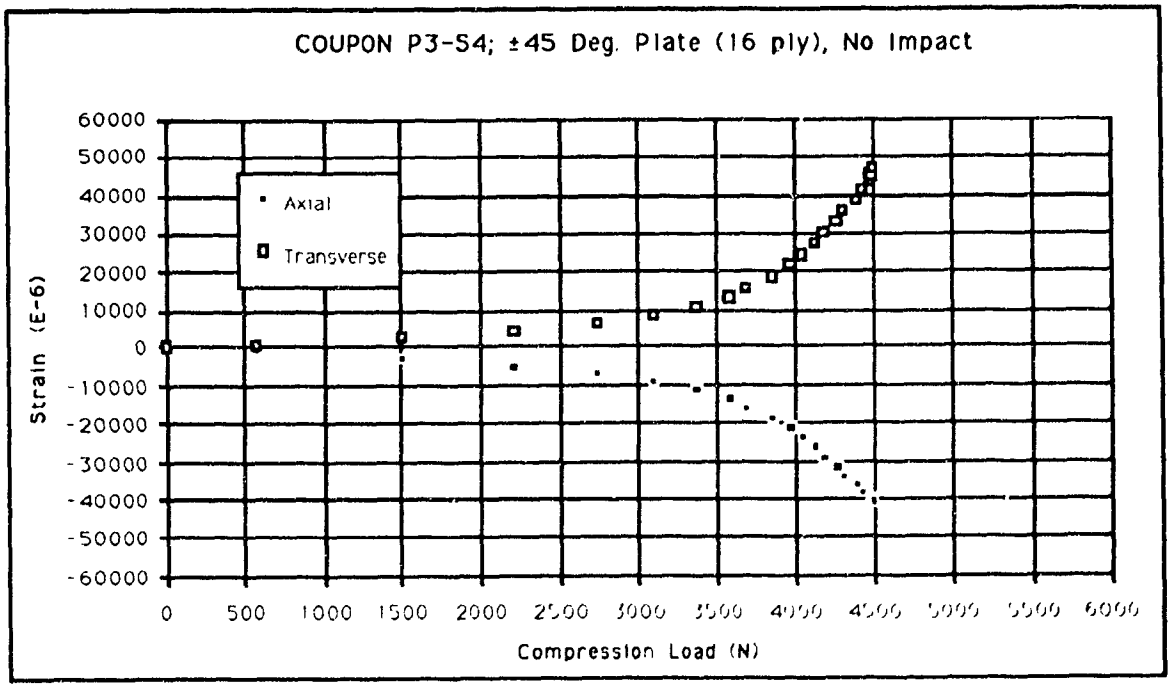

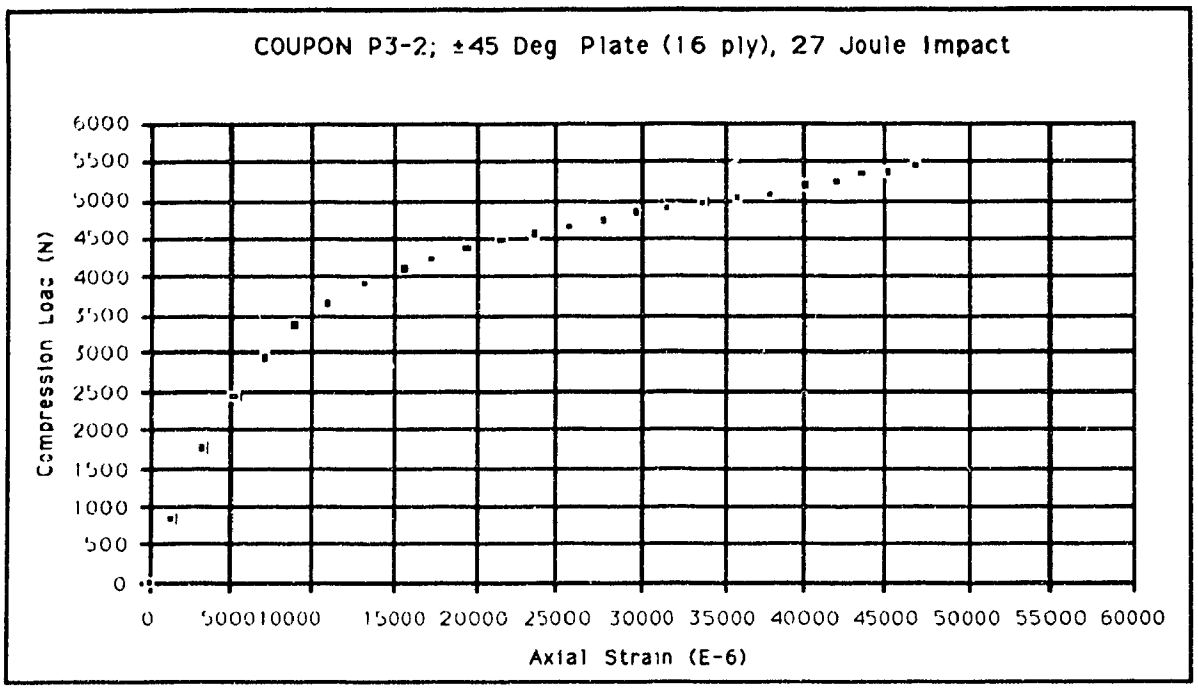

w = 13.91 mm

t = 2.04 mm

$$E = \frac{\Delta P / (w \bullet t)}{\Delta \varepsilon_a}$$

$\Delta P = (2200\text{-}0)$ N

$\Delta \varepsilon_a = (5000\text{-}0) \times 10^{-6}$

$E = 15.5$ GPa

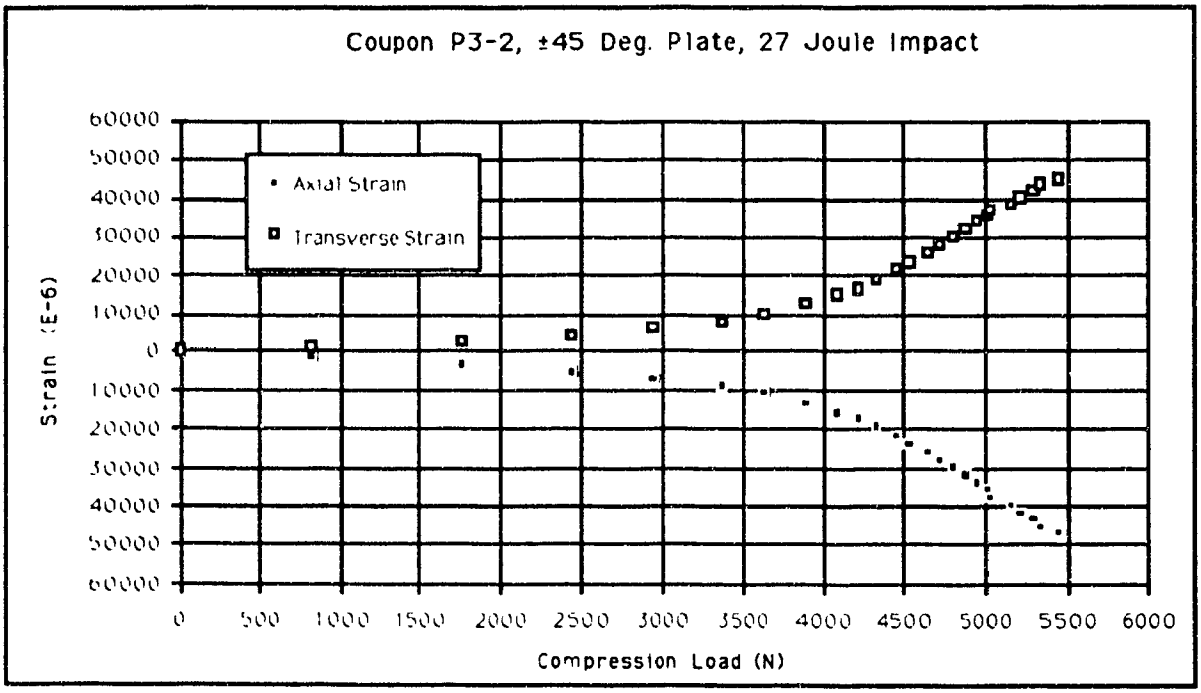

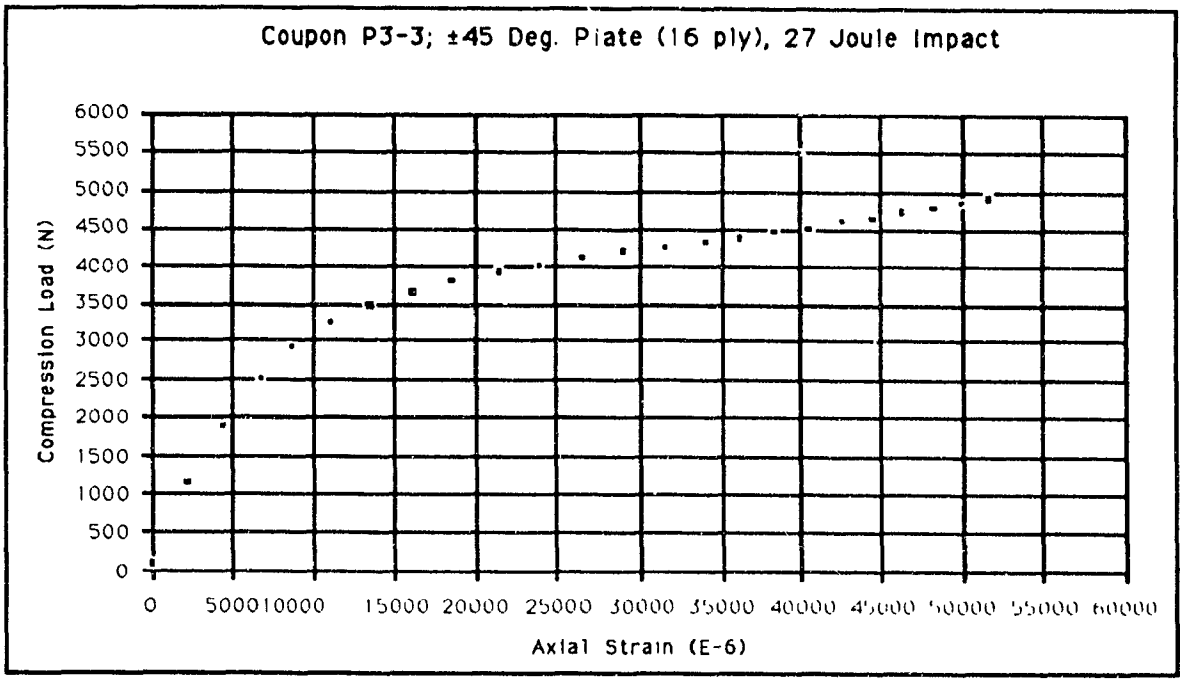

$w = 13.59$ mm

$t = 2.04$ mm

$$E = \frac{\Delta P / (w \bullet t)}{\Delta \varepsilon_a}$$

$\Delta P = (2200\text{-}0)$ N

$\Delta \varepsilon_a = (5000\text{-}0) \times 10^{-6}$

$E = 15.9$ GPa

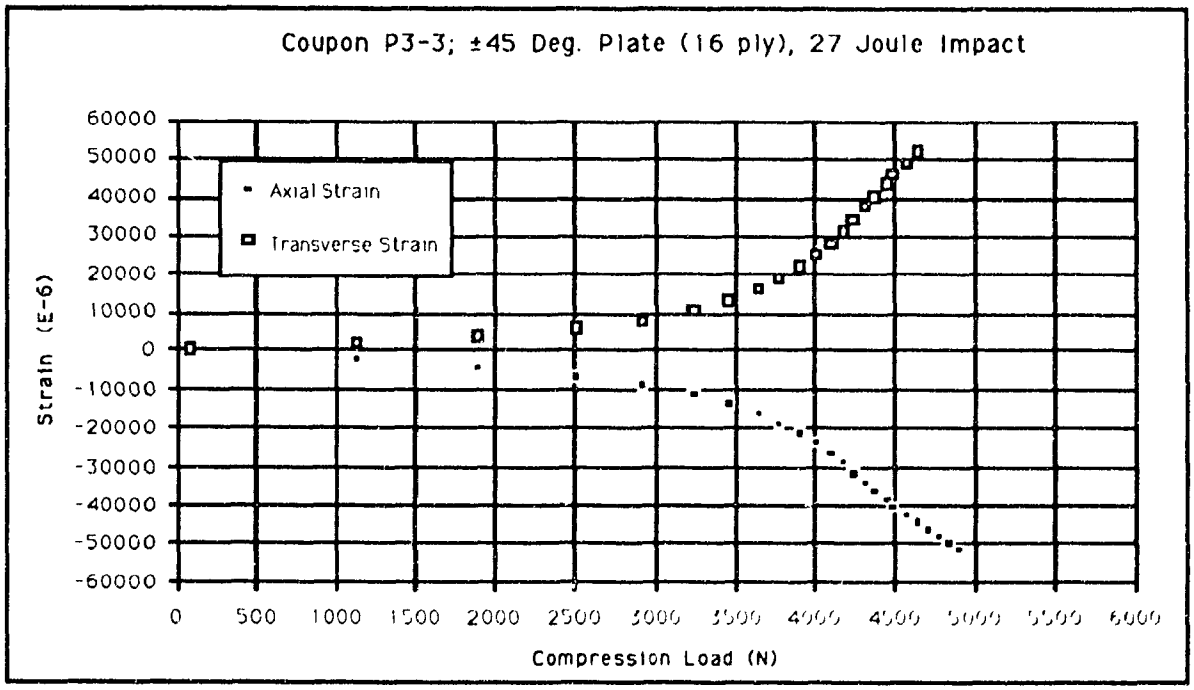

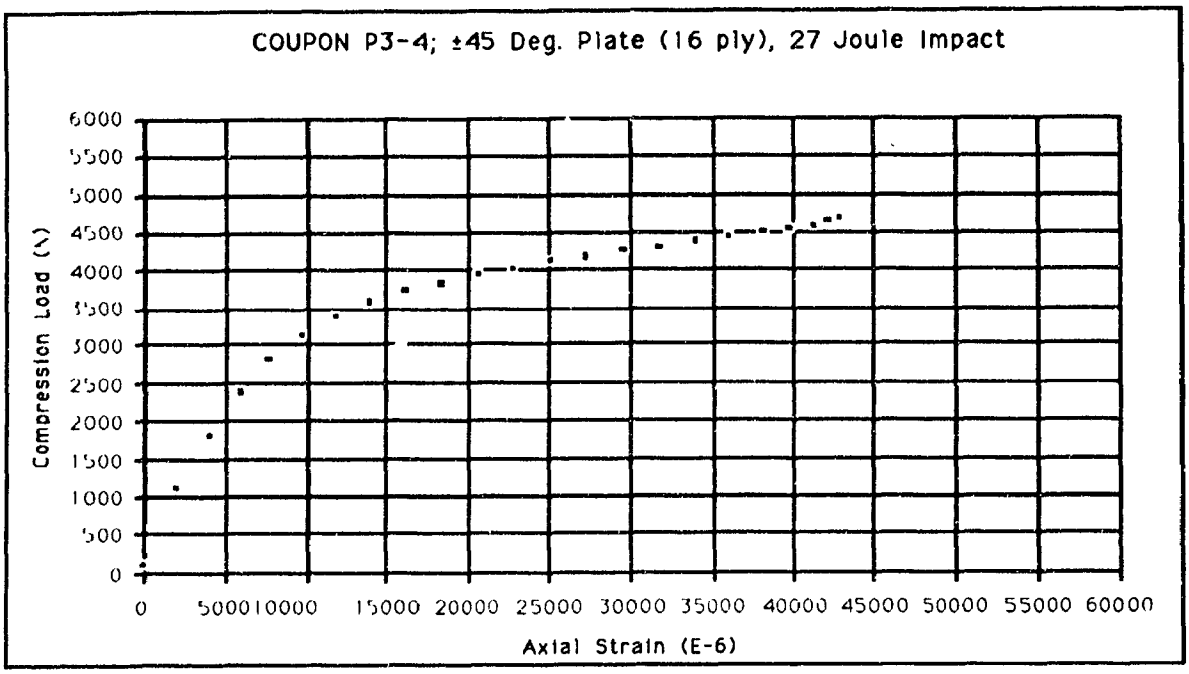

$w = 13.11$ mm

$t = 2.04$ mm

$$E = \frac{\Delta P / (w \bullet t)}{\Delta \varepsilon_a}$$

$\Delta P = (2150\text{-}0)$ N

$\Delta \varepsilon_a = (5000\text{-}0) \times 10^{-6}$

$E = 16.1$ GPa

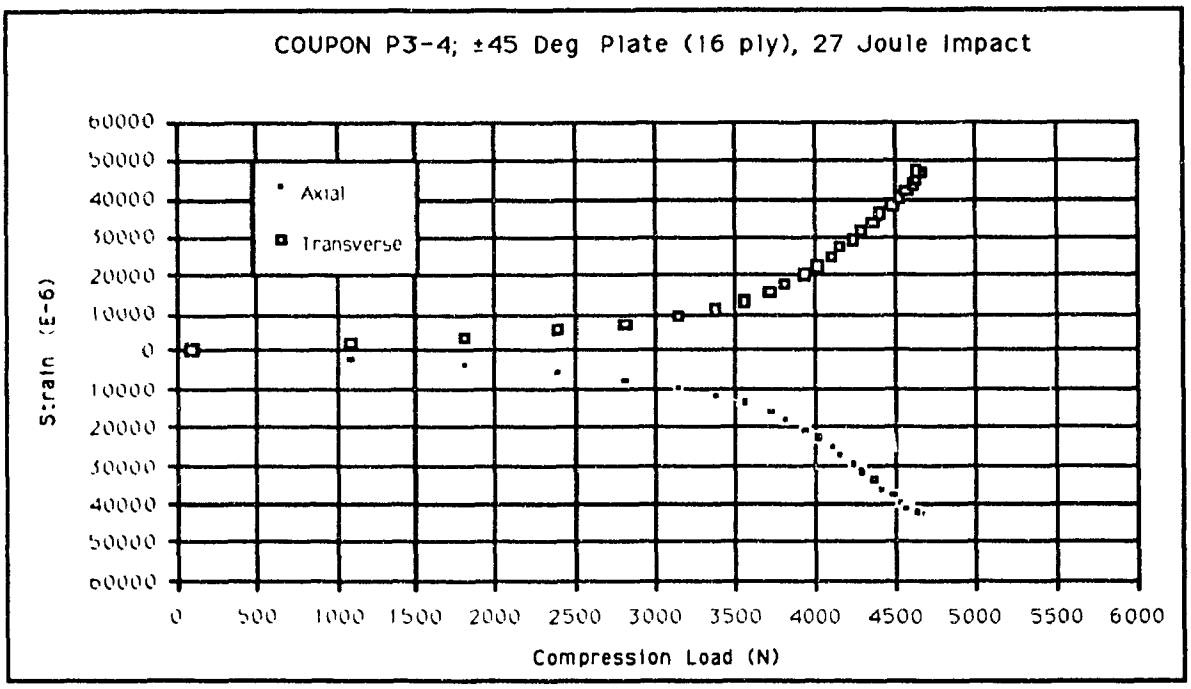

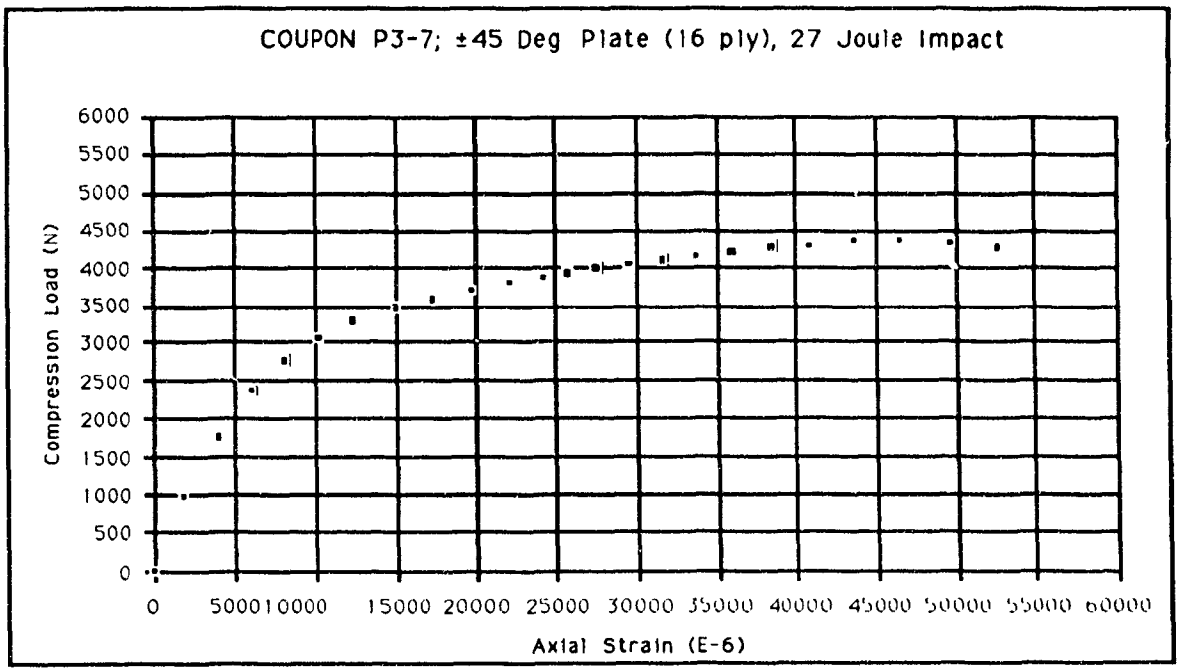

$w = 12.73\ mm$

$t = 2.04\ mm$

$$E = \frac{\Delta P / (w \bullet t)}{\Delta \varepsilon_a}$$

$\Delta P = (2000\text{-}0)\ N$

$\Delta \varepsilon_a = (5000\text{-}0) \times 10^{-6}$

$E = 15.4\ GPa$

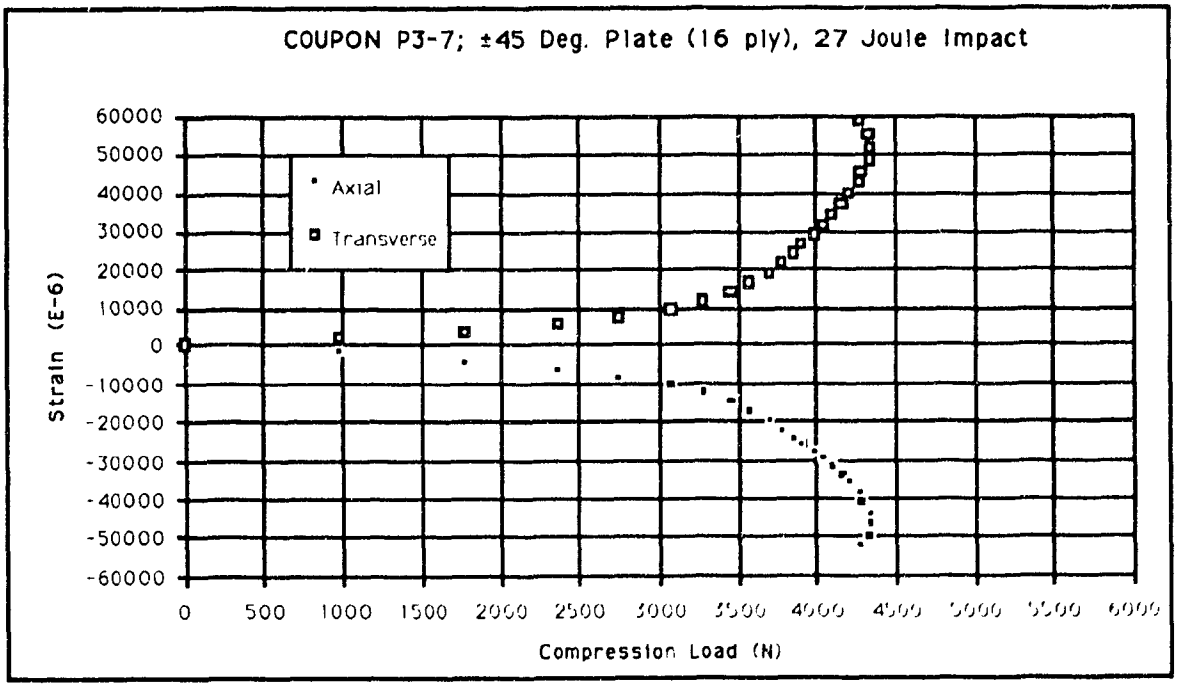

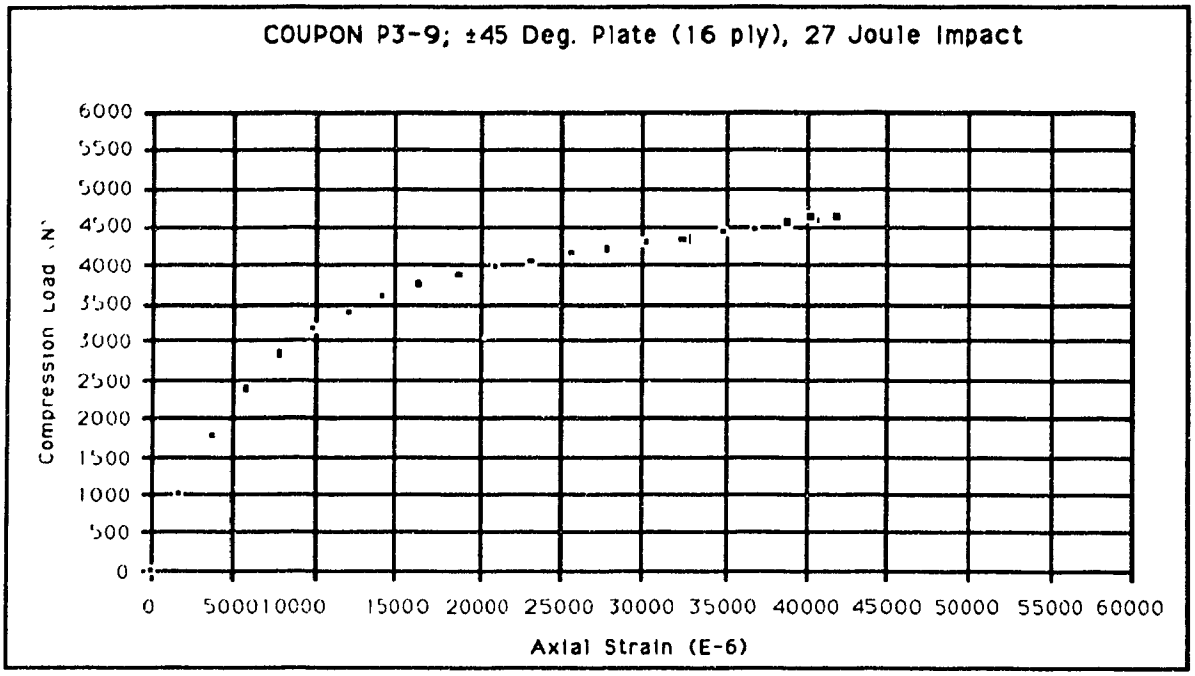

w = 12.83 mm

t = 2.04 mm

$$E = \frac{\Delta P / (w \bullet t)}{\Delta \varepsilon_a}$$

$\Delta P = (2050 - 0)$ N

$\Delta \varepsilon_a = (5000\text{-}0) \times 10^{-6}$

$E = 15.7$ GPa